Cranfield UNIVERSITY

Cranfield University
Cranfield
Bedfordshire MK43 0AL
England
Fax +44 (0) 1234 752391
Tel +44 (0) 1234 750111

David Richardson

Unsteady aerodynamics of high work turbines

Department of Aerospace Sciences, School of Engineering,
Cranfield University

Engineering doctorate Thesis.

October 2009

Academic Supervisor: Dr David MacManus, Cranfield University
Industrial Supervisor: Dr Frank Haselbach, Rolls-Royce plc

Abstract

One method aircraft engine manufactures use to minimize engine cost and weight is to reduce the number of parts. A significant reduction includes reducing the turbine blade count or combining two moderately loaded turbines into one high-work turbine. The risk of High Cycle Fatigue in these configurations is increased by the additional aerodynamic forcing generated by the high blade loading and the nozzle trailing edge shocks. A lot of research has been done into the efficiency implications of supersonic shocks in these configurations. However what is less well understood is the resulting unsteady rotor forces. These unsteady aerodynamics aspects are the focus of this research.

The research investigates where manufacturers might concentrate their resources to reduce Direct Operating Costs (DOC). It compares the relative financial implications of disruption events to the cost of reducing DOC by further efficiency gains. The technical aspects of the research use computational aerodynamic modelling of a high work turbine to explore the unsteady aerodynamics and the resulting rotor forces. Investigation of parametric models into the effect of reaction, axial spacing, pressure ratio, the nozzle wake profile and the significance of the rotor boundary layer in dissipating the high gradient shocks is also investigated. Data from an experimental test program was used to characterise sub- and super-critical shock boundary layer interactions to determine if they are a significant forcing function.

The primary conclusions from this research include the relative merits of targeting resources into reducing disruption events rather than the relatively small financial gains which might be gained through further efficiency improvement by researching advanced technologies. The computational method is validated against an experimental dataset from a high-speed turbine stage rig. Overall, good agreement is found between the measurements and the predictions for both the detailed unsteady aerodynamics as well as the important rotor forces. The effect of different computational modelling standards is also explored.

The relative significance of the primary aerodynamic forcing functions such as the nozzle wake and trailing edge shock system is evaluated. Generally the rotor forces are found to increase with lower reaction, reduced axial spacing and higher pressure ratio. However the phasing of the forcing functions is found to be a critical aspect in determining the resultant net unsteady forces. The sub-critical shock boundary layer interaction is determined to be a second order effect in relation to the other primary forcing mechanisms, however the supercritical shock boundary layer interaction is shown to be a potential contributory factor in rotor forcing.

Finally, several recommendations are proposed which turbine designers should apply in the event that rotor forcing is considered to be a significant concern.

Acknowledgements

The author would like to primarily thank my long suffering, professional, patient supervisor for his continued support through a change in project, and some difficult personal circumstances, Dr David MacManus. I am also grateful to the Cranfield workshop staff for their technical assistance and the generation of test models, specifically Derek Giles and John Thrower. I would like to thank David Mann of Fluent for his considerable technical input into the CFD aspects of this research.

The author would like to acknowledge the support of the sponsors of this project, Rolls-Royce and Dr Guillermo Paniagua of the von Karman Institute for Fluid Dynamics, who provided test data and descriptions.

Additionally I would like to recognize my family's contribution, including my inspiration, my father Brian Richardson, and my patient supportive wife Elizabeth who did well to recognize me after long hours away from home. And finally my entertaining distraction, my little boy Ciaran, who kept insisting "don't go to work daddy" and backed it up with an iron grip on my leg that I think might have permanently restricted blood flow.

Table of contents

List of figures

List of Tables

Nomenclature

Acronyms:

CFD	Computational Fluid Dynamics.
HWSS	High Work Single Stage.
PS	Pressure Side
SS	Suction Side
LE	Leading Edge
TE	Trailing Edge.
ISO	International Organisation for Standardization
VKI	Von Karman Institute
TATEF	Turbine Aero-Thermal External Flows
SBLI	Shock-Boundary-Layer-Interaction
LCF	Low-Cycle Fatigue
HCF	High-Cycle Fatigue
RR	Rolls-Royce
HP	High-Pressure
IP	Intermediate-Pressure
FEM	Finite Element Model
RANS	Reynolds-Averaged Navier-Stokes
ANTLE	Advanced Near Term Low Emission
SST	Shear Stress Transport
BC	Boundary Conditions
RPS	Revolutions Per Second
RPM	Revolutions Per Minute

η	Efficiency [-].
m	Mass flow [Kg / s]
A	Cross sectional area [m2]
F	Force[N] (subscript tangential, axial or modulus)
R	Gas constant [J / Kg K]
T	Total temperature [K]
δ	Boundary layer thickness [m]
γ	Ratio of specific heat capacities (Cp / Cv)
ν	Kinematic Viscosity [m2/s]
μ	Dynamic Viscosity [kg·m−1·s−1]
Re	Reynolds number [-].
U	Velocity [m/s]
a	Speed of sound [m/s]
Ps, p	Static pressure [Pa]
R	Stator-to-rotor-pitch ratio [-]
N	Rotational Speed [RPM]
P	Total Pressure [Pa]
MIS	Isentropic Mach number [-]
ρ	Density [kg/m3]
u; v; w	Velocity magnitude (m/s); also written with directional subscripts (e.g., vx, vy,vz, vr)
k	Kinetic energy per unit mass (J/kg, Btu/lbm)

ε	Turbulent dissipation rate (m2/s3)
ω	Specific dissipation rate (s−1)
x_g	axial distance between nozzle TE and rotor LE

$$\text{Capacity}(Q) = \frac{\dot{m}\sqrt{T_{01}}}{AP_{01}}$$

$$\textbf{Reaction}(\lambda) = \frac{t_2 - t_3}{T_{01} - t_3}$$

$$\textbf{Specific work} = \frac{c_p \Delta T_{01-03}}{T_{01}}$$

$$\textbf{Stage loading (at 50\% radial span)} = \frac{c_p \Delta T_{01-03}}{U_{50\%}}$$

$$\text{Turbine efficiency } (\eta_{TURB}) = \frac{T_{01} - T_{03}}{T_{01}\left[1 - \left(\frac{1}{P_{01}/P_3}\right)^{(\gamma-1)/\gamma}\right]}$$

1 Introduction

1.1 Overview

The design and manufacture of modern jet engines is a complicated, expensive undertaking. One method of reducing the hardware and operating costs (by weight reduction) is to reduce the number of parts. This could be achieved in the turbine by reducing the blade count, or even combining two moderately loaded turbines into one high-work turbine. To maintain comparable shaft power, these high-work turbines operate in the supersonic flow regime, which results in shocks emanating from the nozzle and rotor trailing edge (TE). Along with the potential flow field and wakes, shocks are a significant aerodynamic forcing function which can lead to High-Cycle Fatigue (HCF).

The detailed method of evaluating component life (including HCF) requires representative models, typically utilizing Computational Fluid Dynamics (CFD). The CFD models provide Boundary Conditions (BCs), in the form of unsteady surface pressures for Finite Element (FE) stress models. The CFD models must accurately model the significant forcing functions, including the wake, potential field, secondary flow and the high gradients of static pressure across shocks and their propagation through the nozzle and rotor boundary layer (BL).

Initially this study explores the airline Direct Operating Costs (DOC) and evaluates the relative merits of reducing cost by further efficiency gains and reducing 'disruption events'. The technical aspects of the research involved using CFD to model a well instrumented high-work, supersonic-turbine test rig, to evaluate the modelling requirements, quantify the rotor forces, and develop a generic understanding of how the flow develops. The study includes modelling how sensitive rotor forces are to axial spacing, reaction, pressure ratio and the profile of the nozzle wake. A complimentary experimental programme was carried out to characterise sub- and super-critical SBLIs, including the frequency of the unsteadiness. The characterization was used to evaluate if the SBLI is an important factor in HCF analysis.

1.2 Background

Modern high-pressure turbines can operate at efficiencies in excess of 90% {{13 Vascellari, M. 2004}}. With further gains in operational efficiency likely to be prohibitively expensive, manufacturers of aero-engines are currently emphasising parts reductions to reduce hardware and operating costs. This generic drive towards higher loadings is applicable to both 3-shaft and 2-shaft architectures. A notional example of a three shaft aero engine is included in Figure 1.

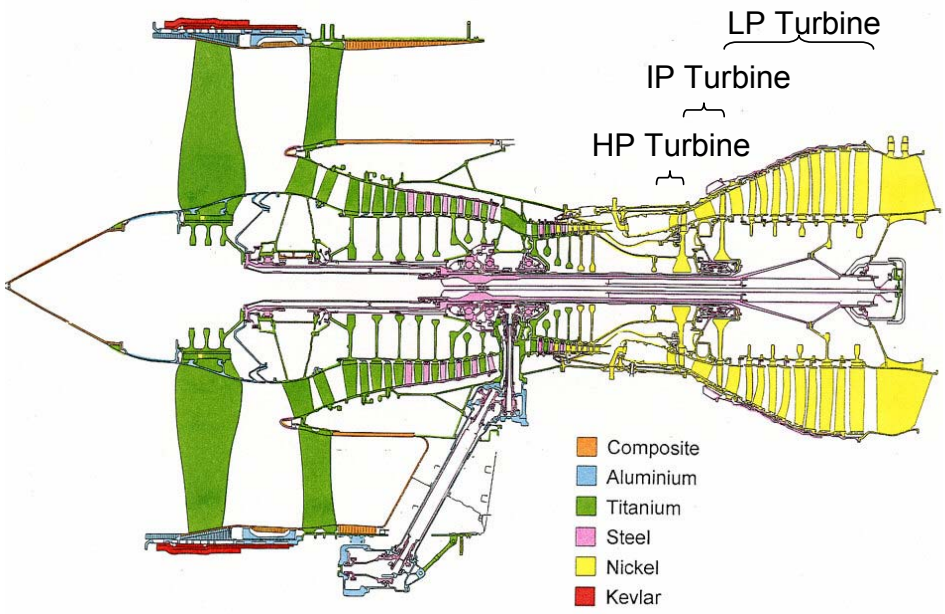

Figure 1 Example of a three shaft aero engine

A substantial part reduction would be to combine two relatively moderately loaded turbines into a High-Work Single Stage (HWSS) turbine. The considerable challenge is to design a single highly loaded turbine that has competitive performance, life and weight that operates in the transonic and supersonic flow regime.

The determining factor in deciding on the application of a single or two-stage HP turbine is the HP compressor pressure ratio. A single stage HP turbine is appropriate for smaller sized engines where the HP compressor operates at a low pressure ratio (Figure 2). In mid-sized engines, where the HP compressor operates at a high pressure ratio, the application of a two-stage HP turbine is more appropriate to avoid excessive blade loading. Potential applications for the introduction of a single stage supersonic HP turbine include helicopter and small turbofan engines.

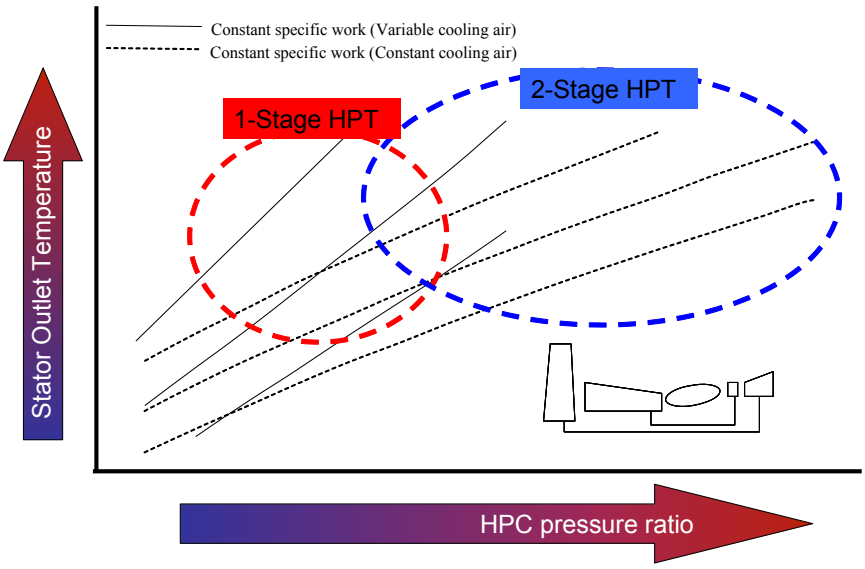

Figure 2 Stator Outlet temperature (SOT) as a function of HP compressor pressure ratio for constant HP turbine specific work (ΔH/T)

Many aero-engine manufacturers are currently investigating HWSS turbines. Unlike conventional turbines where the wake and potential field dominate, for HWSS turbines this study demonstrates the shock is the prominent forcing function. Due to the relative rotation of the turbine, the shock sweeps from the crown of the downstream rotor blade towards the leading edge (LE) with the accompanying, characteristic pressure pulse. The magnitude of the pressure pulse is predominantly a function of the vane exit Mach number and the incidence angle which can produce large shock lambda footprints.

This study investigates previous CFD models of high work turbines and compares the pressure amplitudes and phase with experimental results, acquired with fast response transducers, which are buried in the rotor aerofoil. The investigation has demonstrated current techniques may not match the unsteady pressures around the blade rows. One possible shortcoming of the current modelling technique is thought to include the the turbulence model selection and the mesh density application. Coarse spatial discretization will not capture the high gradients of density and pressure across shocks. Mesh density is also critical in the near wall region for capturing the complex flow within supercritical SBLIs.

1.3 Aim and activities

The aim of this research is to understand aerodynamic forcing within highly loaded turbines. The approach to achieve this aim is to:

- Develop and examine validated 3D computational models of a high work turbine .
- Characterise the flow within a highly loaded turbine with high fidelity quasi-2D CFD models. These models will be used to study the flow physics within high work turbines and to understand the primary forcing functions and their interactions.
- Examine the characteristics of SBLIs, specifically the influence on rotor forcing.

This approach is diagrammatically represented in Figure 3:

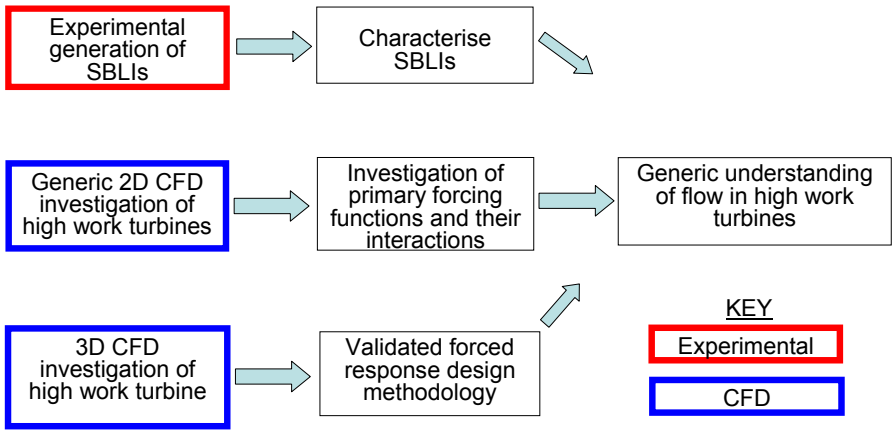

Figure 3 Diagrammatic representation of strategy to achieve project aim

2 Aircraft and engine cost breakdown

This chapter examines if the historical practice of reducing the Direct Operator Costs (DOCs) by efficiency gains is sustainable. An examination of DOCs shows a significant proportion of the costs are incurred from 'disruption events'. The study concludes that the most economical method of reducing DOCs is by designing engines with fewer parts that are less prone to disruption events rather than targeting prohibitively more expensive smaller efficiency gains. The study is complicated by modern contractual obligations between the aero-engine manufacturer and operator which require the manufacturer to provide engine availability. Potentially this could mean high costs to the manufacturer in the event of disruption events. The research element includes structured interviews with senior engineers in the aero-engine industry to determine the manufacturers costs, specifically in capturing HCF issues.

With component efficiencies now in the low ninety percentages {Wisler, 1998}, and further gains becoming prohibitively expensive, the potential for reducing the DOC by further component efficiency gains is limited. Another way of reducing the DOC is to reduce the engine parts count, which reduces the materials costs and engine weight, and the number of unscheduled or disruption events. Disruption events cause considerable financial penalties and reputation damage to the airlines. Modern financial arrangements like 'power by the hour' make the manufacturer, not the operator, responsible for engine availability. Manufacturers are now emphasizing six-sigma or robust design to minimize the likelihood of disruption events.

Reductions in the engine parts count can be achieved by reducing the turbine blade count or even combining two moderately loaded turbine stages into a single stage high work turbine. If the blade count is reduced the designer needs to increase the work done by the remaining blades. Unlike conventional turbines, high work turbines have shocks propagating across the inter-row gap and in the blade passages which generate considerable additional rotor forcing. One of the significant challenges is to design a turbine stage that is resilient to these additional unsteady forces, ensuring that HCF does not result. The scale of the challenge is brought into context by an examination into the causes of unscheduled engine removals. Wisler reports that the turbine is more than twice as likely to be the cause of an unscheduled engine removal as the fan and compressor airfoils, the next most common reason for unscheduled engine removals {Wisler 1998}.

The financial aspects of redesigning a turbine blade that is susceptible to HCF at each stage of the engine program is included. This is broken into a discovery in the design phase, the development phase and on the wing (in fleet). To prevent considerable increases in development costs and disruption events in the fleet a validated approach to predicting unsteady forces, a vital contribution to predicting HCF is proposed.

2.1 Cost reduction through improved efficiency

Airlines use DOCs as a financial metric for business planning. DOCs include costs attributable to:

- Engine cost
- Engine weight
- Engine performance
- Maintenance costs
- Interest and depreciation costs
- Crew costs

It is becoming prohibitively more expensive (for progressively smaller performance gains) to reduce the airlines DOC by continuing the considerable historical SFC reductions achieved in the past 60 years (Figure 4).

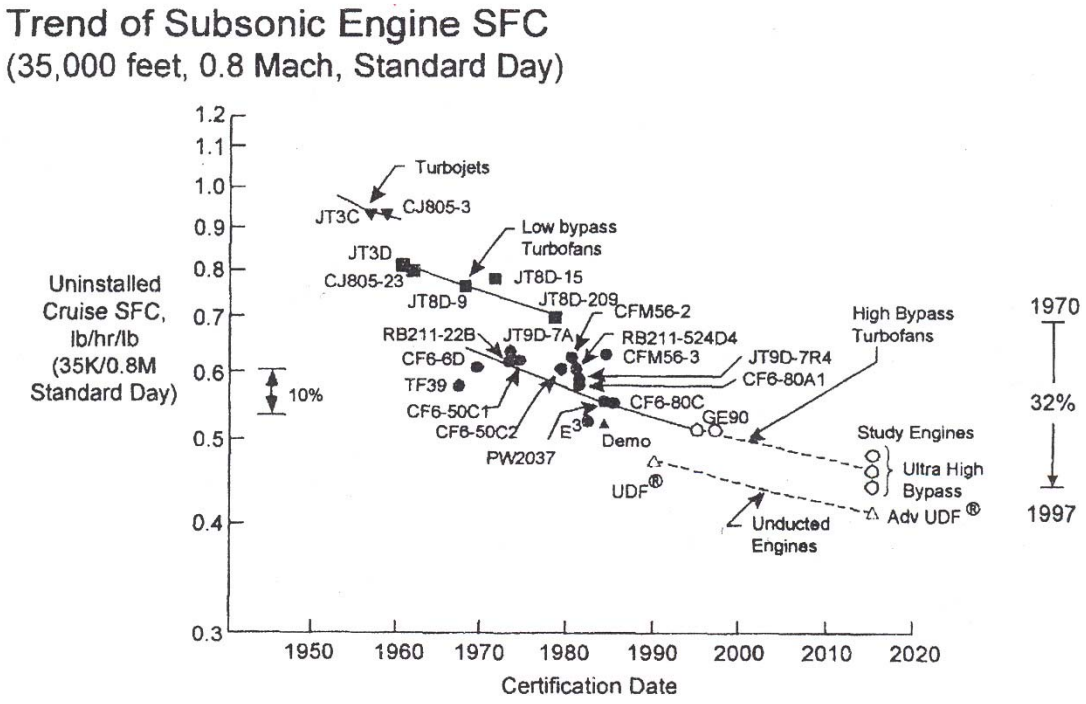

Figure 4 Trend of specific fuel consumption for subsonic engines {Wisler 1998}

Today comparable levels of technology prevail across the competition, with component efficiencies in the low nineties. At these high component efficiencies a one percent improvement in component efficiency would require a reduction in losses of approximately ten percent. A difficult task when achieving and maintaining tenths of a percent improvement throughout the engine life is challenging. Assuming the technical challenges were realized and all component efficiencies (i.e. fan, low pressure and high pressure compressor and turbine) were improved by one per cent, the high gearing means the DOC would only reduce by a modest amount.

2.2 Cost reduction through other methods

A more prudent investment that could deliver considerable DOCs savings would be to reduce:

- engine cost: Interest and depreciation account for 42% of engine DOC (a function of acquisition costs)
- engine weight
- maintenance costs.

Wisler estimates a 25% reduction in engine costs (maintenance and acquisition) would result in a 5% reduction in DOC {Wisler, 1998}. A comparable reduction would require all engine losses to be reduced by half. The engine cost and weight could be reduced by reducing the number of components in the engine (section 2.2.1). The maintenance costs could be reduced by applying processes such as six-sigma or robust design (section 2.6-2.7). To implement robust design processes there is a requirement for validated modelling tools. With regard to HCF this includes accurately modelling unsteady forces to reduce the occurrence of disruption events (section 2.3).

2.2.1 Cost reduction by reduced part count

Engine manufacturers are committing considerable resources into programs that reduce hardware and operating costs by reducing the parts count. The programs require comparable levels of engine performance to be maintained whilst reducing costs associated with:

- hardware
- product-redesign
- overhaul/repair cycle-time
- scrap and re-work
- warranty
- concessions and give-away

One method is to reduce the turbine blade count whilst increasing the loading on the remaining blades or even combining two relatively moderately loaded turbines into a single high-work turbine. High work turbines operate in the transonic and supersonic flow regime. The considerable challenge is to design a highly loaded turbine that operates in this regime that has competitive performance, life and weight. In this regime highly loaded turbine blades are subjected to shocks which emanate from the stator, which can lead to High Cycle Fatigue (HCF). If operator DOC reductions are to be realized the rotor must be resilient to these additional unsteady forces. Potentially the manufacturer might discover HCF issues in the design phase with computational techniques, in the development phase with static and flying test engines or in-service in the fleet. The costs significantly increase as the tooling costs and any contractual obligations are committed to. Even for conventional moderately loaded subsonic blades, the airlines costs can be considerable (see section 2.3).

2.3 Airline costs

Although effective designs and sufficient part quality are paramount in engine manufacture, a significant proportion of airline's costs are a consequence of unscheduled or disruption events. Satisfactory part quality and effective designs are necessary to reduce the costs associated with reliability and scheduled maintenance. Poor part quality reduces reliability and poor designs can make disassembly and assembly problematic, time consuming and consequentially more expensive. However significant costs are incurred by the operator when disruption events occur such as:

- IFSDs (In-flight engine shutdowns)
- ATB / DIVs (Air Turn Back / Diversions: to alternate airports due to engine problems)
- ABTOs (Aborted takeoffs)
- UERs (Unscheduled engine removals)
- Flight delays and cancellations

Even excluding the costs of shop visits, delays and cancellations, there are hidden costs the operator has to bear including costs for:

- Lost revenue from transferring passengers to alternative airlines
- Extra fuel used
- Overnight hotel accommodation
- Aircraft out of position (further cancellations)
- Engine removal at remote site (transport and labor)
- Future revenue lost from concerned passengers
- Crew costs
- Landing fees

It is estimated that the typical likely hidden costs incurred for each disruption costs the operator approximately 3% of annual fuel burn {Wisler 1998}. This cost will be passed onto the customer in the long term even for modern contracts such as 'power by the hour' (see section 2.7) which contractually oblige the engine manufacturer to provide engine availability.

Identification of disruption events in the design and development phase of an engine program is problematic. Reviews of modern engine programs that are currently in-service show that validation testing (which includes flight tests) did not capture 64% of disruptions. Many disruptions do not materialise until the engines are in service because static validation testing does not replicate in-service running conditions. To reproduce each engine cycle over the engine life would be prohibitively time consuming. A development cycle test is transitory, throttling up or down, without spending representative periods of time at the (cruise) operating condition, which means these tests are inappropriate for detecting maturity issues such as the detailed disruptions. Certification requirements have historically been the most important priority for development engines. Serious consideration is now being given to expand these tests to capture these issues before the engine is in service, which can be expensive to correct {Dawkins. A 2007}.

2.4 Unscheduled engine removal

A reduction in operational performance of any one of numerous different engine components might result in an unscheduled engine removal. An extract of data compiled over a two-year period which tracks the causes of unscheduled events, compiled by government agencies, airline operators and airframe manufacturers is presented in Figure 5 and Figure 6. The data does not detail absolute numbers, but relative causes for non-specific engines. The largest contributor to unscheduled engine removals are turbine airfoils (Figure 5), of which the stage 1 HPT rotor is the primary cause, more so than all of the other turbine blades put together (Figure 6). Interviews with experts have qualitatively determined that a significant turbine blade failing mechanism is blade vibratory response which in extreme cases can cause HCF.

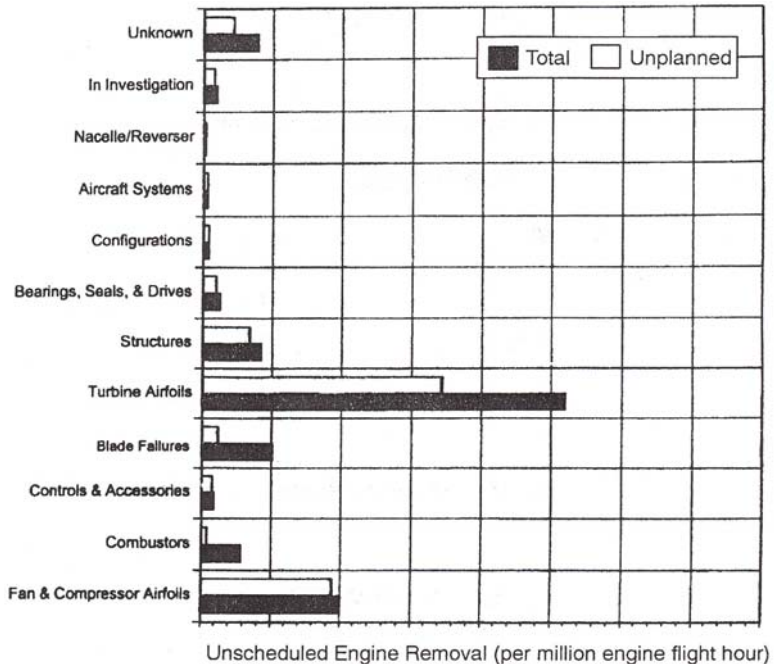

Figure 5 Causes of unscheduled engine removal over a two-year period (Wisler 1998-02)

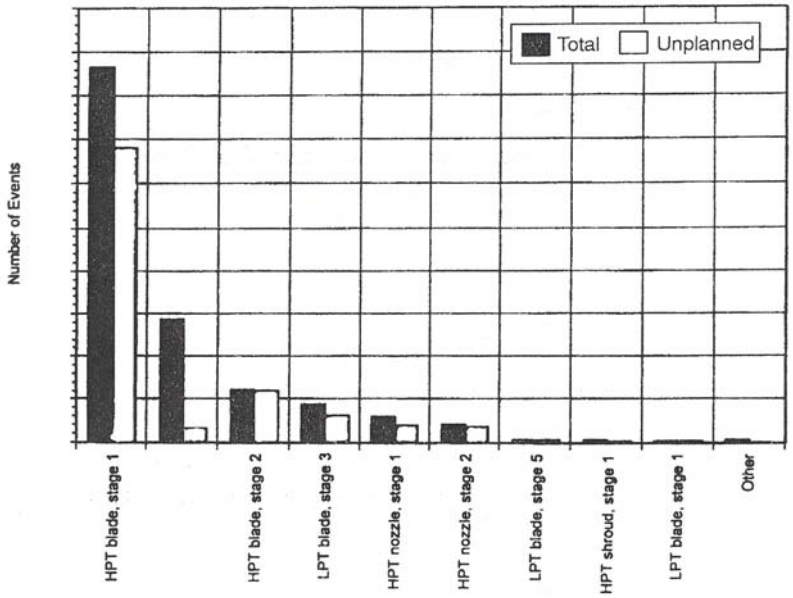

Figure 6 Main contributions to unscheduled engine removals by turbine component (Wisler 1998-02)

2.5 Economics of blade vibratory response

Blade vibratory response in any turbo-machinery component can cause airfoil cracking, failure, flow separation, etc, which can cause significant economic loss. Blade vibratory response is the most safety critical of all the interaction responses. The economical relevance of reducing the occurrence of flow induced blade vibratory response and its impact are critical to the engine business. It is estimated that the average engine development program has to resolve 2.5 serious HCF problems that account for between 10% and 40% of the total engine development problems (Wisler 1998-02). Wisler approximates that only half of the potential HCF problems are discovered in the development testing phase and that approximately 5% of the total engine maintenance cost can be directly related to HCF failures.

The Flutter-Free Turbo-machinery (FUTURE) collaborative project evaluation less pessimistically estimate that 90% of the potential HCF problems are discovered during the development testing, however the remaining problems account for nearly 30% of the total development cost and are responsible for over 25% of all engine distress levels (Fransson 2007). The US Air Force and Navy estimate that HCF-related problems are the leading cause of engine failure and cost approximately $400 Million (US) / annum.

Experimental testing and development of computational analysis tools are critical to engine manufacturers to minimise the occurrence of and limit the consequences of vibratory response.

2.6 Engine manufacturers costs

Development costs for new and derivative aero engines can exceed $1 billion and $500 million (US) respectively. Significant proportions of the design, manufacturing and maintaining of aero engine costs can be attributed to:

- Manufacturing losses in internal and suppliers shops (scrap, rework and repair).
- Reliability issues (Warranty costs, concessions and give-aways).
- Errors (missed operations e.g. heat treatment, non-destructive evaluation, assembly and maintenance errors).

Remedial costs can exceed several hundred million (US) dollars per annum which, ultimately, are passed onto the operator as DOC. Additionally the cost influences product quality and is a contributory factor in un-scheduled in service events. The challenge is how to reduce these incumbent costs which are several orders of magnitude above any cost savings incurred from further performance gains detailed in section 2.1. The issue is which attributes manufacturers prioritise designing for e.g.

- Design for technology
- Design for Manufacturability
- Design for reliability
- Design for ease of maintenance
- Design for low cost
- Design for ease of assembly
- six-sigma (DFSS or robust design)
- weight

- number of parts
- reduced complexity

The issue is further complicated by options for 'Power by the hour' type programs which contractually oblige the engine manufacturer to ensure engine availability (see section 2.7).

2.7 'Power by the hour'

'Power by the hour' provides operators with a fixed engine maintenance cost over a defined period of time. The power by the hour program is an after-sale fleet support option that provides

- Line maintenance replacement parts
- Scheduled and unscheduled engine maintenance
- Life limited part replacement
- Incorporation of service bulletin requirements
- Availability of unit exchange line replaceable units
- Continuous spare parts replenishment

For operators this defines cost projections, eliminating unscheduled maintenance costs by delegating responsibility of engine availability to the manufacturer. The program has implications for manufacturers engineering priorities, as they are contractually liable for significant financial penalties. Manufacturers typically emphasize DFSS or robust design. Robust components perform their intended function regardless of (assessed) manufacturing and operational variability.

DFSS is an analysis technique to determine the extent to which uncertainties in the model affect the results of an analysis. Based on a probabilistic characterization, DFSS enables the quality of a product to be quantified, including warranty costs and reliability, allowing manufacturers to optimize design variables to achieve a particular probabilistic level, such as Six Sigma (3.4 failures per million parts).

2.8 Aero-engine product development

Typically large civil aerospace groups are broken into three businesses:

- Operational Business units (OBUs)
- Project
- Fleet

The OBUs are Not For Profit (NFP) business units which design and manufacture components for project. Typically they are segregated by function i.e. compressors and fans, combustion and turbines. They deliver engine programs using a gated design process (Figure 7). The project department matures, certifies and assesses the performance of the engine with numerous engine tests according to an Engine Development Plan (EDP). The project team will stay together to develop the engine to a stage where it will enter in to service when the fleet engineering team will take over. The fleet engineering team supports the various engine customers and introduces any further modifications, such as performance enhancing modifications to reduce fuel consumption and emissions.

Potentially any HCF issues can be uncovered as the engine progresses through each of the businesses; however modifying any design which is prone to HCF becomes progressively more expensive as the engine program matures. As a proportion of engine development costs, this can range from less than 0.1% to re-design in the design phase (Chapman 2009) up to 20% to re-design an engine that is operating in the fleet (Dawkins. A 2007). Modifications might include targeting the excitation source or excited component by adapting the shape of the aerofoil, cutting the shroud back or tapering the blade, thickening the disc, including or changing the dampers, changing the materials or shank geometry to improve strength. Potentially any modification might have unwanted consequences, such as compromising performance.

2.8.1 Design phase

Typically new engine projects are initially investigated by an advanced project department. They evaluate the relative merits of different engine cycles incorporating input from the OBUs. This iterative process is completed by stage 1 of a gated design process (Figure 7). Upon successful completion of stage 1 the OBUs have component ownership. The turbine OBU is broken into thermofluid, stress and manufacturing sections. The thermofluid section is broken into three disciplines:

- Aerodynamics
- Cooling
- Performance verification

Initially the aerodynamics section refines the through flow model that the advanced project department define. This provides 2D boundary conditions which are used to define the 3D aerofoils. Typically HCF is evaluated using discrete CFD and stress models, although more advanced methods use coupled solvers which allow fluid-solid interactions. In the conventional design approach the aerofoil's boundary conditions (BCs) are passed to cooling and stress which evaluate component life using discrete cooling and finite-element (FE) models, feeding back any constraints that need to be incorporated into the aerofoil design, typically to accommodate cooling passage dimensions and any life requirements. In this conventional design approach HCF is investigated by the application of CFD unsteady pressure BCs onto discrete FE stress models. The stress department calculate if the unsteady forces are occurring at the resonant frequencies of the turbine blade. Although the manufacturing engineers input has been included into the Integrated Product Team (IPT), at this stage of the engine programme there has been no commitment to tooling i.e. the components only exist as computational models. This means that if the rotor blades are predicted to resonate then design modifications can be incorporated relatively cheaply. Using structured interview techniques, the author has quantified the cost to redesign at this early stage in the engine program as less than 0.1% of a typical engine development program (Chapman 2009).

2.8.2 Development phase

The engine program enters the development and validation phase at stage 3b of the gated design process (Figure 7). For new engine programs an engine manufacturer will usually form a project team that is dedicated to build the various engines in the development program and ultimately certify the engine as fit for passenger carrying service. This team will also form the interface with the air frame manufacturer to ensure certification of the whole aircraft package. The team will include a number of

engineering disciplines to support the development process which includes controls and systems engineers to support the engine testing phase. Testing could be at a multitude of test facilities around the world from hot to cold environment testing. Each engine is built to test particular components and is managed by the chief development engineer and the team of development engineers that work for him. The development engineer will ensure that the bill of materials for each engine build is to the required standard and that the parts fitted are adequate for the testing to be conducted, such as component life, especially for critical rotating components. Ultimately the development engineer will write the reports required to certify the particular part of the engine they are responsible for. These reports will need to be issued and agreed with the relevant air worthiness authorities to clear the engine for passenger carrying service. The development program is broken into distinct areas which address different considerations; maturity, certification and performance.

2.8.2.1 Maturity

For an engine to become commercially viable it requires a high ‘on wing’ life with little or no maintenance. Many aero-engine manufactures sell considerable numbers of engines now on a fixed service agreement so the manufacturer and not the operator are liable for any unscheduled engine removals or maintenance costs. Therefore the engine maturity is important to the manufacturer profit levels. To obtain a mature product a number of engine cyclic tests will be completed to simulate in-service operation with thousands of flight cycles achieved during testing. Other maturity testing provides data to correlate thermal computer predictions. A typical test for this is an engine 'Thermal Paint Test' where certain gas path components are painted with a special temperature changing coating. The engine is then tested for a short period of time and then stripped. The removed components can then be inspected for differences in paint colour, which indicate temperature gradients. The comparison with computer predictions can be used to fine tune the engine thermal model and feed in to the stress model to predict component life.

2.8.2.2 Certification

The testing involved during the Certification phase of an engine is usually agreed with the authorities prior to any engine testing. This agreement will define the specific engine manoeuvres required to test the turbo machinery and all other associated engine components including externals. A typical test to clear certification is a 150 hour ‘type test’, which will include harsh engine operation to simulate aircraft take off and climb with extended periods at high combustor outlet temperatures, to induce blade creep, and obtain high shaft speeds. When demonstrated an engine will be certified by the relevant authorities. Other testing includes strain gauge testing to establish static and rotating component stress levels. Another possible test requirement is an engine 'Fan Off' test, where a fan blade is deliberately released at engine take off and climb conditions and must continue to operate for a specific time to achieve a safe take off. Potentially any HCF issues could be discovered in the maturity phase, but are more likely to be discovered in the certification phase with bespoke engine testing.

During both the maturity and certification testing a number of performance curves will be completed to monitor engine condition. For future engine programmes though

the intention is to have dedicated engine builds to test specific engine components to optimise engine performance and thus emissions (Dawkins. A 2007).

2.8.2.3 Performance

As fuel prices increase and aircraft emissions become more apparent to the general public then engine performance is and always has been vitally important to an engine maker. If an engine does not meet its contractual performance targets then compensation to the air frame manufacturer may be required or worst still the engine may not be viable to fly. This would mean a costly redesign of the engine to achieve the required performance levels.

The main measure of engine performance is the fuel economy and is usually expressed as 'Specific Fuel Consumption' (SFC). The SFC is the relationship between fuel used and the engine thrust developed such that an ideal engine would require low amounts of fuel to produce the highest level of thrust. Emissions are also very important with the production of NOx, CO and CO_2 during the combustion process. Engine internal cooling flows have a great impact on the production of these emissions so advanced component film cooling techniques are used together with advanced ceramic component coatings to reduce base metal temperatures which reduces the cooling air requirements.

2.8.3 Cost of forced response during development phase

During the validation phase the development group operates various development engines to quantify performance, evaluate safety margins and certify the engines. As part of this development a dedicated engine is used to quantify fatigue issues by using numerous strain gauges. The testing includes a resonance test where the engine is run at particular operating conditions. Each test costs in the region of 0.06-0.1% of a typical engine development program, and up to nine strain gauge tests may be required to certify an engine from fatigue issues (Elliot 2008). To determine if there are any HCF issues in the development phase can cost up to 0.9%, considerably in excess of the maximum 0.1% required to rectify any HCF issues in the design phase.

2.8.4 In-service phase

The Fleet engineering team will be responsible for the completion of modifications to improve the product for the customer when the engine is on the wing and in service. These modifications could be instigated to improve the life of certain components or to offer increased fuel efficiency and reduce emissions. The Fleet team will also develop engine health monitoring algorithms that will monitor the engine gas path temperatures to give an indication of the remaining engine life and when the engine needs to be removed. This planned removal scenario is better for the customer as it allows the aircraft management and reduces disruption time. Other areas of engine health monitoring will be the analysis and assessment of bearing metallic chip detectors, which can give an early indication of potential main line bearing failures.

In service costs include investigating how extensive any issue is within the fleet, the disruption cost, any redesign cost, any shop cost, clearance costs (certification) & costs to implement the changes into the fleet. Experience has shown that this can be as much as 20% of the engine development cost for a single HCF issue.

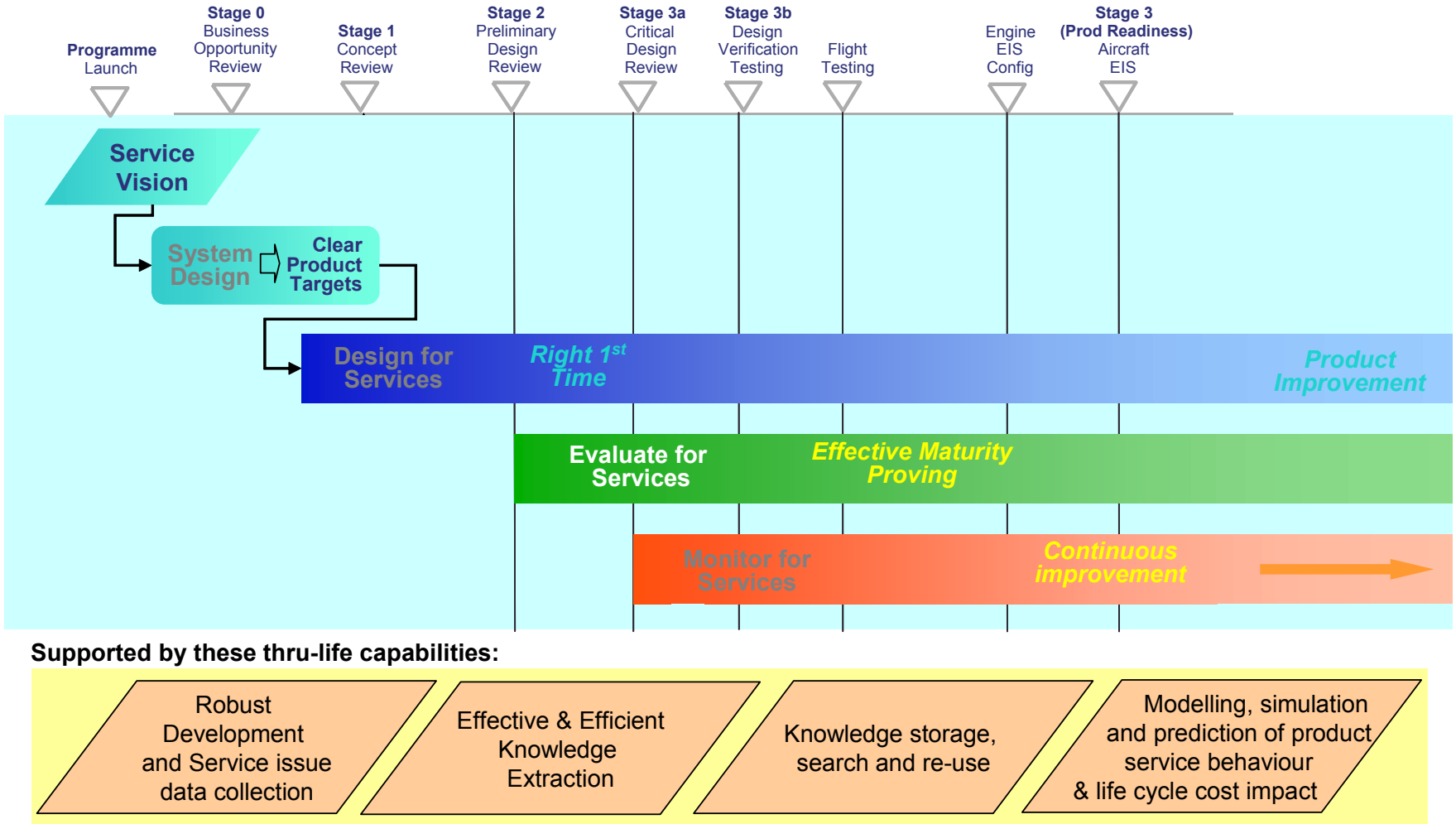

Figure 7 Typical gated design process

2.9 Future direction

In summary the historical advances in efficiency have resulted in similar levels of technology across the competition, resulting in efficiencies in the low nineties. However future gains are becoming prohibitively expensive to research even for small gains in efficiency. There is however the opportunity to deliver reduced DOCs by reducing the parts count and the number of disruption events. If the turbine blade count is reduced, the resulting high work turbines include a significant additional forcing function, supersonic shocks, which could potentially increase the number of disruption events by HCF. Discovering turbine blades that are prone to HCF is preferable as early as possible, ideally in the design phase, before engine validation. Estimates vary between 50-90% of HCF issues are discovered in the validation phase. Even the optimistic estimate of 90% of discoveries would still result in 10% of HCF problems not being discovered until the engine is on the wing. This can be an expensive discovery this late in the engine program, potentially adding on up to 20% of the engine development budget to rectify. Evaluations of unscheduled engine removals demonstrate the turbine is the most common component in unscheduled engine removal, a considerable cost to either the operator or manufacturer, depending on the contractual obligations. HCF can be determined in the design phase, the development phase or even in-service, although the limitations of time and static engine testing limit the potential for discovery in the development phase. The cost of detecting HCF becomes progressively more expensive to rectify in each phase of the engines transition from concept to commercial operation. Using structured interviews, the author has determined this increase can be as much as 200 fold from the design to to in-service phase of an engine program. To minimise the cost of forced response incidents a validated technology is presented to accurately model the unsteady forces which cause HCF that may result from the additional shock forcing function.

3 Turbine flow and interaction.

Blade row interaction occurs when unsteady inviscid and viscous flow features periodically affect adjacent blade rows. For forced response considerations these unsteady flow features are categorised as forcing functions. For high work turbines the three most prominent forcing functions are:

- Potential flow
- Shock waves } Inviscid flow features
- Wakes } Viscous flow feature

Each forcing function is explicitly detailed in section 3.1.1.1, 3.1.1.2 and 3.1.3.1 respectively. The forcing functions interact with non-rigid structures, which can result in forced response (or blade resonance), and potentially High Cycle Fatigue (HCF). The interactions include:

- Upstream blade rows interacting on downstream blade rows, e.g. the potential field, shocks and wakes
- Downstream blade rows interacting on upstream blade rows, e.g. the potential field.
- Upstream blade rows interacting on downstream blade rows which reflect back to upstream blade rows, e.g. shocks

3.1 Turbine aerodynamic flow features

3.1.1 Inviscid flow features

If the flow is considered to be inviscid the prominent forcing functions would be the potential flow field and supersonic shocks (for transonic turbines), which are independently detailed below.

3.1.1.1 Potential flow

Any obstruction in the flow, such as a stator, produces a pressure disturbance which is termed the potential field (Figure 8). If the axial flow is subsonic, this pressure disturbance propagates upstream and downstream, superimposing itself onto adjacent blade rows. If the flow is axially supersonic then the potential flow will not propagate upstream due to the sonic transmission constraint. The blade loading and lift distribution determines the potential field strength. For turbines that operate within a supersonic flow regime, the potential interaction is strong due to the high Mach number. In practise the nozzle's potential field is not independent; it interacts with the rotor's potential field, to generate a resultant static pressure field, which alters with the rotor passing. As the rotor passes through the potential field of multiple nozzles it is subjected to an oscillatory force. In practise experimental segregation of potential flow field effects is difficult, and advances in potential flow field understanding have largely been accomplished with computational techniques, where viscous effects can be numerically segregated.

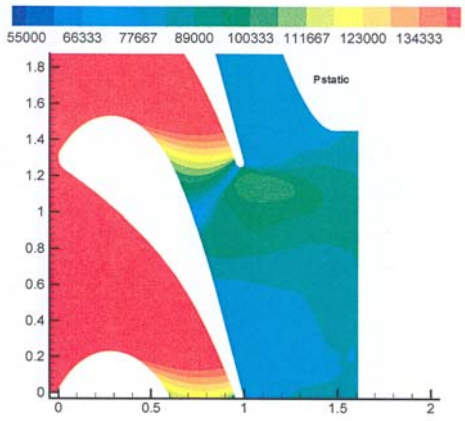

Figure 8 Example of the potential field of a transonic stator {Denos, R. 2005}

The magnitude of the potential field is a function of the Mach number {Korakianitis 1992}. For subsonic turbomachinery applications it decays exponentially with distance from the obstruction as a function of the blade pitch {Korakianitis 1992} with a typical length scale of one chord {Hodson 1983}. However the typically applied axial distances between adjacent blade rows is approximately ¼ to ½ of the airfoil chord, consequently this can result in significant flow unsteadiness in both the upstream and downstream blade rows {Dring, Joslyn et al. 1982}.

Kemp and Sears conducted early studies in blade row interaction {Kemp, and Sears 1953} {Kemp, Sears 1955}. They applied simple linearized potential flow solutions to thin airfoils with small turning. They concluded that for realistic axial spacing between two rows of airfoils the unsteady lift amplitude could be as much as 18 % of the steady value, with the unsteadiness being predominantly in the upstream row. They also found that the unsteady forces arising from the passage of an airfoil through viscous wakes are of about the same size as those due to the potential flow interaction.

Using validated CFD models Miller et al. notes the potential field of a low aspect ratio IP vane in a 1.5 stage transonic turbine extends upstream into the HP rotor passage up to the Mach one condition {Miller, Moss et al. 2002}. The downstream vane does not affect the pressure field around the suction surface leading edge or the pressure surface. Upstream of the crown the rotor suction surface pressure field is dominated by the upstream vane's potential field and shock.

Using airfoil chords approximately 5 times engine scale, with an aspect ratio of approximately 1, in a single HP stage operating incompressibly at representative Reynolds number, Dring demonstrated that with rotor-stator axial gaps of 15% chord, the periodically fluctuating pressure on the stator was due to the potential flow interaction with the downstream passing rotor (Figure 9).

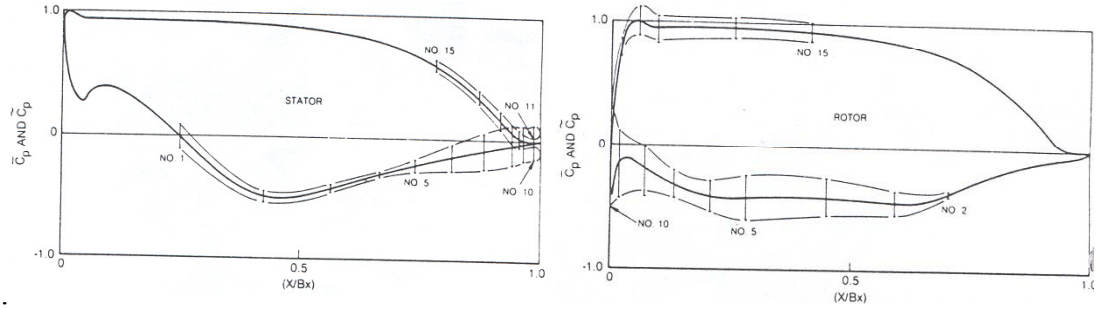

Figure 9 Stator (left) and rotor (right) unsteady pressure envelope, 15 percent of chord gap, C_x/U= 0.78, Site numbers relate to instrumentation positions {Dring, Joslyn et al. 1982}

3.1.1.2 Shocks

Over the years increases in engine core pressure ratio have led to the desirability of high pressure and work capacity turbines. If the nozzle or rotor exit Mach number is supersonic in these highly loaded turbines then shocks will form in the region of high curvature, i.e. the trailing edge (TE) (Figure 10). The shocks emanating from the nozzle or rotor TE are categorised into Left Running Shocks (LRS) and Right Running Shocks (RRS).

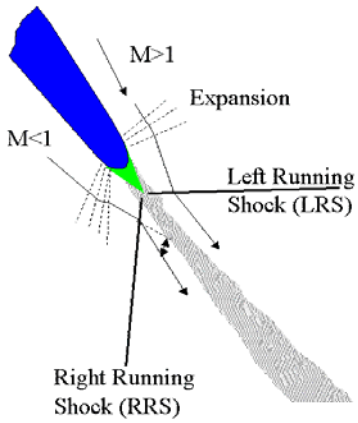

Figure 10 Shock origin at the region of high local curvature (TE) including naming convention of Left and Right Running Shock (LR and RRS respectively) {Haselbach, Janke et al. 2005}

Although there are notable viscous effects due to the severe local gradients within a shock, it is frequently considered and modelled as an inviscid flow feature. Across a shock there are large gradients of pressure and density (ΔPs and $\Delta\rho$, respectively), a total pressure loss (ΔPt), and a flow turning ($\Delta\alpha$) for oblique shocks. They interact directly and indirectly with each blade row impinging onto the downstream rotor and, typically, the adjacent nozzle (Figure 11). The complex shock patterns include upstream and downstream reflections which impinge through the rotor boundary layer and generate unsteady lift. If the shock or shock reflections are at resonant frequencies of the blade or disc, vibrations can occur which could result in HCF.

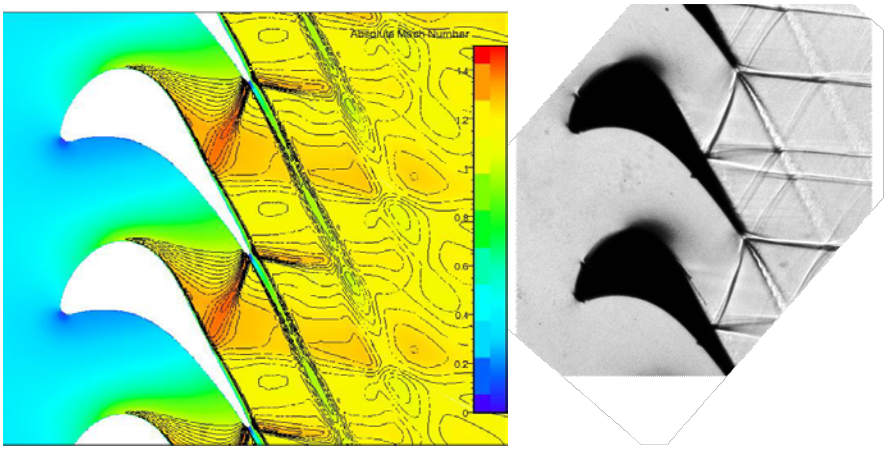

Figure 11 CFD prediction (left) and experimental (Schlieren) (right) results of the Göttingen rig stator operating at Mach 1.2, demonstrating shock propagation

Shocks which impinge onto rotor boundary layers are generically termed Shock-Boundary-Layer-Interactions (SBLIs) and are one of the primary forcing functions. They often result in detrimental effects, especially if the shock is strong enough to cause boundary layer flow separation, which reduces turbine efficiency and potentially increases the risk of HCF. Accurately predicting the dissipation of shocks through the rotor boundary layer using computational techniques is an important aspect of evaluating the unsteady forces that transonic turbine blades are subjected to. A separate section is dedicated to this flow feature, which includes an experimental program to characterise SBLIs at representative engine conditions.

The nozzle TE shock strength and propagation angle is not constant, it is modulated by the transient convergent-divergent nozzle, formed by the rotor passing {Denos, Arts et al. 2001}. When the nozzle trailing edge shock impinges onto the rotor crown a convergent divergent duct is formed, with the throat position between the late nozzle suction side and the rotor stagnation position (Relative position A in Figure 12). As the length of the divergent portion of the duct decreases, with the rotor passing, the nozzle TE shock becomes weaker (Relative position B in Figure 12). The convergent divergent channel no longer exists when the shock impinges onto the rotor leading edge due to the shock and throat being coincident (Relative position C in Figure 12).

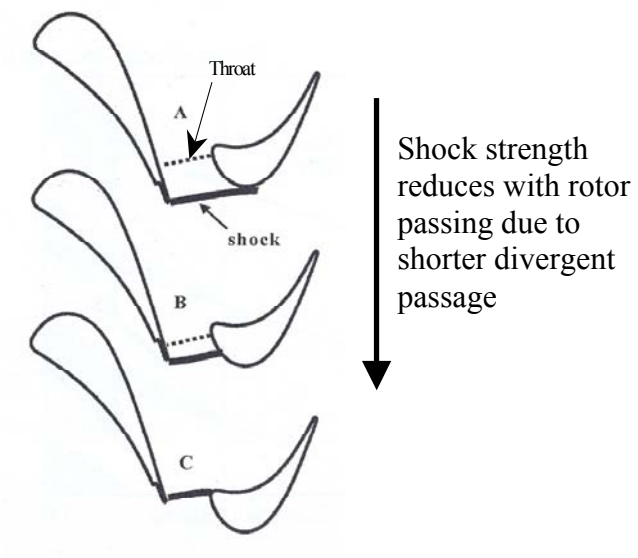

Figure 12 Convergent-divergent duct formed by the rotor/stator passages {Denos, R. 2001}

The convergent-divergent nozzle formed significantly effects the relative total pressure the rotor is subjected to. As the vane LRS sweeps from the rotor crown to the leading edge it modulates the relative total pressure by as much as 40% with large pitchwise static pressure gradients distorting the wake path ±5° in the relative frame of reference {Denos, R. 2005}

Using a 2D Euler unsteady computation for a transonic turbine stage (stator exit Mach number of 1.12) Giles et al. {Giles 1988} demonstrates the sweeping of a shock from the crown of a rotor blade toward the leading edge (from t=0.875 to t=0.375 in Figure 13), which was experimentally confirmed by Doorly {Doorly et al. 1985} and Ashworth {Ashworth et al. 1985}

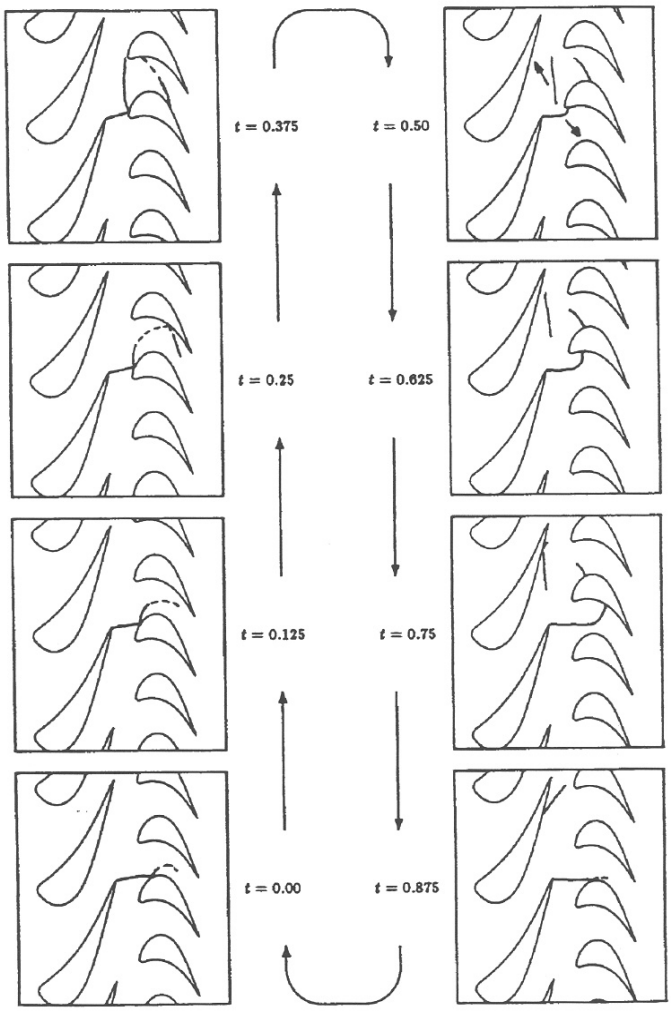

Figure 13 Shock pattern evolution during one rotor blade cycle in a transonic turbine stage {Giles 1988}

Other flow features include the shock reflection from the rotor suction side and the adjacent rotors pressure side (t=0.25), which end up impinging back onto the late suction side of the same rotor (t=0.375). The shock sweeps across a significant proportion of the rotor pressure side due to it's curving nature as it propagates through the rotor boundary layer (t=0.5 to t=0.75). Shocks which reflect from the rotor suction side sweep the pressure side of the adjacent blades in the next half period (t=0 to t=0.375) impinging from the trailing edge to the leading edge respectively with time. Shocks generated at t=0.375 also reflect upstream and impinge on the stator up to t=0.875. By performing 3D inviscid computations Saxer {Saxer 1993} confirmed this unsteady shock pattern. Features which will influence this shock pattern development include the spacing between the nozzle and rotor, Mach number and nozzle and rotor design differences.

Future design trends to have higher loading, lower aspect ratios and reduced engine lengths, will increase the strength of the shock forcing function. Designing turbine blades that are resilient to the increasing strength of the shock forcing function will be challenging.

3.1.1.3 Characterisation of SBLIs

SBLIs are inherently unsteady. Research by authors such as Dussauge and Dupont et. al. {Dussauge et al. 2006 and 2008 and Dupont et al. 2005} have characterized the frequency of supercritical SBLIs. The apparatus involved using a sting mounted wedge (θ=9.5°) to generate a shock which impinges onto a fully developed turbulent boundary layer. The incoming boundary layer has a thickness δ_0 of 11mm (99%U_e), an integral momentum thickness of δ_2=0.95mm and a Reynolds number based on the momentum thickness of $Re_{\delta 2}=\rho_e U_e \delta_2 / \mu_e = 4500$ (Table 1).

Mach No.	U_{edge} [m/s]	δ_0 [mm]	$Re_{\delta 2}$	C_f	T_t [K]
2.3	550	11	4500	0.0021	300

Table 1 Aerodynamic parameters of the flow upstream of the interaction

By calculating the Power Spectral Densities (PSD) of wall pressure signals, Dussauge et. al. demonstrates that the frequency range in the SBLI is distributed into three distinct zones, each of which involves characteristic temporal scales:

(1) The unsteady reflected shock characterised by very low frequencies (a few hundred Hz).
(2) The interaction zone (1-10kHz)
(3) A high frequency zone corresponding to the incoming turbulent boundary layer with energetic frequencies higher than 10kHz.

For turbomachinery applications, if any of these frequencies were integer multiples of the blades passing frequency (BPF) then HCF might result. During this research, no equivalent data was uncovered at conditions that are analogous to high work turbines. Therefore an experimental programme was designed and run to generate the required data, the results are included below.

3.1.1.4 Aim and objectives of SBLI investigation

The aim of this investigation is to characterise SBLIs at representative engine conditions to resolve if they are a significant factor in rotor forcing. To achieve the aim an experimental program generated unsteady test data to investigate characteristics such as the amplitude and unsteady frequencies within SBLIs.

The experimental program consisted of generating oblique shocks using a sting mounted (wedge) shock generator in the Cranfield 2.5” x 2.5” supersonic wind tunnel facility. The shocks reflected from a fully turbulent boundary layer on the working section top wall, generating a sub and super critical SBLI. The wall was instrumented with fast-response micro-kulites to measure the unsteady pressures. The experiments were designed to match the operating conditions of the VKI nozzle and rotor, specifically the:

- boundary layer thickness
- angle of incidence
- shock strength
- Reynolds number

A more detailed description of the experimental set-up, including the operating conditions is included in Appendix 2 and 3.

An examination of the Power Spectrum Density (PSD) of the micro-kulite test data is used to evaluate if the SBLI is a significant forcing function. This test data was also complimented by oil flow and high-speed Schlieren. Together the test data was used to determine SBLI characteristics including:

- Pressure rise
- Re-circulation lengths
- Unsteady frequencies

3.1.2 Shocks and SBLIs

Shock waves which interact with boundary layers effect the performance of turbo-machines {Wang, H. 1996}, but what has not been investigated is if they are a significant forcing function. The two main factors that characterise the SBLI are the upstream boundary layer (shape factor and Reynolds number) and the pressure rise imposed by the incident shock. When shocks impinge onto the boundary layer a complex interaction occurs in the shock foot region where intense adverse pressure gradients are imparted to the boundary layer. In subcrical SBLIs the flow through the boundary layer remains attached through the adverse pressure gradient, in contrast the adverse pressure gradient in supercritical SBLIs generates a local separation.

The inherently unsteady supercritical SBLI has two distinct low and high frequency regions. The mechanism which causes the low frequency unsteadiness is not well understood. Two potential mechanisms include the incoming boundary layer and the downstream separation bubble {Dussauge, 2008}. The reflected shock oscillates in phase with this low frequency unsteadiness. The second higher frequency unsteady region ($>10^4$Hz) is generated by the turbulent nature of the flow {Hemsch, 1986}.

3.1.2.1 Oblique shock reflections from subcritical SBLIs

When an oblique shock wave propagates through a boundary layer (Figure 14), the Mach number steadily decreases, progressively bending and weakening the shock until it reaches the sonic line. In the subsonic region the adverse pressure gradient propagates upstream, thickening the incoming boundary layer. This generates upstream compression waves which weaken and deflect the incident shock wave, before coalescing to form the reflected shock. As the shock propagates through the boundary layer the characteristic high pressure gradient in the free stream is imparted onto the wall as a continuous relatively low gradient pressure rise, consistent with the shock equations, due to the viscous boundary layer forces. This continuous evolution or spreading of the pressure rise is termed the interaction, or upstream influence length. The subsonic portion of the boundary layer, downstream of the incident shock impingement region, contracts due to the acceleration of the inner region, where the expansion waves form, as the viscous forces become predominant again.

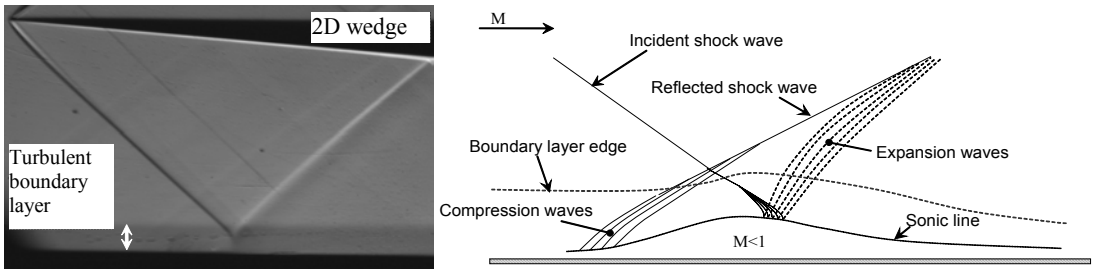

Figure 14 Oblique shock reflection without separation, Schlieren picture of flow field (left, M=1.74, $\alpha_r=4^0$), schematic representation of flow field (right).

3.1.2.2 Oblique shock reflections from supercritical SBLIs

Shock induced boundary layer separation is more complex than un-separated shock-boundary layer reflections, with dissipative phenomena playing a crucial role. A separating oblique shock reflection in a supersonic stream is presented in Figure 15. The boundary layer separation (S) is considerably upstream of the incident or impinging shock position. Compression waves are generated in the supersonic portion of the boundary layer by the rapid pressure rise, induced by separation, which coalesce to form the reflected shock. The incident shock penetrates the reflected shock into the boundary, dissipative layer, from which it is reflected as a system of expansion waves. The pressure rise imparted by the shock is compensated for by this expansion system, such that the pressure in the separated zone is continuous. A deflection of the flow towards the reattachment point (R) also results from the incident shock reflection system.

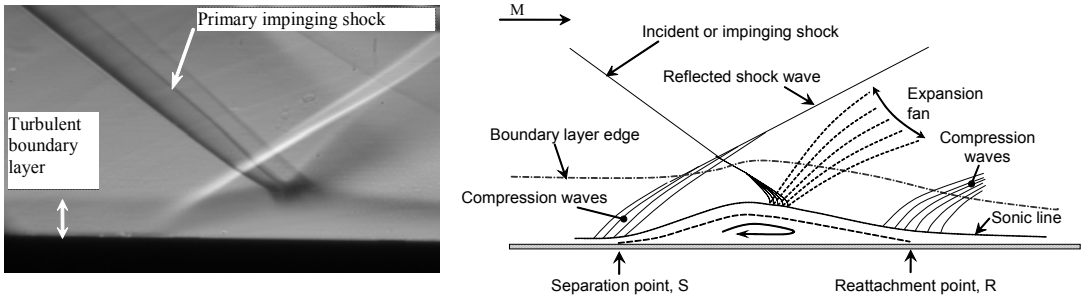

Figure 15 Oblique shock reflection with separation, Schlieren picture of flow field (left, M=2.4, $\alpha_r=13^0$), schematic representation of flow field (right).

3.1.2.3 Subcritical SBLI unsteadiness

An evaluation of the subcritical SBLI frequency spectrum is included. The power spectra of the signals obtained from the fast-response micro-kulites are broadband i.e. they contain no dominant frequency. To improve the interpretation of the signal a method defined by Dupont and Dussauge {Dupont et al. 2005 and Dussauge et al. 2006} is applied where:

$$\overline{p'^2} = \int_0^\infty G(f)df = \int_0^\infty fG(f)d(\ln f) \qquad \textbf{Equation 1}$$

where p' is the wall pressure fluctuation and

$$G(f) = \lim_{\Delta f \to 0} \frac{1}{(\Delta f)} \left(\lim_{t_f \to \infty} \frac{1}{t_f} \int_0^{t_f} p^2(t, f, \Delta f)\, dt \right)$$

Equation 2 Power Spectral Density (PSD) of the temporal frequency of the pressure signal

The result of applying this process to the unsteady pressures measured by the micro-kulite in the sub-critical SBLI region, where the incident shock impinges, is presented in Figure 16. Two plots are included, the spectral energy of the undisturbed turbulent boundary layer and the incident shock impingement position (right photo). An examination of the incoming turbulent boundary layer shows that most of the unsteady energy (approximately 80%) is at a frequency in excess of 10kHz. An examination of the spectral energy in the SBLI region shows an amplification in spectral energy across all frequencies, most notably at 10.2kHz, where the impinging shock amplifies the turbulent energy by a factor of three. The amplification of the turbulent energy at this high frequency would be problematic if the amplitude was significant and the interaction length scale was more substantial, due to modern aero-engine HP turbines operating at a BPF between 5-12kHz. If any forcing function is equal to or a divisible integer of the BPF, and phase aligned, they will increase the possibility of HCF. However it should be noted that the amplitude of the pressure change in the SBLI region is less than 1000Pa, an order of magnitude less than the shock forcing function (40kPa), and the area the subcritical SBLI affects, the lambda footprint, is considered negligible. An examination of the unsteady high speed Schlieren images indicate that the incident and reflected shock are essentially steady for the subcritical case. In conclusion, even though sub-critical SBLIs amplify the inherent turbulence within the boundary layer at problematic frequencies, they are not considered to affect the rotor forcing to any significant extent due to the low amplitudes of pressure change and the relatively small area they affect.

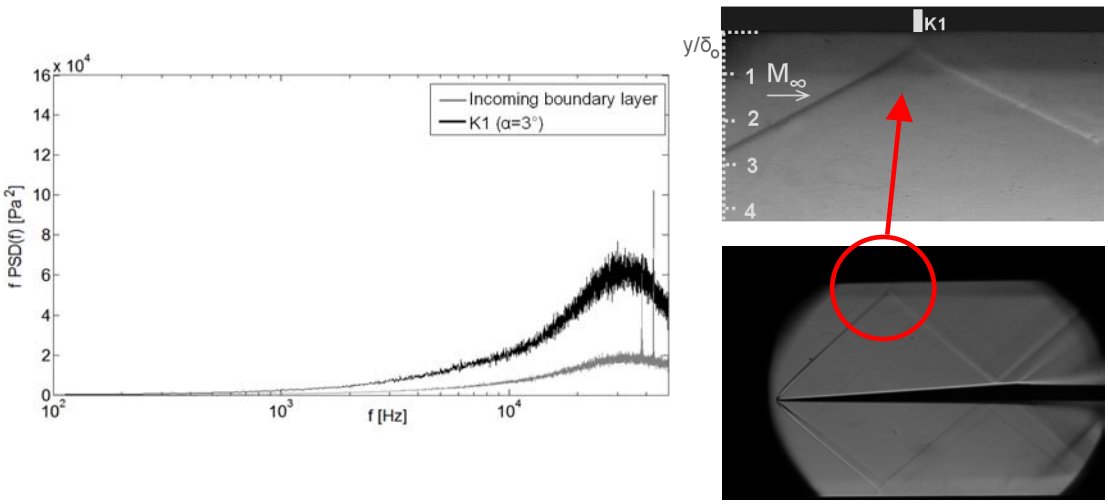

Figure 16 Unsteady pressure measurements of incoming boundary layer and under shock impingement position of subcritical interaction (left, α=3°) with relative kulite position (right).

3.1.2.4 Supercritical SBLI unsteadiness

Using the same method as described in section 3.1.2.3, the results of the supercritical SBLI experiment (α=13°) are presented in Figure 17. The results of the incoming boundary layer and three micro-kulites are included. The probe K1 is located where the reflected shock originates and the probes K2 and K3 are located in the interaction region, between the impingement and reflected shock position. A schematic representation of the flow field is included in Figure 18 for reference.

For the supercritical SBLI the energy spectrum monotonically increases from the reflected shock origin up to the re-attachment position. An assessment of the amplification from upstream to downstream across the SBLI is included. Most of the energy (approximately 80%) of the incoming boundary layer is broadband and at high frequencies (>10^4Hz). From K1 at the origin of the reflected shock position, a small amplitude addition of spectral energy occurs up to 10.2kHz in the intermittent region, just upstream of the separation position. In contrast to the sub-critical SBLI case, the super-critical SBLI reflected shock is unsteady and oscillates over probe K1. Using optical techniques detailed by Estruch {Estruch, D. et al. 2008} the reflected shock is demonstrated to oscillate at a frequency of approximately 150Hz, displacing approximately 4mm at y/δ_0=1.5 due to the separation mechanism. At this location only approximately 45% of the energy is greater than 10^4Hz, compared to 70-80% in the rest of the interaction region. Moving closer to the separation (K2) the spectral energy is significantly amplified from frequencies >10^3Hz, however most of the spectral energy (70-80%) is in a region >10^4Hz, with an amplification of 7 at the peak of the energy spectrum occurring at 10.2kHz. Within the re-circulation region at the impingement locus position (K3) there is a further amplification at frequencies >10^4Hz, with the most significant amplification again occurring at 10.2kHz. The low and high frequency (≥10^3Hz) amplification continues closer to re-attachment.

Using the oil flow visualization technique the separated region is shown to be approximately 65mm (Figure 19). The Schlieren images also show the boundary layer thickens by approximately 30% through the shock from 5 to 6.5mm. The maximum pressure oscillation in the SBLI region is approximately 5200 Pascals at K1.

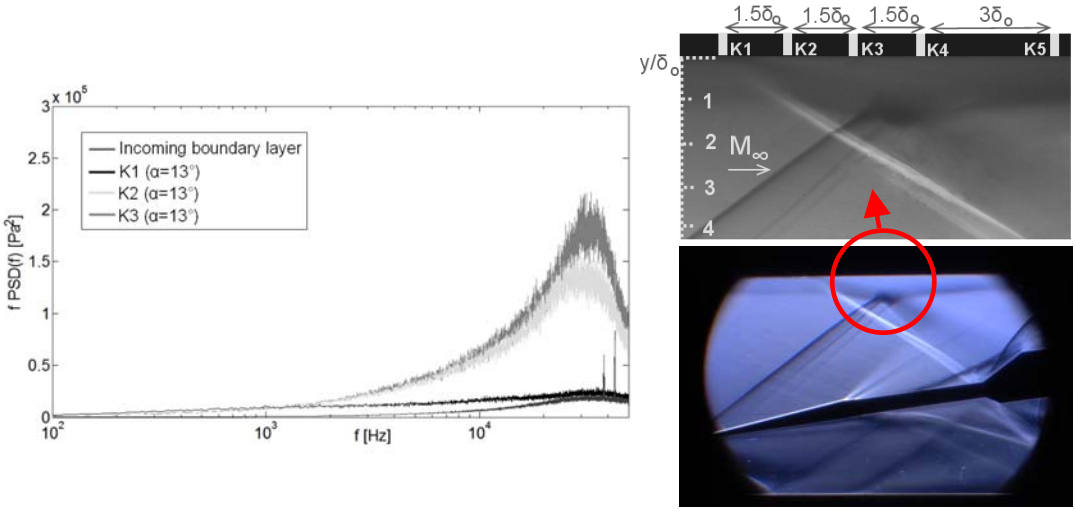

Figure 17 Unsteady pressure measurements for supercritical test case (left, α=13°) with relative kulite positions (right).

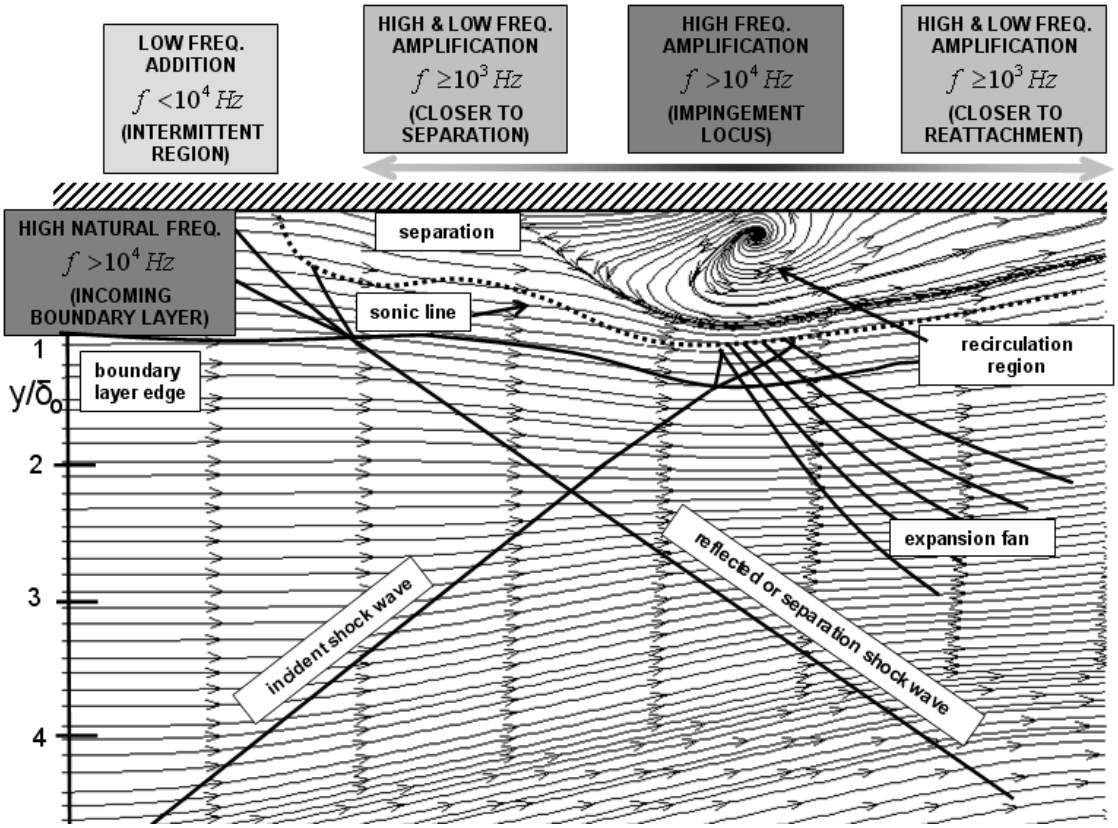

Figure 18 Schematic diagram of supercritical SBLI flow field (α=13°)

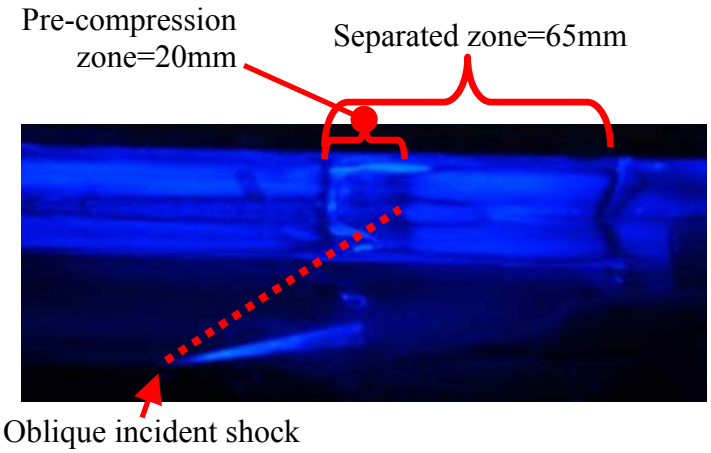

Figure 19 Oil flow visualisation of the supercritical SBLI (α=13°)

More complicated than the subcritical SBLI, the supercritical SBLI contains an unsteady separation that oscillates the reflected shock at approximately 150Hz. For forced response applications, this relatively low frequency oscillation is negligible because the BPF is at a considerably higher frequency (5-12kHz). Like the subcritical case, the amplification of the turbulent energy is a factor due to it's high frequency which is similar to the BPF. However unlike the subcritical SBLI case the maximum pressure oscillations in the intermittent region are significant (5200Pa), at 13% of the amplitude of the shock forcing function (40kPa) they are not inconsequential. Further more the relatively larger separated area that the super-critical SBLI affects will make this flow feature a contributory forcing function.

3.1.3 Viscous flow features

Viscous flow structures which are convected downstream through the blade rows include:

- Wakes (section 3.1.3.1)
- Secondary flows (section 3.1.3.2)
  - Passage vortices (3.1.3.2.1)
  - Trailing edge vortex sheets
  - Horseshoe vortex (3.1.3.2.2)
- Blade surface and end wall boundary layers
- Overtip leakage

3.1.3.1 Wakes

The suction and pressure side boundary layers mix to form viscous wakes behind blade trailing edges. Wakes are the locus of a velocity deficit, of a change of vorticity and of a turbulence increase which are characterised by total pressure drops concentrated in small portions of the pitch. Just downstream of the blockage, the low velocity central core of the wake has a width of similar order to the thickness of the trailing edge and is bounded by steep velocity gradients. The velocity gradients generate turbulent mixing, which transfer momentum across the streamlines during the wake convection which cause the intensity of the velocity deficit to reduce and the wake to broaden (Figure 20). This mechanism is most prominent up to downstream distances less than 40% chord or the "near wake" region, where the velocity gradients are greatest.

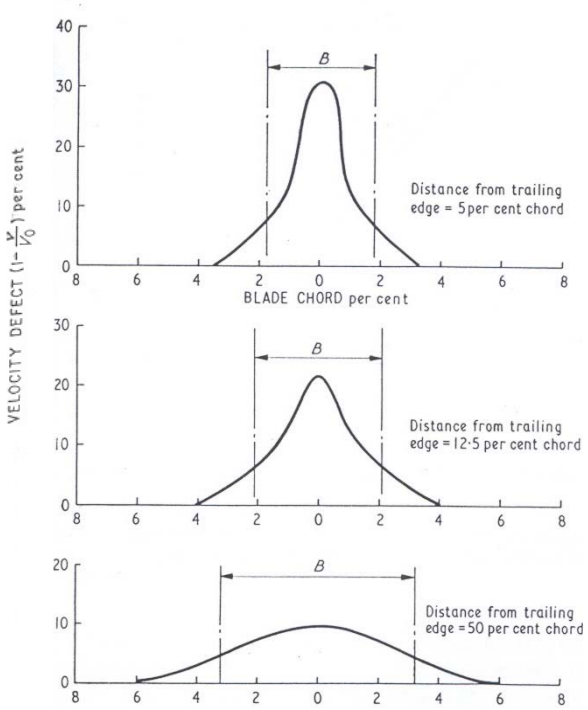

Figure 20 Variation of wake profile with distance downstream of an aerofoil trailing edge operating in Reynolds number range of 10^5 {Parker, R. 1972}

Blade wakes decay much more gradually than the potential flow field and considerably in excess of the axial spacing between the blade rows (Figure 21). Unlike the potential field, convected blade wakes may still be observed several chords downstream of their origin. Experiments on single-stage subsonic axial flow compressors have shown that except for very small axial gaps (approximately 5% of the axial chord) it is the wake that dominates the interaction {Walker, G., Gallus, H.}. Doorly et al. confirms that for conventional turbines it is the wake that dominates the interaction if the spacing between the rows is more than 5% of the axial chord of the stator {Doorly, D. 1985}. However for high work turbines, where the flow reaches transonic velocity, an additional significant source of unsteadiness arises through shock impingement

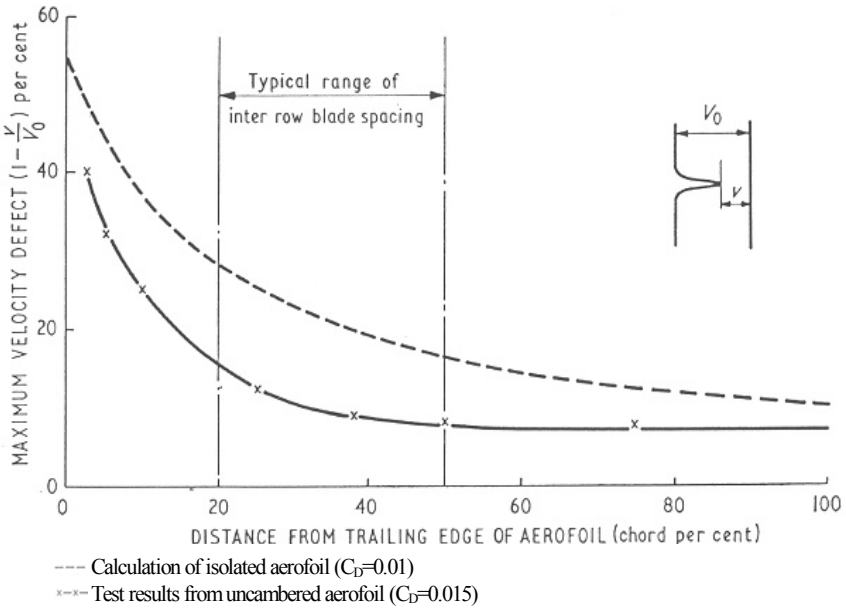

Figure 21 Maximum (wake) velocity deficit with distance from blade trailing edge {Parker, R. 1972}

In their respective reference frames both rotating and stationary blades are continually swept by the wakes of upstream blade rows. During their relative movement through the wakes the blade surfaces encounter transient pressure fluctuations. For a downstream blade row, upstream blade wakes appear as local regions of increased inlet angle (i.e. the incidence angle oscillates as the blade passes through the wake), which modify the pressure distribution around the blade, and hence blade lift. This unsteady change in the pressure distribution around the blade is a major source of vibration excitement.

Dietz {Dietz, A. 1992} categorised wake passing into two areas, both of which have been observed experimentally {Denos, R. 2005}:

- The wake effect.
- The wake distortion effect (Figure 22).

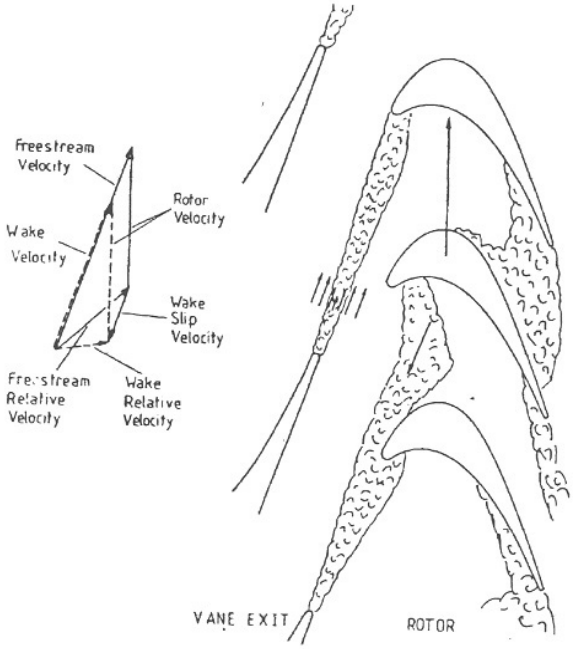

Figure 22 The wake distortion effect {Dietz 1992}

Evolving from perturbation theory of isolated thin aerofoils in incompressible flow, the wake effect is a pressure perturbation that travels at acoustic speed. The effect occurs when the wake reaches the blade leading edge. The temporary reduction in flow angle modifies the circulation around the blade, increasing the pressure on the suction surface and decreasing the pressure on the pressure surface. Once the wake has passed the leading edge its effect decreases until it is some distance downstream of the rotor.

Not modelled by the small perturbation theory of isolated thin aerofoils, Lefcort {Lefcort, M. 1965} first termed the secondary wake distortion effect. Meyer {Meyer, R. 1958} predicted that the wake distortion effect would result in a local decrease in pressure on the suction surface and an increase in pressure on the pressure surface as the local influence of the wake is convected through the rotor passage. The wake distortion effect generates perturbations two times smaller than the wake effect.

The situation is further complicated by the relative position of each wake in the downstream rotor passages. As one wake is impinging onto the rotor LE the adjacent nozzle wake might be leaving the adjacent rotor passage. In practise superimposition of numerous perturbations (including non-wake related aspects) makes it difficult to differentiate the source.

The actual wake forcing function comprises of discrete Von Karman vortices, which include high frequency non isotropic fluctuations. For conventional turbines they are shed at a frequency that is a function of the trailing edge thickness and the mainstream velocity (Strouhal number). For a transonic turbine stage shocks periodically reflect from the passing rotor, generating pressure waves that propagate back upstream onto the nozzle suction side, enforcing the vortices to shed at a phase-locked frequency with the rotor passing (Figure 23). For subsonic flow in conventional turbines the wake convection onto the downstream blade initiates turbulent spots within the boundary layer, which may cause transition (by-passing Tollmein-Schlichting waves).

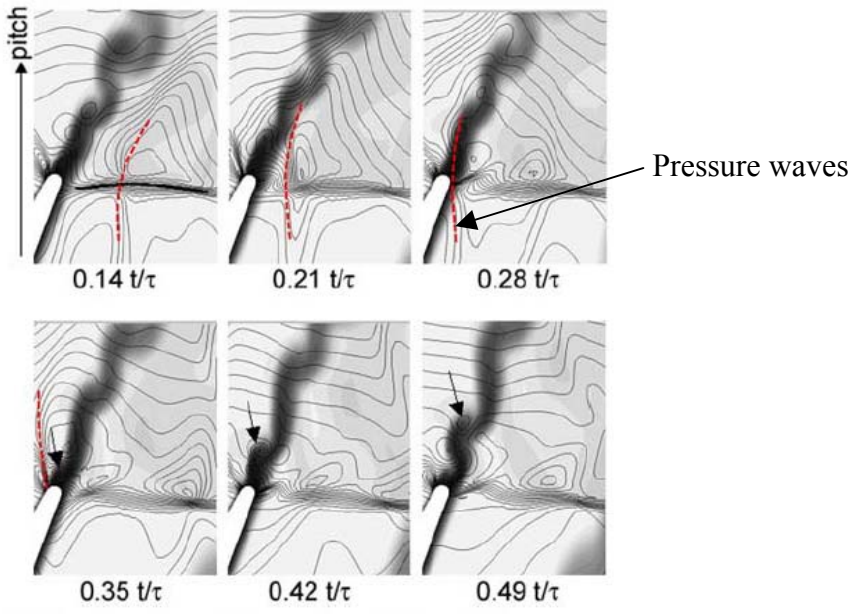

Figure 23 Nozzle wake at 50% span, lines indicate pressure isobars, greyscale indicates entropy {Gottlich, E. 2005}

3.1.3.2 Secondary flow

The intensity of secondary flows are mainly driven by the inlet boundary layer thickness and the turning of the blade row. Secondary flows include passage vortices, trailing edge vortex sheets and horse shoe vortices.

3.1.3.2.1 Passage vortices

First described by Hawthorne {Hawthorne, W. 1955}, the secondary flow vortex system originates in the hub and tip endwall boundary layers (Figure 24). Vorticity with a component normal to the flow direction is generated within the boundary layer. The curved passage, formed by adjacent blades, generates a pressure gradient across the blade passage. This pressure gradient causes flow migration towards the suction side of each blade row, which progressively distorts the vortex filaments into a streamwise vorticity component known as the passage vortex.

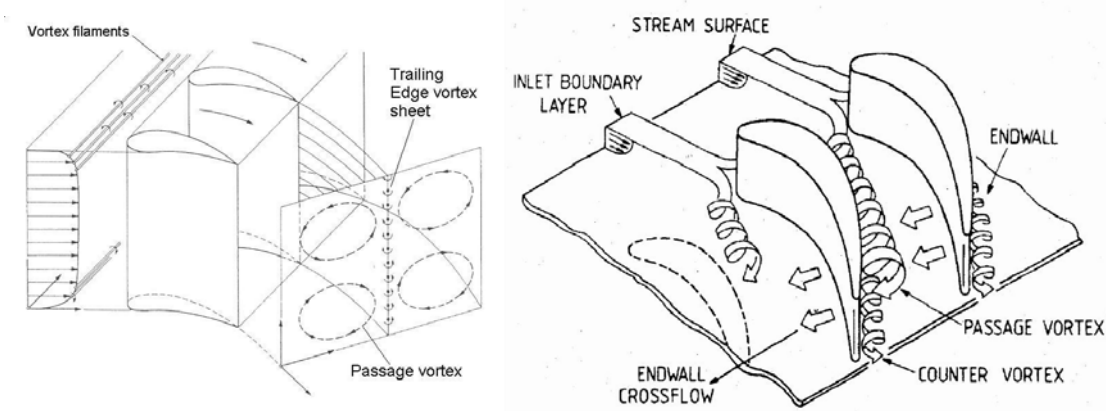

Figure 24 Secondary flow system {Hawthorne, W. 1955} and {Langstone, L. 1980}

Each blade passage generates opposite rotation vortices, the strength of which depends on the inlet boundary layer conditions and fluid turning, generated by the blade loading {Sieverding, C. 1984}. The understanding was verified by Moore et al. {Moore, J. 1985} and Yamamoto {Yamamoto, A. 1987}.

Passage vortices locally change the flow angle distribution and the pitch wise averaged flow angle. Figure 25 includes the secondary velocity vectors of a passage vortex in the lower half of a blade passage. The superimposition of the secondary vectors upon the pitch wise averaged flow angle can result in local overturning or under turning, most prominently at the channel height extremities of the passage vortex and where the corner vortex decreases the flow angle very close to the endwall. The outlet flow angle change can be affected across the entire span of low aspect ratio, high turning blades due to the large extension of the passage vortices.

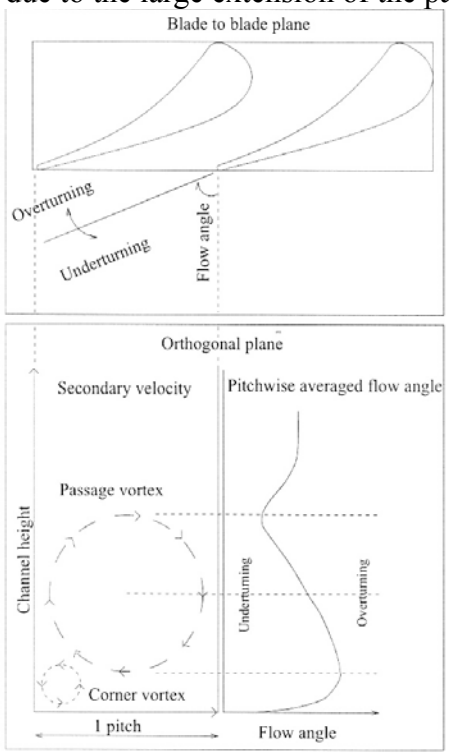

Figure 25 Influence of passage vortex on flow angle and velocity {Denos, R. 2005}

3.1.3.2.2 Horseshoe vortex

Upstream of a blade leading edge the adverse pressure gradient causes the boundary layer to separate from the annulus wall and roll up into a vortical structure. The vortical structure passes either side of the leading edge, generating the pressure and suction side leg vortices. First recorded by Klein {Klein, A. 1966}, Langston {Langston, L. 1980} went onto qualitatively and quantitatively demonstrate the evolution of the horseshoe vortices in a turbine cascade. Sharma et al. {Sharma, O. 1987} records the most dominant feature is the pressure surface leg of the horseshoe vortex (which becomes the passage vortex) migrating across the blade passage, due to cross-passage pressure gradients, meeting with the suction side leg of the horseshoe vortex at the minimum pressure point on the suction surface (Figure 26).

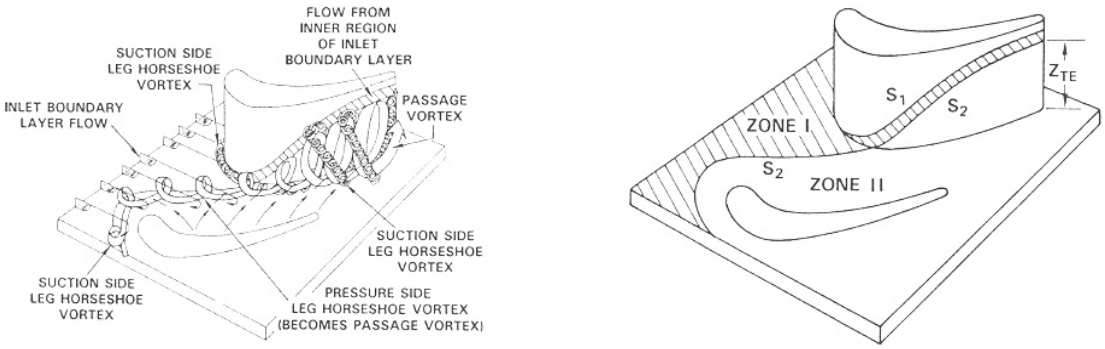

Figure 26 Cascade endwall flow structure and separation lines respectively {Sharma, O. 1987}

3.2 Wake and potential field interaction.

Wakes and pressure disturbances do not act independently, they interact. Korakianitis computationally investigated the generation of unsteady forces on turbine blades from upstream blade rows due to potential flow and viscous wake interaction {Korakianitis, T. 1991}. For the assumption of a moderately loaded turbine, in which shocks do not exist, Korakianitis demonstrated the primary parameter which determines whether the wake or potential effects dominate is the stator-to-rotor-pitch ratio (R). For values of R≈1 the wake interaction is dominant, for values of R>3, the potential flow interaction is dominant (Figure 27). For intermediate values the potential field and wake interaction effects are most substantial.

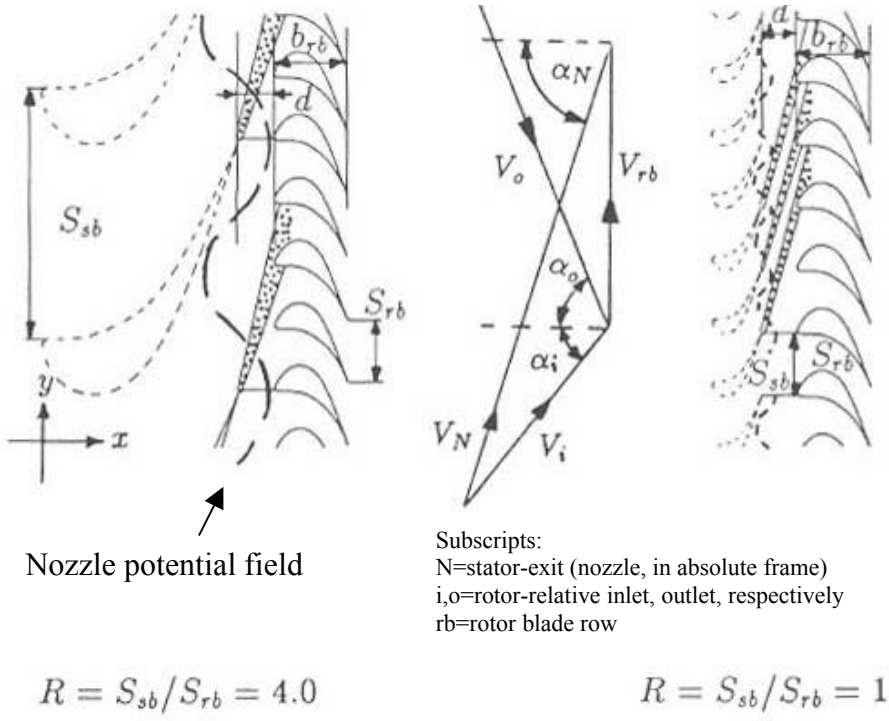

Figure 27 The effect of R on the stage geometry. The rotor velocity diagrams and the downstream rotors (flow from left to right) are identical {Korakianitis, T. 1991}

Figure 28 shows an excited turbine blade, at two loading conditions, experiencing a wake/potential interaction from an upstream vane. The wake and potential pressure field interact producing blade forces that constructively interfere for the low loading case, whilst the destructive interference produces smaller net blade loads for the highly loaded case.

Constructive interference for the more highly loaded turbine
reduces circumferential (F'y), axial (F'x) and moment (T'z) forces

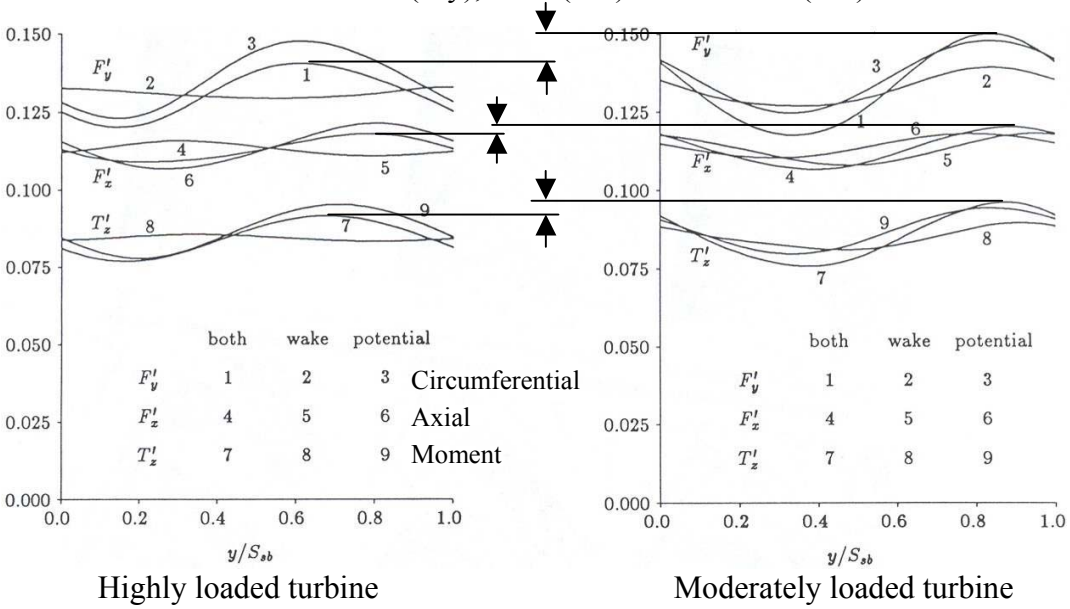

Highly loaded turbine Moderately loaded turbine

Figure 28 Time evolution of the forces and moment over a full stator pitch for the high loading case (left, nozzle angle, α=74.49°) and low loading case (right, nozzle angle, α=66.75°) {Korakianitis, T. 1991}

4 Aero-elasticity in turbo-machines

Aero-elasticity is the branch of science concerned with the interaction between aerodynamic forces and non-rigid structures. There are two important types of aero-elastic problems in turbo-machinery applications: flutter and forced response.

4.1 Flutter.

Flutter occurs when the unsteady gas flow (caused by the blade motion) and the vibrating blade (caused by the unsteady aerodynamic forces) interact, resulting in blade vibration. The dynamics of the fluid and structure couple, either or both of which can be non-linear in nature, producing this self-excited phenomena. Due to this interaction, any initial dynamic perturbation of the blade, irrespective of magnitude, could lead to unbounded growth of the amplitude of vibration (unstable flutter), to a decay to zero (stable flutter) or to a stabilisation at a finite value (limit cycle flutter). Flutter is of particular concern for fan blade designers, where the thin, large aspect ratio blades make them more susceptible to the aerodynamic forces, which are significantly larger than for compressors or turbines.

4.2 Forced response.

For turbomachinery rotor blades, forced response is defined as the vibration induced by time-periodic aerodynamic excitations, generated by the relative rotation of flow non-uniformities generated upstream or downstream of the rotor. Flow non-uniformities (detailed in chapter 3) or forcing functions result in unsteady pressure acting on the rotor, they include:

- Wakes
- Shocks
- Potential disturbances
- Boundary layers
- Tip flows
- Secondary flow;
    - passage vortices
    - trailing edge vortex sheets
    - horseshoe vortices

The three most dominant forcing functions in a turbine stage are shocks, wakes and the potential field which are illustrated in Figure 29. When the blades pass through these flow non-uniformities large unsteady loads can occur on the rotor blades which can lead to High Cycle Fatigue (HCF). HCF is distinct from Low-Cycle fatigue (LCF) by the root of the cause.

- LCF of rotating components is brought on by the continuous imposing and relaxing of centrifugal loads, caused by speed fluctuations. Typically the resulting creep causes thinning of the blade sections, stretching the blades in the radial direction and in extreme cases failure can occur.
- HCF is a result of the forcing function which drives the blade or disc at a frequency which matches it's own natural frequency. The continuous energy transfer from the fluid resonates the structure at a given vibration mode. The resulting stresses alternate around a mean value and can cause cracks or failure when the response exceeds the material endurance limit. The frequency of the

periodic load is proportional to the engines revolution frequency, often referred to as a multiple of the revolution frequency or engine order.

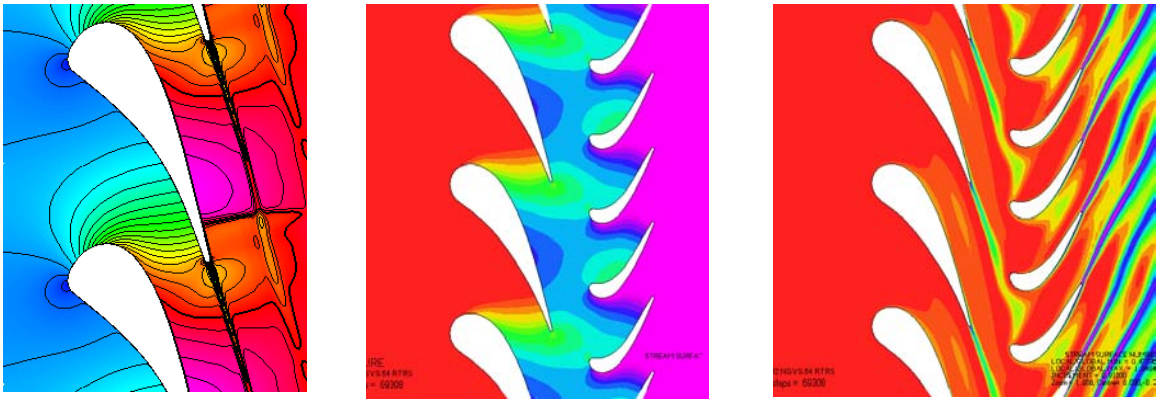

Figure 29 Examples of shocks, potential field and wakes respectively in a turbine stage {MacManus, D. 2008}

4.3 Analysis techniques

Historically designers try and avoid resonant conditions in the design phase, using tools such as the Campbell diagram (see section 4.3.1.1), which would be entirely adequate if all the resonant conditions were avoidable. Unfortunately this is impossible, which has required judgement, based on experience, to decide the acceptability of any potential blade design. In conjunction with Campbell diagrams designers have more recently augmented traditional blade response design processes with computational techniques which can be used to help identify failure mechanisms, and evaluate potential fixes when vibration problems are encountered. Blade resonation consists of three phases:

- time-periodic aerodynamic excitations generated by the relative rotation of flow-non uniformities.
- Unsteady blade loads
- Blade response

By combining the unsteady blade loads, generated by the flow-non uniformities, onto a structural model the mode shape response can be determined. Depending upon the accuracy required by the designer, the following forced response design and analysis systems are available:

- The Campbell diagram is a zero order forced response design system that indicates operating points where potentially significant increases in vibratory blade response occurs (see section 4.3.1.1). A Campbell diagram provides no measure of the amplitude of the resulting stress as the diagrams do not consider either the detailed aerodynamic forcing function or the resulting airfoil row unsteady aerodynamics.
- A 1st order forced response design system predicts the amplitude of the resulting stress at resonant speeds by using a linearized unsteady aerodynamic solution, where the unsteady flow is considered as small harmonic perturbations superimposed onto a baseline steady solution. The solution satisfies the linearised equations of fluid motion, which is adequate for a surprisingly large range of applications. The unsteady aerodynamic modelling

is performed in the frequency domain which requires the unsteady aerodynamic forcing function to be defined. The source of the aerodynamic forcing function is generally a distortion in the inlet or exit flow field of an airfoil row such as wakes from upstream airfoils. Each forcing function is decomposed into harmonics which are assumed to be comprised of disturbances being swept past non-responding airfoils, termed the gust unsteady aerodynamics i.e. unsteady aerodynamic forcing functions such as wakes are considered to be composed of a uniform mean flow and a superimposed harmonic gust. The airfoil vibratory response to each harmonic is then determined where the disturbance is referred to as the motion-induced unsteady aerodynamics or aerodynamic damping.

- 2^{nd} order forced response design systems use non-linear flow solutions to predict the amplitude of the stresses at resonant speeds. Unsteady flow is modelled in the time domain, using a forcing function, such as a wake, which interacts with the steady flow. The complete flow field solution is harmonically decomposed into steady and unsteady components, with the unsteady component harmonically decomposed for structural analysis.
- Fully coupled 3D non-linear unsteady viscous methods which compute the interaction between structures and fluids using time-accurate integration are the latest state-of-the computational techniques for calculating aeroelasticity. By combining the unsteady blade loads, generated by the flow defects, and the vibratory motion with a suitable structural model the blade response can be determined. This enables failure mechanisms, and potential fixes to be evaluated. Coupled approaches are necessary when unsteady fluids and vibrating structures interact (flutter) such as high aspect ratio fans, compressors and Low Pressure (LP) turbine stages. However these methods are prohibitively expensive and not typically used within industry for forced response analysis on low aspect ratio HP and Intermediate-Pressure (IP) turbine blades. More typically forced response of low aspect ratio turbine blades is treated by considering the fluid and structural dynamics independently. Uncoupled linearised or possibly non-linearised unsteady CFD solutions (1^{st} or 2^{nd} order detailed above) are generated to derive unsteady pressures, which are used as boundary conditions for finite element structural models. This uncoupled approach is carried out at operating points of concern i.e. a number of fixed frequencies of unsteadiness. This is a compromise to the expensive fully coupled aerodynamic / structural response approach.

Depending upon the fidelity required, calculations typically range from a simple 3D Euler linearised solver to a fully unsteady Reynolds-Averaged Navier-Stokes (RANS) code. More recent developments include Large Eddy Simulation (LES), Detached Eddy Simulation (DES) or Implicit Large Eddy Simulation (ILES), but in practise these are rarely used in industry, as they are prohibitively expensive. The most representative forced response models that are practically used in industry are 3D and unsteady, typically writing data, such as the unsteady rotor pressures, at a discrete number of rotor positions from which Fourier harmonics can be transferred to a stress model. Current viscous unsteady 3D flow solvers are capable of modelling:

- Inlet temperature distortions
- Blade cooling flow and end wall leakage flows.
- Non-axisymmetric end wall surfaces.

- Over tip leakage flows for unshrouded blades.
- Calculations with variable gas properties.
- Calculations with dissimilar aerofoils in a blade row (circumferentially dissimilar).

As part of the risk mitigation process, a forced response calculation is conducted at any resonance of interest from the Campbell diagram (see section 4.3.1.1). Typically a through-flow model at the correct operating conditions will be generated to provide the boundary conditions, however scaling of unsteady pressures with mean engine pressure level, has proven adequate if the operating point is close to the point of interest. If a linearised 3D inviscid assessment indicates an unhealthy level of forcing, then a higher fidelity 3D unsteady CFD analysis at the specific performance point is typically used to assess the performance.

The application of this process can still result in areas around the rotor where the predictions can be considerably different to experimental results. A comparison between two predictions and experimental results around the Oxford rig {Kammerer, A. 2003} is included in Figure 30 where the predictions are particularly poor. The predictions solve the RANS equations and the Ensemble Averaged NS equations (EANS) equations. The y-axis is non-dimensionalized static pressure perturbation.

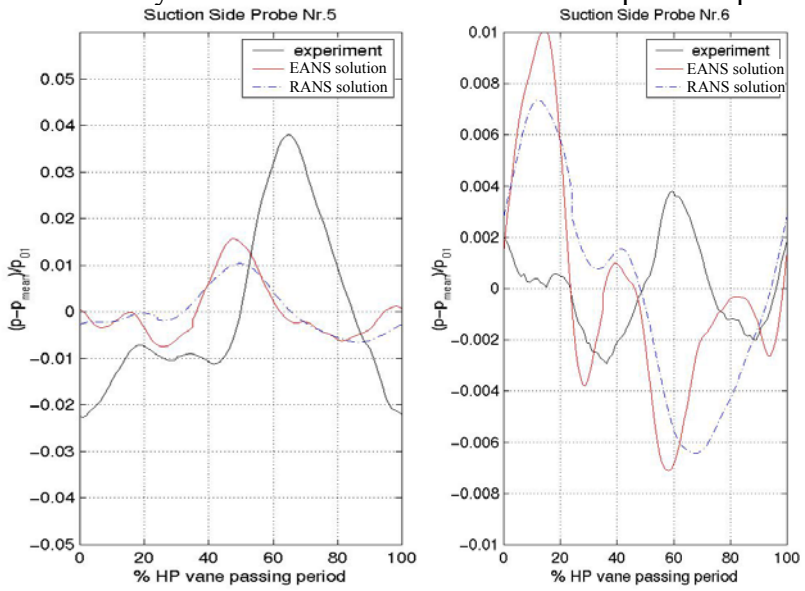

Figure 30 Comparison of RANS and Ensemble Averaged NS predictions with experimental results using non-dimensionalised pressure traces on oxford HP rotor suction side at 47% and 63% surface length respectively.

4.3.1.1 Campbell diagrams and mode shapes

There are three temporal types of forced response:

- Synchronous excitation: Either aerodynamically driven e.g. potential flow & wakes or mechanically driven e.g. tip rubs.
- Non-synchronous excitation: Primarily aerodynamic in origin such as separated flow vibration or rotating stall.
- Transient: Compressor stall or bird ingestion

The Campbell diagram allows the designer to identify operating regions of synchronous resonant frequency. The designer uses the Campbell diagram to determine if a natural blade frequency is excited by a forcing frequency, it's harmonics, or sub harmonics. A notional example is included in Figure 31 where the engine rotational speed (or forcing frequency) is along the X axis, the system frequency is along the Y axis. The linear lines that intersect at the origin are the engine order lines. If the calculated natural frequency of the blade and the rotational speed intersect within close proximity of the engine order lines (termed resonant speeds), then the forcing frequency will excite that natural frequency of the blade. At this point resonance is likely to occur and will increase the vibratory blade response. Examples of resulting blade deflections at various modes are included in Figure 32.

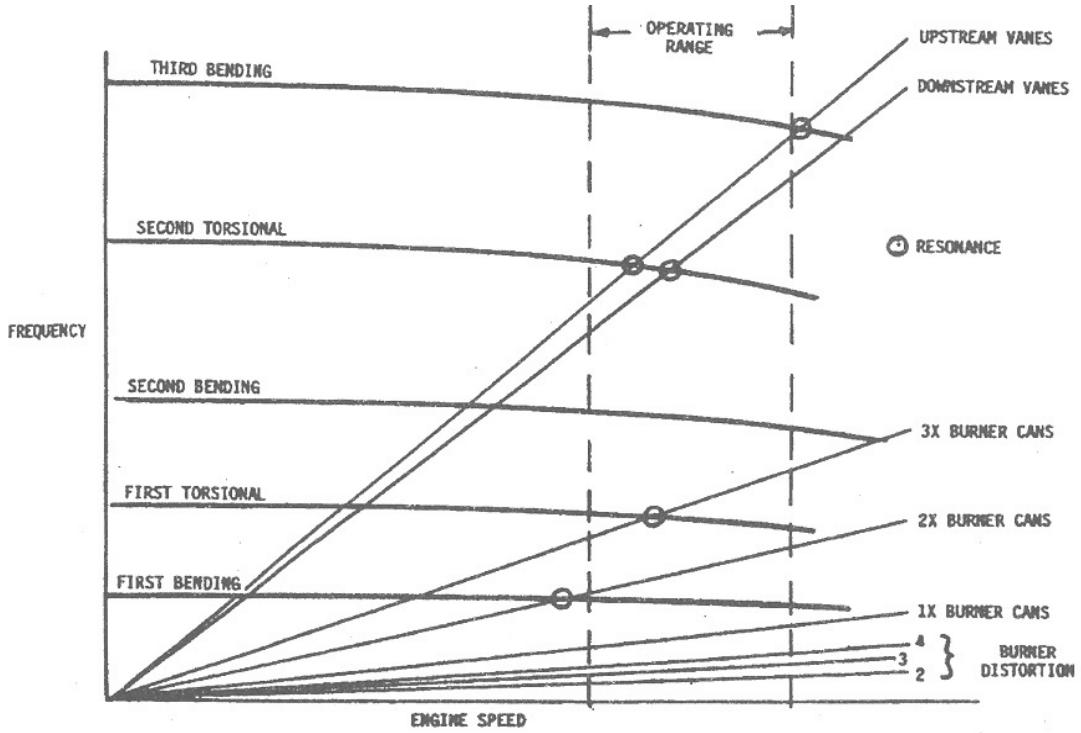

Figure 31 Notional Campbell diagram of a HP turbine stage showing various types of aeromechanical problems.

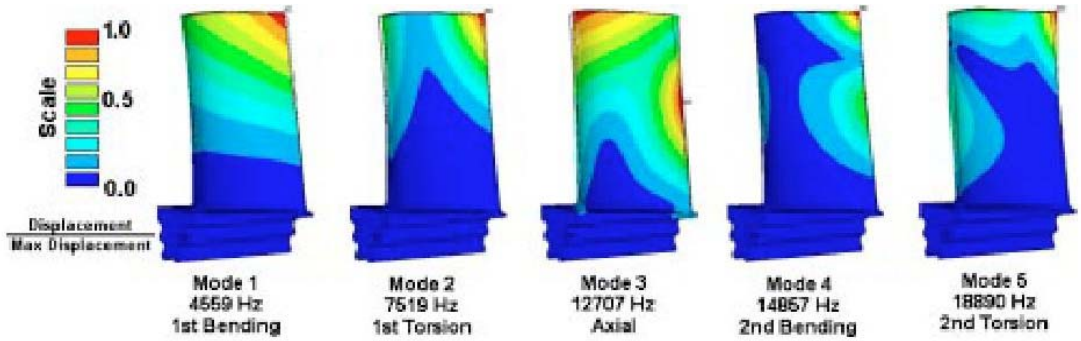

Figure 32 Blade mode shapes {Kielb, R. 2003}

Although the Campbell diagram identifies regions of potential problems, it does not consider either the detailed aerodynamics or damping and provides no measure of the

resulting stress at the various resonant speeds. The actual magnitude of the aerodynamic excitation can only be obtained from experimental measurements or unsteady aerodynamic modelling. A compromise is typically made by the designer in the form and number of blades in each row to ensure that resonant blade vibration is not excited. Blade row interaction should be taken into account for multi-stage machines.

4.4 Forced response design

There are several methods designers can use to change the rotor forcing including changing the space between each blade row, wake shaping, damping, changing the blade count and loading. Each forcing function decays with axial spacing. If the forcing functions do not interact then increasing the axial spacing will reduce the rotor forcing. If the wake is shaped then it will not impinge onto the rotor across the span at the same phase. Mechanical dampers can also be incorporated to alter the resonant frequency. A change in the blade numbers will inherently change the engine order and Campbell diagram characteristics.

4.4.1 Axial gaps

The axial spacing is one parameter that can be relatively painlessly altered in the design phase to reduce the rotor forcing. The designer can utilise this to reduce the rotor forcing if care is taken to ensure that each discrete function does not become phase aligned, as this will increase the overall rotor forcing. However, an increase in the axial spacing conflicts with the overall engine requirement to minimise engine size and weight. There is an optimum axial gap between rotors and stators that is hard to generalize a value to. Changes in axial spacing over the ranges that are commonly found in current engines can change overall turbine or compressor efficiency by as much as 2 percent {Dring, R. 1982}.

4.4.2 Wake shaping

The nozzle wake acts as an impulsive force as it impinges onto the downstream rotor at discrete time intervals. The rotor forcing is at a maximum if the wake impinges across the rotor span at a common phase. One method of reducing the rotor forcing at problematic vane passing resonance's is by shaping the wake to be less radial. This is typically achieved by stacking the aerofoil sections using circumferential or mixed lean. This results in the rotor passing through each stator wake across a finite angular range rather than impacting onto the convecting wake at a single point in time. Consequently the rotor passes through the wake momentum deficit over a longer period in time and reduces the peak forcing level and thus likelihood of HCF.

4.4.3 Damping

Damping is one of the most important and widely used methods of controlling blade forced response and flutter. It is impossible to design a turbine blade which is free from being excited at it's natural frequencies. Therefore, damping is required to limit resonant responses and decrease the risk of HCF. The complexity of the components that are involved in damping studies has made it difficult to predict and measure the levels that are experienced during engine operation. To predict forced response during the design phase, damping is assumed, based on practical experience, due to the lack of experimental data on aerodynamic and structural damping in blades operating at engine conditions. Turbine blade damping is composed of three major sources:

1. *Material damping* is due to inherent material properties, however for typical metal alloys used in turbine blades the *material damping* is negligibly small and often ignored {Srinivasan, A. 1984}.
2. *Structural damping* is due to frictional contacts, the complex nature of which makes analysis difficult. Research such by Yang and Menq {Yang, B. 1997} and Sanliturk {Sanliturk, K. 1999} has concentrated on contact kinematics for predicting wedge type dampers (see Figure 33) and shroud contacts. All frictional damping has a positive effect, but wear might reduce this effect during operation. Structural damping is an effective means of reducing forced response vibration levels. Nearly all turbomachinery has at least one stage which includes a blade friction damper.

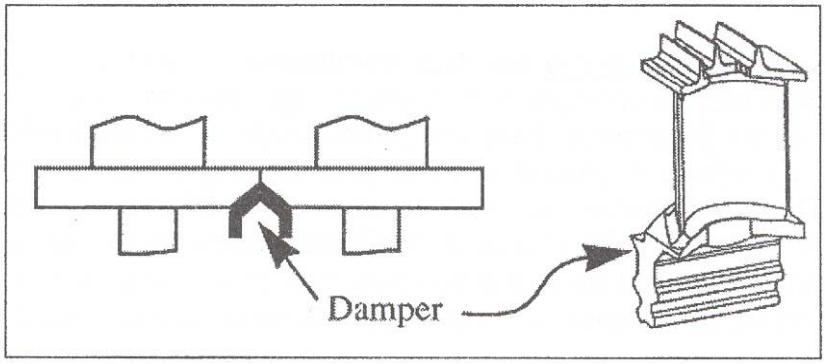

Figure 33 Example of under-platform damper

3. *Aerodynamic damping* is due to the gas loading on the blade, it is the primary source of damping for most blading. Prediction has advanced due to CFD developments such as Chiang and Kielb {Chiang, H. 1993} and Abhari and Giles {Abhari, R. 1995}. Typically the CFD calculations consider the forcing function (see chapter 3) and aerodynamic damping in two separate categories, with the latter category including blade motion in the CFD prediction to determine the aerodynamic damping.

More advanced damping concepts include “smart” materials such as strain-voltage generating materials for active and passive control, although the consensus appears to be that current technology and understanding are not sufficient to use damping for active vibration control.

4.4.4 blade count and loading

The drive for reduced parts counts has implications for rotor forcing. Reducing the number of nozzles should lead to an increased signature from the aerofoil wake, and the strength of the potential interaction. One method designers have to reduce this signature is to forward load the nozzles. Figure 34 compares two very different lift styles, a conventional number off ‘aft’ loaded design and a low number off forward loaded design. Although these two aerofoil designs have slightly different exit conditions, it is clear from the figure that a rotor passing downstream of the forward loaded aerofoil will pass through a weaker pressure signature than passing behind the conventionally loaded design, even though the peak pressure from the low number of aerofoils is significantly greater. Any reduction in the nozzles potential field reduces the rotor forcing from this forcing function.

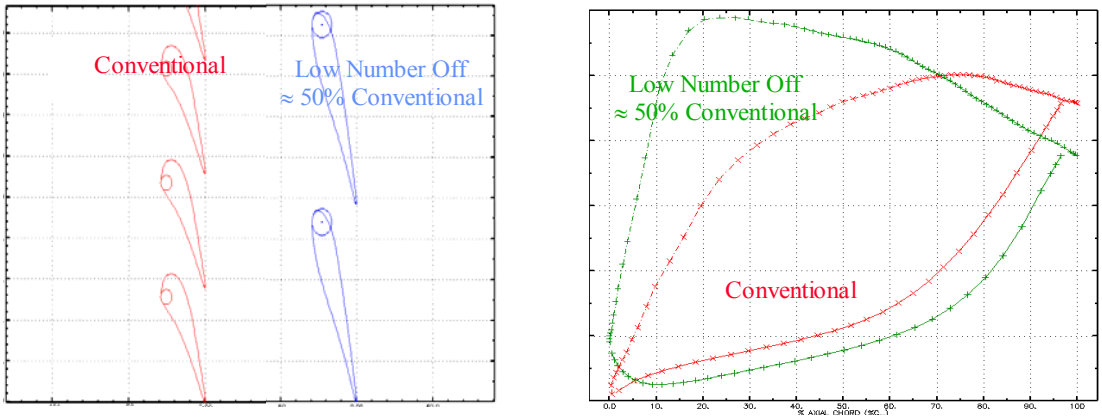

Figure 34 Mid-height NGV sections (left) and lift plots (right) demonstrating 'rear loading' {Taylor, M. 2003}

Other demonstrated techniques of controlling forced response by re-distributing the massflow include spanwise loading, lift stack, endwall contouring and the application of compound lean, defined as 'convex pressure surface, concave suction surface'.

5 Scope and strategy (research roadmap)

The aim of this research is to understand the main aerodynamic characteristics associated with forced response for a highly-loaded turbines. This topic has been tackled through three main strands as follows:

- A fundamental experimental investigation of unsteady shock boundary layer interactions.
- Validation of a computational method (chapter 7)
- Application of the method to investigate the sensitivity to design parameters (chapter 8)

A vital part of understanding the unsteady aerodynamics of a highly loaded turbine is the aspects surrounding the interaction between the shocks and the viscous boundary layers. Although a large body of research has been previously conducted to look at SBLIs, there are some elements which are poorly understood, including the amplitude and frequencies of the SBLI at typical engine conditions. An experimental program is presented which generated test data for analysis of sub and supercritical SBLIs at representative engine conditions.

The validation of the CFD method is a vital step in the development of a useful tool for predicting the complex unsteady turbine aerodynamics. The main vehicle selected for this is a set of high-quality tests which were performed on a model scale high-work turbine stage, the Von Karman Institute (VKI) transonic turbine. This test case is ideally suited as it comprises a well instrumented rig which was operated at a high specific work and pressure ratio. The validation is performed using 3D unsteady RANS stage calculations. By applying an order of merit approach an appropriate modelling standard was established. The metric for validation was the axial and tangential forces around the rotor at 50% span. The model was also used to analyse the distribution of forces and pitching moments at 15, 50 and 85% span. Key aerodynamic forcing functions are detailed and discussed. Fourier analysis was also used to examine the temporal composition of the rotor forces.

The final pillar of the thesis is the application of the CFD method in performing some computational investigations into some of the primary design parameters. Designers can influence the rotor forcing by the reaction, the inter-row gap between the blade rows, the pressure ratio and controlling the wake profile, by dimensioning the trailing edge (TE) size and, or, using TE ejection. To determine how effective these methods are in reducing the rotor forces several CFD models which alter each parameter independently have been evaluated. Additionally a CFD study has been completed which includes a slip condition on the rotor to determine how significant the rotor boundary layer is in dissipating the shock.

6 CFD model generation and methodology.

This chapter reports the methodology used to generate the CFD models and details some consequences that arise from unsatisfactory modelling standards. The study uses quasi-2D and 3D configurations of the VKI rig (see section 7.1.1) to investigate the sensitivity of the solution to mesh density and different turbulence models. Four quasi-2D models, each with a common geometrical base, have been used to investigate the effect of mesh density. The application of different mesh densities enables the quantification of numerical diffusion across the sliding plane and to investigate the consequences of near wall modelling. The consequence of unsatisfactory meshing standards includes erroneous predictions of the unsteady rotor forces and pitching moments.

The turbulence model study included an investigation of two turbulence models. The relatively high fidelity two equation k-ω SST turbulence model, which is appropriate for low Reynolds number flows and complex near-wall flow features, and the single equation Spalart-Allmaras model, which is appropriate for wall-bounded flows subjected to adverse pressure gradients were investigated. Two 3D CFD configurations, which both use a common meshing standard, have been used for this investigation.

6.1 Turbine stage modelling

The turbine stage modelling process involves generating a discrete 2D axi-symmetrical through flow calculation which is used to assign boundary conditions onto a 3D configuration. A 2D gas path through-flow calculation is a key element of the aerodynamic design process. The calculation iteratively solves the radial equilibrium equation to form an axi-symmetrical flow solution for the turbomachinery stages. The calculation includes flow passing through the turbine, the effects caused by secondary flows and over tip leakage. A through-flow calculation was generated of the Von Karman high-work turbine which was used to generate a 3D CFD stage model in a proprietary turbomachinery design package. This model was converted into a Gambit journal file using a Perl script. The Perl script constructs the annulus, nozzles and rotor within Gambit (version 2.4.6). Hybrid meshes for both the Q2D and 3D domain were generated using Gambit in conjunction with the surface wrapping tool TGrid. The commercial CFD code Fluent was used to solve for the flow field using an unsteady Reynolds Averaged Navier-Stokes formulation (URANS). To allow the flexibility of running the nozzles and blades independently each blade row was meshed separately using Gambit and combined in Tgrid. Fluent version 6.3 was used to converge each of the stage calculations. A schematic of this process is included in Figure 35 for reference. This method allowed a domain to be constructed which represents the VKI high work turbine rig (Figure 36).

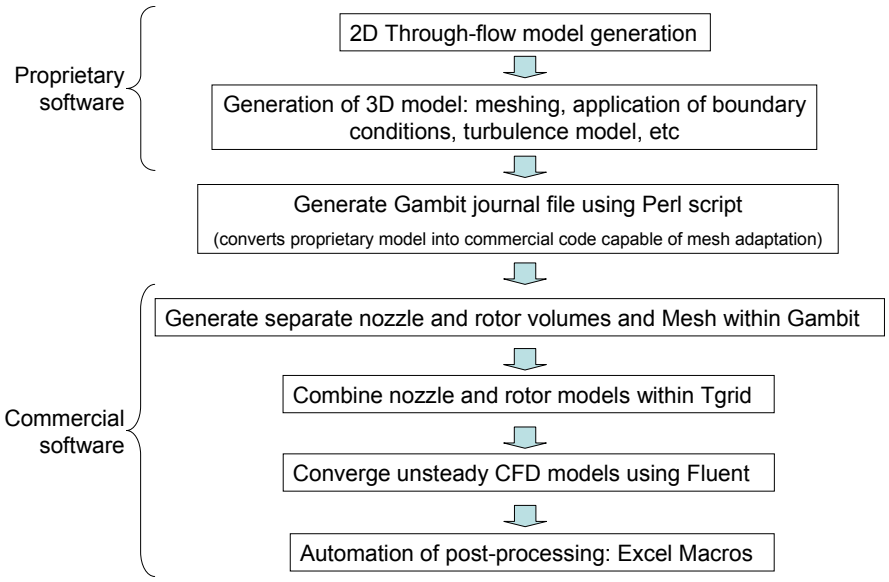

Figure 35 Schematic of transferring VKI rig into commercial CFD application

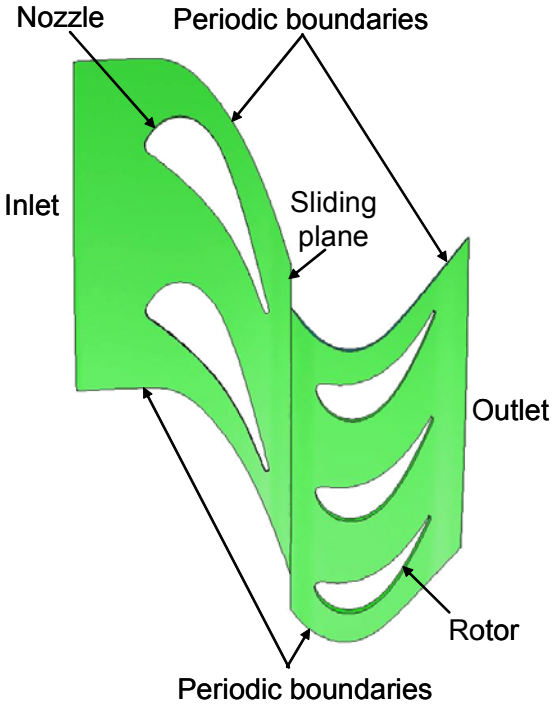

Figure 36 Unsteady transonic turbine CFD model domain: VKI cross section at 50% span.

To achieve a manageable CFD domain size, the 43 nozzles and 64 blades in the VKI rig were reduced to a devisable integer of 42 nozzles and 63 blades. This enabled a 2 nozzle / 3 blade count domain size (See Figure 36). The nozzles and rotor were skewed to match the rig capacity (Q=0.01008) and reaction (λ=31.5%). The turbine operating point characteristics for the CFD models used in these investigations are included in Table 2-Table 5.

Reaction (λ)	Stage loading ($\Delta H/U_{50\%}^2$)	Specific work ($\Delta H/T_{01}$)	Flow co-efficient ($V_A/U_{50\%}$)	Efficiency (η_{turb}) $\frac{T_{01}-T_{03}}{T_{01}\left[1-\left(\frac{1}{P_{01}/P_3}\right)^{(\gamma-1)/\gamma}\right]}$
28.4%	2.1	303	0.5	0.906
31.1%	2.1	301	0.49	0.904
41.3%	2.05	295	0.45	0.903

Table 2 Characteristics of the CFD models investigation reaction (P_{01}/P_{03}=4, Non-dim speed=12)

Case	Pressure ratio (P_{01}/P_{03})	Stage loading ($\Delta H/U_{50\%}^2$)	Specific work ($\Delta H/T_{01}$)	Non-dim. speed ($U_{50\%}/\sqrt{T_{01}}$)	Flow co-efficient ($V_A/U_{50\%}$)	Axial gap (x_g/C_{NGV})
Ax5C	4	2.1	303	12	0.49	0.27
Ax0	4	2.1	301	12	0.49	0.39
Ax5A	4	2.1	302	12	0.49	0.52

Table 3 Characteristics of the CFD models investigating the effect of axial spacing

Case	Pressure ratio (P_{01}/P_{03})	Stage loading ($\Delta H/U_{50\%}^2$)	Specific work ($\Delta H/T_{01}$)	λ	Non-dim. speed ($U_{50\%}/\sqrt{T_{01}}$)	Flow co-efficient ($V_A/U_{50\%}$)	M_2
PR219	2.19	1.3	188	0.12	11.97	0.43	1.04
PR319	3.19	1.9	276	0.22	11.97	0.49	1.23
PR385	3.85	2.1	303	0.31	12	0.49	1.24

Table 4 Characteristics of the CFD models investigating the effect of pressure ratio

	3D CFD model	Exp. Results WP22H
Capacity	*0.0101*	0.0101
Reaction	*0.312*	0.315
Specific work $\frac{c_p \Delta T_{01-03}}{T_{01}}$	*289*	299
Stage loading @ 50% span $\frac{c_p \Delta T_{01-03}}{U_{50\%}^2}$	*2.003*	2.076
Pressure ratio (P_{01}/P_{03})	*3.85*	3.85
η_{TURB}	0.76	0.78

Table 5 Comparison of 3D CFD and experimental operating parameters

6.2 Grid generation.

Mesh sensitivity studies included multiple configurations of quasi-2D (Q2D) and 3D stage calculations. A similar process was used in the generation with the exception of mesh inclusion between the rotor tip and casing in the 3D configurations and the use of mesh adaptation in the fine Q2D cases.

6.2.1 Quasi-2D grid generation.

All of the Q2D and 3D CFD configurations use hybrid meshes, with structured hexahedral cells in the nozzle and rotor near wall regions and unstructured wedge cells in the rest of the domain (Figure 37). The Q2D configurations extend to between approximately 45-50% of the radial span. Four Q2D hybrid meshes were evaluated (Table 6). Cases 1 and 2 have 8 hexahedral cells in the near wall region, case 3 has 16, and case 4 has 32. For cases 1 and 2, the cells in the near wall region are 0.01mm thick and are grown out by a factor of 1.2. Cases 3 and 4 were generated by progressively adapting the previous configuration.

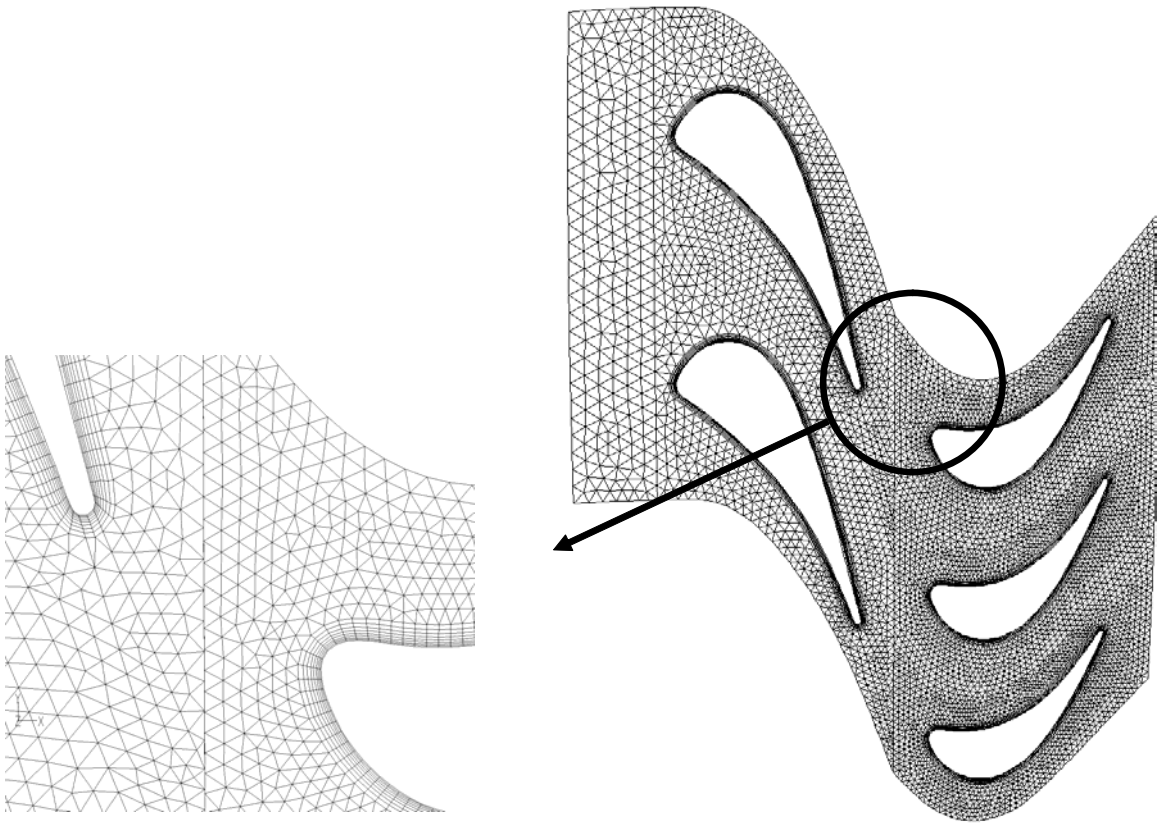

Figure 37 Mesh sensitivity study: Case 1 (Table 6), Coarse hybrid mesh density of 13,666 cells; Structured near wall region, unstructured for rest of domain

Case Number	Number of cells at 50% span	Number of cells at 50% span in nozzle domain	Number of cells at 50% span in rotor
1	13,666	4,078	9,588
2	30,775	10,909	19,866
3	69,262	24,442	44,820
4	208,816	71,662	137,154

Increasing mesh density

Table 6 Mesh sizes for Q2D turbine stage grid sensitivity study.

6.2.2 3D grid generation.

Two 3D turbine stage models were constructed (Table 7). Configuration *3D_baseline* (Figure 38) is a baseline mesh that has approximately the same mesh density that is typically applied in industry during the design process. Configuration *3D_high_fid* is a high mesh density configuration (Figure 39) which is used to investigate the effect of a substantial increase in the spatial resolution on the CFD predictions. Each CFD configuration uses a hybrid mesh, with structured hexahedral cells in the near wall regions of the nozzle and rotor and unstructured wedge cells in the rest of the domain. The nozzle mesh was initially constructed at 50% span and then extruded to the casing and hub. The rotor mesh was also initially constructed at 50% span, but was only extruded up to the blade tip, which was meshed independently to blend with the rotor passage. The combined mesh at the blade tip height was then extruded up to the casing to mesh the Over Tip Leakage (OTL) region. For all meshes the grid density is increased in the main region of interest which is between just upstream of the nozzle throat to the rotor crown. The main mesh characteristics are included in Table 8.

Configuration name	Total No. cells	No. 2D facets at 50% span in nozzle domain	No. 2D facets at 50% span in rotor domain	No. radial cells	Cell size at sliding plane [mm]
3D_baseline	1,402,922	6,013	5,995	46	0.88
3D_high_fid	5,700,036	40,364	69,858	60	0.44

Table 7 Mesh sizes for 3D turbine stage grid sensitivity study.

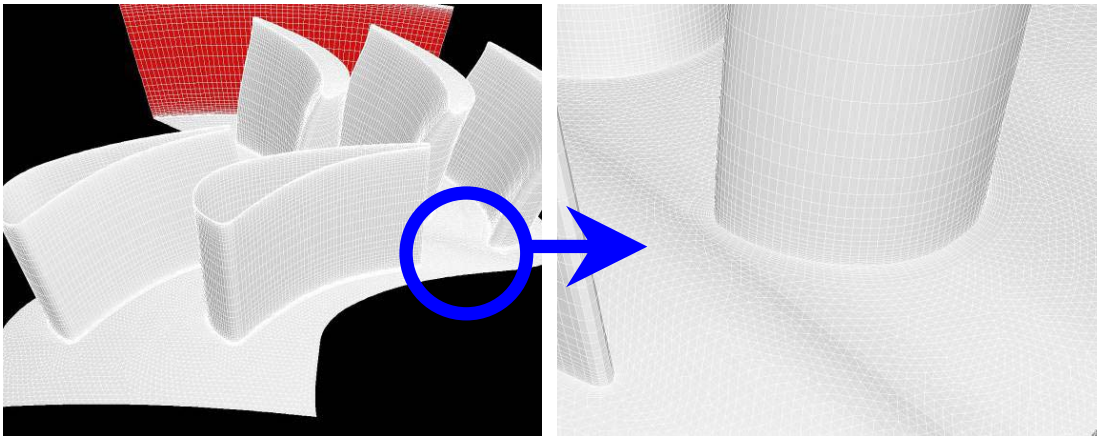

Figure 38 Configuration *3D_baseline*, hybrid mesh of approximately 1.4 million cells

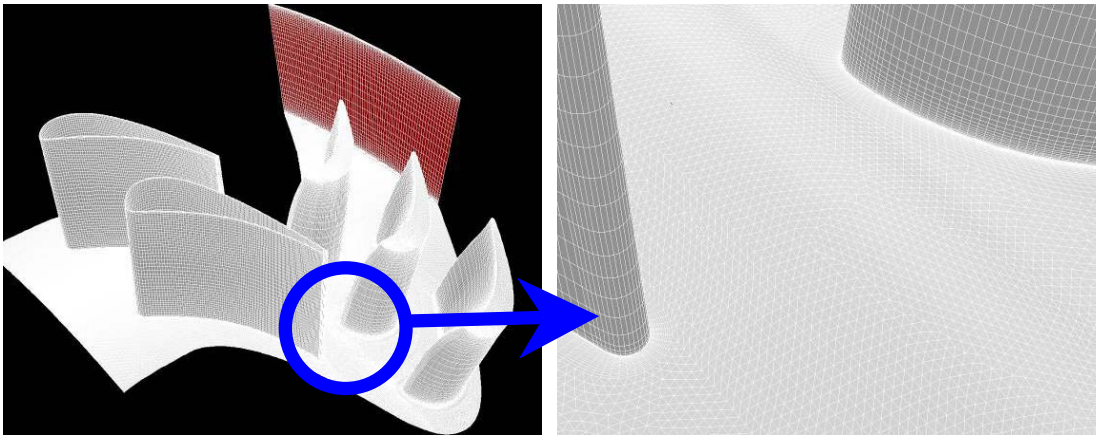

Figure 39 Configuration *3D_high_fid*, hybrid mesh of approximately 5.7 million cells

	Configuration name	
	3D_baseline	3D_high_fid
Total No. cells	1,402,922	5,700,036
No. 2D facets on nozzle quasi-annulus face at 50% span	6,013	40,364
No. 2D facets on rotor quasi-annulus face at 50% span	5,995	69,858
No. radial cells	46	60
Cell size at sliding plane [mm]	0.88	0.44
No. nozzle BL cells	10	20
nozzle growth factor	1.2	1.1
first nozzle cell depth [mm]	0.049	0.001
No. rotor BL cells	10	30
rotor growth factor	1.2	1.2
first rotor cell depth [mm]	0.076	0.002
rotor tip gap [mm]	0.595	0.595
rotor tip gap radial cell count	4	7

Table 8 3D CFD turbine stage mesh characteristics

The entire rotor hub line for configuration *3D_baseline* rotates at the blade speed. Configuration *3D_high_fid* has an extended rotor duct and an independent rotor blade rotating platform that extends 5mm downstream of the rotor TE. The performance of the baseline and high mesh density models are assessed in chapter 7.

6.3 Boundary conditions and time steps

The inlet and outlet boundaries were modelled as pressure inlet and pressure outlet boundary conditions (BCs) respectively, set to match the WP22H turbine conditions (see section 7.1.1). All of the walls were defined as no-slip boundaries. The time step for the 3D configurations was calculated as 3.446×10^{-6} seconds to achieve 128 movements of a rotor blade past two nozzle pitches, which is the same number of samples used in the experimental evaluation. Each time step was converged with up to 1000 iterations per time step. The higher mesh density Q2D configurations used a time step of 0.2153×10^{-6} to achieve 2048 movements of the rotor past two nozzle pitches, using 20 iterations per time step. The reduced time step for the quasi-2D configurations was necessary to eliminate shock reflections from the sliding plane which were observed at lower temporal resolutions. The number of time steps was

selected to be 2^n to enable a Fast Fourier Transform (FFT) analysis of the resultant rotor pressures to determine the harmonic composition.

6.4 Convergence.

When the capacity at the domain inlet for the 3D baseline configuration stabilised to within 0.3% of the target capacity after approximately 1400 time steps the solution was considered suitable for detailed analysis (Figure 40). The configuration was initially converged with first-order temporal discretization to obtain the approximate flow field and then switched to second order discretization after the transient had been traversed. The configuration was initially converged using 100 iterations per time step for the first order section and then 75 iterations per time step for the second order section. Both sections were converged using Fluent's default relaxation factors and a Courant number of 1.5 using the density based implicit solver to typically reduce the residuals to less than 1e-02 (Figure 41)

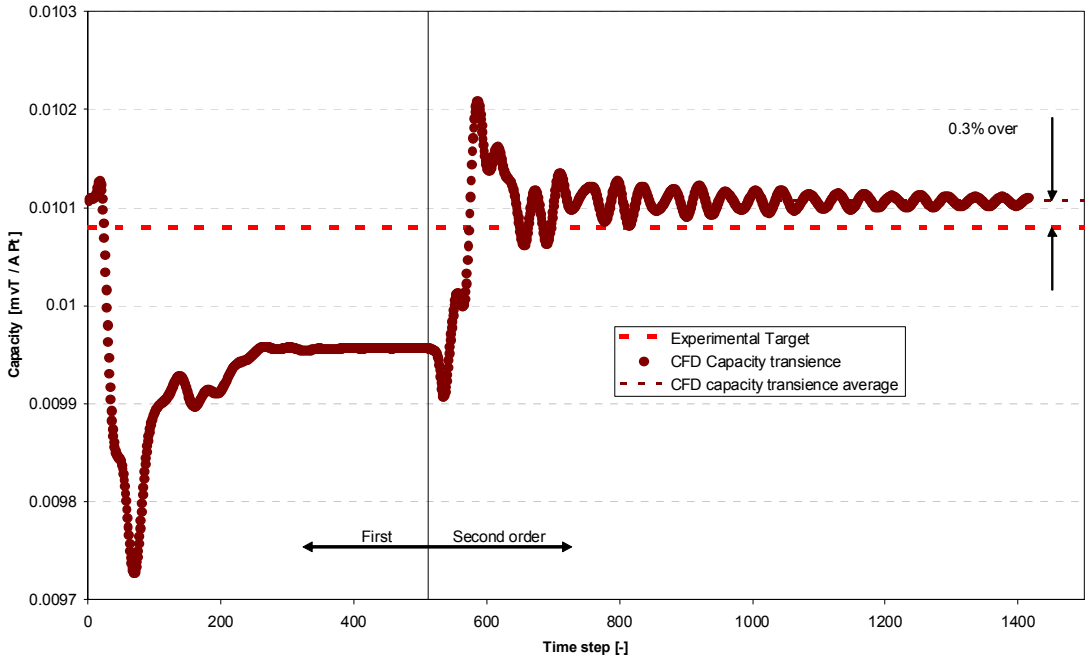

Figure 40 Transience convergence for the 3D unsteady stage calculation using 100 iterations per time step initially, then increasing to 75 iterations per time step for second order discretization

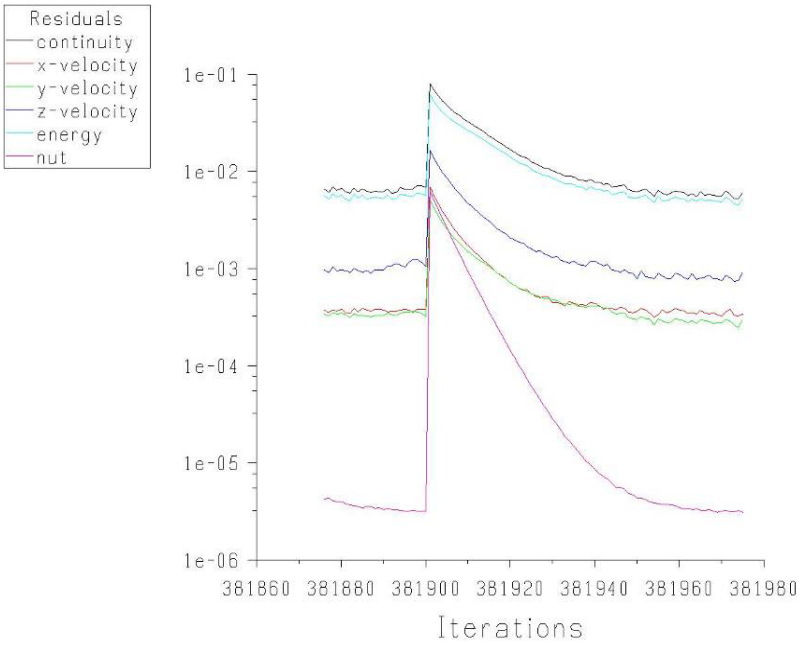

Figure 41 3D Baseline residuals (Table 7) across a single time-step

6.5 The effect of turbulence models

An evaluation of two turbulence models is presented. Each model is evaluated by comparing the rotor forces and pitching moments with the experimental results. The study compares the k-ω Shear Stress Transport (SST) and the Spalart-Allmaras turbulence models using the *3D_baseline mesh* detailed in section 6.2.2. The k-ω SST and Spalart-Allmaras 3D stage models will be referred to as *3D_k_omega_SST* and *3D_Sp_All* respectively.

The relatively high fidelity two equation k-ω SST turbulence model is appropriate for low Reynolds number flows and flows with complex near-wall flow features (such as SBLIs). The k-ω SST model is more accurate and reliable than the standard k-ω model for a wider class of flows (e.g., adverse pressure gradient flows, airfoils and transonic shock waves) which means it should be the most appropriate model for evaluating high work turbines. The model applies a derivation of the Enhanced Wall Treatment (EWT) model which explicitly resolves the near-wall region using a very fine near-wall mesh (Y^+=1). A more coarse near-wall mesh is acceptable provided it is inside the viscous sublayer (Y^+<4-5). The k-ω SST model has been demonstrated to be the most appropriate model for predicting flows which include SBLIs when the fine mesh requirements are applied {Fluent}.

In contrast the lower fidelity single equation Spalart-Allmaras model solves a transport equation for the kinematic eddy (turbulent) viscosity. The model also applies a derivation of the EWT for fine meshes (ideally Y^+=1, or greater provided Y^+<4-5) or a standard wall function where $30 < Y^+ < 300$. Either way the mesh should be fine or coarse enough to avoid the buffer layer (Y^+=5 to 30). This makes it a sensible choice for coarse meshes, where accurate turbulent flow computations are not critical. The Spalart-Allmaras model was designed specifically for aerospace applications involving wall-bounded flows and has been demonstrated to give good results for boundary layers subjected to adverse pressure gradients {Fluent}.

Both the *3D_k_omega_SST* and *3D_Sp_All* stage models reasonably predict the unsteady axial forces that occur within the high work turbine experimental rig (Figure 42). However, surprisingly the tangential forces are more accurately predicted at the Blade Passing Frequency (BPF) by the lower fidelity Spalart-Allmaras model. To better understand this unexpected result, a more detailed evaluation of the tangential force distribution at the BPF is compared with the experimental results in Figure 43. Both turbulence models over predict the tangential forces in the region of the rotor crown on the pressure and suction side. The *3D_Sp_All* model more accurately predicts the forces on the suction side near the rotor LE, where the strong LRS impinges. Reynolds Averaged Navier-Stokes (RANS) models are known to give spurious results in this stagnation region {Mann 2009}. Other factors which may be affecting the results are the separation predictions where the k-ω SST model tends to over predict the separation size and conversely the Spalart-Allmaras model tends to under predict the separation size.

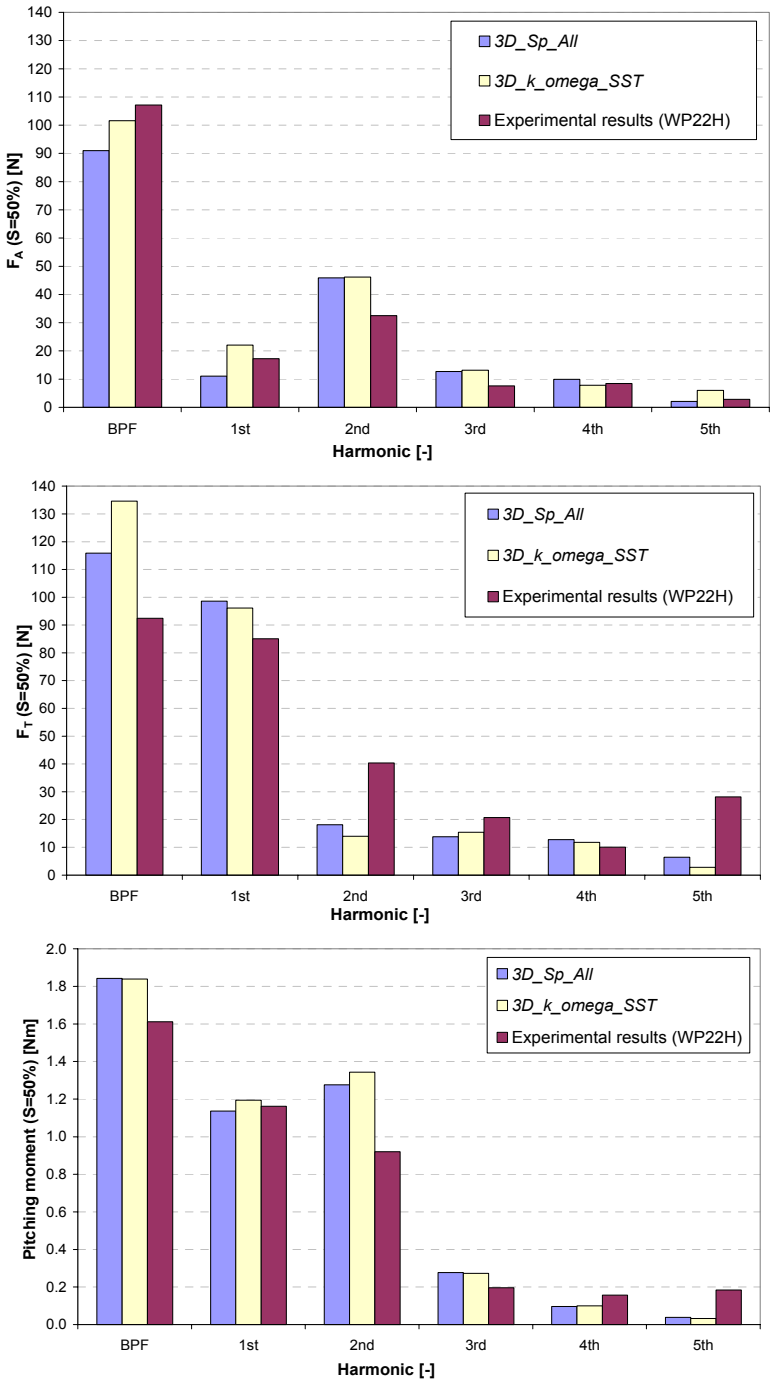

Figure 42 Comparison of the k-ω SST, Spalart-Allmaras turbulence models and experimental results using the harmonic distribution of unsteady axial force (top) tangential force (middle) and pitching moment (bottom) at 50% span

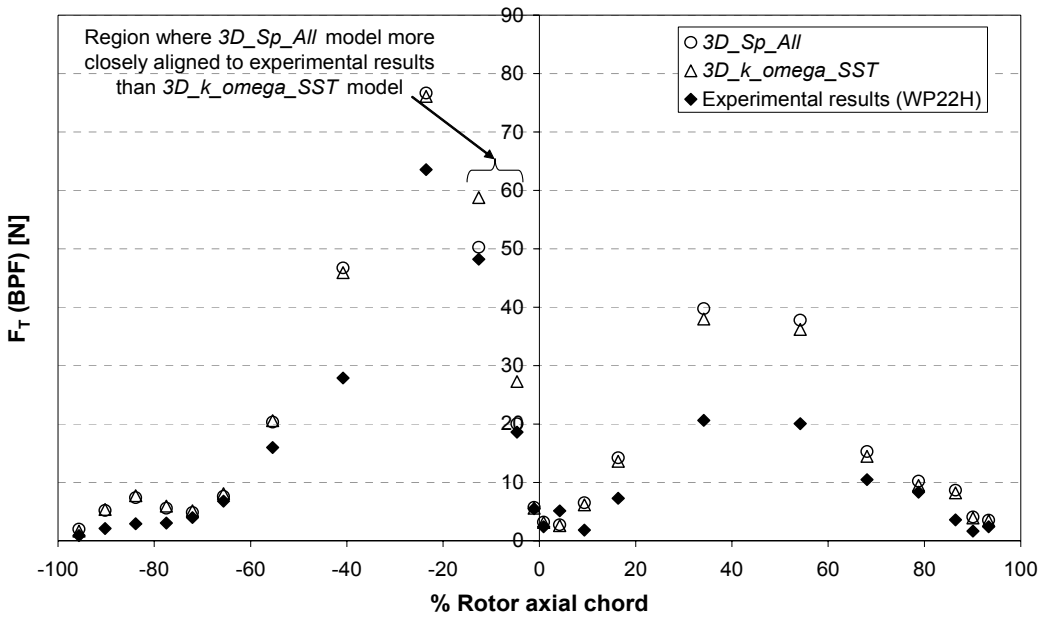

Figure 43 Comparison of turbulence models (k-ω SST and Spalart-Allmaras) with experimental results (tangential force at the BPF)

The conclusion is that the relatively simple single-equation Spalart-Allmaras model is more appropriate than the two-equation k-ω SST turbulence for predicting unsteady rotor forces and pitching moments of high work turbines for relatively coarse mesh density configurations.

6.6 Turbine stage grid sensitivity

6.6.1 Numerical diffusion through the sliding plane

Spatial discretization of continuous partial differential equations into finite difference equations can lead to numerical diffusion in the solution. All flow non-uniformities numerically diffuse through a non-conformal mesh interface, such as a sliding plane as a product of flow re-distribution across non-aligned cells (Figure 44).

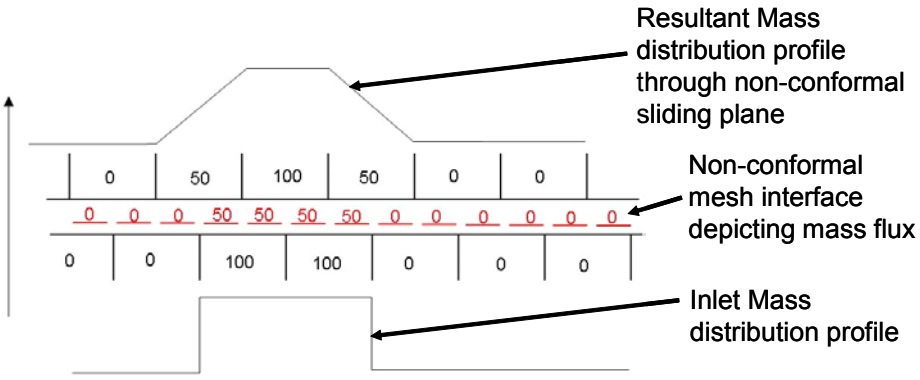

Figure 44 Diagrammatic representation of profile diffusion through non-conformal mesh interface.

Diffusion through the sliding plane has significant implications for forced response analysis. Any smearing of a pressure pulse such as a shock (or any flow non-uniformity) will re-distribute the force onto the blade across a larger area, resulting in

erroneous results. This is a significant concern for high work turbines where the physically correct conservation of both the frequency content and forcing amplitude between the NGV and the rotor are expected to play an important role. To determine the magnitude of the diffusion a mesh sensitivity study is included which quantifies the maximum total pressure, static pressure, total temperature and entropy redistribution across the sliding plane, demonstrating reducing numerical diffusion with increasing mesh density.

For all of these Q2D test cases the k-ω SST turbulence model is used which applies a form of the enhanced wall treatment (EWT). The EWT model essentially blends the two-layer zonal model and the enhanced wall function model. The two-layer zonal model is applied for fine mesh densities to resolve the viscous sublayer (see section 6.6.2). The enhanced wall function blends linear and logarithmic laws of the wall using a function to represent the entire near wall region (laminar sublayer, buffer region and fully turbulent outer region). Cases 3 and 4 have high mesh densities from the nozzle throat to the rotor crown, including the near wall region. The nozzle and rotor domain for cases 1 and 2 are only one cell deep across the radial span, but due to a lack of control of radial adaptation, cases 3 and 4 have progressively finer radial mesh densities. The cell sizes across the sliding plane are detailed in Table 9.

Case No.	circumferential cell size at sliding plane; nozzle side (mm)
1	1.5
2	0.9
3	0.45
4	0.225

Table 9 Mesh sizes for each case

Figure 45 and Figure 46 quantify the maximum variation in total and static pressure respectively across the sliding plane for case 4 at a time step when the difference across the sliding plane is at a maximum. Table 10 quantifies the change in total and static pressure, total temperature and entropy for all cases, demonstrating the numerical diffusion reduction with increasing mesh density. The maximum numerical diffusion of total pressure occurs where the wake convects through the sliding plane (Figure 45). The maximum diffusion of static pressure occurs where the LRS crosses through the sliding plane (Figure 46). The graphical presentation of total and static pressure change across the sliding plane is included in Figure 47 and Figure 48 respectively for clarity. The diffusion for the fine mesh (case 4) is considered negligible and therefore applied to the Q2D high work turbine flow studies (chapter 8).

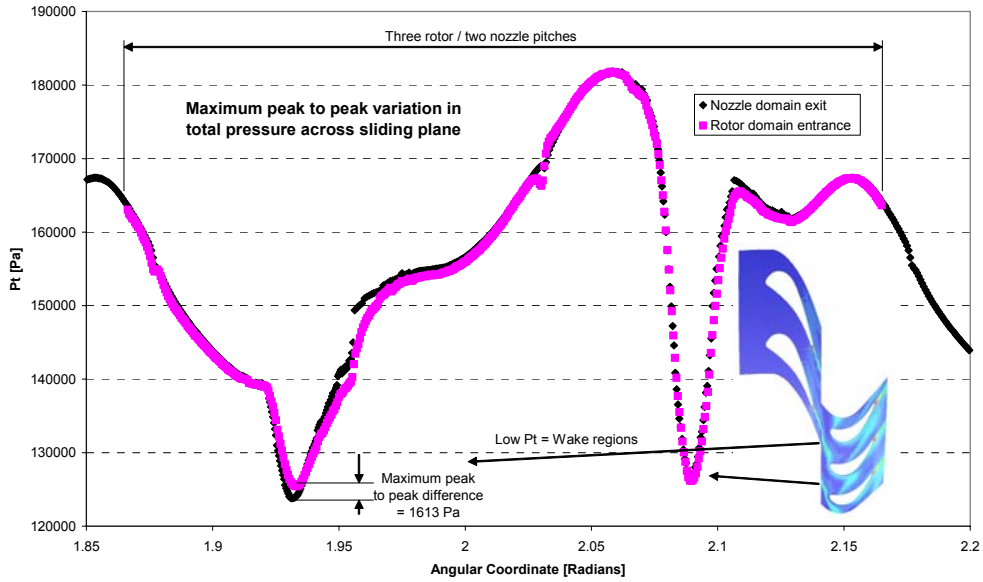

Figure 45 Snaphot of circumferential distributions of total pressure on both sides of the stage sliding plane (Case 4). Time instant for when the maximum difference is observed.

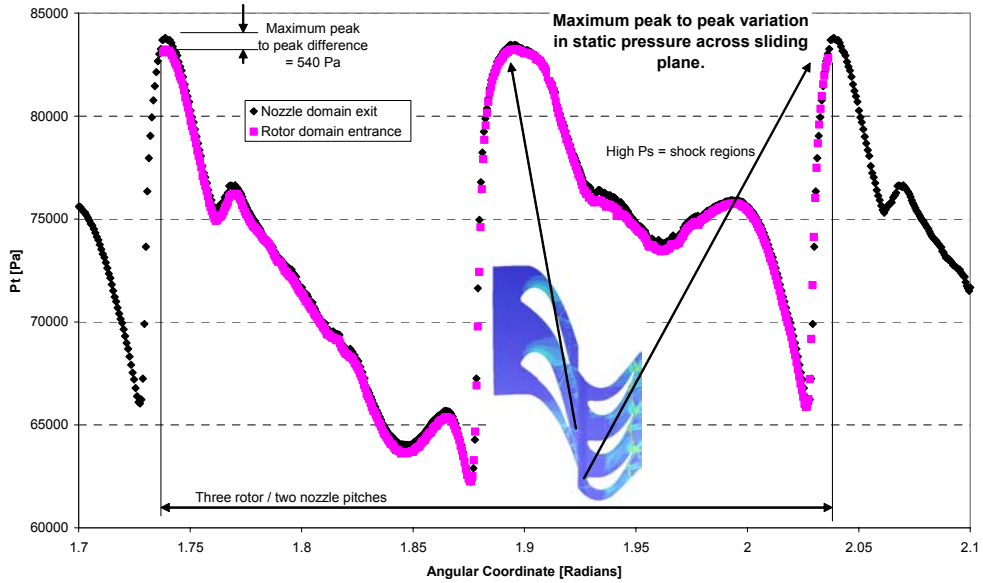

Figure 46 Snaphot of circumferential distributions of static pressure on both sides of the stage sliding plane (Case 4). Time instant for when the maximum difference is observed.

Case No.	Cell size at sliding plane [mm]	ΔPt [Pa]	% of Pt	ΔPs [Pa]	% of Ps	ΔTt [K]	% of Tt	ΔEntropy [-]	% of Entropy	Increasing mesh density
1	1.5	13704	11.6	1631	1.7	3.6	0.9	31	47.5	
2	0.9	7600	7.9	1257	1.4	1.4	0.3	28.6	28.5	
3	0.45	2940	2.4	443	0.5	1	0.2	3.2	10.1	
4	0.225	1613	1.3	540	0.6	1.1	0.3	2.7	12.5	

Table 10 Maximum peak to peak change across sliding plane

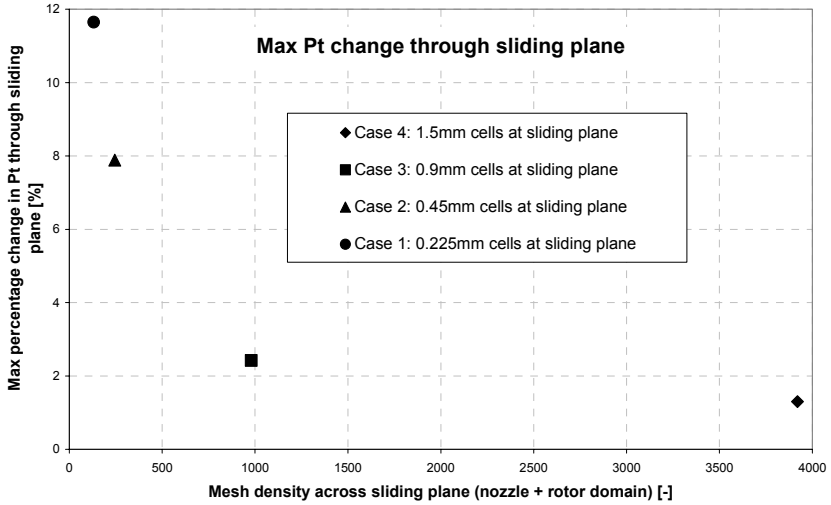

Figure 47 Sensitivity of total pressure change through sliding plane with mesh density

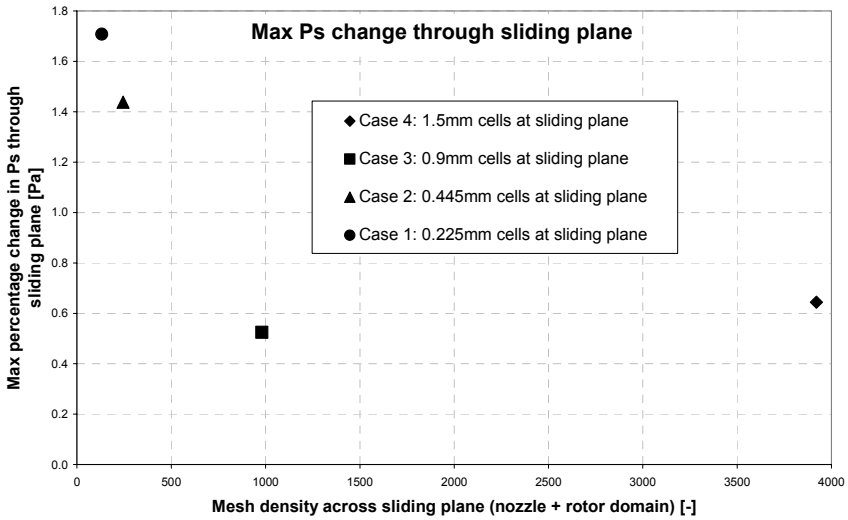

Figure 48 Sensitivity of static pressure change through sliding plane with mesh density

6.6.2 Near wall modelling.

Accurate modelling of complicated near wall flows is challenging. The flow includes a viscous sub-layer, a buffer layer or blending region where the flow is in a state of transition and a fully turbulent region within the inner layer (Figure 49). Dissipation of the turbulent kinetic energy is greater than the production in the sub-layer region and 'Turbulent equilibrium' occurs in the blending region when turbulent kinetic production and dissipation are nearly equal. Computational techniques include blending a wall function with the explicitly resolved near wall region. This is done by combining enhanced wall functions and a two-layer model which explicitly resolves the flow in the sub-layer. As the mesh gets coarser the model weights the wall function more until eventually it is just a wall function.

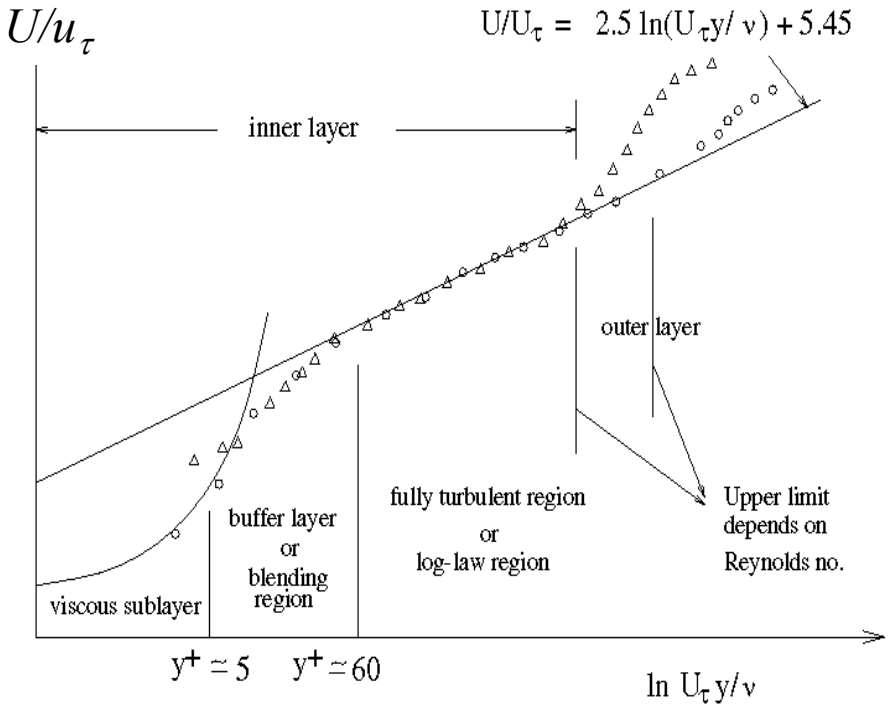

Figure 49 near wall velocity profile exhibits layer structure {Fluent}

For the mesh densities of case 1 and 2 the RRS impingement onto the adjacent nozzle does not generate an, as predicted, separation within the SBLI (sub-critical SBLI). The cause is the applied wall function model due to the coarse mesh densities in the near wall region (8 cells across), which results in a Y^+ of 20-25. This causes the inappropriate wall function model to be applied across most of the SBLI region. For cases 3 and 4 the higher mesh densities in the near wall region (18 and 32 hexahedral cells respectively) result in a $Y^+<1$ which results in the near wall region being explicitly resolved using the more appropriate two-layer zonal model. For these configurations there is an, as predicted, separation in the SBLI region (supercritical SBLI). This has profound implications for forced response modelling. If the most important forcing function in transonic turbines, the shock, is not dissipated through a supercritical SBLI then the forcing function will be erroneously high. This is demonstrated with stronger reflected shocks across the sliding plane in Figure 50 for case 2 where shock reflections from the adjacent nozzle are not dissipated before transmission through the sliding plane. The sensitivity to mesh density is included in Figure 51[dr1].

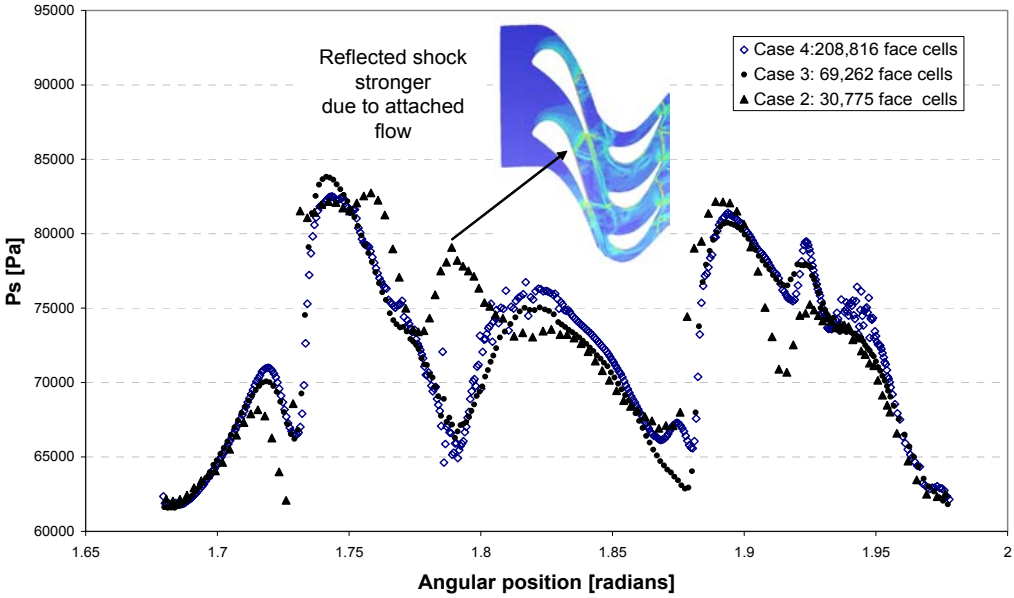

Figure 50 Comparison of static pressure for various mesh densities at the nozzle domain exit.

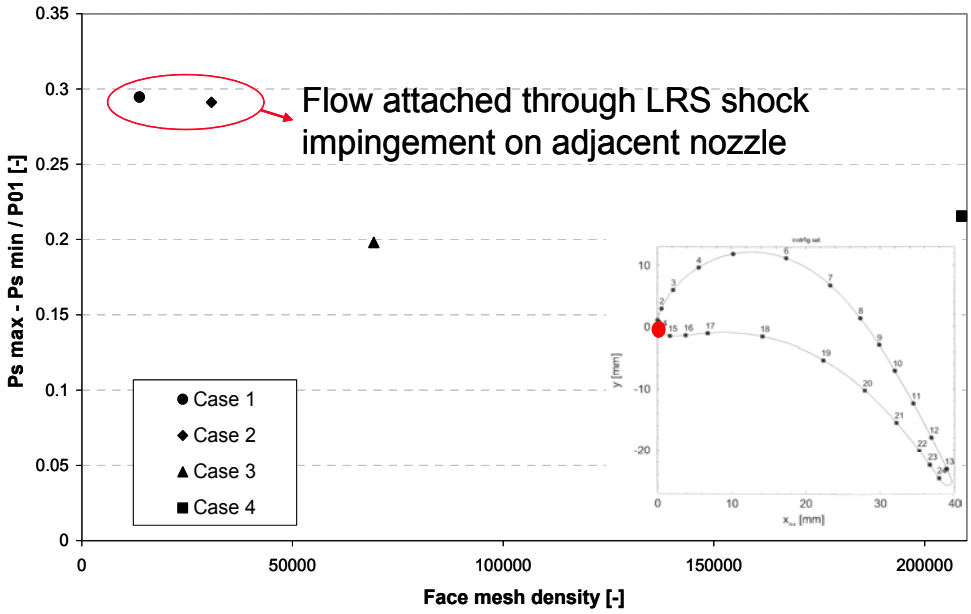

Figure 51 Comparison of different mesh densities using the maximum variation of static pressure at the rotor LE (Probe 1).

7 Validation and analysis

This chapter is broken into two sections which present the validation and analysis of a 3D high work turbine. In the validation section the experimental test rig is introduced from which test data is used to evaluate different modelling standards. The metric for evaluation involves comparisons between the predicted and experimental unsteady rotor forces at 50% span. An order of merit approach is defined to assess each modelling standard. A more detailed comparison of the predictions, using the best modelling standard, and experimental distribution of rotor forces is used to evaluate where small differences occur at the blade passing frequency (BPF). Time traces of axial and tangential force in prominent regions are also compared. In the analysis section of this chapter there is a detailed examination and discussion of the rotor forces and aerodynamic features across the height of the rotor (span). The key aerodynamic forcing functions are identified and discussed.

7.1 Validation

Data from the VKI rig, primarily the unsteady pressure measurements from the rotor, is the principal source for validation of modelling standards, including mesh density and turbulence model investigations. By calculating the rotor forces as detailed in appendix 1, from the geometrical features of the rotor and the unsteady pressures a reference source was generated from which to compare against.

7.1.1 Von Karman Institute transonic turbine test rig.

The VKI rig developed into a shroudless 1.5 stage piston driven, blow-down type which runs for between 0.5-1 sec (Figure 52: which excludes downstream vane). Utilised to support the Turbine Aero-Thermal External Flows (TATEF) research programs I and II; the 43 nozzle, 64 blade configuration contributes to the TATEF II project with four Work Packages (WP) (Table 11). The rig was operated at three operating points: low, nominal and high pressure ratios (Table 12). The author's analysis was carried out at the high operating condition henceforth referred to as WP22H. For a detailed description of the uncertainty analysis see {Perez, 2002}

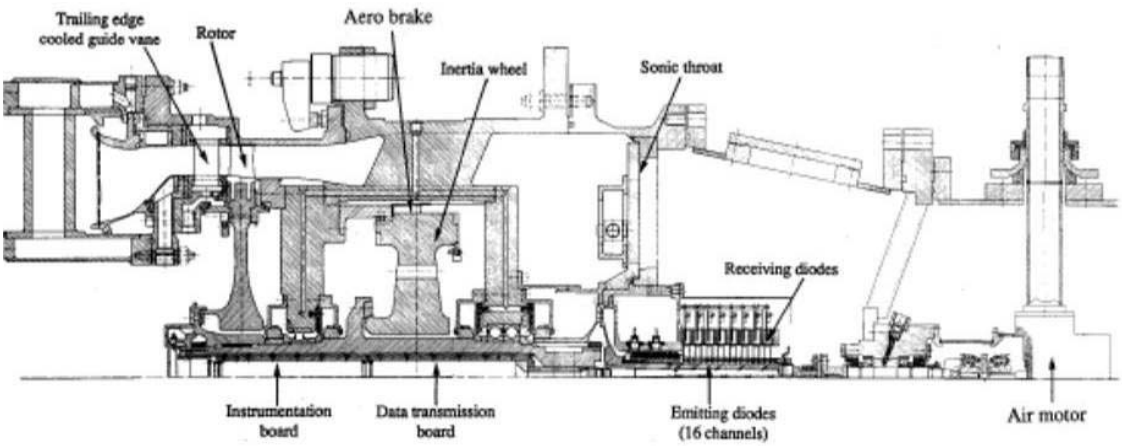

Figure 52 Meridional view of the VKI Rig (pre-downstream nozzle; single stage).

TATEF II	WP2.1	Steady Overall Performance of the Brite Cooled HP Stage. (Includes TE Ejection; NO downstream vane)
	WP2.2	Brite HP Stage Unsteady Aerothermal Flows in Presence of Strong Shock Waves
	WP2.3	HP Rotor Platform Cooling and Hub Disk Leakage Impact
	WP2.4	HP Stage LP Vane Interaction

Table 11 TATEF II Research program packages of work

TEST CONDITIONS mean levels at mid-span

		P01 [bar]	T01 [K]	Ps2 [bar]	Mis2	P03 [bar]	T03 [K]	Ps3 [bar]	Mis3	P01/P03	P01/Ps3	RPM	ACC [RPM/s]	Power [MW]
LOW	Mean	1.647	434.8	0.799	1.071	0.752	349.3	0.679	0.38	2.19	2.42	6475	566	0.713
	Stdev	0.013	2.3	0.010		0.011	3.0	0.011	0.025	0.03	0.03	44	68	0.085
	Tests	30	30	88		30	30	30		30	30	14	14	14
NOM	Mean	1.649	435.0	0.644	1.242	0.517	322.6	0.427	0.53	3.19	3.86	6468	796	1.003
	Stdev	0.012	2.2	0.005		0.010	1.9	0.006	0.031	0.07	0.05	75	16	0.019
	Tests	60	60	104		58	58	59		58	59	18	18	18
HIGH	Mean	1.647	433.9	0.637	1.249	0.426	306.5	0.321	0.64	3.85	5.12	6477	879	1.108
	Stdev	0.012	2.7	0.005		0.012	2.1	0.004	0.033	0.06	0.07	31	10	0.012
	Tests	29	29	92		28	29	28		27	28	17	17	17

Table 12 Mean operating parameters at mid-span of the VKI rig for WP2.2. Subscript 1, 2 and 3 refer to the NGV inlet, NGV exit and rotor exit respectively.

Instrumentation around the rotor includes:

- 33 pressure tappings in the casing positioned between the HP stator and rotor in a 27¼° sector.
- 24 high frequency response pressure sensors which are distributed over 3 rotor blades (Figure 53).
- 24 surface temperature measurements (buried thin film gauge, flush with surface); distributed over 6 rotor blades.
- Total pressure and temperature by rotor fast response pressure probe and dual hot wire aspirated probe (nose mounted at 50% height).

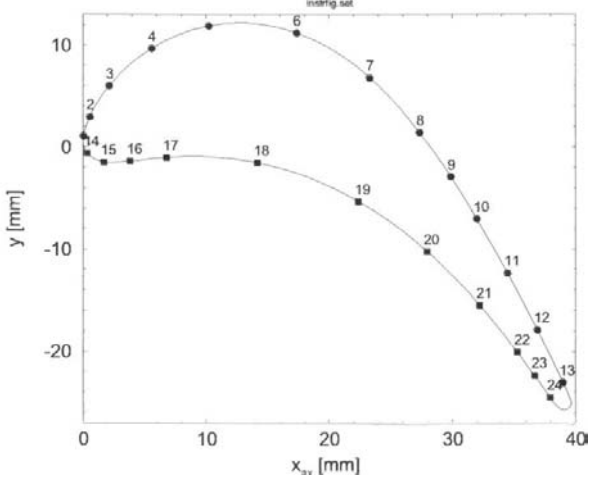

Figure 53 High frequency response pressure transducers locations around the VKI HP rotor at 50% span

Rig work to date includes unsteady pressure measurements of the rotor at 50% for WP 2.2H. These measurements are the primary data used for validation of the CFD models.

7.1.2 Order of merit

Three configurations of the Von Karman institute CT3 rig running at the high operating condition (WP2.2H; see section 7.1.1) have been assessed. Each configuration has a different mesh density or turbulence model (Table 13). It was initially planned to perform these 3D stage calculations at two grid resolutions (1.4 and 5.8 million cells) for both turbulence models (S-A and K-W SST). This would have enabled an unambiguous assessment of the sensitivities to the spatial resolution and the turbulence modeling standard. However, the configuration for a high mesh density using the Spalart-Allmaras model did not converge sufficiently well and the results are not considered to be credible. These predictions are therefore not presented in the thesis. This presents a problem in the research strategy as it is therefore impossible to know the relative benefits of the Spalart-Allmaras model using the fine mesh. Nevertheless, some comments can be made to underwrite the three assessed models. It is known that there are strong shocks present in the turbine stage and that SBLIs are expected to play an important role. Furthermore, it is known from the 2D assessment that the K-W SST model is better at predicting flow separations as long as the spatial discretisation is sufficient (section 6.6.2). In addition, during the course of initial studies during this research, simple two-dimensional predictions for compression ramps were performed which showed that for fine mesh resolutions the K-W SST gave the best results. Finally, the figure of merit shows that the fine mesh K-W SST shows a substantial improvement relative to the two coarse mesh simulations. Although, it is unknown if an S-A fine mesh model could provide a better solution, the fine mesh K-W SST is the best prediction within this research and is therefore chosen for more in-depth analysis. The mesh densities of configurations A and B are typically used within industry for blade design. For details of how each CFD model was constructed see chapter 6. The operating conditions for the predictions and experimental rig are summarised in Table 14.

3D CFD Model Configuration	Turbulence model	No. cells in nozzle and rotor domain
A	Spalart-Allmaras	1.4 million
B	k-ω SST	1.4 million
C	k-ω SST	5.8 million

Table 13 3D CFD configurations turbulence model and mesh sizes

	3D CFD model	Exp. Results WP22H
Capacity	*0.0101*	0.0101
Reaction	*0.312*	0.315
Specific work $\frac{c_p \Delta T_{01-03}}{T_{01}}$	*289*	299
Stage loading @ 50% span $\frac{c_p \Delta T_{01-03}}{U^2_{50\%}}$	*2.003*	2.076
Pressure ratio (P_{01}/P_{03})	*3.85*	3.85
η_{TURB}	0.76	0.78

Table 14 Comparison of CFD and experimental operating parameters

A comparison of the harmonic distribution of unsteady rotor forces at 50% span (S=0.5) between the experimental results and each of the evaluated modelling standards (Configurations A-C) is included in Figure 54. To compare each model an order of merit approach has been defined, which is tabulated in Table 15 to Table 17. The predicted axial and tangential forces at 50% span are calculated as a proportion of the experimental results at each harmonic ($X=F_{CFD} / F_{EXP}$). A weighting factor (n) is applied to the modulus of the difference from the experimental results ($|X_a-1|$) for each of the axial and tangential forces (e.g. $Y_{axial}=|X_a-1| \times n_{axial}$). The weighting factor (n) is calculated at each harmonic as a proportion of either the axial or tangential force at the BPF (e.g. $n_{axial\ 5th\ harmonic}=F_{A\ EXP(5th)} / F_{A\ EXP(BPF)}$). The tangential and axial resultant (Y) are summed (Z) at each harmonic, and the overall accuracy of the model is defined as the resulting sum (ΣZ). The results are tabulated in Table 18, where the models are more accurate as ΣZ tends to zero. The conclusion is that the Spalart-Allmaras turbulence model is the most appropriate turbulence model for coarse meshes, however the most accurate modelling standard applies the k-ω SST turbulence model onto a fine spatially discretized domain. Model C is significantly superior in predicting the tangential forces at the BPF, and only becomes unreliable in predicting the trends at higher harmonics.

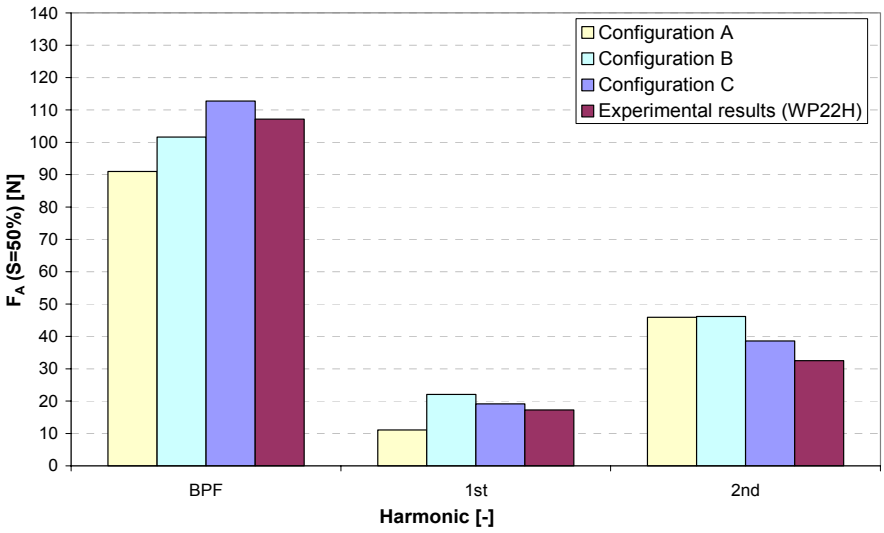

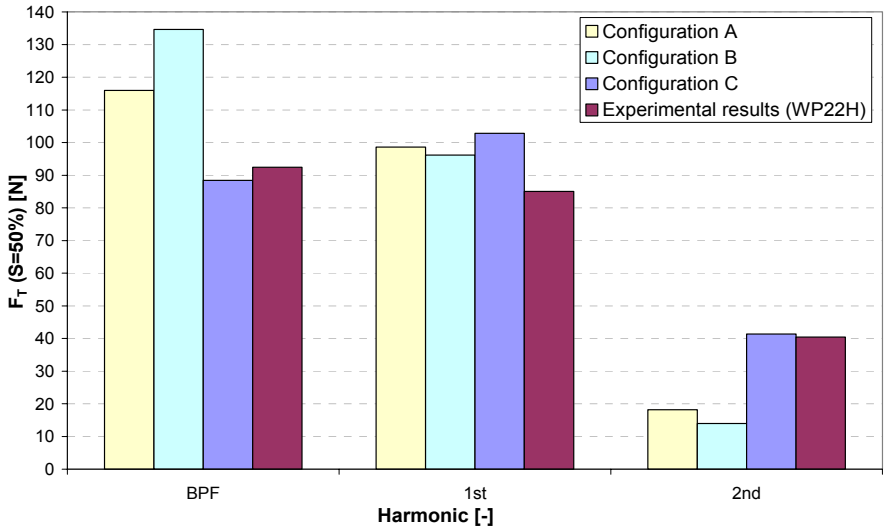

Figure 54 Comparison of harmonic distribution of unsteady axial force (top) and tangential force (bottom) at 50% span for different modelling standards and experimental results

	BPF	1st Harmonic	2nd Harmonic	3rd Harmonic	4th Harmonic	5th Harmonic
$X_a=F_{A\ CFD}/F_{A\ EXP}$	0.89	0.64	1.41	1.66	1.18	0.73
$X_t=F_{T\ CFD}/F_{T\ EXP}$	1.25	1.16	0.45	0.67	1.26	0.23
n_{axial} (weighting)	1	0.16	0.3	0.07	0.08	0.03
$n_{tangential}$ (weighting)	1	0.92	0.44	0.22	0.11	0.31
$Y_{axial}=\|X_a-1\| \times n_{axial}$	0.11	0.06	0.12	0.05	0.01	0.01
$Y_{tangential}=\|X_t-1\| \times n_{tangential}$	0.25	0.15	0.24	0.07	0.03	0.24
$Z=Y_{axial}+Y_{tangential}$	0.36	0.21	0.36	0.12	0.04	0.25

Table 15 Validation of configuration A (ΣZ=1.34)

	BPF	1st Harmonic	2nd Harmonic	3rd Harmonic	4th Harmonic	5th Harmonic
$X_a=F_{A\ CFD}/F_{A\ EXP}$	0.95	1.28	1.42	1.73	0.93	2.11
$X_t=F_{T\ CFD}/F_{T\ EXP}$	1.46	1.13	0.35	0.74	1.17	0.1
n_{axial} (weighting)	1	0.16	0.3	0.07	0.08	0.03
$n_{tangential}$ (weighting)	1	0.92	0.44	0.22	0.11	0.31
$Y_{axial}=\|X_a-1\| \times n_{axial}$	0.05	0.04	0.13	0.05	0	0.03
$Y_{tangential}=\|X_t-1\| \times n_{tangential}$	0.46	0.12	0.29	0.06	0.02	0.28
$Z=Y_{axial}+Y_{tangential}$	0.51	0.16	0.42	0.11	0.02	0.31

Table 16 Validation of configuration B (ΣE=1.53)

	BPF	1st Harmonic	2nd Harmonic	3rd Harmonic	4th Harmonic	5th Harmonic
$X_a=F_{A\ CFD}/F_{A\ EXP}$	1.05	1.11	1.19	0.7	0.6	4.04
$X_t=F_{T\ CFD}/F_{T\ EXP}$	0.96	1.21	1.02	0.84	0.6	0.62

n_{axial} (weighting)	1	0.16	0.3	0.07	0.08	0.03
$n_{tangential}$ (weighting)	1	0.92	0.44	0.22	0.11	0.31
$Y_{axial}=\|X_a-1\| \times n_{axial}$	0.05	0.02	0.06	0.02	0.03	0.09
$Y_{tangential}=\|X_t-1\| \times n_{tangential}$	0.04	0.19	0.01	0.04	0.04	0.12
$Z=Y_{axial} + Y_{tangential}$	0.09	0.21	0.07	0.06	0.07	0.21

Table 17 Validation of configuration C (ΣE=0.71)

3D configuration	ΣZ	Turbulence model	No. cells in nozzle and rotor domain
A	1.34	Spalart-Allmaras	1.4 million
B	1.53	k-ω SST	1.4 million
C	0.71	k-ω SST	5.8 million

Table 18 Validation summation

7.1.3 Steady results

A comparison of the predicted steady nozzle and rotor pressures between configuration C and the experimental results is presented in Figure 55. The predictions on both airfoils are considered to be in reasonable agreement with the experimental results. The largest differences around the nozzle occur downstream of the RRS impingement position. For the rotor the largest differences occur on the pressure side, which will add some error to the calculated rotor forces.

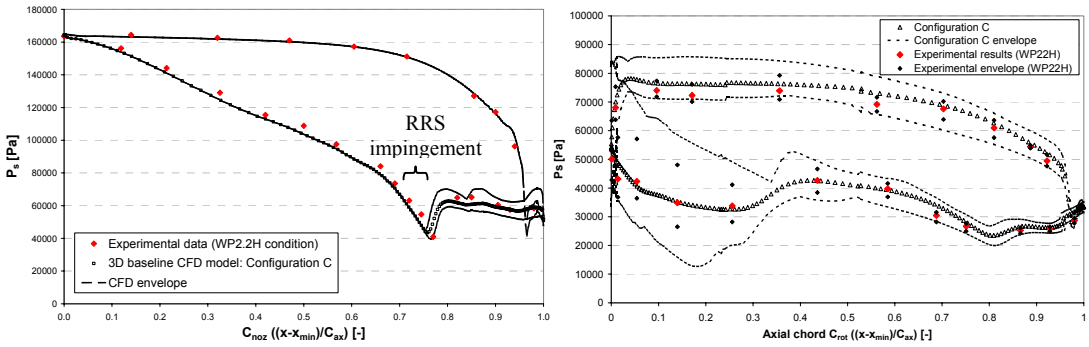

Figure 55 Comparison of predicted nozzle (left) and rotor (right) static pressure (configuration C) and experimental results at S=0.5

7.1.4 Force and pitching moment comparison

A comparison of the best modelling standard (configuration C) and the experimental rotor force and pitching moments at 50% span is presented in Figure 56. The only major discrepancy between the predictions and the experimental results is the pitching moments at the lower harmonics. This is due to the sensitivity of the pitching moments to forces applied towards the rotor TE. In this region relatively small discrepancies between the predictions and the experimental results accentuate the pitching moment error due to the large distance from the centre of rotation. This is demonstrated in the comparison of the forces and pitching moment as a function of rotor axial chord at the BPF in Figure 57, where the large differences between the predicted pitching moments and experimental results are predominantly towards the rotor TE. The most significant differences between the predicted and experimental forces occur on the pressure side where the predicted axial forces are larger than the experimental results downstream of

50% axial chord and the tangential forces are larger than experimental values downstream of 30% axial chord.

An examination of the unsteady forces in prominent regions, where high axial and tangential forces occur is included between the LE and rotor crown, and approximately half way along the rotor pressure side (Figure 58-Figure 60). One of the most challenging aspects of accurately modelling the rotor forces for high work turbines is the shock impingement contribution. Figure 58 and Figure 59 demonstrate that the modelling standard is appropriate in this region where the shock strength is at a maximum. The modelling standard is considered to be a good match with the experimental results.

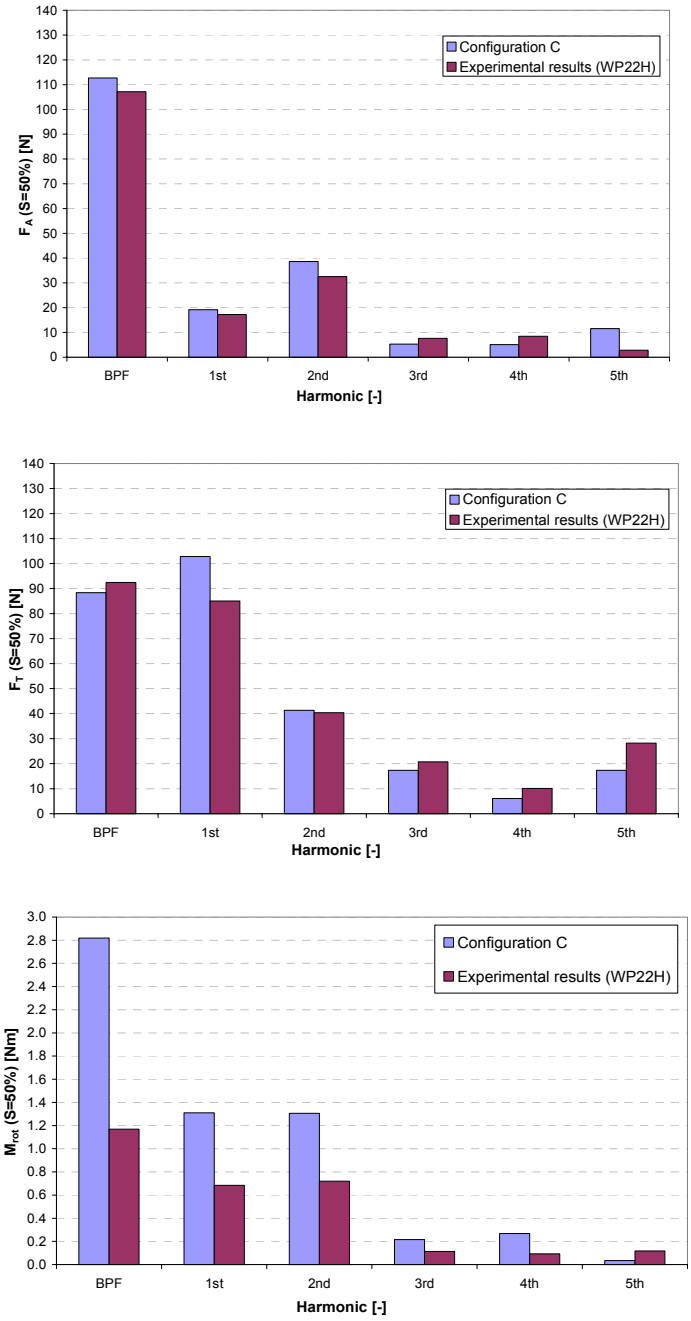

Figure 56 Comparison of harmonic distribution of unsteady axial force (top) tangential force (middle) and pitching moment (bottom) between configuration C and experimental results at 50% span

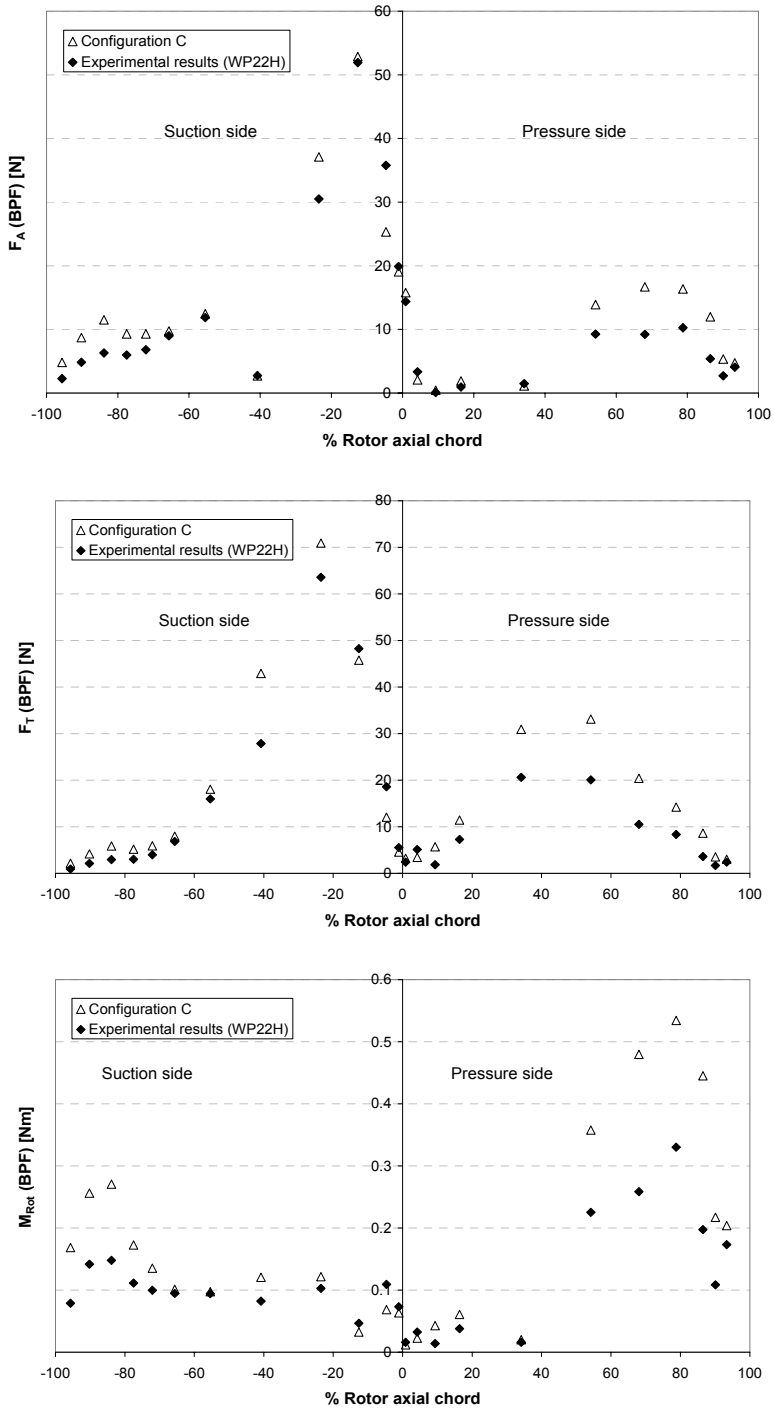

Figure 57 Comparison of configuration C and experimental rotor unsteady axial force (top), tangential force (middle) and pitching moment (bottom) at the BPF (S=0.5).

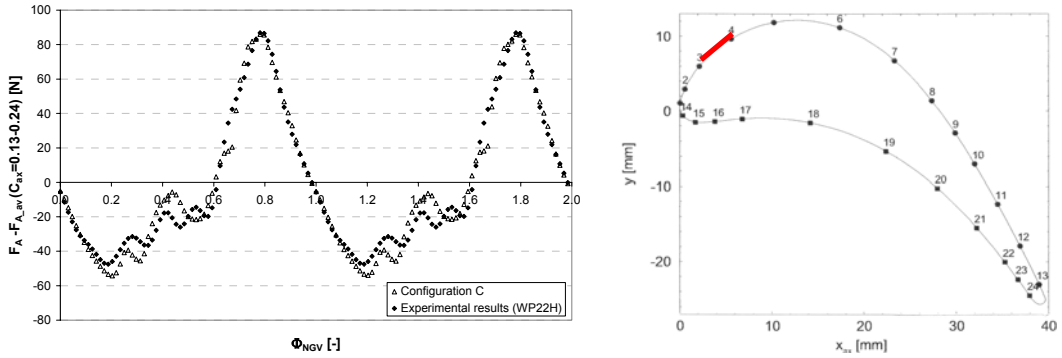

Figure 58 Comparison between predicted and experimental unsteady axial force at C_{ax}=0.13-0.24 on the rotor suction side.

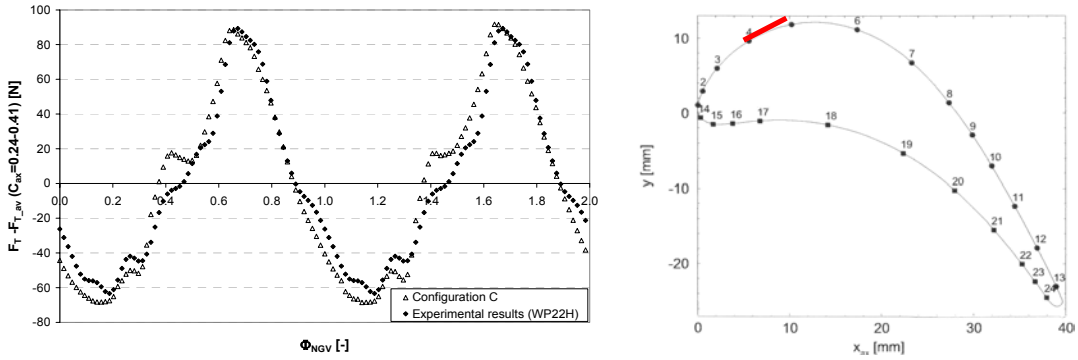

Figure 59 Comparison between predicted and experimental unsteady tangential force at C_{ax}=0.24-0.41 on the rotor suction side.

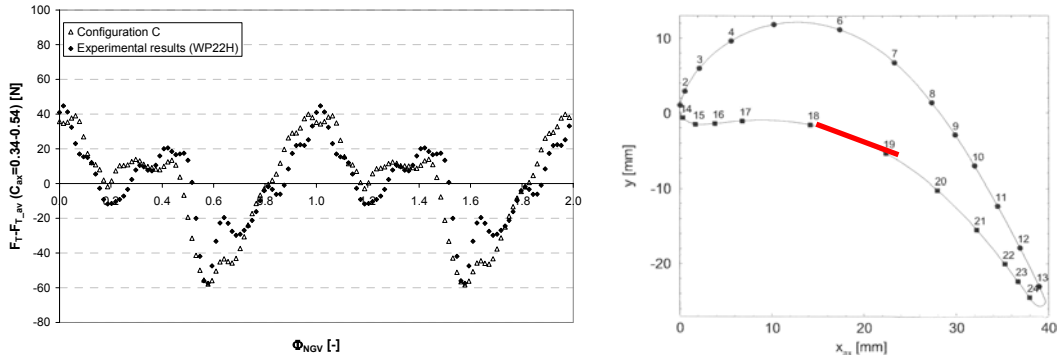

Figure 60 Comparison between predicted and experimental unsteady tangential force at C_{ax}=0.34-0.54 on the rotor pressure side.

7.2 Analysis

The objective of this section is to quantify the unsteady rotor forces and pitching moments at 15, 50 and 85% span and detail the flow features that generate them within a high work turbine stage using the highest fidelity CFD configuration (Configuration C).

The three most important forcing functions are:

- the nozzle TE shocks (L1 and R1, Figure 61)
- the nozzle wake, which acts as a direct forcing function and locally reduces the incidence onto the rotor, which modulates the blade loading
- the nozzle potential field, which is not explicitly detailed.

Each forcing function repeats on the rotor as it passes each nozzle pitch which can produce excitation at the relative blade passing frequency (BPF) and integral multiples where BPF=(n×t)/60 (n=rotational velocity (RPM) and t=number of nozzles). For the case considered the BPF is 4534Hz.

A mechanism which affects the potential field and shock forcing function includes the transient convergent-divergent duct formed between the nozzle and passing rotor. The effect is to modulate the potential field and the shock strength and phasing. The naming convention for each shock in this analysis is detailed in Figure 61.

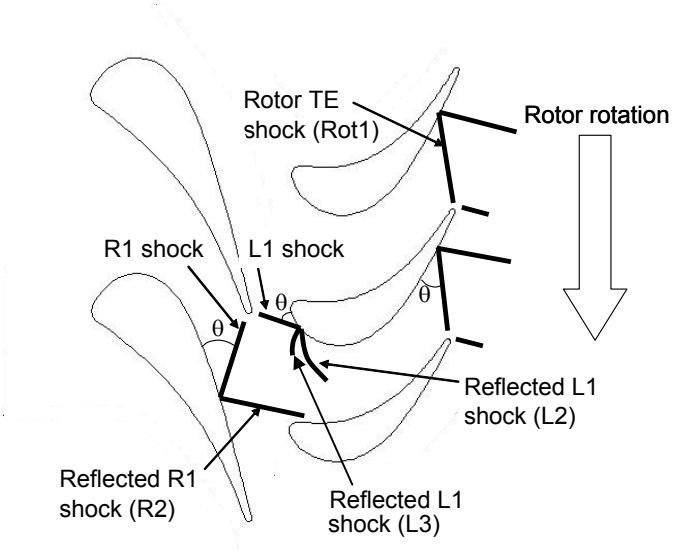

Figure 61 Schematic of shock structure in a high pressure turbine stage

7.2.1 Blade forces and pitching moments.

The rotor forces for the lowest six harmonics at 15, 50 and 85% span (S=0.15, 0.5 and 0.85 respectively) are presented in Figure 62. At the Blade Passing Frequency (BPF) the axial force monotonically increases from 15-85% span by a factor of nearly 3, whilst the tangential force decreases by a factor of more than 6. The first 3 tangential force harmonics follow a similar trend. This is examined in more detail below. The pitching

moment does not monotonically increase, or decrease due to a highly sensitive region at 50% span, examined in more detail below.

7.2.2 Harmonic distribution.

An examination of the distribution of forces and pitching moments at the BPF is included (Figure 63). Most of the axial force occurs between 54-86% of axial chord on the pressure side and between the stagnation position and 24% of axial chord on the suction side. The axial force is high in these regions due to the nozzle shocks directly impinging onto a relatively large 'frontal area' that is perpendicular to the engine centre line and also due to wake impingement. It is also in these regions that the largest differences across the span occur, where the axial force increases towards the hub line where the shocks are strongest. However a reduction of the net axial forces is demonstrated to occur from tip to hub (Figure 62) due to the relative phase alignment of each discretely calculated facet around the rotor.

At all spans the tangential force is highest on the pressure side at approximately 54% and between 13-24% axial chord on the suction side. The tangential force is highest in these regions due to the relatively high surface area that is perpendicular to the shaft rotation direction (radial plane). In both these regions the tangential force is highly sensitive to span, significantly increasing towards the hub line due to the higher shock strength. The net result is tangential forces that are 6 times higher at the hub than the tip (Figure 62).

The pitching moments at 50% span are distinctly different from the 15% and 85% span results. There are no distinct peaks between 13-24% on the suction side and 34% of axial chord on the pressure side. This distinct difference is thought to be a contributing factor to the relatively large pitching moments at 50% span (Figure 62).[e2]

7.2.3 Forcing function at 50% span

This section details flow features that generate the unsteady blade force and pitching moments in the mid-span region (S=0.5). At the BPF two prominent regions of force unsteadiness occur, the first is between the rotor LE and the rotor crown on the suction side between 0.13-0.41 of the axial chord (C_{ax}), where large unsteady tangential and axial forces occur, and the second is on the pressure side mid chord (0.34-0.54C_{ax}) where large tangential forces occur (Figure 63). Time traces of the forces in these regions are presented to enable a better understanding of how the unsteady forces develop in these proximities (Figure 64-Figure 66). The figures also include annotation that details the driving forcing function. The unsteady axial force generated between 0.13-0.24C_{ax} on the suction side from Φ_{NGV}=1-1.55 is generated by the wake and impinging inter-row shock reflections (L2 and L3). At Φ_{NGV}=1.55 the L1 shock impinges, which generates a rapid increase in axial force up to Φ_{NGV}=1.78 (Figure 67 and Figure 68). The unsteady tangential force between 0.24-0.41C_{ax} on the suction side increases from Φ_{NGV}=1.16 due to the wake convecting past, and the impingement of the rotor passage shock reflections (L3). From Φ_{NGV}=1.32 the unsteady tangential forces considerably increase, initially from the reflected L2 shock impinging, followed shortly afterwards by the adjacent nozzles L1 shock impingement. The unsteady tangential forces between 0.34-0.54C_{ax} on the pressure side increases from Φ_{NGV}=1.58 due to forward propagating reflected shocks impinging and wake convection, which is exacerbated as the L1 shock impinges to generate a maximum force at Φ_{NGV}=1.97.

7.2.4 General flow field

A more detailed description of particular flow features, such as the shock propagation, the wake forcing function and the nozzle unsteadiness at 50% span (S=0.5) are detailed in section 7.2.4.1 to 7.2.4.3 respectively. The modulation of the shock forcing function and the wake forcing function are detailed in section 7.2.4.4 and 7.2.4.2 respectively. 3D flow features are detailed in section 7.2.5 and a separation prediction tool is introduced in section 7.2.6.

7.2.4.1 Shock propagation at 50% span

This section details how the nozzle TE shocks propagate in the blade passages and inter-row gap. The description captures rotor progression by nozzle phase, where Φ_{NGV}=0, 2, 4 etc when the nozzle and rotor periodic faces become aligned (Figure 36). Starting from Φ_{NGV} **= 1** (Figure 67), L1 has already impinged from the rotor crown past the leading edge, progressing past a rotor separation, and reflecting as two forward propagating shocks L2 and L3. One element of L2 has impinged onto the adjacent rotors pressure side near the LE and is reflecting back across the rotor passage towards the rotor crown. A second element has propagated through the wake and is just past halfway between the rotor LE and nozzle TE, heading upstream towards the downstream portion of the nozzle suction side. L3 has propagated upstream towards the nozzle suction side and impinged onto the nozzle at C_{ax}=0.88, partially reflecting back towards the rotor. As the rotor passes the nozzle, a transient convergent-divergent duct is formed (see section 7.2.4.4) which modulates the R1 shock from Ps_2/Ps_1=1.32 to 1.44 (Figure 69). The shock is of sufficient strength to generate a continuous separation on the nozzle suction side. The size of the separation modulates in phase with the R1 shock strength. The reflected shock strength is also modulated, ranging from Ps_2/Ps_1=1.03 to 1.33.

By Φ_{NGV} **= 1.125** the two elements of L2 are about to impinge onto the rotor crown and late nozzle suction side. L3 continues to reflect from the nozzle suction surface at C_{ax}=0.87 towards the rotor.

At Φ_{NGV} **= 1.25**, the two elements of L2 have impinged near the nozzle TE and the rotor crown, L3 continues to reflect from the nozzle suction side towards the rotor at C_{ax}=0.85.

At Φ_{NGV}**=1.375**, the two elements of L2 have reformed as a single shock, impinging near the rotor crown. The transient convergent-divergent nozzle formed from the rotor movement increase the nozzle TE shock strength, increasing the size of the nozzle separation and causes R2 to reflect as two discrete shocks, a leading compression shock and a re-attachment shock (R2) (Figure 70).

At Φ_{NGV}**=1.5** The reformed L2 shock is in the process of merging with the adjacent nozzles L1 shock half way between the rotor crown and LE. Rotor passage shock reflections are propagating upstream towards the rotor crown. The adjacent rotor L2 shock is impinging onto the rotor pressure side near the LE and the adjacent rotor L3 shock is impinging on the adjacent nozzle suction side.

By Φ_{NGV}**=1.625** the adjacent nozzle L1 and the L2 shock have formed into a single shock that impinges closer towards the rotor LE. The adjacent rotor L2 shock has

reflected from the rotor pressure side, and the rotor passage shock reflections are impinging just downstream of the rotor crown.

From Φ_{NGV}=**1.75** to **1.875** the adjacent nozzle L1 shock impinges closer towards the rotor LE, the L2 shock has impinged near the adjacent rotors LE on the pressure side and is about to reflect back towards the rotor crown. The forward propagating rotor passage shock reflection has impinged onto the rotor crown.

7.2.4.2 Wake Forcing function at 50% span

The wake is a significant forcing function which accounts for as much as 60% of the unsteady axial force and 40% of the unsteady tangential force in a transonic turbine stage (see section 8.6). The total pressure deficit in the wake varies by as much as 0.22-0.44 (P_{t_inlet}/ $Pt_{max\_sliding\_plane}$-$Pt_{min\_sliding\_plane}$). The total pressure deficit variation is a consequence of the relative position of discrete Von Karman vortices and rotor modulation of the back pressure (see Figure 71). As the rotor passes the wakes, the relative incidence varies by as much as 43° at the sliding plane (Figure 72). This large variation significantly affects the blade loading, temporarily reducing it enough to significantly reduce the rotor crown separation between Φ_{NGV}=1-1.125 (Figure 68).

7.2.4.3 NGV flow unsteadiness at 50% span

The unsteadiness around the nozzle is predominantly downstream of the throat on the suction side (0.77-1C_{ax}) (Figure 73). This region of the nozzle is exposed to rotor interaction effects, including the rotor potential field and forward propagating shocks. Both the L1 and R1 shocks are modulated by blade row interaction effects, where the shock strength (Ps_2/Ps_1) of R1 varies from 1.32 to 1.44 (Figure 69) and the impingement angle of the R1 shock onto the adjacent nozzle varies from approximately 42 to 48° between 0.77-0.79C_{ax}. The impinging shock generates an unsteady SBLI of sufficient adverse pressure gradient along the nozzle suction side (Figure 74) to generate a small separation at all nozzle phases (Φ_{NGV}). The reflected R1 shock (R2) is a considerable forcing function, modulated at the same Blade Passing Frequency (BPF) as the impinging R1 shock, it varies from Ps_2/Ps_1=1.03 to 1.33 due to the rotor passing.

7.2.4.4 Transient convergent-divergent nozzle at 50% span

As the rotor passes the nozzle a throat is formed between the suction side of the nozzle and the suction side of the rotor near the LE. The throat area reduces as the rotor LE becomes aligned with the nozzle TE (Figure 76). Blade row interaction effects are significant at this phase when the rotor potential field significantly increases the local back pressure and the area ratio expansion in the divergent portion of the convergent-divergent nozzle is at a local maximum. This transient effect results in the Mach number just upstream of the L1 shock reaching a local maximum when the rotor LE is nearly tangentially aligned with the nozzle TE at Φ_{NGV}=1 and every 2/3rd of a nozzle phase thereafter (Figure 77). The Mach number just upstream of L1 ranges from 1.2 to 1.37. The pressure rise across the L2 shock varies from Ps_2/Ps_1=1.37 at Φ_{NGV}=1.69 to Ps_2/Ps_1=1.51 at Φ_{NGV}=1.48 with the rotor passing. The minimum pressure rise (Ps_2/Ps_1=1.37) occurs when the Mach number upstream of L1 is at the local maximum due to the large static pressure field downstream of the shock, generated by the close proximity of the rotor. Conversely the maximum pressure rise (Ps2/Ps1=1.51) occurs when the Mach number upstream of L1 is at a local minimum due to the relatively large distance from the rotors potential field. The reflected R2 shock is also modulated,

however when R1 is at a maximum the reflected shock R2 reflects as two discrete shocks, a leading compression and a re-attachment shock (Figure 70).

7.2.4.5 Rotor separation at 50% span

The highly loaded rotor has a boundary layer (BL) separation across the entire nozzle phase in the rotor crown region (Figure 68). The separation size reduces as the wake convects past due to the lower swirl angle within the nozzle wake (and hence reduced rotor incidence). From $\Phi_{NGV} = 1$ to **1.125**, the rotor crown separation is at a minimum as the convecting wake reduces the rotor loading. By $\Phi_{NGV} = 1.25$ the wake has convected past the rotor crown, increasing the incidence angle again, which then increases the rotor loading and separation size, which is extending towards the rotor LE. The separation is increased and extended downstream to the rotor crown by the impinging rotor passage shock reflection (L2). The separation size is further exacerbated by the impingement of the adjacent nozzle L1 shock at $\Phi_{NGV} = 1.5$. From $\Phi_{NGV} = 1.5$ to **1.875** the rotor crown separation is in the process of convecting down the rotor suction side.

In conclusion there is perpetual BL separation at the rotor crown. The separation size is modulated by the convecting nozzle wake and impinging shocks. The shocks exacerbate the separation size and the wakes relieve the loading, reducing the separation size. Periodically a separation disengages from the rotor crown separation and convects down the rotor suction side at each nozzle phase.

7.2.5 3D flow features

The shock strength and propagation angle from the nozzle TE is a function of the inter-row Mach number, which reduces with increasing radial span (Figure 78), due to the prismatic nozzles turning the flow into an increasing cross sectional area at higher radial span. This results in the nozzle TE shocks propagating more obliquely at the hub than the tip (Figure 79). As a result the shocks propagating from the nozzle tip region impinge onto the rotor at an earlier phase than the shocks propagating from the nozzle root region. For forced response considerations, this is akin to the conventional methodology of wake shaping from the nozzle design, or tangential lean on the rotor, which can be applied to ensure that the wake does not impinge across the rotor span at a common phase. Typically in conventional turbine design the TE of the nozzle is crafted to ensure that the wake forcing function impinges onto the rotor across a range of phases. A more subtle aspect of the nozzle TE shock propagation angle includes the relative phasing of the nozzle TE shock and wake forcing functions which varies across the radial span (Figure 80).

The rotor crown separation detailed in section 7.2.4.5 occurs over the entire span of the rotor due to the high loading (Figure 81). However the increased propagation angle of the nozzle hub L1 shock phase shifts the separation growth at the rotor crown across the rotor span i.e. the rotor crown hub separation growth phase lags the tip separation growth. The separations include considerable three dimensional effects, the vortical structure of the separation migrates towards the rotor tip beyond S=0.5 (Figure 82). Like the L1 shock, the reflected R2 shock becomes a more significant forcing function towards the hub, where the steady shock strength (Ps_2/Ps_1) reaches 1.29.

7.2.6 Shock induced separation prediction

Predicting shock induced separations in highly loaded turbines is a difficult exercise. It is made difficult by the complex flow physics such as the modulating shock strengths, (due to the convergent-divergent throat formed from the rotor passing), the changing boundary layer characteristics, and the curvature of the blades. A simplistic approach to predicting turbulent BL separations from impinging shocks would be to apply the work of Reshotko and Tucker {Reshotko, E. 1955} who categorise separation criteria of impinging shocks in terms of the upstream boundary layer shape factor (H) and the upstream and downstream Mach number (M_1 and M_2 respectively). The compressible shape factor is derived from:

$$H = H_i\left(1+\frac{\gamma-1}{2}M_1^2\right)+\frac{\gamma-1}{2}M_1^2$$

Equation 3: Compressible shape factor

Where H_i is the incompressible shape factor, derived from:

$$\text{Constant}\times M_1 = \frac{H_i^2}{\left(H_i^2-1\right)^{1/2}(H_i+1)}e^{1/(H_i+1)} \equiv f(H_i)$$

Equation 4 Incompressible shape factor

To determine if a separation is predicted the incompressible shape factor (H_i) is derived from Figure 83, from an upstream Mach number (Y axis). M_2 is plotted as a function of M_1 onto Figure 84, from either oblique shock theory or CFD predictions. A separation is predicted if the resulting position lies beneath the upstream boundary layer shape factor value (H_1 derived from Equation 3). The shape factor and isentropic Mach number for the VKI operating condition WP2.2H are included in Table 19, where the Mach numbers are isentropically derived from the experimental static pressure tappings around the nozzle and rotor. Although in the initial design phases these values would be extracted from CFD models. Separations are expected from the SBLIs generated by the L1 and R1 shock impinging onto the rotor and adjacent nozzle respectively. The rotor trailing edge shock which impinges onto the adjacent rotor is predicted to be close to separation. The recommendation to designers is to apply this simple approach in the initial phases of high work turbine design to understand the implications of blade loading.

	M_1	M_2	H
$L1_{S=0.5}$	1.05*	0.81*	2.95*
$R1_{S=0.5}$	1.56	1.23	2.4
Rot_1	1.45*	1.34*	2.25*

Table 19 Experimental time averaged isentropic Mach number and shape factor properties at S=0.5 (*=relative Mach number and shape factor), see Figure 83 for H_i derivation.

7.2.7 Conclusions

The nozzle TE shock is the most significant forcing function. The L1 and reflected R1 shock (R2) significantly affect the rotor unsteady forces across the entire span. The strength of the most significant shock (L1) becomes progressively stronger towards the rotor hub due to the higher Mach numbers (from 1.39-1.46P_{s2}/P_{S1}). The shock is considerably modulated by the rotor passing, changing the strength and phasing onto the rotor.

The significant wake forcing function impinges onto the rotor at approximately the same phase across the entire span. The loading of the rotor reduces as the wake convects across the rotor suction side due to the local swirl angle change within the wake. The reduction in loading reduces the size of the rotor crown separation. The wake is modulated and the swirl angle at a given nozzle pitch can vary by as much as 43° (relative), far in excess of the typical industry standard of designing to ±10° incidence onto the rotor.

The separation in the rotor crown proximity is highly 3 dimensional, convecting as a vortical flow structure from the hub towards the rotor tip. Furthermore, a well established empirical correlation for SBLI is assessed in the context of turbine aerodynamics and appears to be valid and perhaps an appropriate tool for preliminary design work.

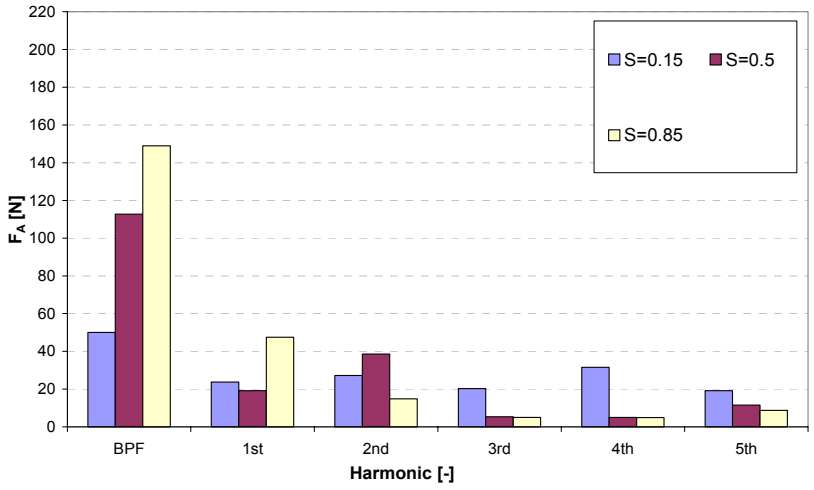

[CU3]

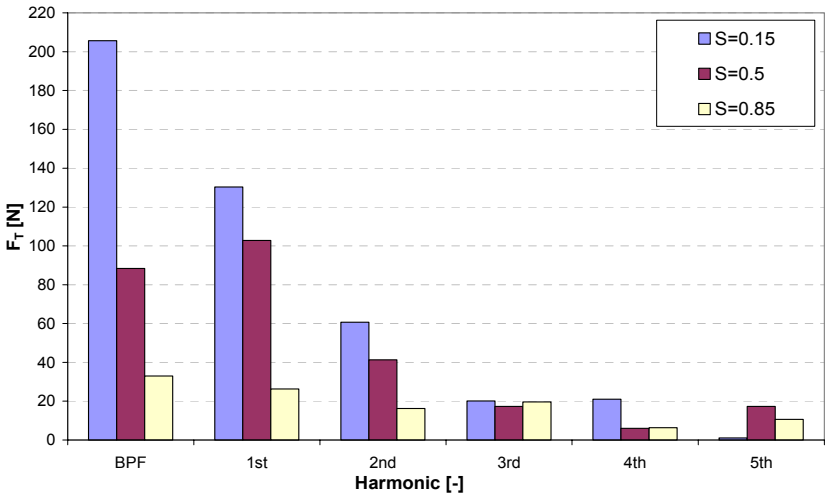

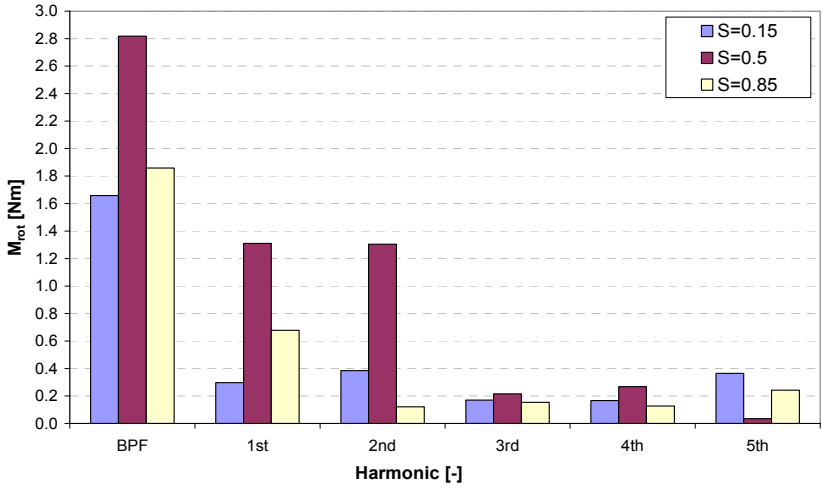

Figure 62 Axial forces (top), Tangential forces (middle) and pitching moments (bottom) at 15, 50 and 85% span (configuration C).

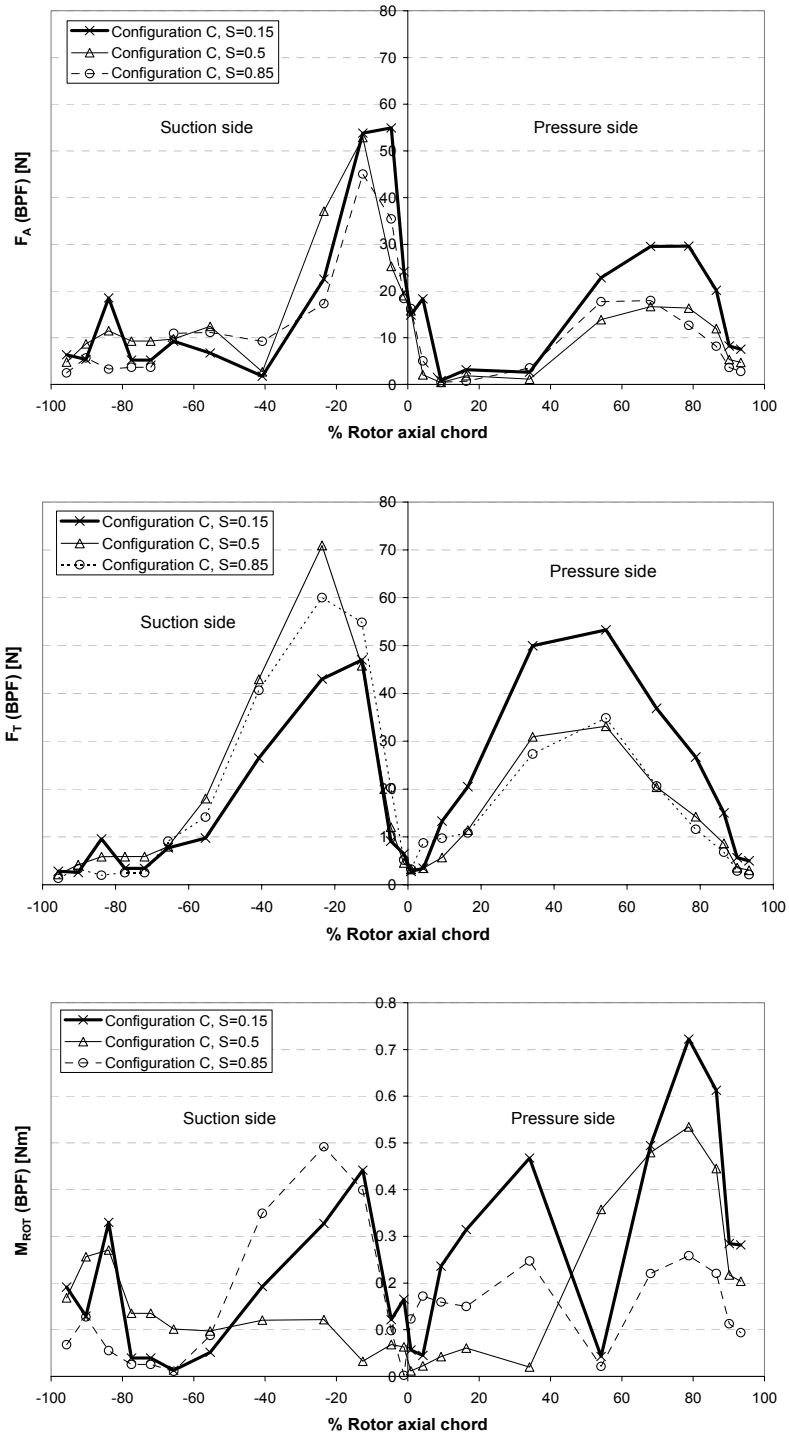

Figure 63 Comparison of rotor unsteady axial force (top), tangential force (middle) and pitching moment (bottom) at the BPF for 15, 50 and 85% span.

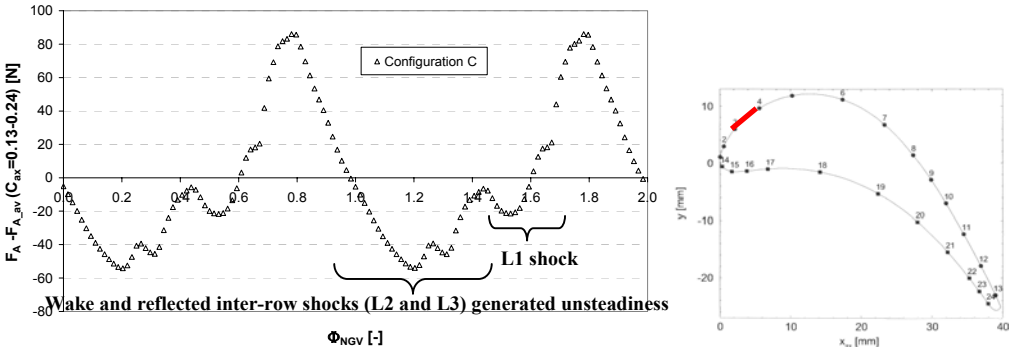

Figure 64 Predicted axial force – time averaged axial force ($F_A - F_{A\_av}$) at C_{ax}=0.13-0.24 on the rotor suction side (S=0.5)

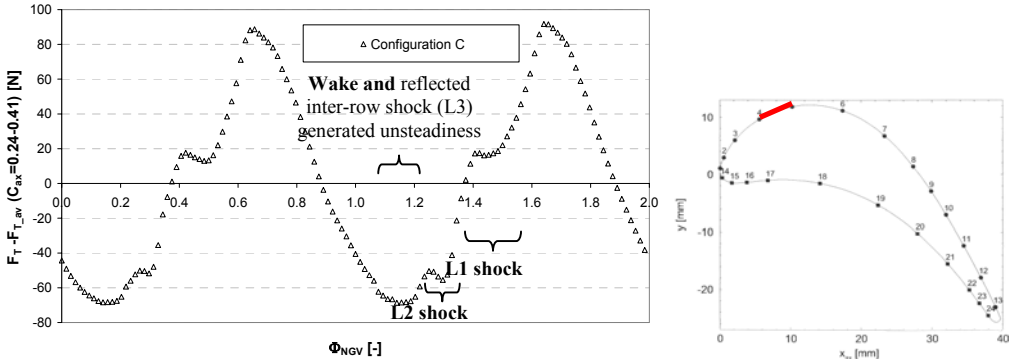

Figure 65 Predicted tangential force – time averaged tangential force ($F_T - F_{T\_av}$) at C_{ax}=0.24-0.41 on the rotor suction side (S=0.5)

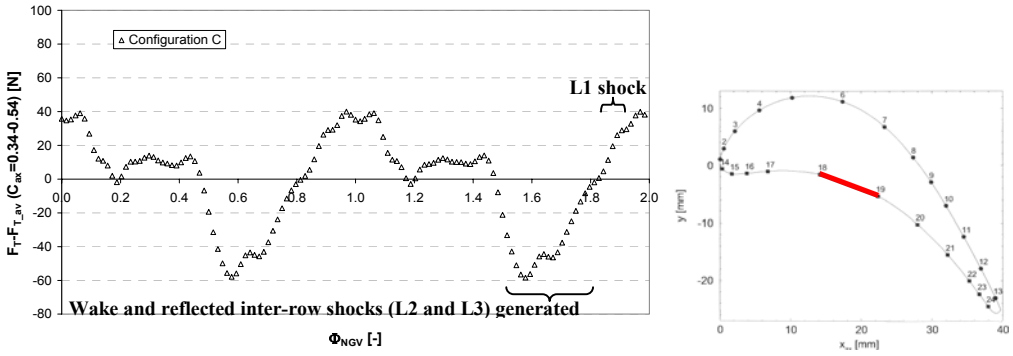

Figure 66 Predicted tangential force – time qaveraged tangential force ($F_T - F_{T\_av}$) at C_{ax}=0.34-0.54 on the rotor pressure side (S=0.5)

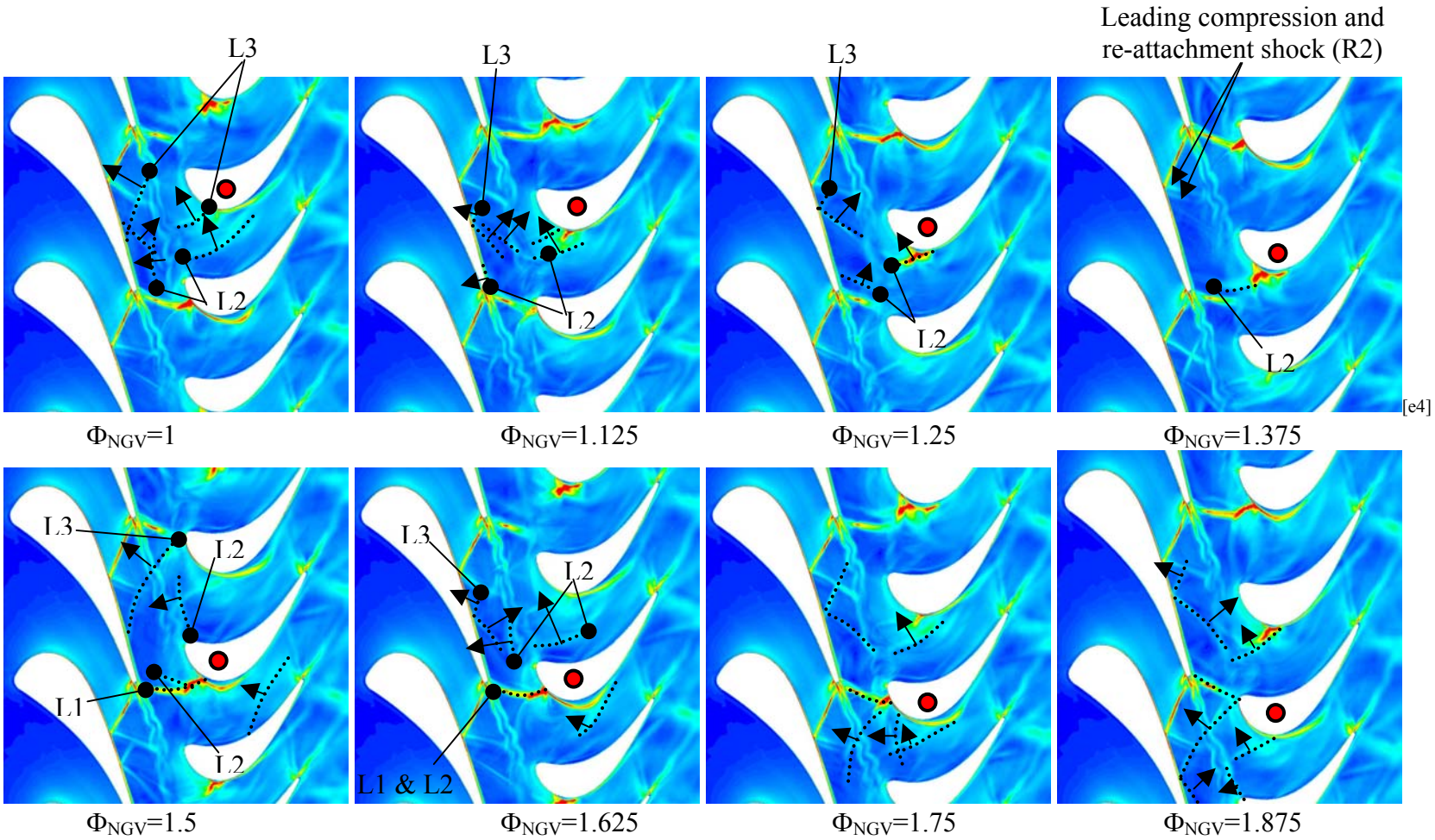

[e4]

Figure 67 contours of |∇ρ| at S=0.5

← = shock propagation direction

Rotor crown separation increases post wake passing

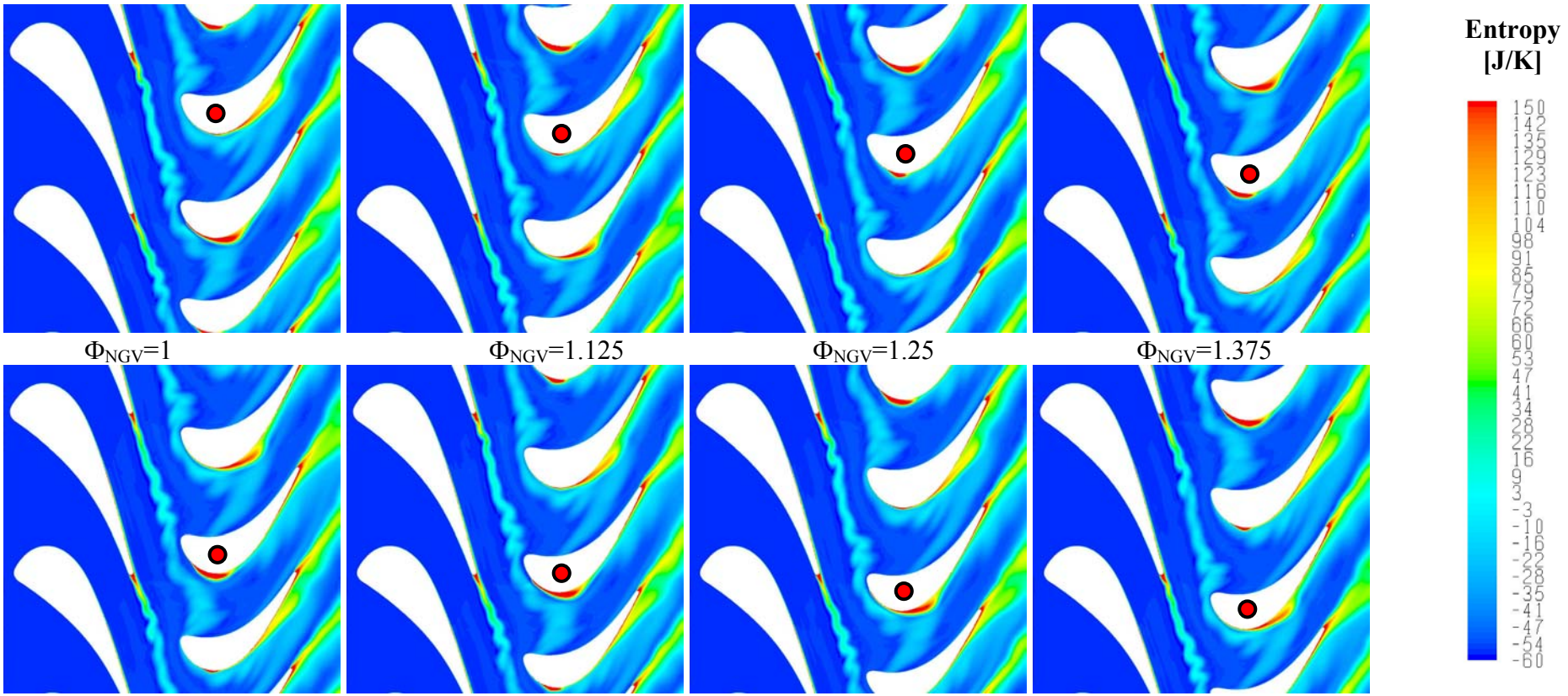

Figure 68 Contours of entropy at S=0.5

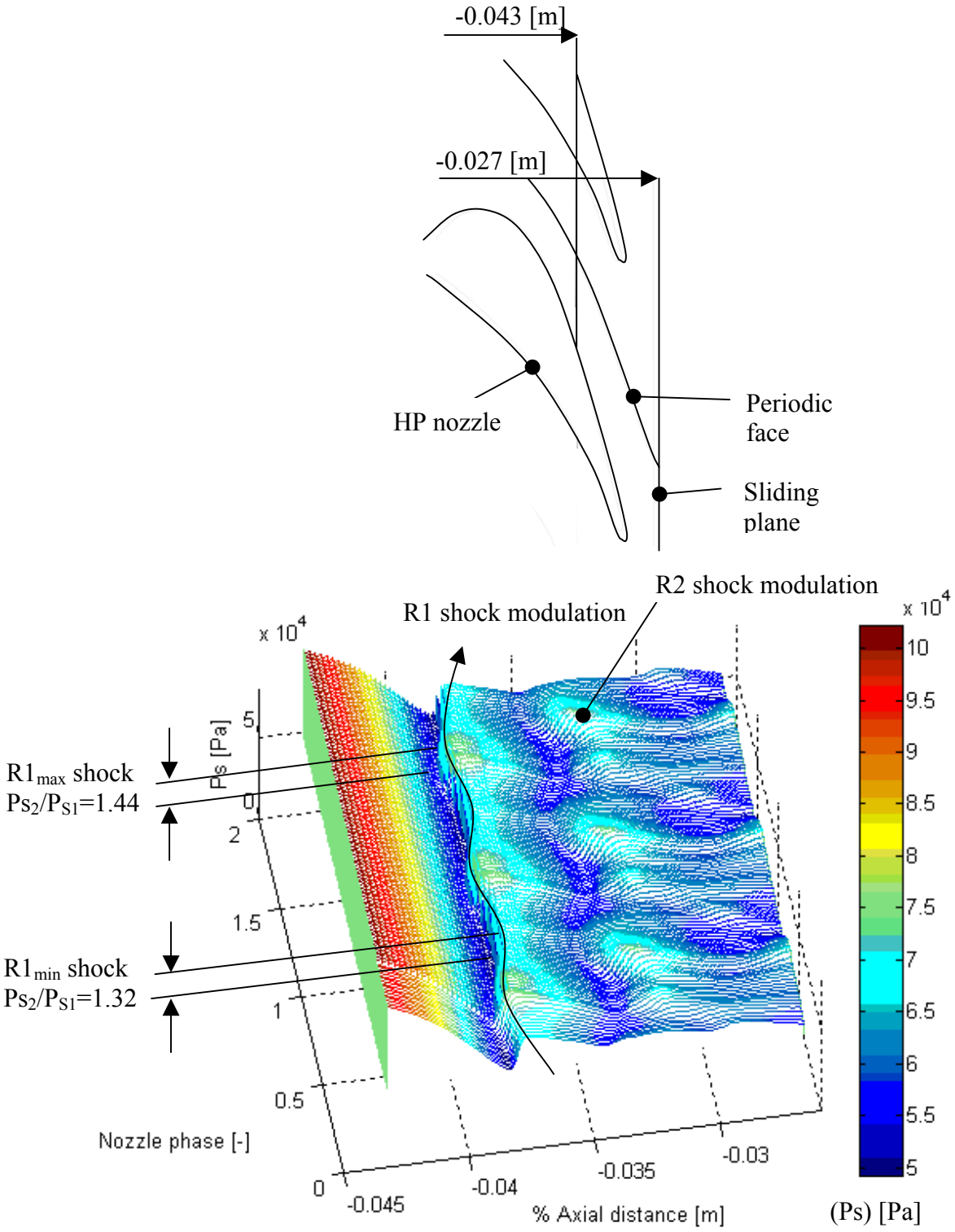

Figure 69 R1 shock and reflection (R2) through nozzle domain periodic face (top) at S=0.5

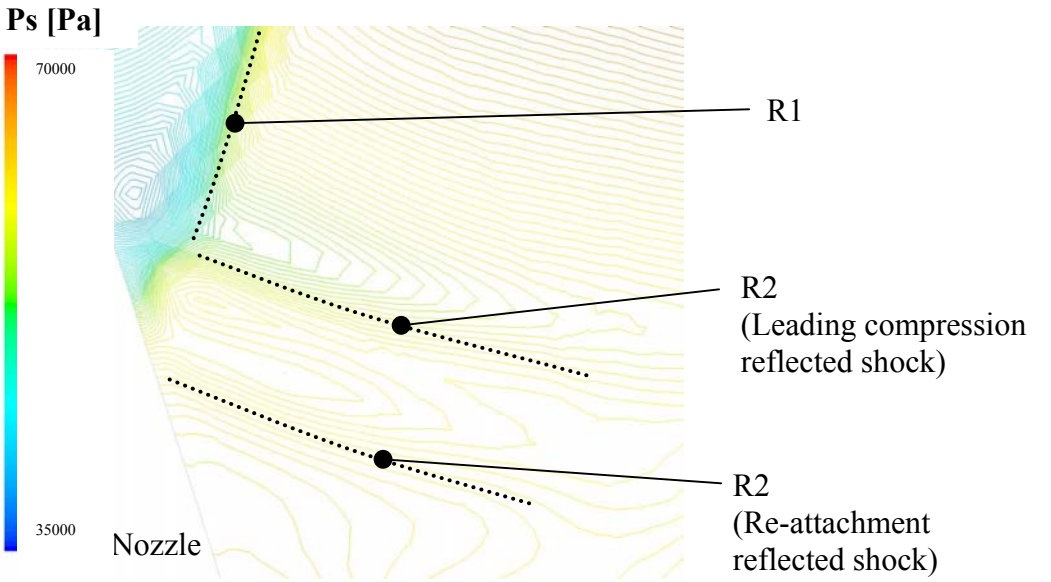

Figure 70 Contours of Ps at Φ_{NGV}=1.375 (S=0.5), reflected nozzle shock comprises of a leading compression and re-attachment shock

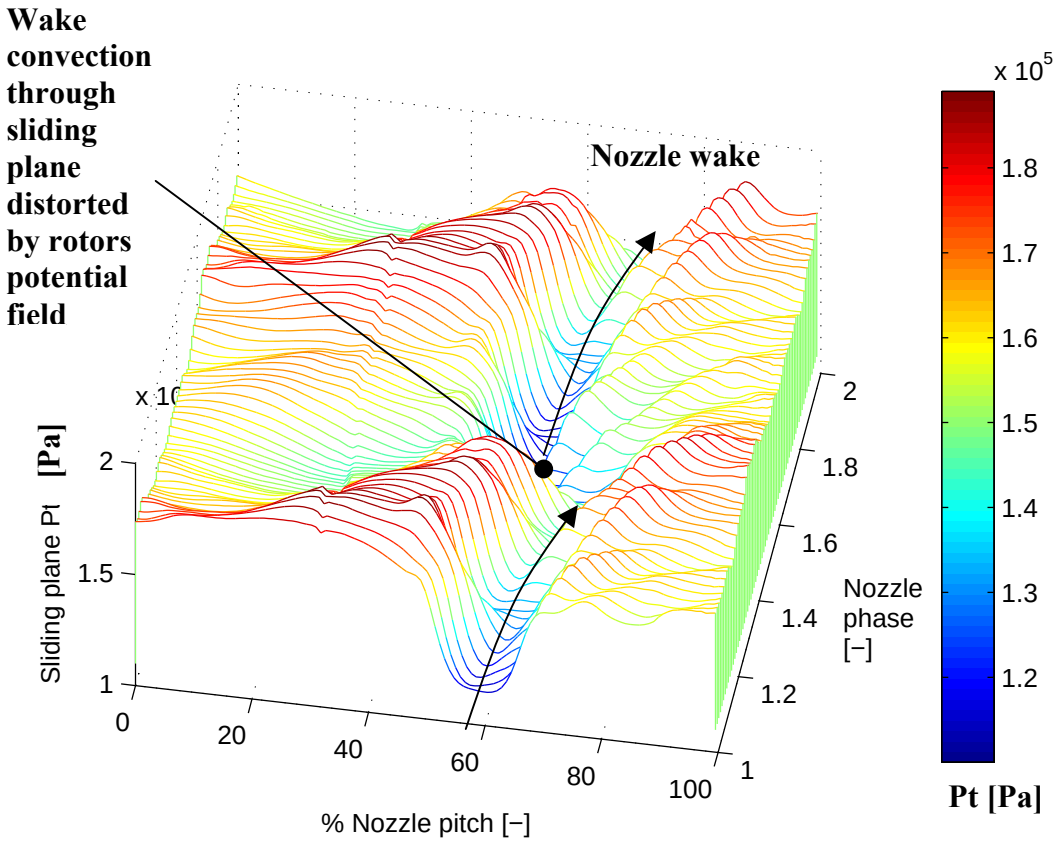

Figure 71 Pt at sliding plane, modulated nozzle wake due to rotor passing

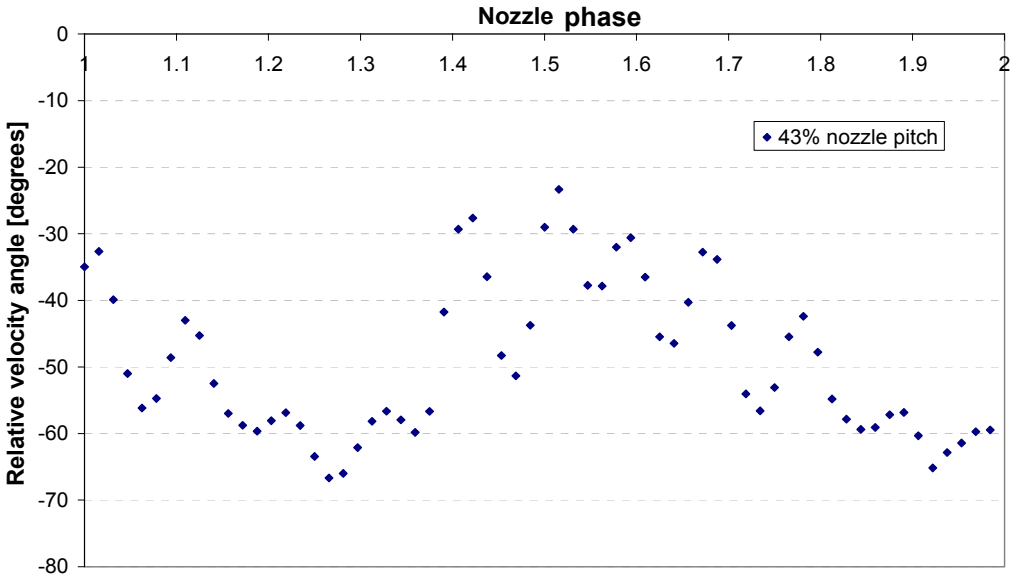

Figure 72 Region of maximum swirl angle change at the sliding plane (43% nozzle pitch)

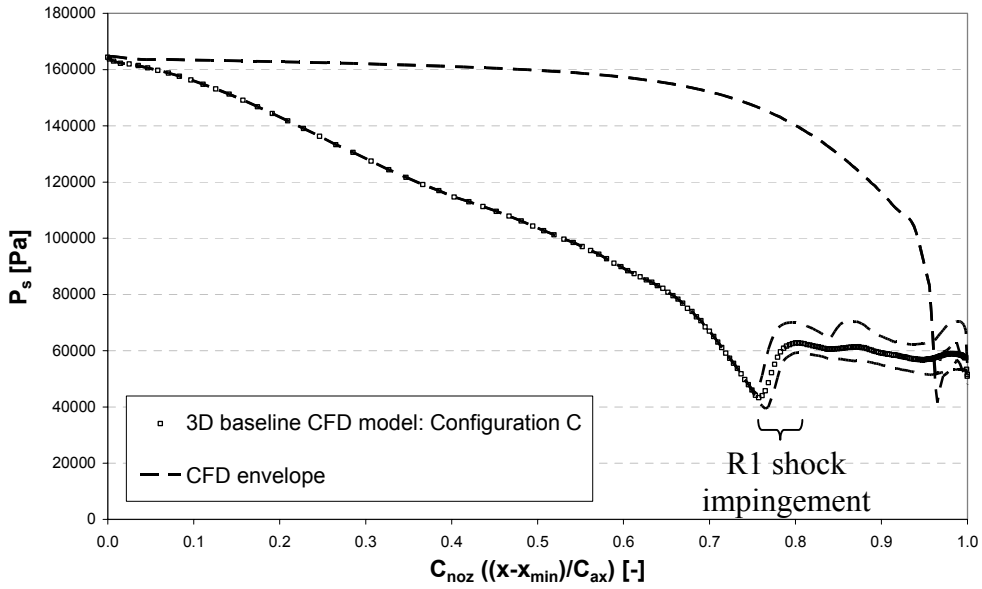

Figure 73 unsteadiness around the nozzle is limited to downstream of R1 shock impingement at S=0.5 on the nozzle.

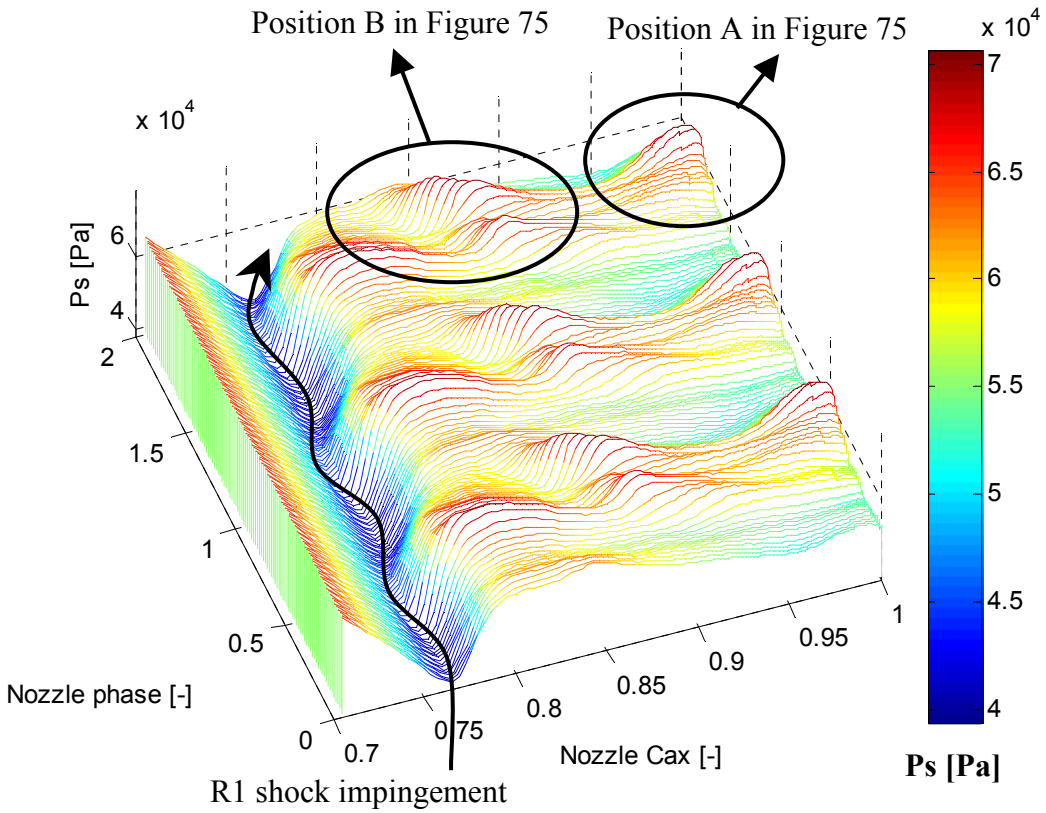

Figure 74 Nozzle suction side static pressure (C_{ax} 0.7-1), including modulated impingement position and regions of blade row interaction.

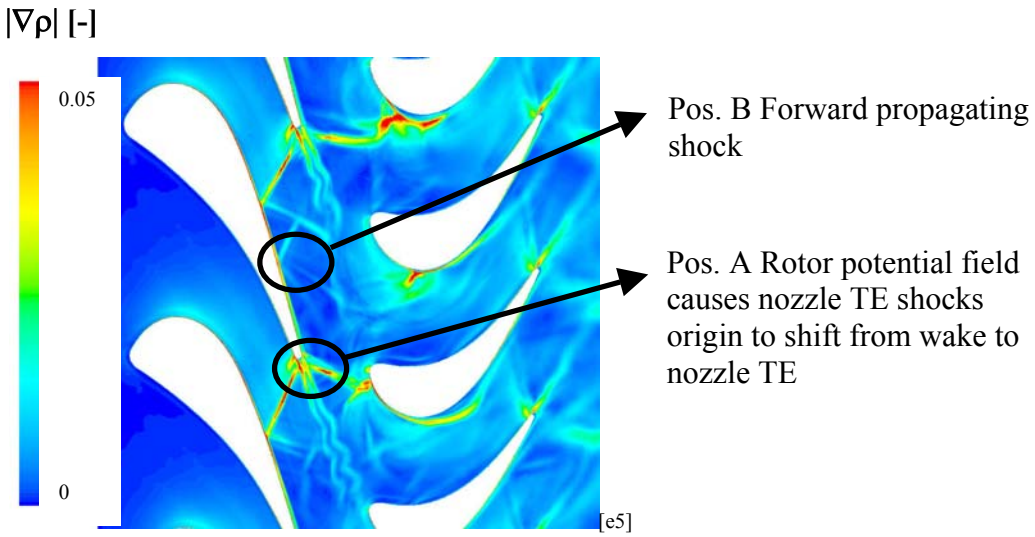

Figure 75 Rotor interaction on nozzle, position A and B in Figure 74 (Φ_{NGV}=1.78)

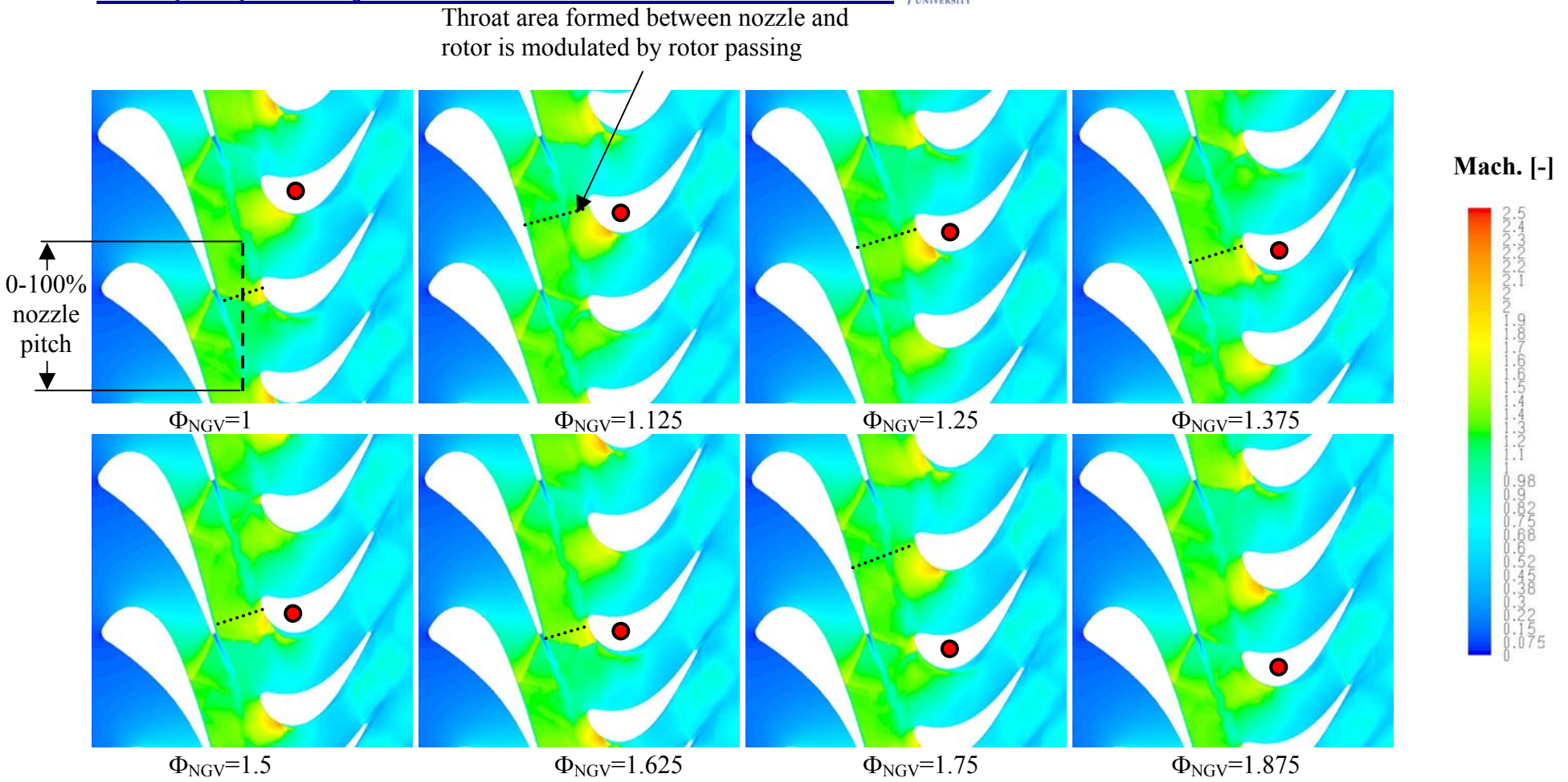

Figure 76 Contours of absolute Mach number at S=0.5

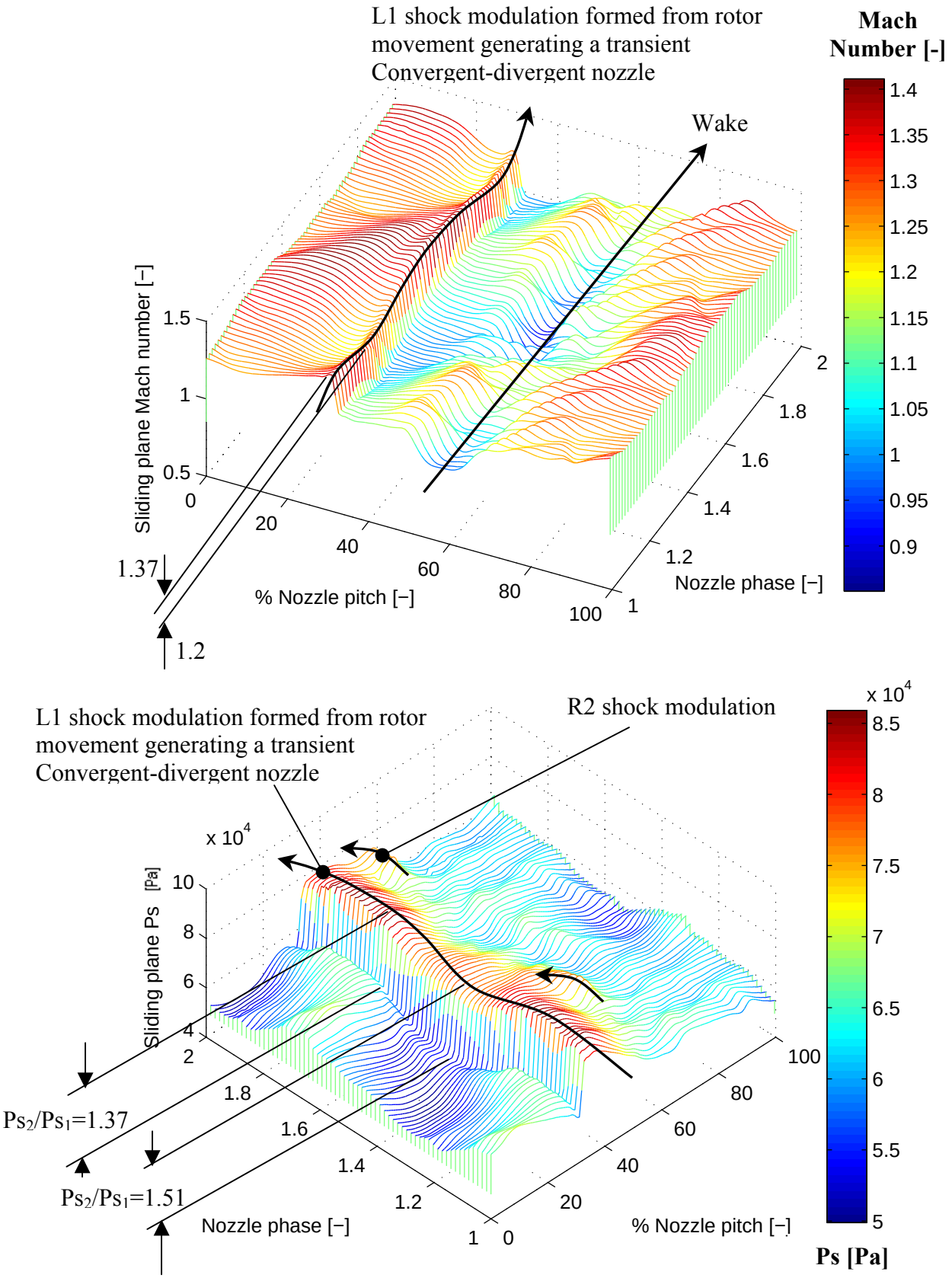

Figure 77 Mach number (top) and Ps (bottom) at sliding plane. Convergent-duct is formed by rotor passing

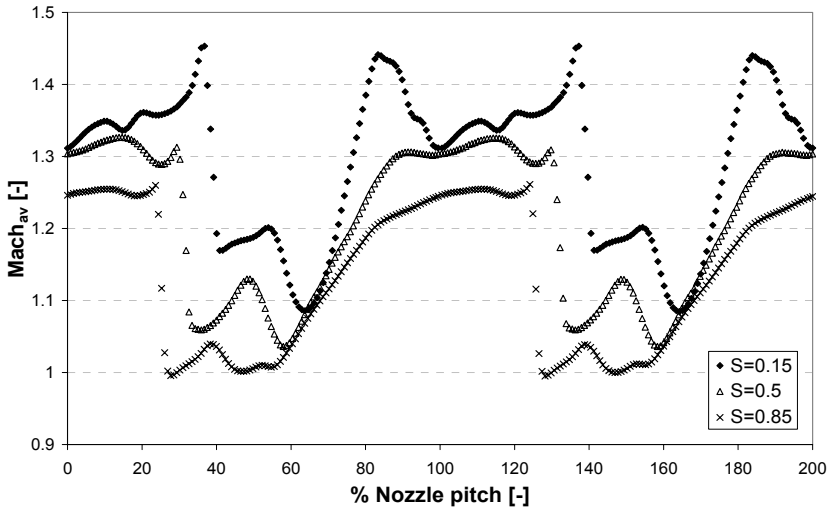

Figure 78 Time averaged Mach number at sliding plane. Mach number increases towards hub

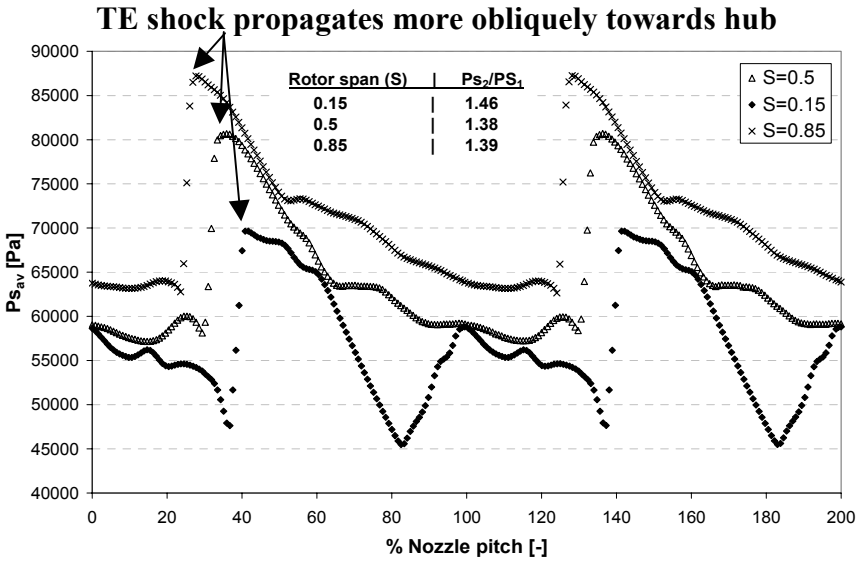

Figure 79 Time averaged Ps at sliding plane. L1 shock strength increases towards hub.[e6]

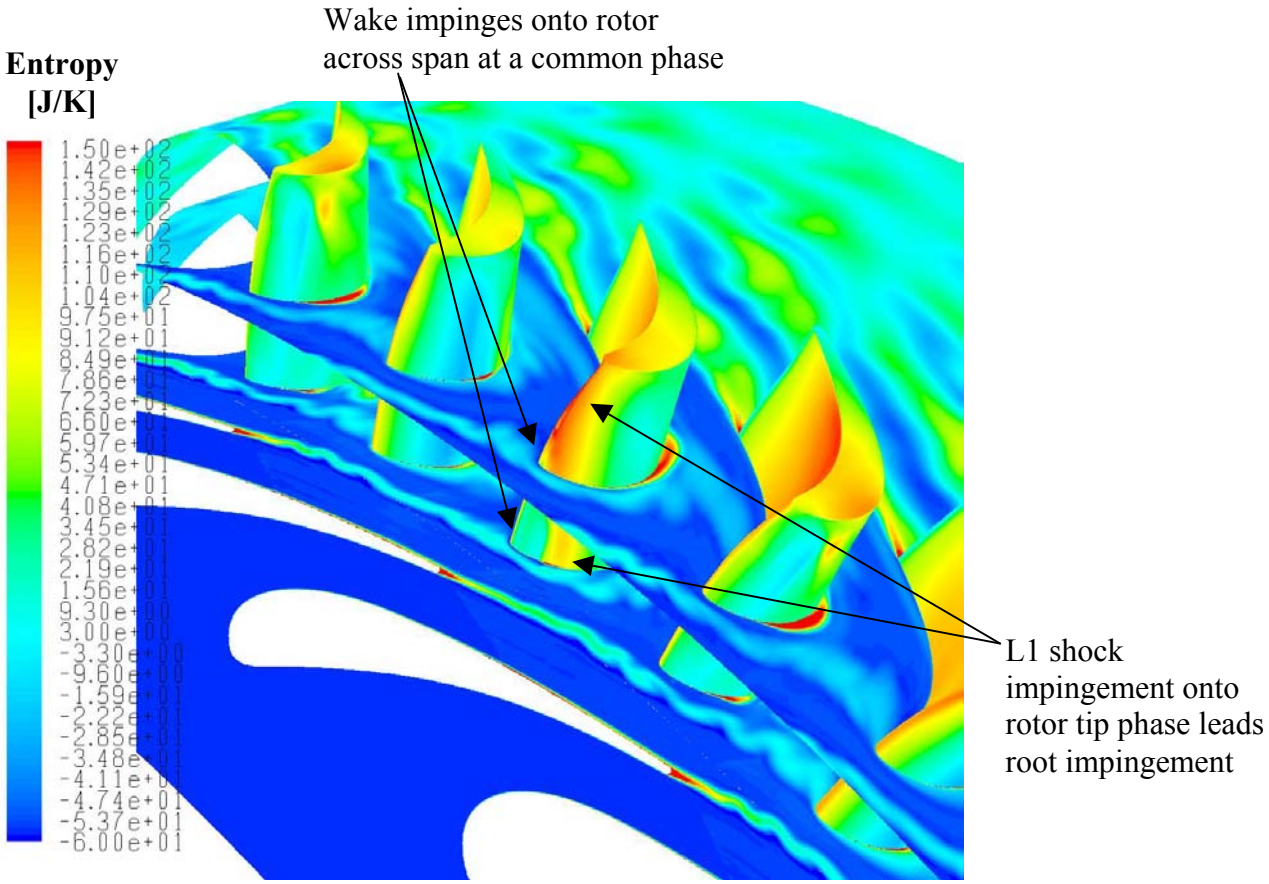

Figure 80 Overlay of contours of entropy at 15 and 50% span (contour bar) and contours of rotor Ps on rotor. Increased shock strength towards hub relatively phase shifts the wake/shock forcing functions (Φ_{NGV}=1.5).

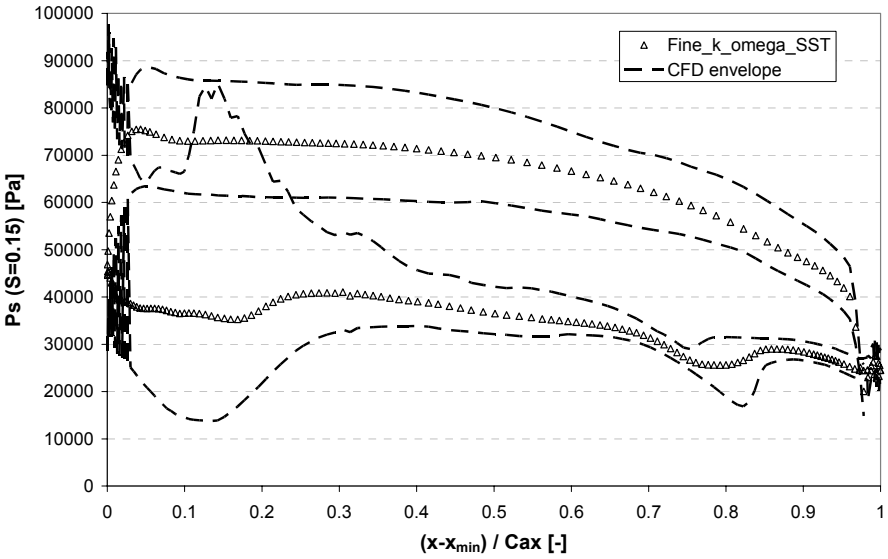

[e7]

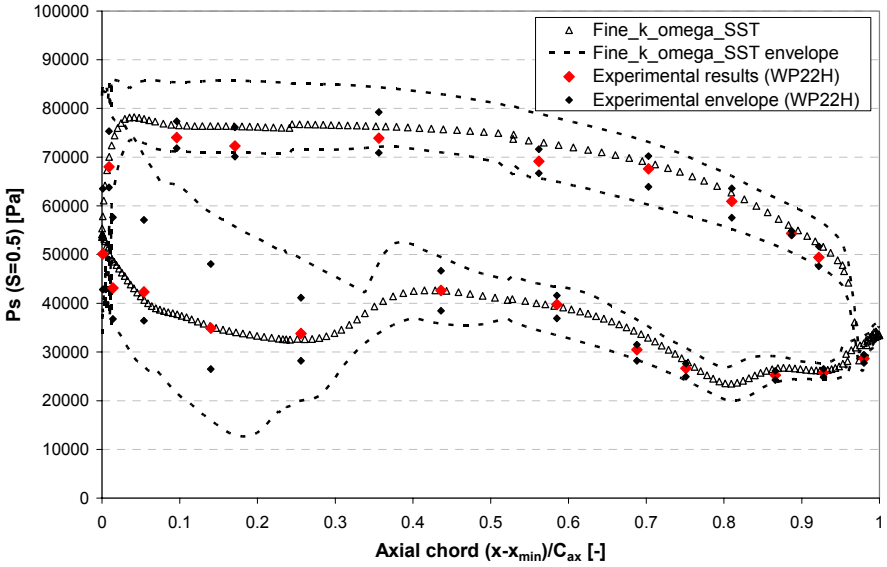

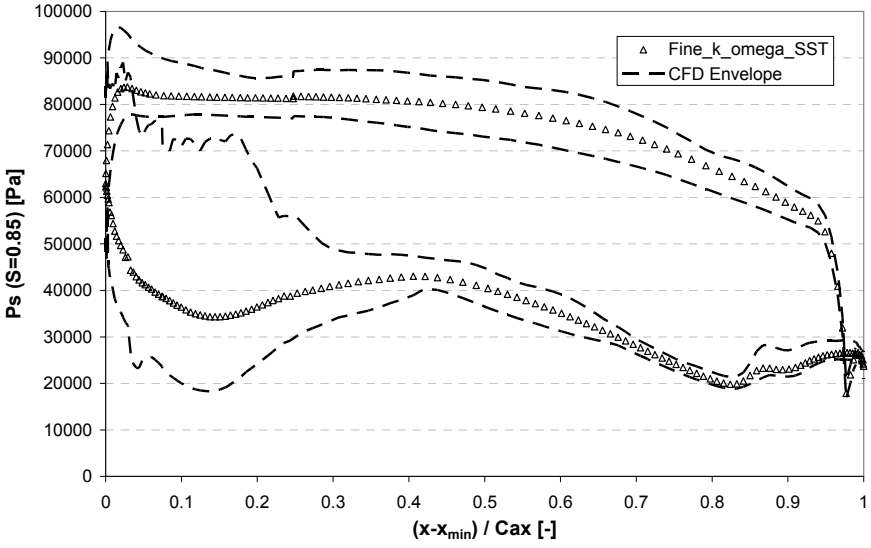

Figure 81 Rotor static pressure at 15 (top), 50 (middle) and 85% span (bottom)

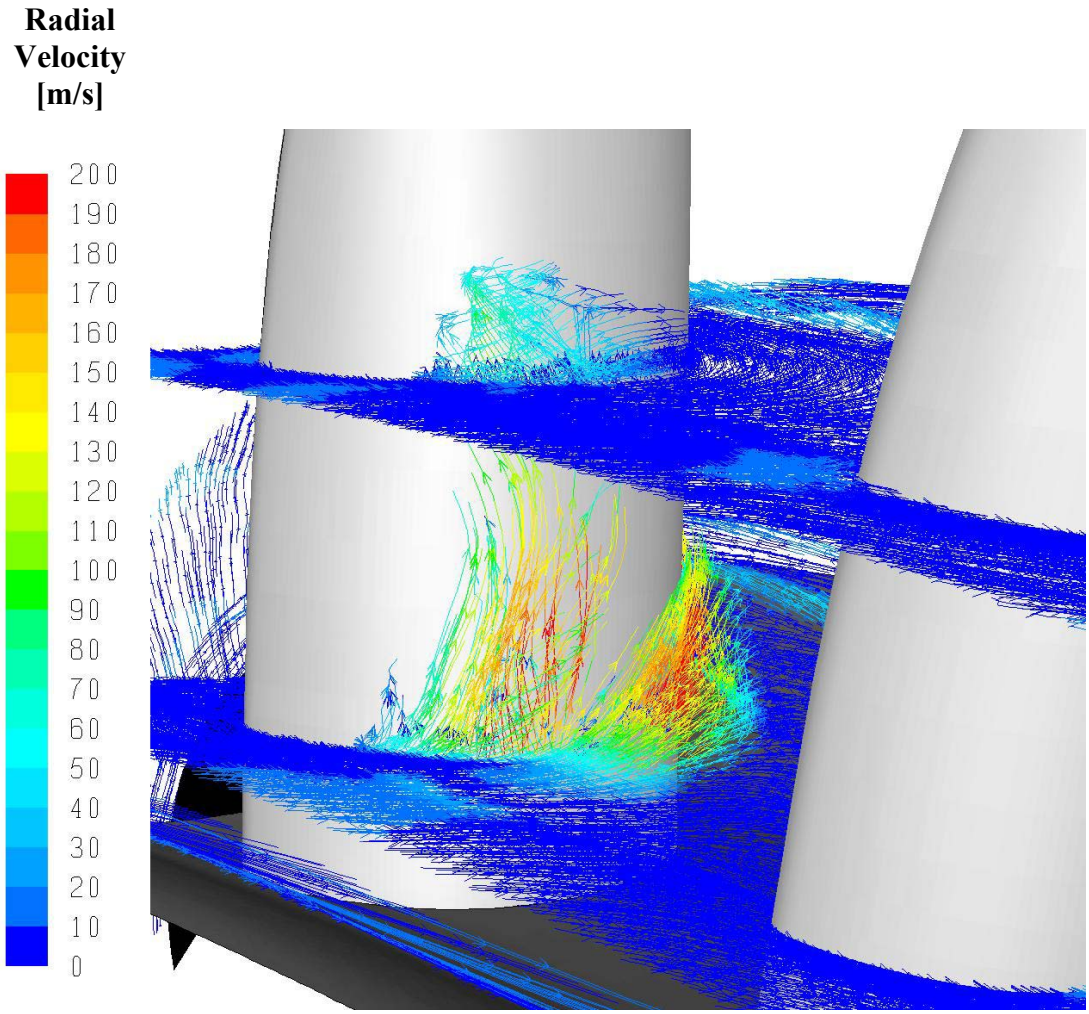

Figure 82 Relative pathlines released at S=0.15 and 0.5 (coloured by radial velocity [m/s]) at Φ_{NGV}=1.5. Radial pressure gradients migrate rotor crown separation towards blade tip

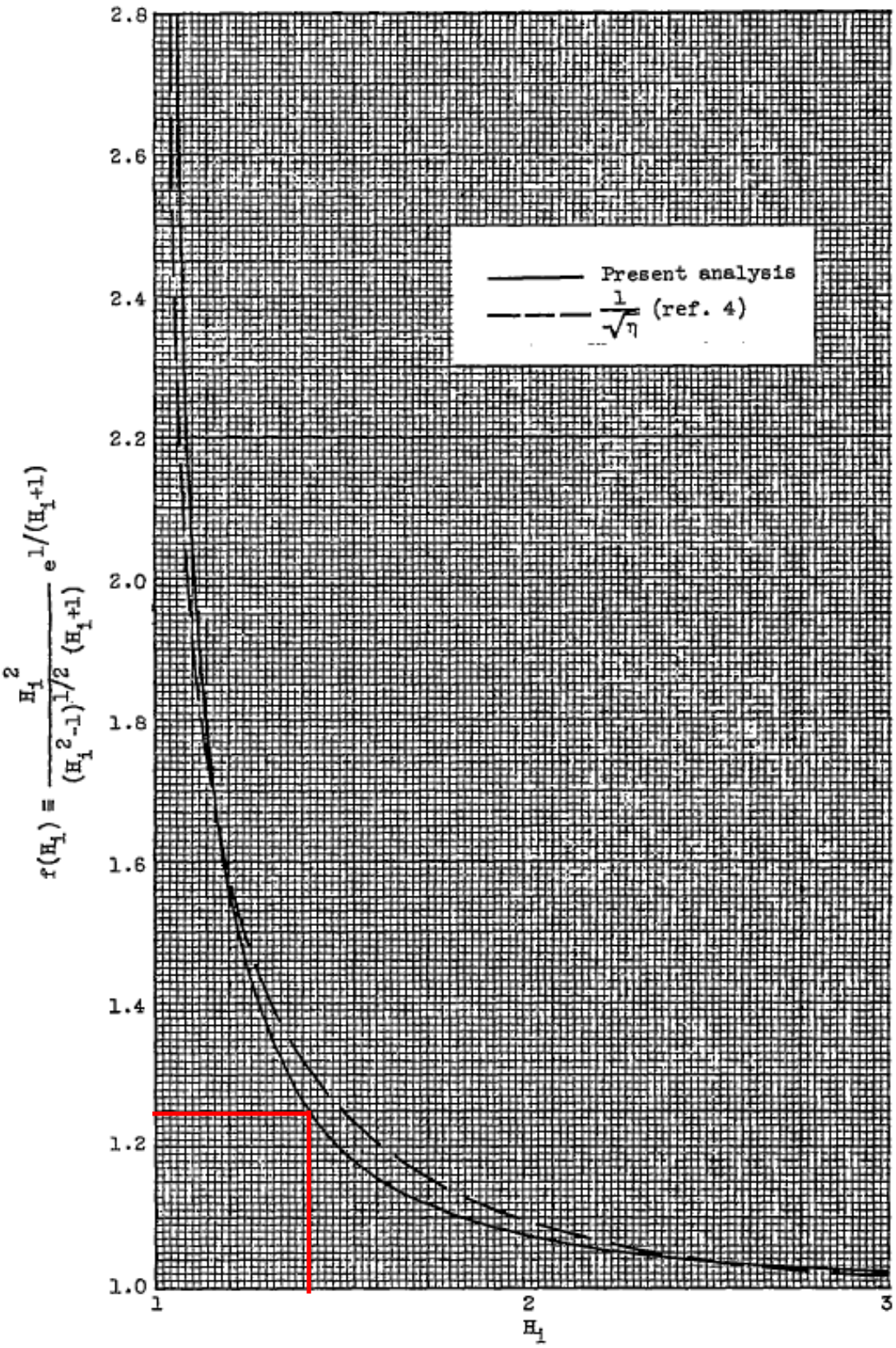

Figure 83 Function for determining Mach number ratio $\frac{M_2}{M_1} = \frac{f(H_{1,2})}{f(H_{1,1})}$ **(See NACA TN3454)**

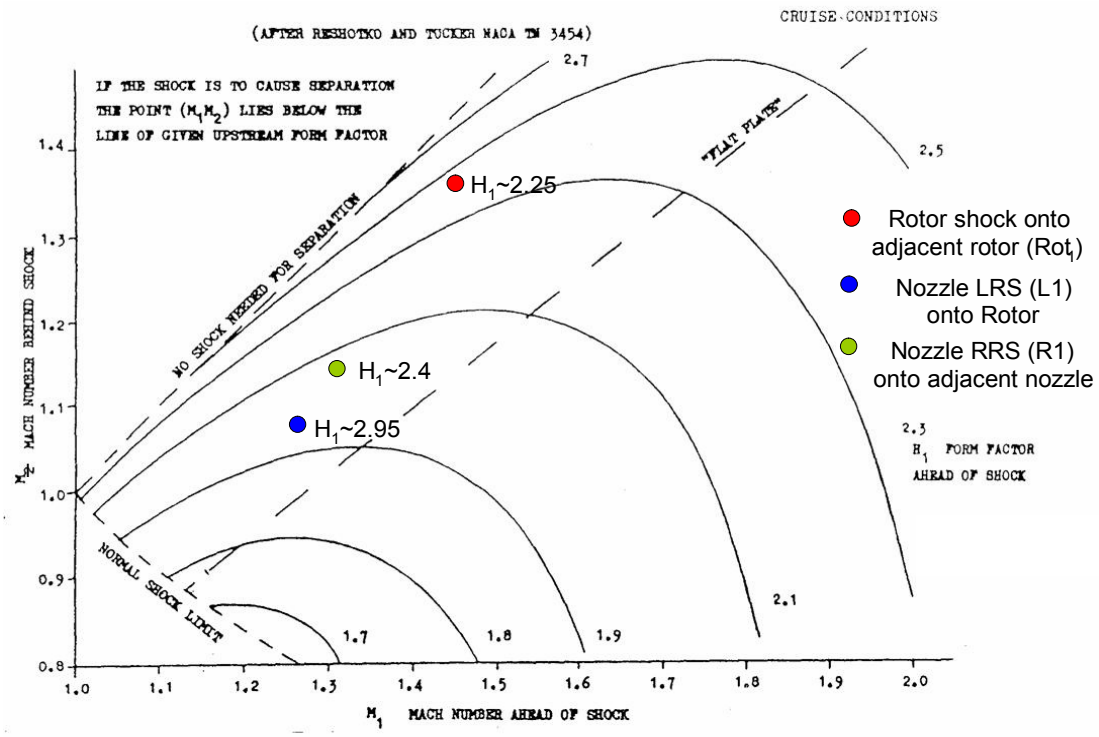

Figure 84 L1 and R1 shocks predicted to cause separation on the rotor and nozzle respectively at S=0.5 (See NACA TN3454).

8 High work turbine flow studies

This chapter analyses in detail the time-resolved flow features predicted using high spatial and temporal resolution quasi-2D (Q2D) unsteady CFD stage models. Based on the TATEF work package 2.2 (WP2.2H, see section 7.1.1) each stage calculation uses a throughflow model (section 6.1), of the VKI CT3 turbine rig to define the radial extremities between approximately 45 to 50% of the span, which are modelled as a slip condition. The throughflow model includes radial flow components, so only one cell is required across the radial span. Each stage calculation comprises two nozzles and three rotors and a fine mesh density was used in each domain (see chapter 6). These models were generated to explore typical parameters that a designer might change to control rotor forcing.

8.1 2D models

Parametric studies of the effect of reaction (λ), axial spacing, pressure ratio and wake characteristics have been performed. Each of these design parameters could be modified in the design process to minimize the rotor forcing. The wake characteristics could be modified by trailing edge (TE) design or TE ejection. There is also a study on the effect of the rotor boundary layer in dissipating the high gradients of pressure in shocks. The different models are detailed below.

- A range of different stage reaction cases are considered. The reaction was changed by skewing the rotor about the LE and the skews are quoted as relative to the 3D baseline model. The reactions investigated are:
  - 0.28 (2 degrees rotor skew open)
  - 0.31 (0.5 degrees rotor skew open: Baseline model)
  - 0.41 (2 degrees rotor skew closed)
- The effect of axial spacing between the NGV and the rotor was investigated for the following cases :
  - 1.4mm (27.4% of nozzle axial chord)
  - 16.4mm (39.4% of nozzle axial chord: Baseline model)
  - 21.4mm (51.5% of nozzle axial chord)
- The effect of a pressure ratios was also considered and the configurations modelled are the same as those examined on the VKI experimental operating conditions P_{01} / P_{03} :
  - 2.19
  - 3.19
  - 3.85 (Baseline model)
- The influence of the NGV wake in the aerodynamic forcing was also considered. Five total pressure profiles were generated to study these effects as follows:
  - Parameterization of the WP2.2 high operating condition wake (Baseline)
  - Increased width, 50% reduction in depth. (matched overall total pressure loss)
  - Reduced width, 50% increase in depth (matched total pressure loss)
  - The effect of wake frequency content using a 50% deeper thin wake profile
  - Investigation of wake frequency content using a 50% shallower thin wake profile

- To investigate the effect of the rotor boundary layer in dissipating forcing functions the rotor is modelled using a wall slip condition. A comparison with the no-slip stage calculation will identify the effect of shock dissipation through the boundary layer.

The reaction study (including baseline model) used 2048 time steps per nozzle passing (20 iterations per time step). Upon completion of a temporal domain study it was concluded that this temporal resolution was excessive and each of the remaining cases were modelled using 1024 time steps per nozzle passing (20 iterations per time step). The test matrix of computational models is presented in Table 20. A detailed description of the flow field and the resulting unsteady forces is presented and analysed. Each of the configurations used the k-ω SST turbulence model with second order discretization. When the nozzle and rotor domains periodic faces tangentially align the nozzle phase (Φ_{NGV}) is zero (Figure 85). A nozzle phase is completed when a rotor traverses one nozzle pitch ($\frac{1}{42\ nozzles} \times 360° = 8.57°$).

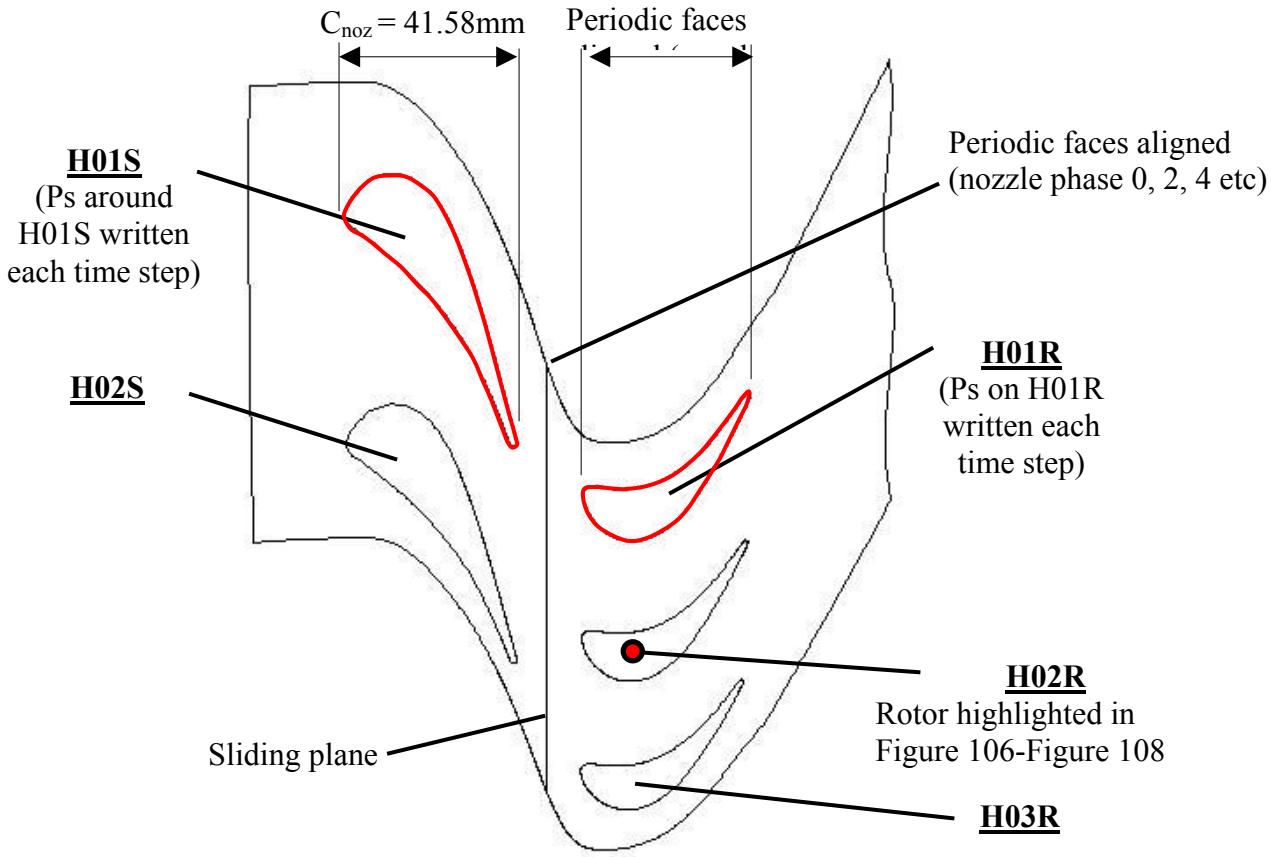

Figure 85 Rotor alignments at nozzle phase (Φ) 0, 2, 4, etc

	Reaction study			Rotor axial position study			Pressure ratio study			Rotor BL study	High op. point
Configuration name	R41_Ax0 PR3.85	**R31_Ax0 PR3.85**	R28_Ax0 PR3.85	R33_Ax5C PR3.85	**R31_Ax0 PR3.85**	R32_Ax5A PR3.85	R12_Ax0 PR2.19	R22_Ax0 PR3.19	**R31_Ax0 PR3.85**	R31_Ax0 PR3.85_slip	WP22H
No. Hybrid cells	*~270k*	***~270k***	*~270k*	*~270k*	***~270k***	*~270k*	*~270k*	*~270k*	***~270k***	*~270k*	n/a
Turb. Model	*k ω SST*	***k ω SST***	*k ω SST*	*k ω SST*	***k ω SST***	*k ω SST*	*k ω SST*	*k ω SST*	***k ω SST***	*k ω SST*	n/a
Capacity	*0.0101*	***0.0101***	*0.0101*	*0.0101*	***0.0101***	*0.0101*	*0.0101*	*0.0101*	***0.0101***	*0.0101*	0.0101
Reaction	*0.413*	***0.311***	*0.284*	*0.327*	***0.311***	*0.316*	*0.116*	*0.215*	***0.311***	*0.314*	0.315
Specific work	*303*	***303***	*306*	*305*	***303***	*306*	*188*	*276*	***303***	*303*	299
efficiency (η) (ideal expansion)	*0.924*	***0.902***	*0.916*	*0.921*	***0.902***	*0.908*	*0.904*	*0.926*	***0.902***	*0.906*	0.916
Rotor skew [deg.]	*-2*	***0.5***	*2*	*0.5*	***0.5***	*0.5*	*0.5*	*0.5*	***0.5***	*0.5*	n / a
Stage loading @ 50% span	*2.105*	***2.100***	*2.124*	*2.118*	***2.100***	*2.124*	*1.313*	*1.925*	***2.100***	*2.105*	2.076
	Quasi 2D CFD configurations										*Experimental Results*

Table 20 Operating parameters of 2D CFD models investigating effect of reaction, axial spacing, pressure ratio and the effect of the rotor boundary layer. For reference the experimental equivalent operating parameters are included (bold indicates baseline model)

8.2 2D Baseline model

The 2D baseline model is a reference model to compare with the other stage calculations. The model closely matches the capacity, reaction, specific work, efficiency and stage loading of the experimental results (Table 20). A detailed evaluation of the baseline stage calculation is presented which examines the range of aerodynamic flow features and serves as a reference in comparison with the subsequent changes to reaction, spacing, pressure ratio and wake characteristics. The resulting rotor forces are detailed in each of the parametric studies.

8.2.1 Nozzle guide vane characteristics

8.2.1.1 Steady features

The stator outflow is supersonic (inter-row Mach number $M_{NGV\ exit}$=1.24) and produces oblique shocks at the nozzle trailing edges. The shocks impinge onto the adjacent nozzle suction side and the rotor. A schematic of the complex supercritical SBLI formed on the adjacent nozzle is included in Figure 86. An expansion fan formed around the nozzle TE, accelerates the flow up to the Right Running Shock (R1). The impingement of R1 on to the adjacent nozzle forms a pre-compression shock, due to the adverse pressure gradient within the subsonic portion of the boundary layer. The separation with in the SBLI region exists across an entire nozzle phase (Φ_{NGV}). R1 reflects from the SBLI as an expansion fan. A second reflected shock is generated upon re-attachment. At each rotor passing, a separation disengages from the SBLI region and is convected down the nozzle suction side generating a shock due to the local displacement, the origin of which convects with the separation. Therefore R1 directly (by reflection) and indirectly (by separation convection) generates three distinct shock forcing functions which impinge onto the rotor.

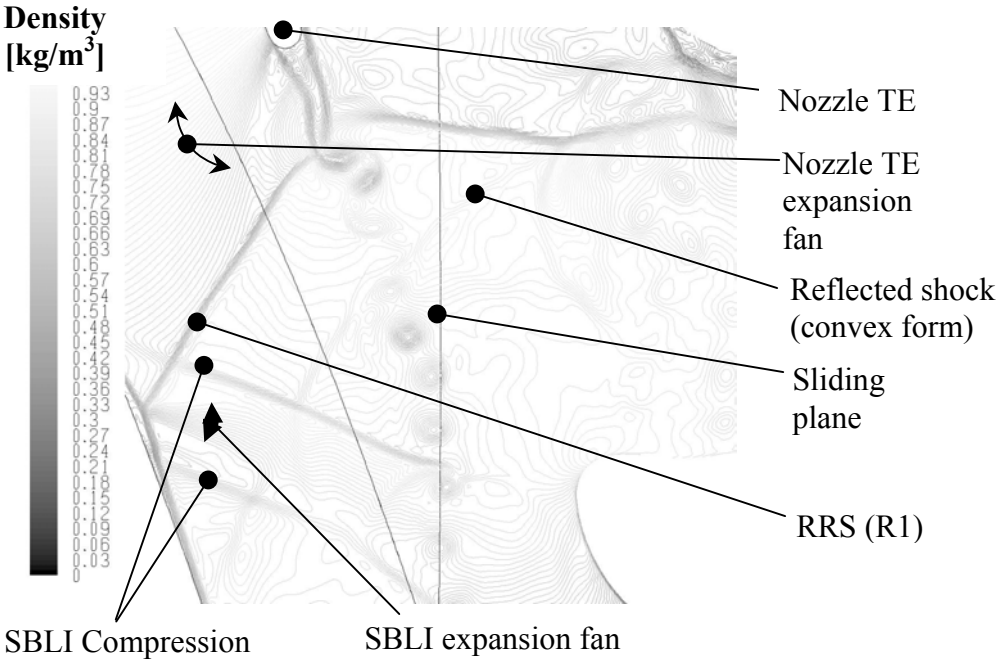

Figure 86 Contours of density (kg/m^3) at nozzle phase (Φ_{NGV}) 1.47. Schematic representation of supercritical SBLI formed on adjacent nozzle by impinging TE shock.

The predicted time average static pressure around the nozzle shows reasonable agreement with the experimental results (Figure 87). The largest differences occur just upstream of the RRS impingement position (approximately 77% of the axial chord (C_{ax})). A transient convergent-divergent duct is formed between the nozzle and rotor which modulates the Left Running (L1) and R1 shock strength and propagation angle, causing the R1 impingement position on the adjacent nozzle to oscillate (see 7.2.4.4). The downstream portion of the nozzle suction side is also subject to shocks reflecting back from the rotor.

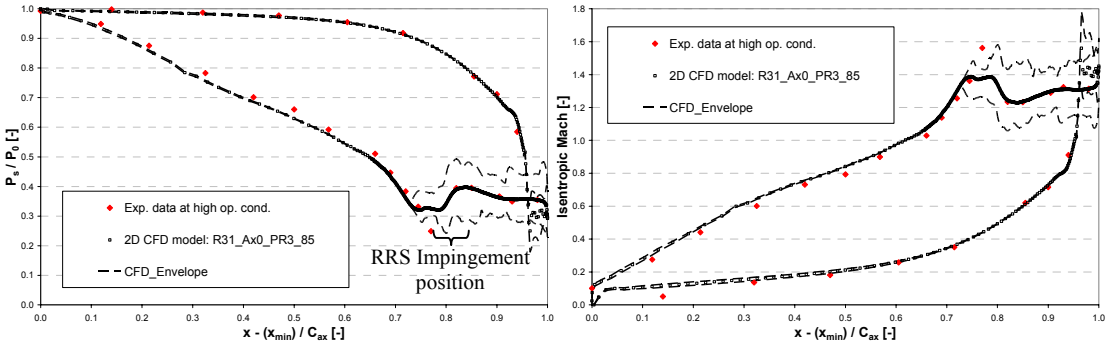

Figure 87 Baseline CFD non-dimensionalized, time averaged, nozzle static pressure distribution (left) and isentropic Mach number distribution (right)

8.2.1.2 Unsteady NGV features

A detailed description of the nozzle unsteadiness, which is predominantly limited to downstream of the nozzle throat on the suction side is included below. Within this description the leading edge (LE) of the rotor H01R becomes tangentially aligned with the trailing edge (TE) of the nozzle H01S at Φ_{NGV}=1.75, 3.75, 5.75 etc. The naming convention for each shock is detailed in Figure 88. A detailed description of how the shocks propagate, including a diagrammatic representation is included in section 8.2.4.2.

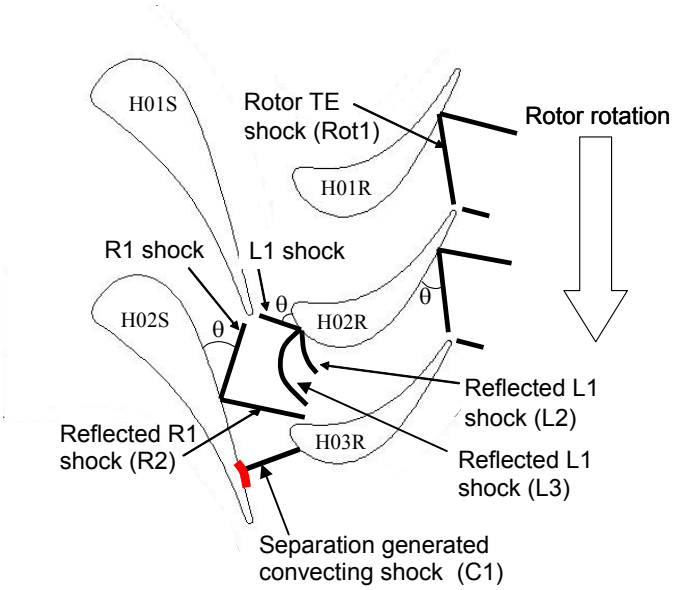

Figure 88 Schematic of shock structure in a high pressure turbine stage

The analysis begins from nozzle phase 1.375 (Φ_{NGV}=1.375) (Figure 95). The R1 shock impingement generates a supercritical SBLI, which reflects as a leading compression and re-attachment shock (R2). There are multiple re-circulating regions within the SBLI (Figure 89). A separation is in the process of detaching from the SBLI region due to the L3 shock impingement from the previous rotor passing. A 'detached separation' from the previous rotor passing is close to shedding from the nozzle TE. The combined L3 and re-attachment R2 shock generate a significant pressure rise at this nozzle phase ($Ps_2/Ps_{1[MSOffice8]}$=1.7).

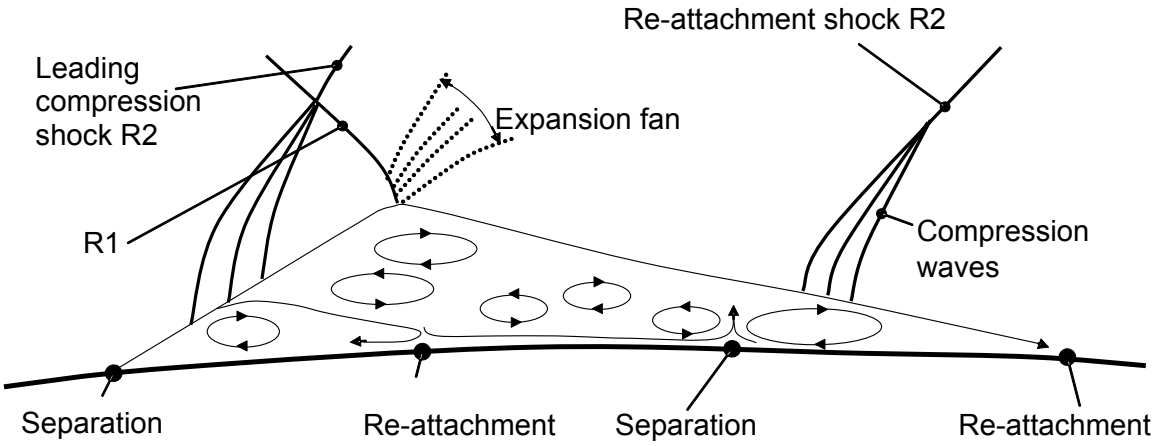

Figure 89 SBLI on nozzle suction side at nozzle phase (Φ_{NGV}) =1.375

As the reflected R2 shock propagates upstream it diffracts through the nozzle wake and impinges on to the late nozzle suction side at approximately 96% of the axial chord (C_{ax}). The shock continues to impinge either side of the initial position, due to the convex form until the downstream side propagates past the nozzle TE (to impinge on to the adjacent nozzle) and the upstream side is constrained by the free stream Mach number in the SBLI region. By $\Phi_{NGV[MSOffice9]}$=1.5 it reaches 0.93C_{ax}. The R1 impingement position has shifted downstream by approx. 3.6% of the axial chord as the shock strength increases due to the convergent-divergent nozzle formed by the rotor passing (see section 8.2.3). A separated region disengages from the SBLI region to form an autonomous convecting separation bubble (Figure 90). The boundary layer displacement generates an additional shock (C1), the origin of which convects with the disengaged separation.

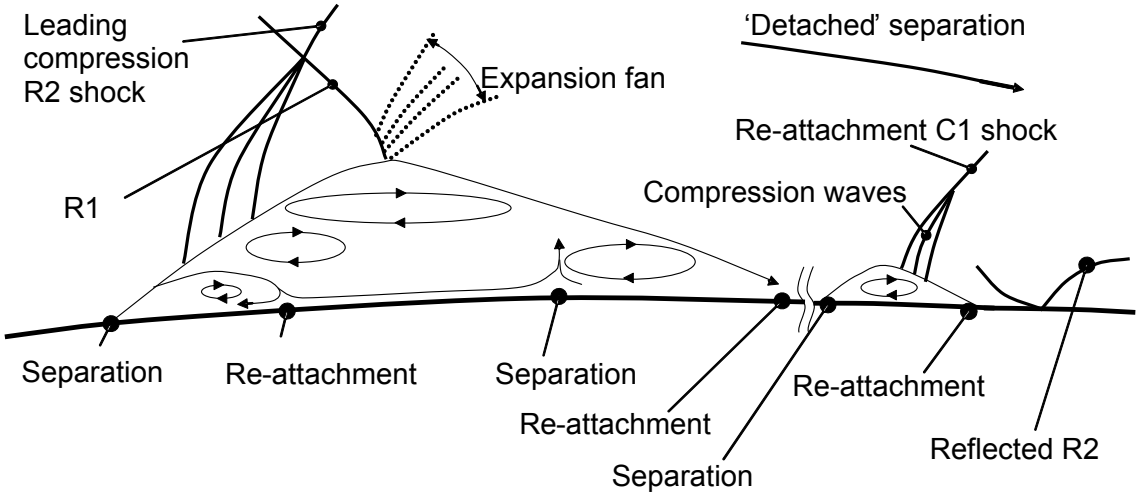

Figure 90 Nozzle suction side at Φ_{NGV} =1.5

By Φ_{NGV}=1.625 the detached separation bubble includes a pre-compression shock (Figure 91). The reflected R2 shock propagates upstream, past the convecting detached separation, reaching $0.87C_{ax}$ (Figure 96). The C1 re-attachment shock strength is increasing as the convecting separation migrates down the nozzle suction side into higher velocity flow (Ps_2/Ps_1=1.53, C_{NGV}=80-85%).

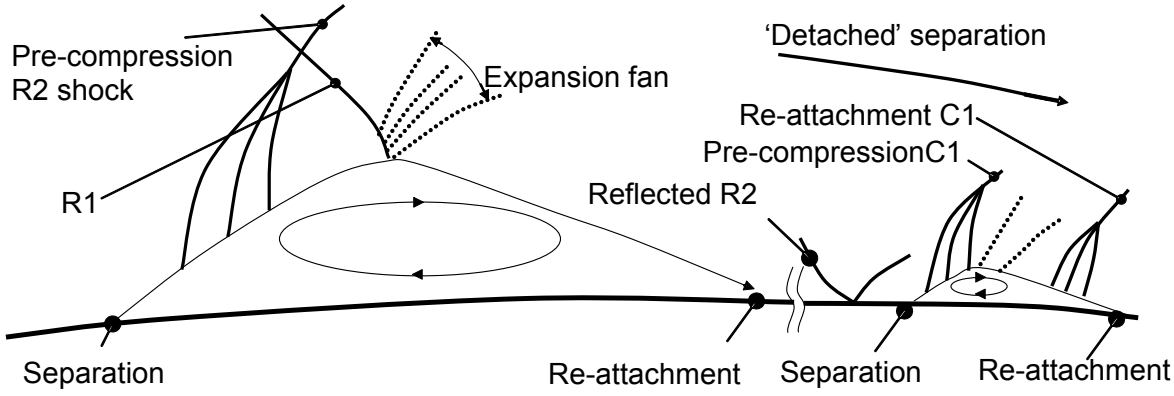

Figure 91 Nozzle suction side at Φ_{NGV} =1.625

Like the reflected R2 shock, the forward propagating L3 shock diffracts through the adjacent nozzle wake and first impinges at approximately $0.96C_{ax}$. By Φ_{NGV}=1.75 the impingement has reached approximately $0.94C_{ax}$ and has superimposed onto the re-attachment C1 shock, generating a significant combined shock strength (Ps_2/Ps_1=1.65) (Figure 96).

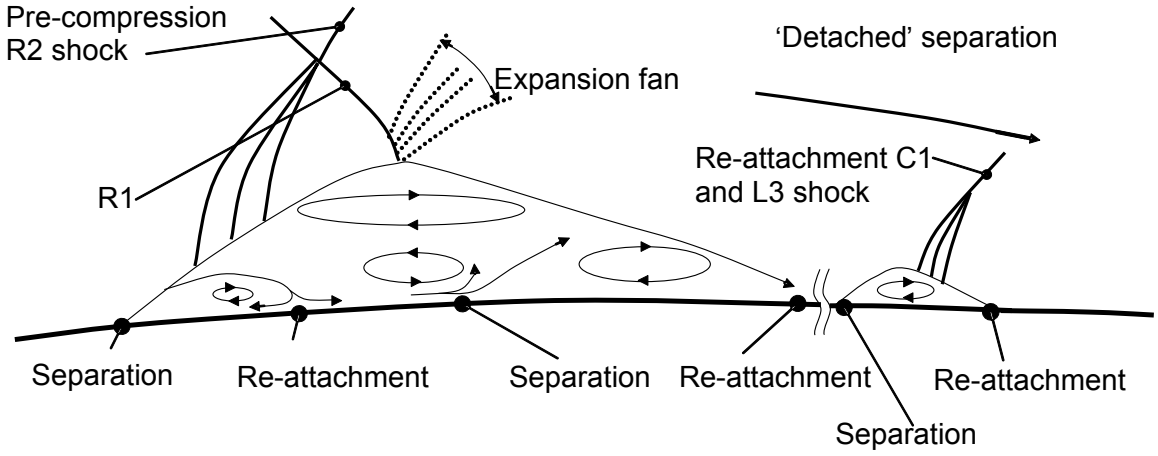

Figure 92 Nozzle suction side at Φ_{NGV} =1.75

At Φ_{NGV}=1.875 the L3 shock impingement position has extended upstream to $0.87C_{ax}$ (Figure 97). L2 has impinged onto the nozzle and propagated to $0.98C_{ax}$ to

superimpose onto the C1 re-attachment shock (Figure 93). A leading compression C1 shock has formed from the 'detached' separation region.

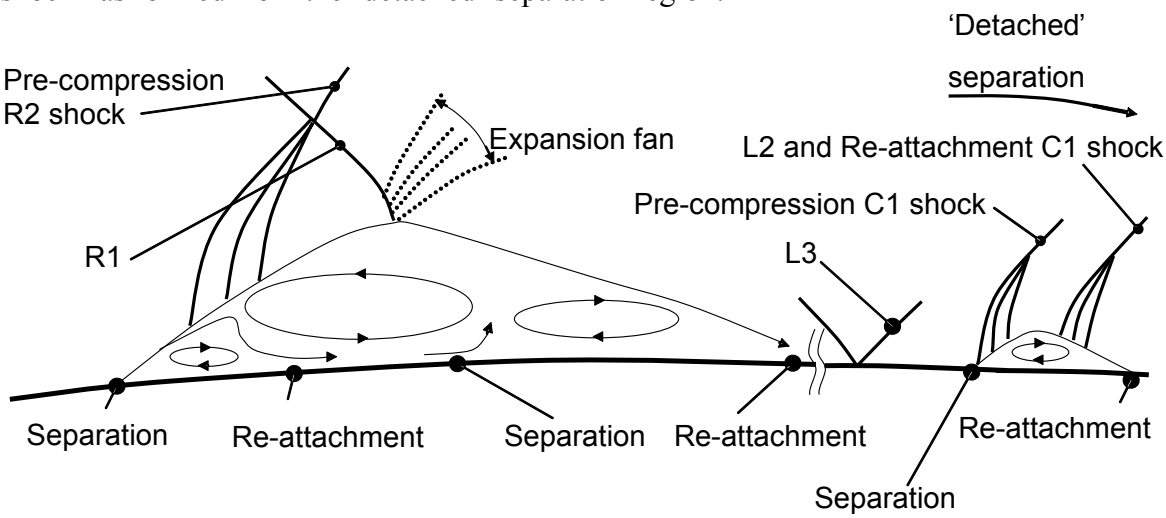

Figure 93 Nozzle suction side at Φ_{NGV} =1.875

At Φ_{NGV}=2 the separation is detaching from the nozzle TE and L3 has propagated upstream to the SBLI region (Figure 94).

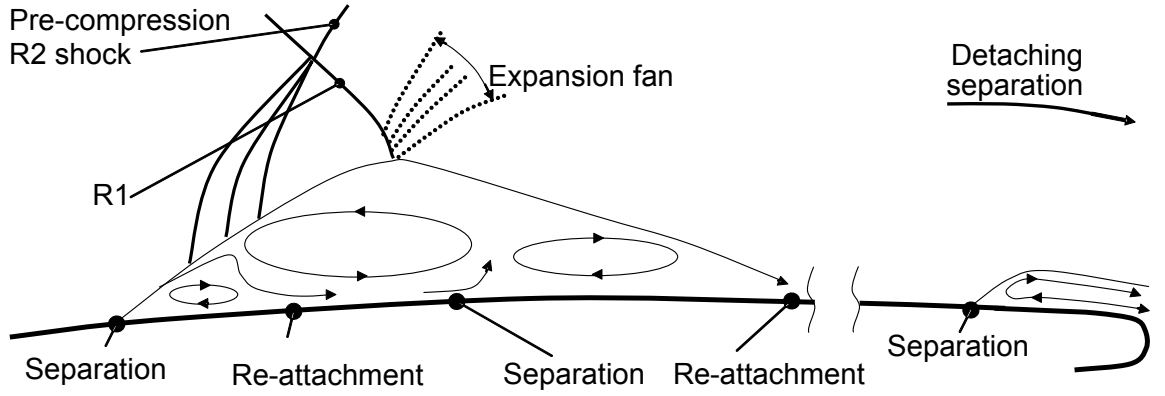

Figure 94 Nozzle suction side at Φ_{NGV} =2

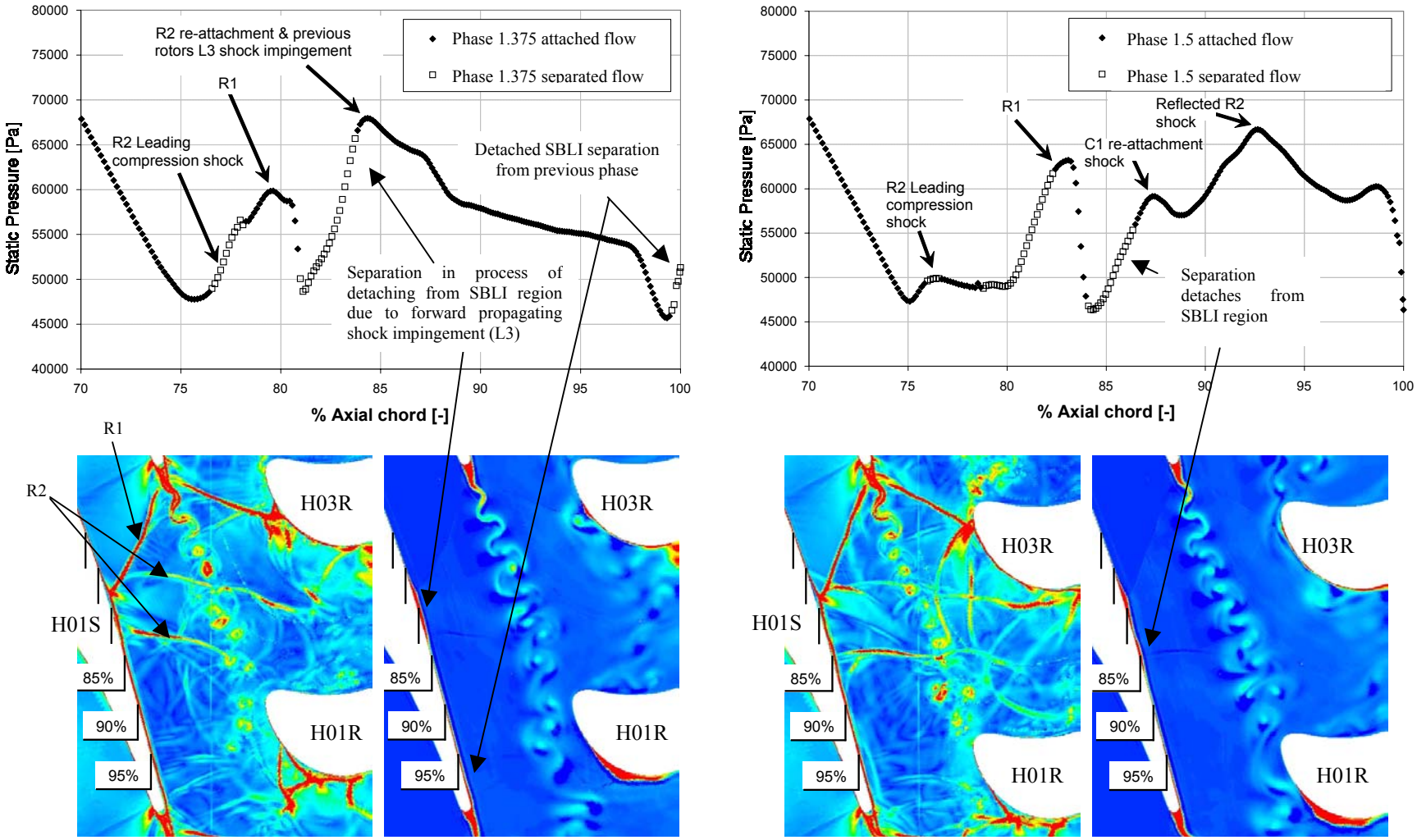

Figure 95 Nozzle unsteadiness between C_{ax}=0.7-1 at Φ_{NGV}=1.375 (left) and 1.5 (right). Top: Ps development, Bottom: Gradient density and entropy respectively

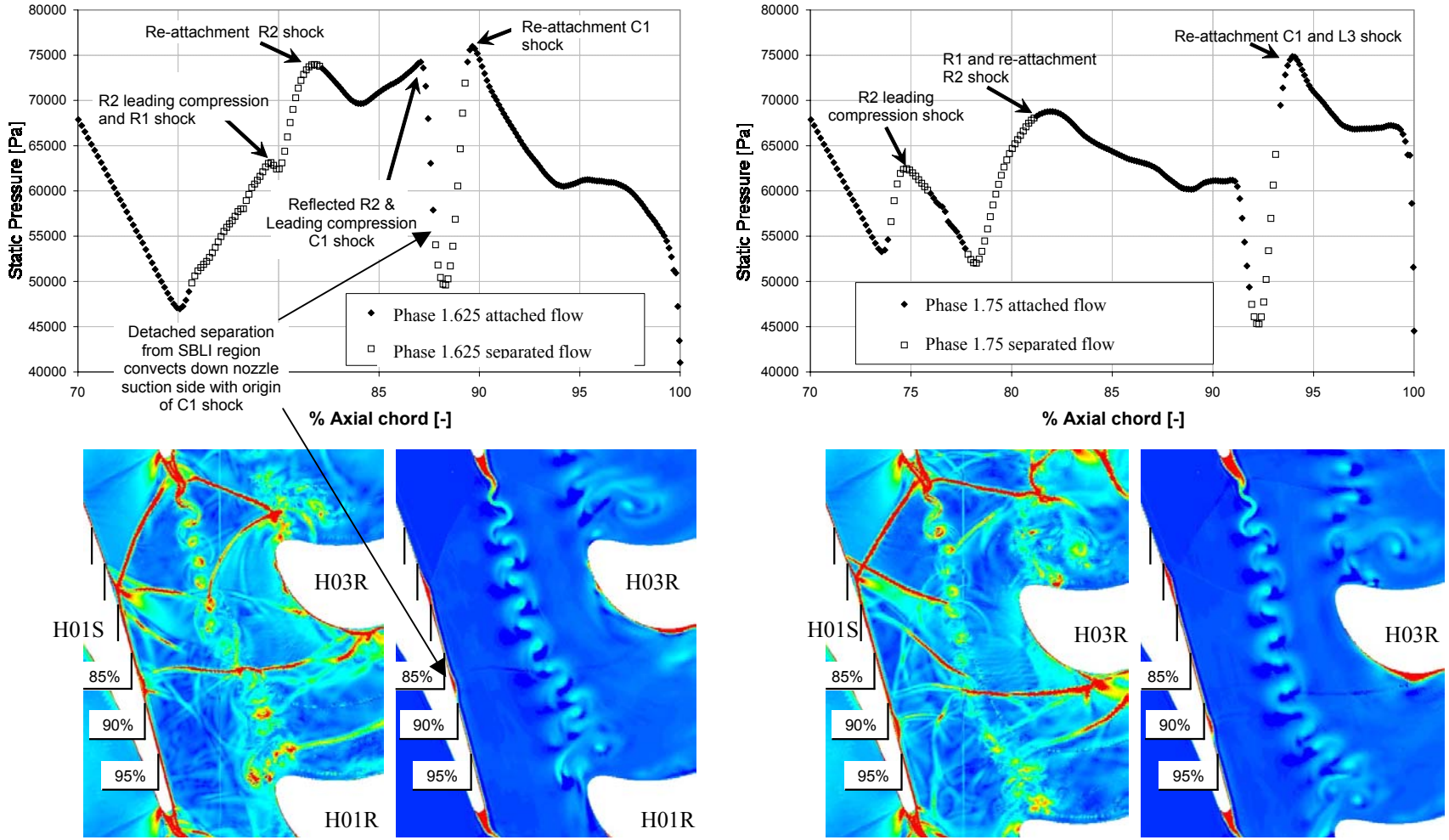

Figure 96 Nozzle unsteadiness between C_{ax}=0.7-1 at Φ_{NGV}=1.625 (left) and 1.75 (right). Top: Ps development, Bottom: Gradient density and entropy respectively

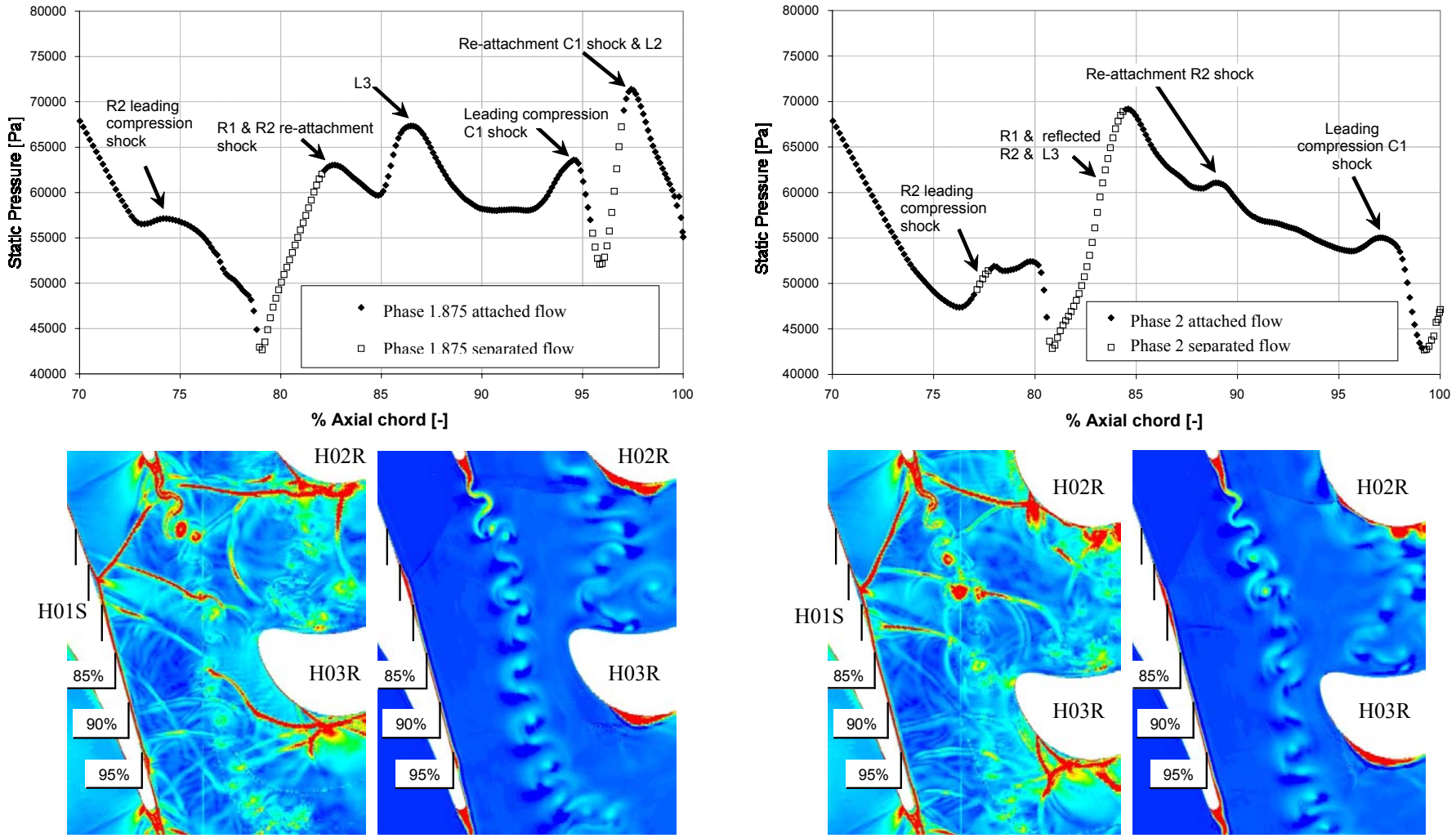

Figure 97 Nozzle unsteadiness between C_{ax}=0.7-1 at Φ_{NGV}=1.875 (left) and 2 (right). Top: Ps development, Bottom: Gradient density and entropy respectively

In conclusion, the flow is highly complex within and downstream of the SBLI region. Impinging reflected shocks generate a periodic separation that detaches from the SBLI region each rotor passing (Φ_{NGV}=1). The boundary layer displacement generated by the convecting separation generates an additional pre-compression and re-attachment shock which are transported down the nozzle suction side at the same speed as the separation convection (Figure 98). The pressure rise through the pre-compression and re-attachment shocks is periodically exacerbated by further reflecting shocks superimposing onto the shocks which are covected with the separation.

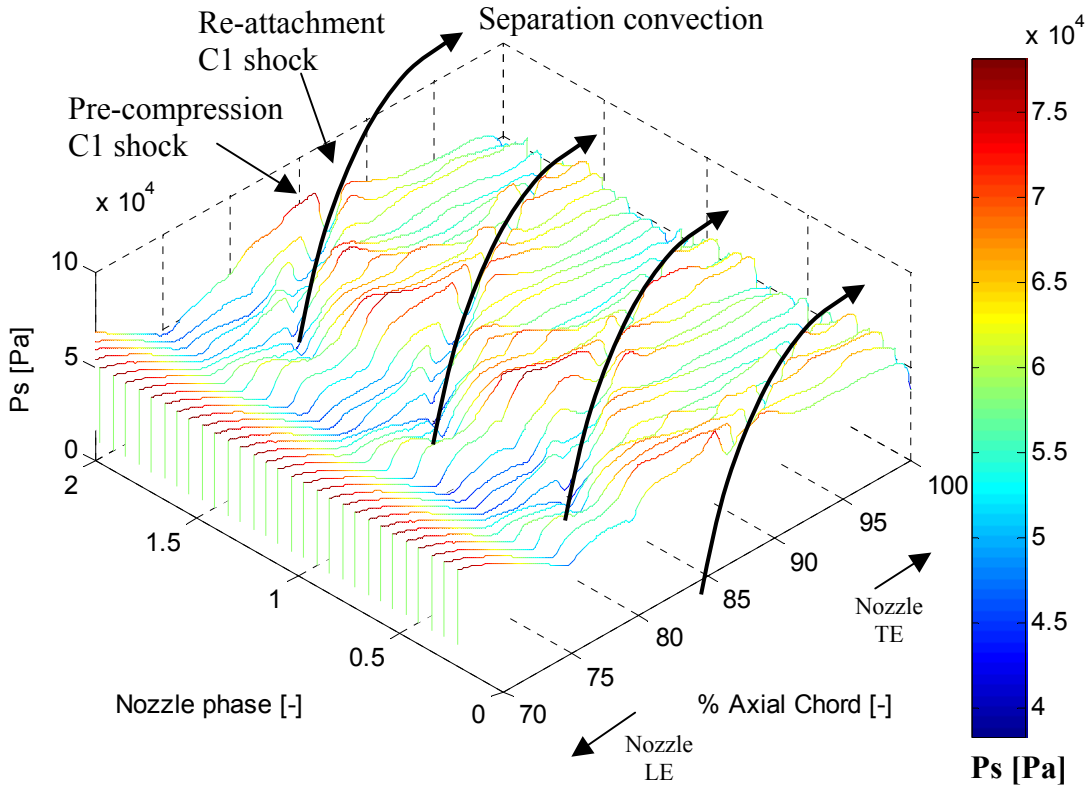

Figure 98 Nozzle SS static pressure: 'detached separation'

Even the R1 impingement position is highly oscillatory, an explanation of the mechanisms is included. The nozzle TE shock strength and angle oscillate in phase with the rotor passing due to the transient convergent-divergent duct formed between the nozzle and rotor. Also the R1 and L1 shock origins are not constant, they peridocially detach from discrete Von Karman vortices to reform on upstream vortices as they convect away from the nozzle TE (Figure 99). The process is repeated at the shedding frequency of the vortices (63.5kHz). The combined effects cause the impingement position of the R1 shock on the adjacent nozzle to oscillate between 0.79 to 0.84C_{ax} depending on phase.

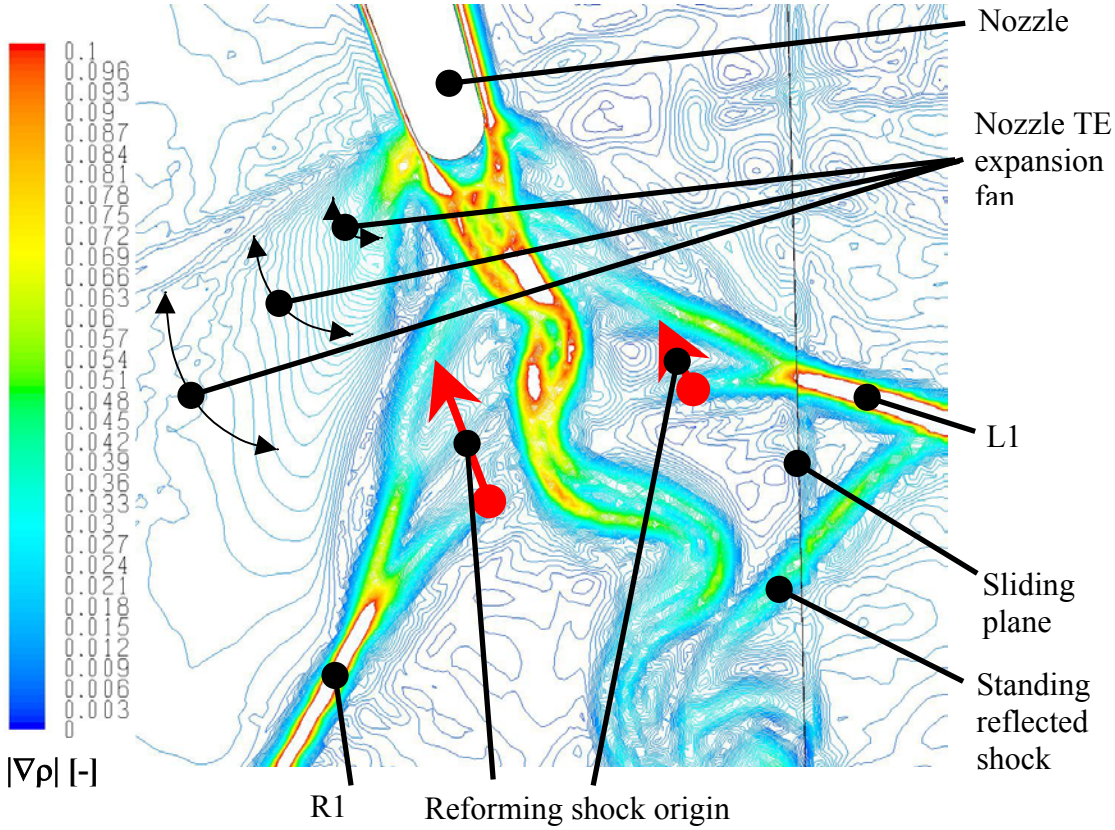

Figure 99 Nozzle shock origin re-forming on upstream Von Karman vortex (contours |∇ρ|)

8.2.2 Inter-stage forcing function

There are three mechanisms that generate the total pressure deficits at the sliding plane (Figure 100). The deficits at approximately 45 and 145% of the nozzle pitch are due to pressure loss through the L1 (Figure 101). The deficits at approximately 70 and 170% of the nozzle pitch are due to the nozzle TE wake. The deficit at approximately 88 and 188% of the nozzle pitch are due to the pressure loss through the reflected shock R2. Clearly the wake total pressure deficit is of primary concern.

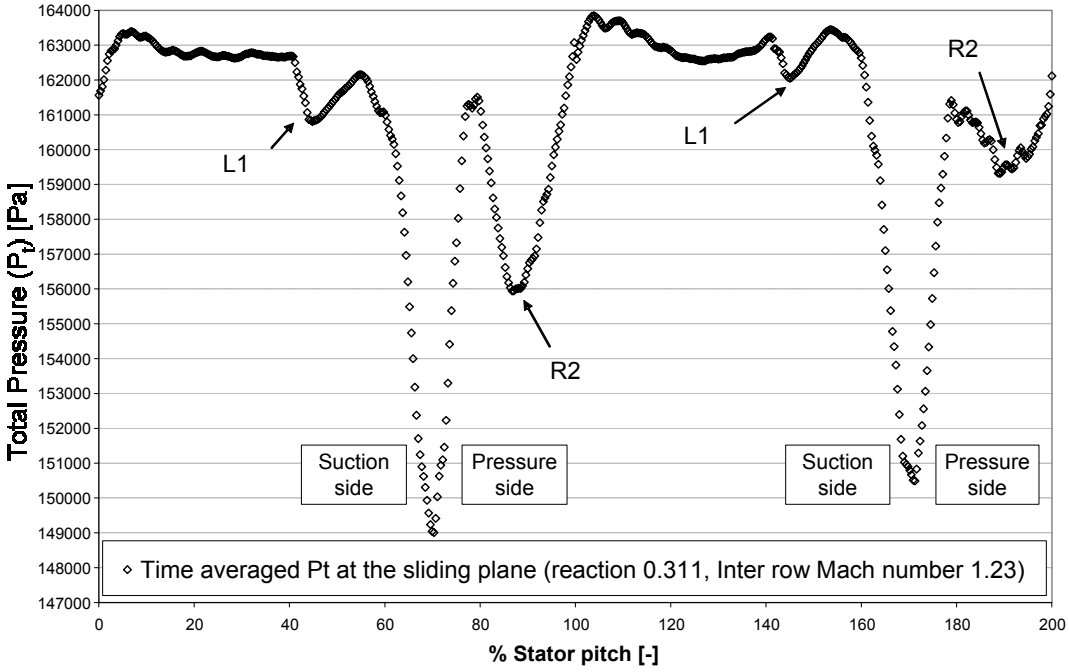

Figure 100 Time averaged total pressure at the nozzle domain exit (sliding plane) (λ=0.31)

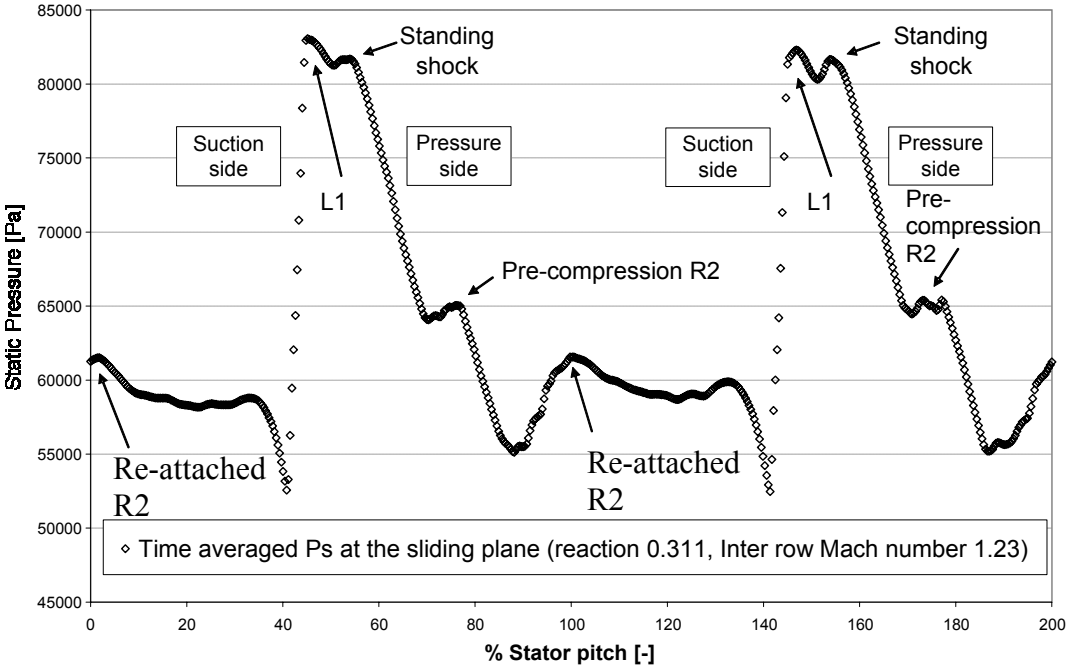

Figure 101 Time averaged static pressure at the nozzle domain exit (sliding plane) (λ=0.31)

8.2.3 2D transient convergent-divergent nozzle

As the nozzle trailing edge L1 shock sweeps across the blade suction surface, an effective throat of a convergent-divergent duct is formed between the rotor LE and the nozzle suction side (Figure 102). As the rotor passes the throat becomes progressively smaller, and the area ratio across the divergent portion increases which raises the vane exit Mach number (Figure 103). The minimum throat area occurs at nozzle phase 0.3125 which coincides with the maximum sliding plane Mach number. The accelerating flow in the divergent channel generates stronger shocks at this minimum throat condition.

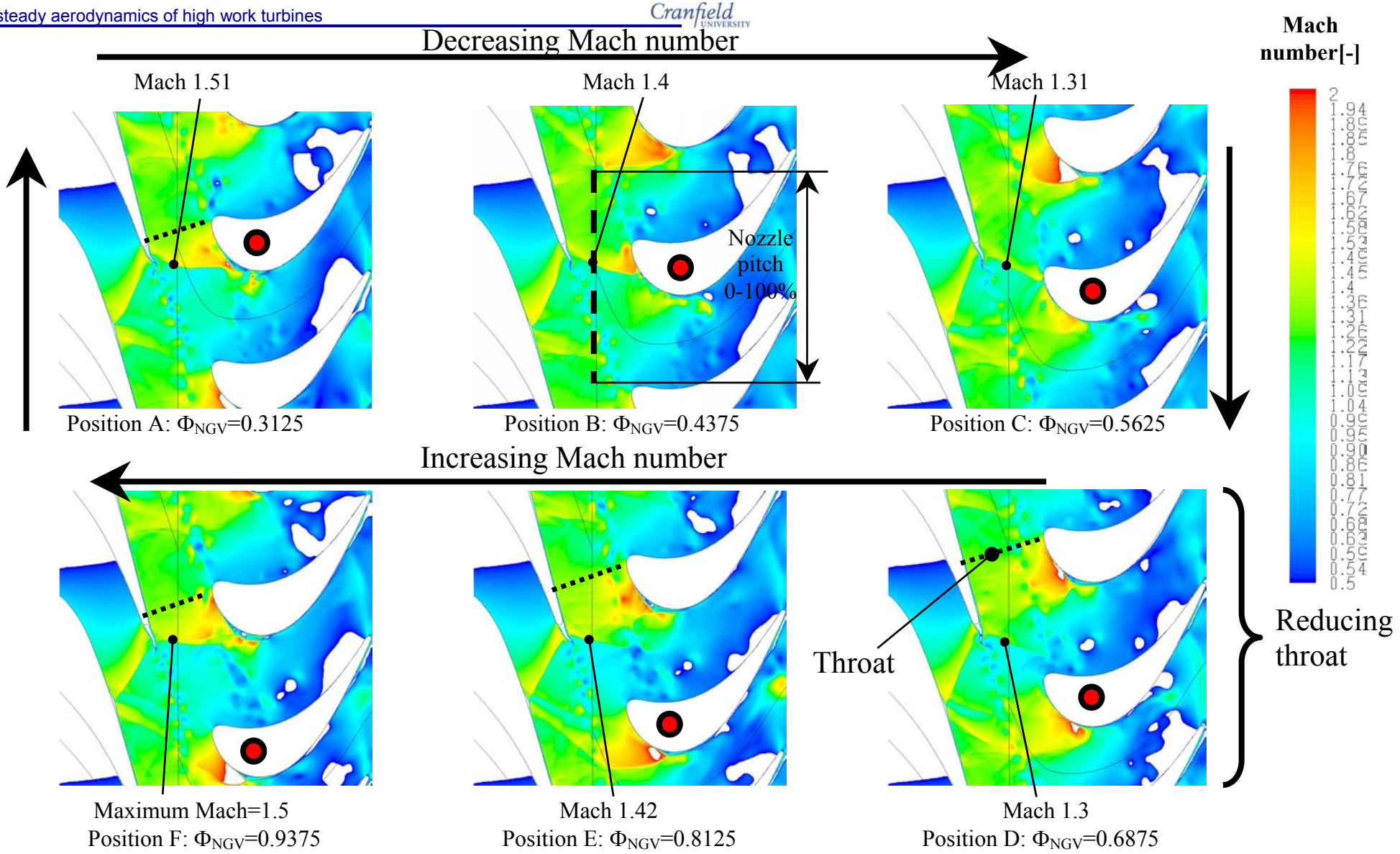

Figure 102 Contours of absolute Mach number (See Figure 103)

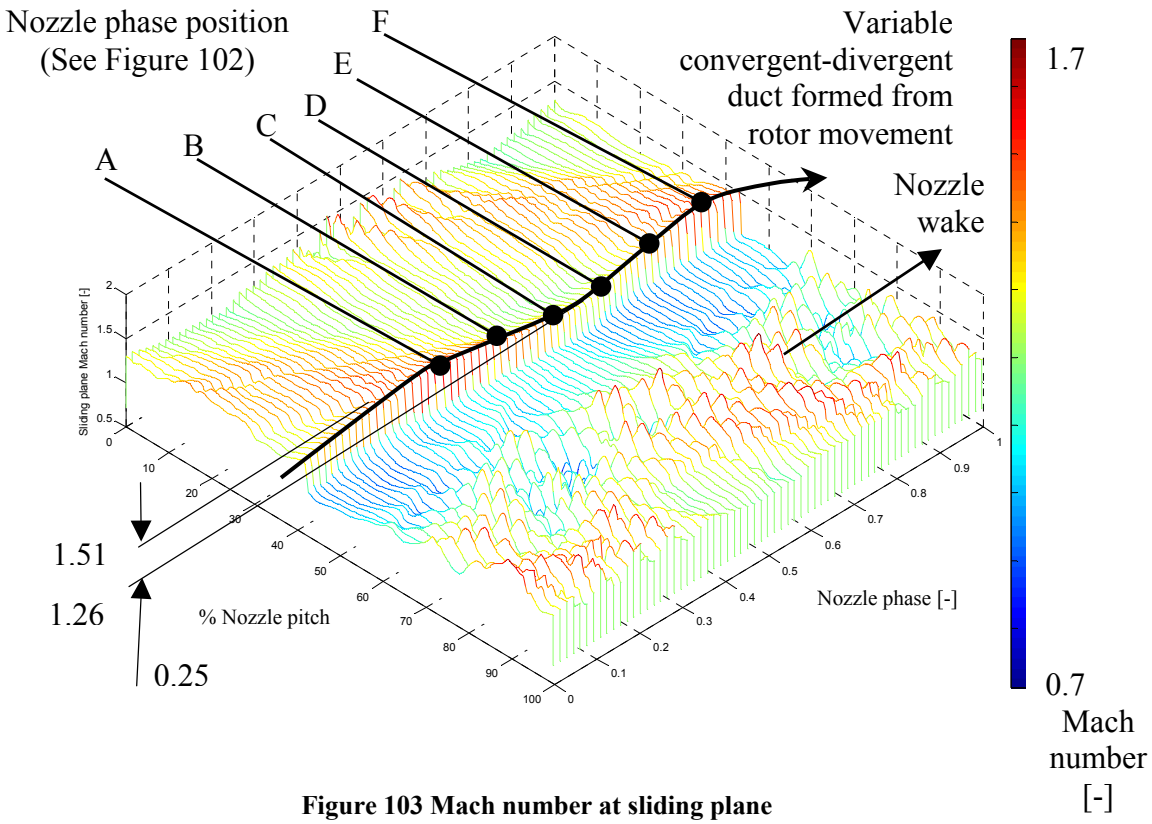

Figure 103 Mach number at sliding plane

8.2.4 Rotor characteristics

8.2.4.1 Steady features

The computational model over-predicts the time-averaged static pressure on the rotor pressure side (Figure 104). The model under-predicts and over-predicts at approximately 0.25 and $0.38C_{ax}$ respectively on the rotor suction side. The differences are attributable to reflecting shocks propagating in the blade row passage, impinging onto the rotor pressure side, and reflecting back onto the adjacent rotors crown.

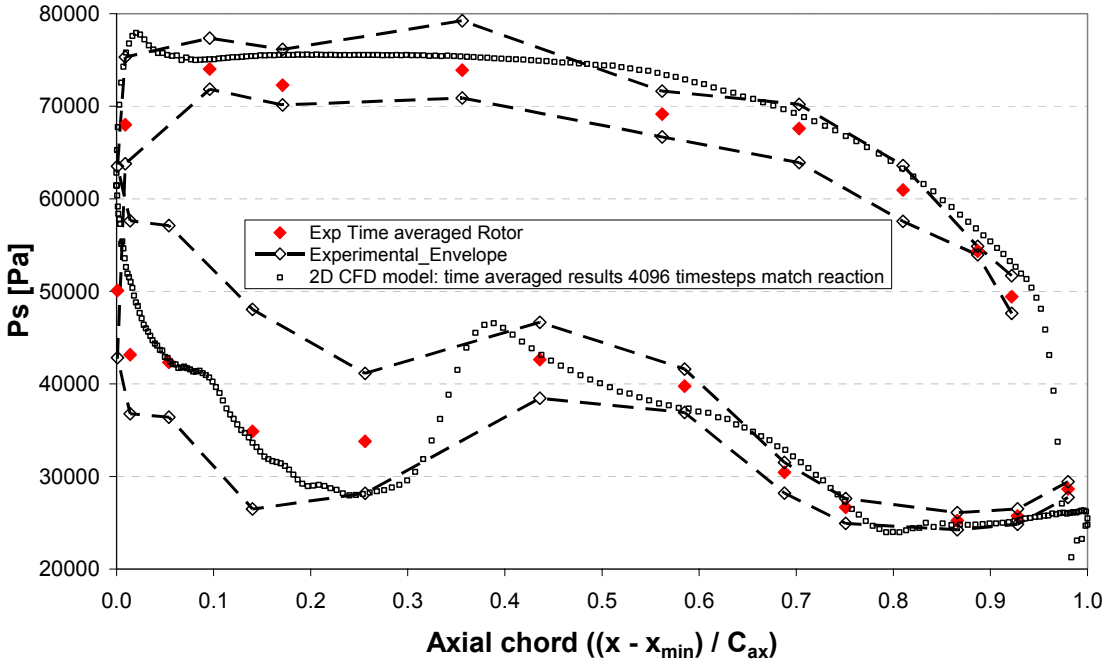

Figure 104 Baseline CFD, time averaged rotor static pressure distribution.

8.2.4.2 Unsteady flow features

Figure 106, Figure 107 and Figure 108 show gradients of density, entropy and absolute Mach number contours respectively at sixteen intervals throughout one nozzle phase (Φ_{NGV}). To aid the following flow description, intermittent schematics of the unsteady flow features are included in Figure 109.

Pre Φ_{NGV}=1, R2 has impinged near the rotor crown at the same phase as an element of the reflected L2 shock, generating an upstream propagating shock (reflected R2). A separation is in the process of detaching from just downstream of the rotor crown.

At Φ_{NGV}=1 the R1 shock reflects from the supercritical SBLI on the adjacent nozzle as two discrete shocks, the pre-compression and re-attachment shocks, R2. L1 has initially impinged near the rotor crown and, as the rotor passed the shock swept towards the LE, progressing through a separation, and reflecting as two discrete forward propagating shocks (L2 and L3). The reflected R2 shock precedes L3 which precedes L2 in their upstream propagation. The incidence angle of the L1 shock impingement onto the rotor increases with the rotor passing, causing the reflected shocks to propagate back towards the nozzle suction surface in a convex form. An element of the reflected R2 and L3 shock that extend between the nozzle wake and the LRS are more directly aligned into the free stream and consequentially stall when they reach the sonic component of the flow that is normal to the shocks. The remaining portion of the reflected R2 shock has diffracted through the wake into discrete overlapping convex forms. The pre-compression R2 shock penetrates through the adjacent nozzle wake, to the axial position of the rotor crown, at mid-rotor passage. The re-attachment R2 shock extends from the nozzle suction side (SS) to the adjacent nozzle wake.

At Φ_{NGV}=1.125 a high entropy flow region has detached from the rotor crown separation and is convecting down the rotor suction side (Figure 105). The flow locally deviates, relatively, away from the rotor suction side, and then back onto the rotor suction side, without re-circulation, generating high entropy by shear. A separation has detached from the nozzle SBLI region, and is convecting along the nozzle suction side.

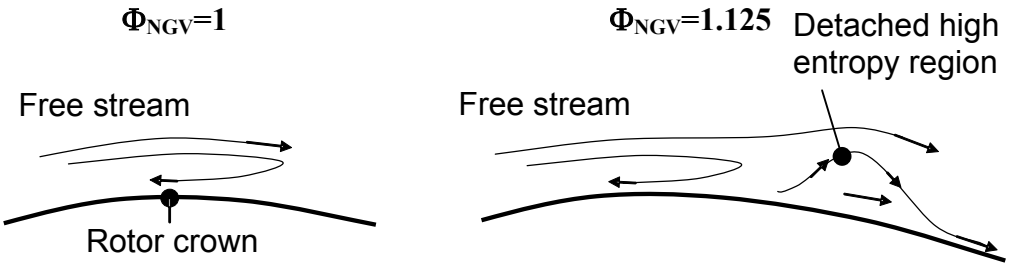

Figure 105 Schematic of high entropy detached flow region.

L3 is in the process of diffracting through the nozzle wake. The extremity of L2 has almost reached the adjacent rotor pressure side. The reflected R2 shock has initially impinged onto the nozzle SS at $0.96C_{ax}$ and continuously impinges upstream and downstream due to its convex form. By Φ_{NGV}=1.125 the upstream portion has reached $0.93C_{ax}$. The R2 reflected shock has begun to propagate back towards the rotor as a weak shock reflection. The adjacent rotor's L3 shock has propagated through L1 and nozzle wake towards the nozzle SBLI region.

By Φ_{NGV}=1.25 L3 has diffracted through the nozzle wake and is propagating towards the nozzle as multiple, discrete, convex shock waves. L2 is in the process of diffracting through the nozzle wake and an element has reflected back from the adjacent rotor pressure side. L1 continues to reflect, not from the rotor, but the adjacent nozzle wake. L2 from the adjacent rotor has impinged onto the nozzle and reflects as a nearly continuous stream with the reflected R2 reflection. A pre-compression C1 shock impinges just upstream of the rotor crown. The high entropy, flow discontinuity continues convecting along the rotor suction side without re-circulation.

By Φ_{NGV}=1.375 the reflected L2 shock has been strengthening with it's propagation across the rotor passage towards the high Mach number flow near the rotor crown. It impinges in the same position as the C1 shock on the rotor crown generating a significant adverse pressure gradient. Figure 110 details the rotor suction side pressure development across two nozzle pitches. The shock reflected L2 and C1 impingement generate the largest adverse pressure gradient the rotor crown is subjected to, excluding the L1 shock impingement.

Although the C1 impingement position has remained on the nozzle crown, the origin has propagated down the nozzle suction side with the detached separated region. The pre-compression and re-attachment R2 shocks have been impeded by the nozzle wake. L3 has impinged onto the nozzle SS at $0.96C_{ax}$ and like the reflected R2 shock

continuously impinges either side of the original impingement position due to it's convex form. The high entropy flow discontinuity region is convecting past the separation generated at the late rotor suction side, generated by the rotor trailing edge shock (Rot1).

By Φ_{NGV}=1.5 L3 has progressed to 0.87C_{ax}, just downstream of the nozzle SBLI region. L2 has impinged on to the nozzle suction side near the TE and is continuing to impinge upstream, whilst a downstream portion has passed through the adjacent nozzles L1 shock, propagating towards the adjacent nozzle suction side. The reflected L2 shock continues to impinge onto the rotor crown. The nozzle separation continues to convect down the nozzle suction surface. The high entropy region convecting down the rotor suction side has pasted the rotor SBLI region generate by Rot1, increasing the separation length in the SBLI during its transit.

By Φ_{NGV}=1.625 the adjacent rotor is approaching rotor phase 1 (Φ_{ROT} =1) and has begun to repeat the processes of Φ_{NGV}=1. The C1 and reflected L2 shocks have impinged just upstream of the rotor crown and are in the process of reflection. The pre-compression R2 shock has impinged past the rotor stagnation position and onto the pressure side, and is being dissipated by convecting turbulence from the nozzle TE.

By Φ_{NGV}=1.75 the convecting nozzle separation has detached from the nozzle TE. The adjacent rotors reflected R2 shock has impinged onto the nozzle, and is beginning to reflect back.

By Φ_{NGV}=1.875 the adjacent nozzle L1 shock has impinged onto the rotor crown.

The important factors in this detailed description are the supercritical SBLI region on the adjacent nozzle and the detached separation which convects along the nozzle suction side, which generates additional forcing functions.

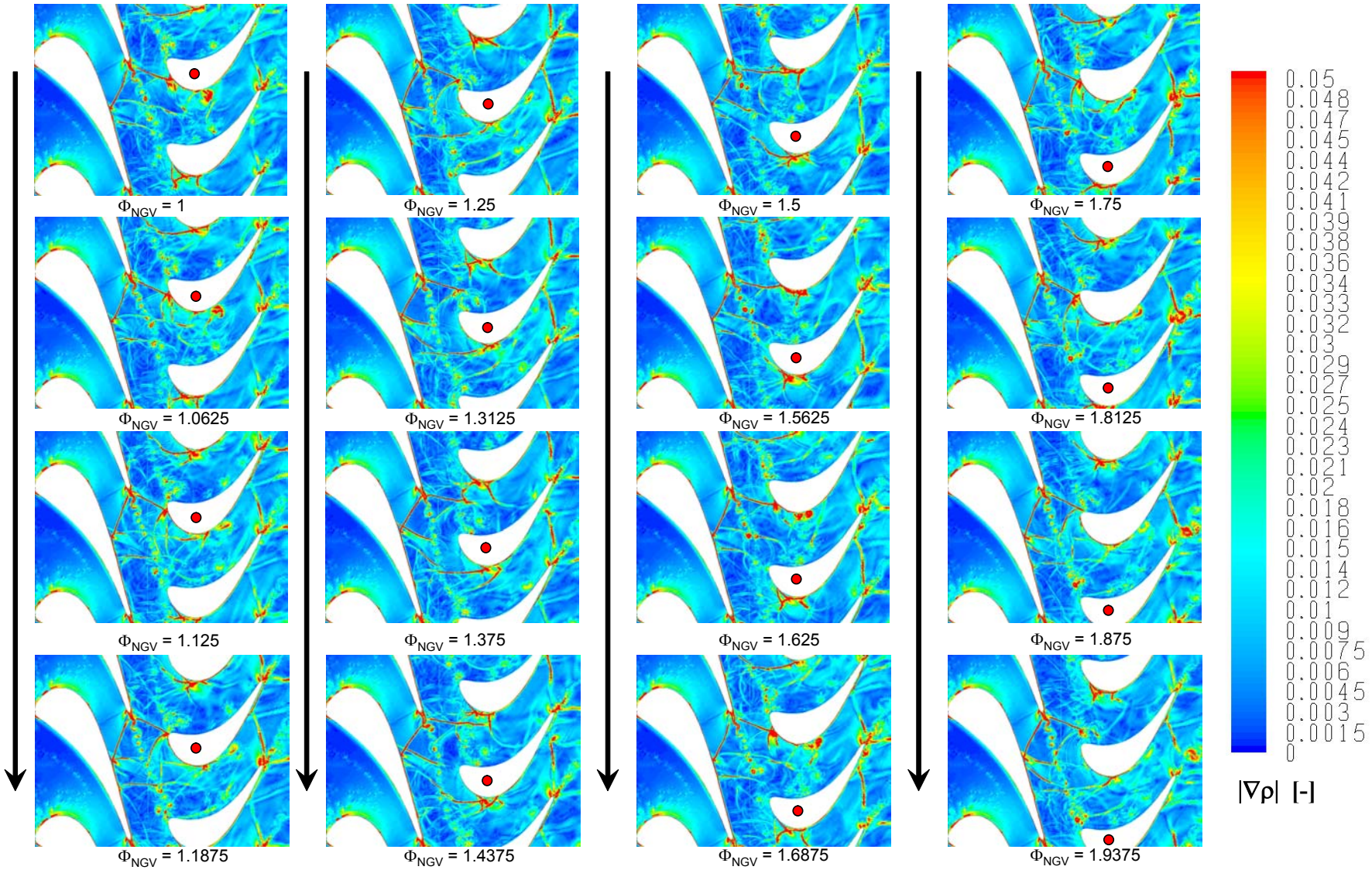

Figure 106 Gradients of density contours (|∇ρ|) at 50% span

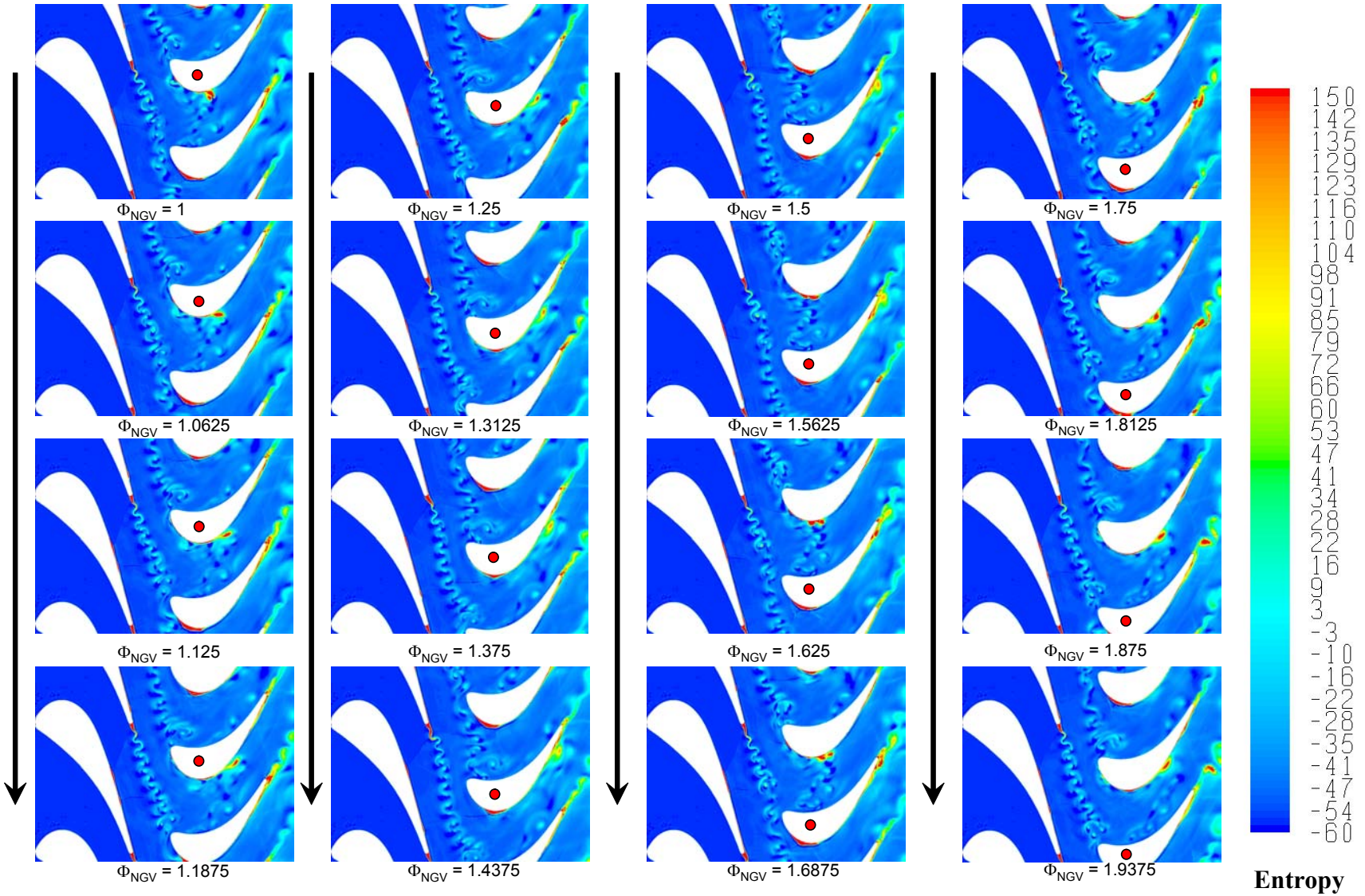

Figure 107 Entropy contours at 50% span

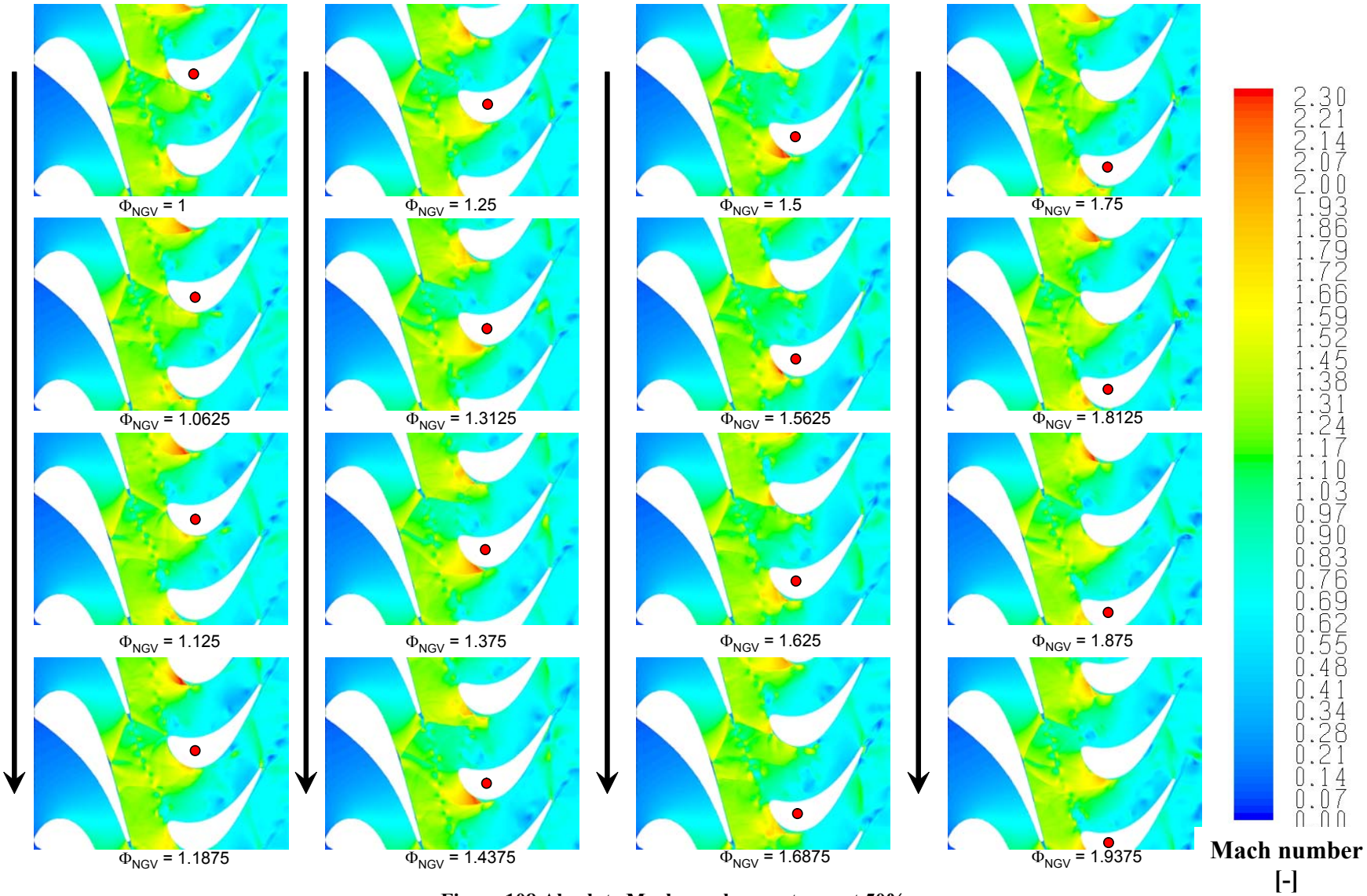

Figure 108 Absolute Mach number contours at 50% span

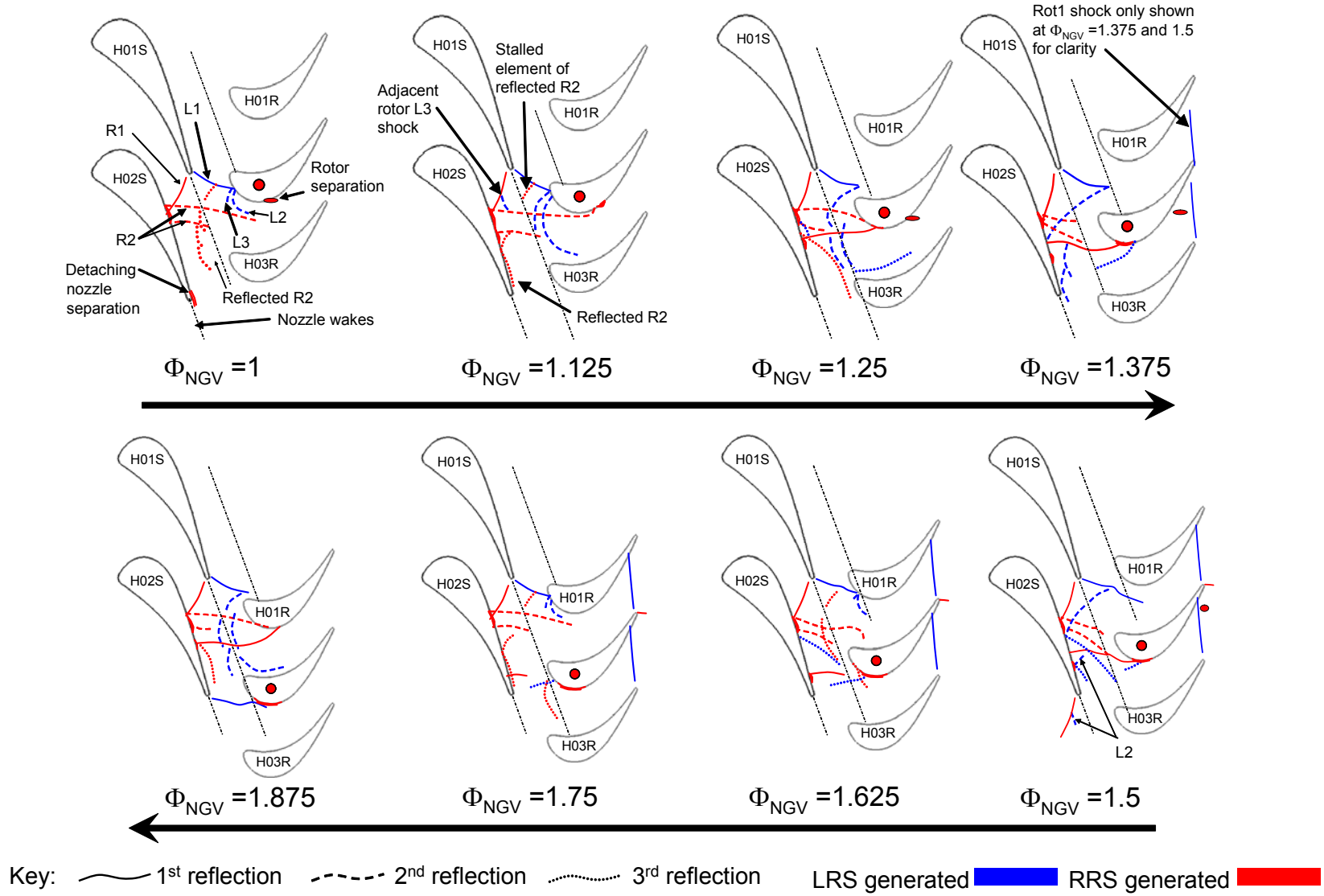

Figure 109 Schematic of shock motion, and induced separations.

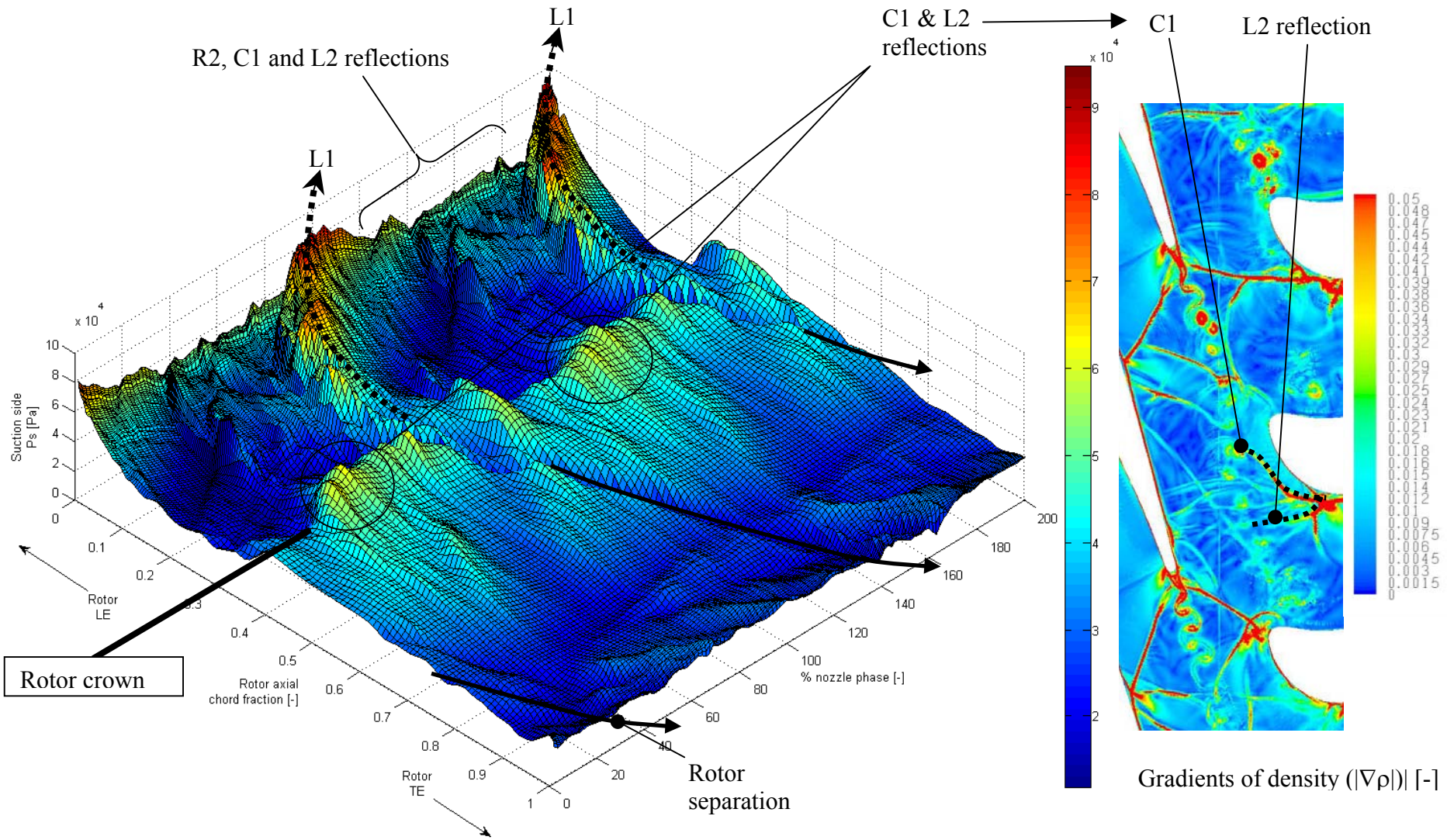

Figure 110 Rotor suction surface static pressure development

8.2.4.3 Rotor steady forces

Although not pertinent to unsteady forced response, a comparison of the predicted and experimental time averaged axial and tangential force is included for reference (Table 21). For a detailed description of how the rotor forces and pitching moments are derived see appendix 1. A comparison with the tangential and axial force distribution is also included (Figure 111 and Figure 112 respectively), which demonstrates a biasing error on the predicted pressure side tangential forces. Aerodynamic differences between the baseline model and the parametric studies are included in section 8.3 to 8.6, where the harmonic composition of unsteady forces is also analysed.

	CFD [kN/m]	Experimental [kN/m]	% difference
Axial force	1.048	0.980	6
Tangential force	-1.442	-1.220	15

Table 21 Time averaged forces

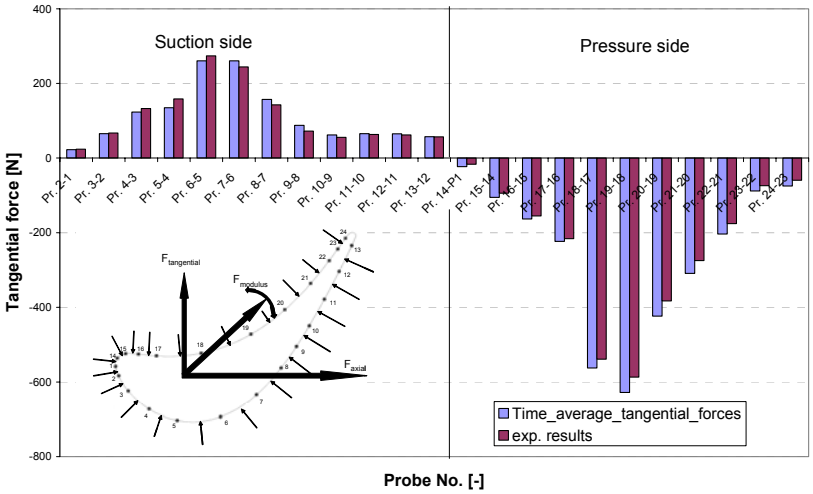

Figure 111 Time averaged tangential forces between probes

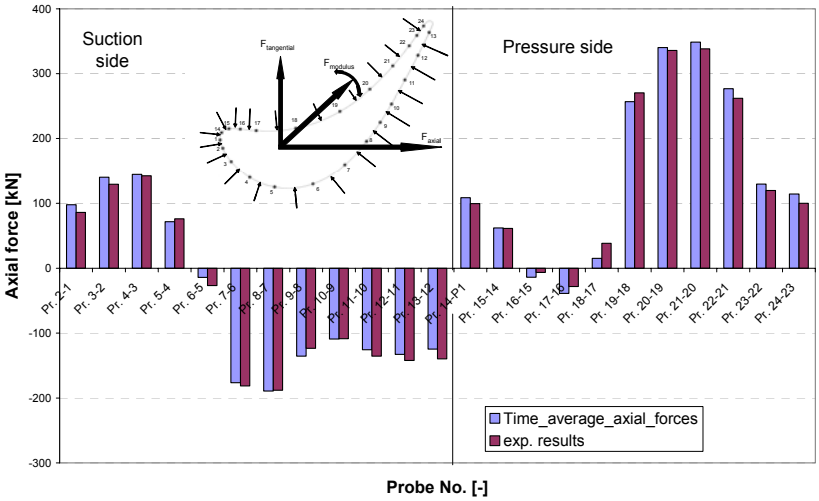

Figure 112 Time averaged axial forces between probes

8.3 Effect of Reaction

Reaction expresses the proportion of working fluid expansion which occurs in the rotor blade passages. In a zero reaction stage the flow area through the rotor passage is constant, there is no change of static pressure and work is extracted from the fluid purely by the reduction in its momentum (i.e. as an impulse turbine). In high reaction stages most of the expansion occurs across the rotor blades and less through the nozzles. In most conventional turbines, engineers typically distribute the expansion approximately evenly between the nozzle and rotor blades (50% reaction). This generates an enthalpy drop which is equally divided between the stator and rotor, which means the relative flow angle onto the stator and rotor are common. A 50% reaction turbine provides high efficiency with manageable tip speeds.

In this work the reaction is defined as:

$$\textbf{Reaction, } \lambda \textbf{ (\%)} = \frac{t_2 - t_3}{T_{01} - t_3} \textbf{ (x 100)} \qquad \textbf{Equation 5 Reaction definition (Constant gas properties)}$$

where T_0 and t denote the total and static temperatures respectively. The suffix denotes the stage axial position where 1, 2 and 3 are upstream of the nozzle, inter-row and downstream of the rotor, respectively. Three reaction cases have been studied (28.4, 31.1 and 41.3%; Table 22), each variation in reaction was achieved by skewing the rotor blade about the LE relative to the 3D baseline case (2° open, 0.5° open and 2° closed respectively).

Reaction (λ)	Stage loading ($\Delta H/U_{50\%}^2$)	Specific work ($\Delta H/T_{01}$)	Flow co-efficient ($V_A/U_{50\%}$)	Efficiency (η_{turb}) $\frac{T_{01}-T_{03}}{T_{01}\left[1-\left(\frac{1}{P_{01}/P_3}\right)^{(\gamma-1)/\gamma}\right]}$
28.4%	2.12	306	0.5	0.92
31.1%	2.1	303	0.49	0.9
41.3%	2.1	303	0.45	0.92

Table 22 Reaction cases modelled: P_{01}/P_{03}=4, Non-dim speed=12

For forced response applications the most important effects of increasing the reaction in a supersonic turbine are:

- reducing the inter-row Mach number
- reducing the shock strength
- reducing the angle the shocks propagate from the NGV TE
- relatively phase shifting the shock and wake forcing functions
- deflecting the wake through the reflected R1 shock
- altering the swirl angle through the shocks
- broadening and deepening the total pressure profile of the wake
- reducing the higher frequency content of the wake

A more detailed description of each of these effects and how they are interrelated is included in the discussion. Increasing the reaction (λ) from 28 to 41% causes the inter-row Mach number to fall from 1.27 to 1.12. As the inter-row Mach number reduces, the static pressure increases, reducing the shock strength from Ps_2/Ps_1=1.6 to

1.49. The propagation angle from the nozzle TE of the weaker shock reduces from 41 to 32°, which phase shifts the shock and indirectly the wake forcing function, diagrammatically represented in Figure 113. Although the wake does not convect through the L1or R1 shocks, it does phase shift with respect to the shock forcing function as it turns through the reflected R1 shock and is deflected by the potential field. The phase shift is a function of the shock propagation angle, shock strength and rotor potential field strength. The magnitude of the wake turning is determined by the potential field and shock strength (a function of reaction for the considered cases). The nozzle L1 and R1 turn the flow away from the wake by as much as 9 degrees.

In summary the L1 shock reduces the swirl angle and R1 increases the swirl angle, the shock reflection from the adjacent nozzle reduces the swirl back towards the axial direction. This affect is superimposed onto the resulting potential field which increases the swirl angle. Another aspect of the higher inter-row pressure includes generating a broader deeper wake, which is examined in more detail below. Increasing the reaction reduces the amplitudes of each harmonic due to weaker shock and shock reflections.

8.3.1 Flow characteristics in the nozzle domain

There are three important flow features which are specific to supersonic turbines that are sensitive to reaction:

- the unsteady SBLI on the nozzle suction side
- the separation which periodically detaches from the SBLI region
- the blade row interaction effects, which include forward propagating reflected shocks (see section 8.3.1.1)

Each of these features affects rotor forcing. The SBLI on the nozzle suction side is generated by the impinging nozzle TE R1. SBLIs with separations are known to be inherently unsteady (see chapter 3). From the experimental program the reflected shock is shown to oscillate at a relatively low frequency of less than 200Hz. However in a high work turbine this SBLI unsteadiness is superimposed onto an impinging shock which is oscillating at the BPF (4534Hz in this case). This is caused by the nozzle TE shock strength and propagation angle modulating in phase with the rotor passing, causing the impingement position along the nozzle suction side to oscillate. This oscillation occurs about a time averaged position which is dependent upon the reaction. As the reaction decreases the nozzle TE shock propagates and reflects at a more oblique angle, impinging onto the adjacent nozzle at a higher axial chord location (Figure 114).

The impinging RRS reflects as two discrete shocks; a leading compression and a re-attachment shock. Multiple separations and re-attachments occur within the nozzle SBLI region between the two reflecting shocks (see section 8.2.1.2). Periodically a separated region disengages from the SBLI and convects along the nozzle suction side until it detaches from the TE at each rotor passing. As the separation convects it displaces the streamlines, generating a shock, the origin of which is transported along the nozzle suction side with the convecting separation. The strength of the convecting shock and size of the separation reduces as reaction is increased.

8.3.1.1 Inter-row shocks

For supersonic turbines the nozzle TE shock is the most significant forcing function (see section 8.6). The shock strength is sensitive to reaction, reducing the reaction from 41 to 28% increases the pressure rise through the nozzle TE shock from 1.49 to 1.6 (Figure 115). In terms of forcing the nozzleL1 is more important than R1 due to its unobstructed line of sight to the rotor. The R1 shock is less significant because it impinges onto the adjacent nozzle and reflects as two discrete shocks (for λ=28 and 31%); dissipating as it propagates through the nozzle boundary layer. For the high reaction case (λ=41%) the RRS is not sufficiently strong and does not reflect, terminating at the SBLI (Figure 116).

As the reaction reduces, the nozzle TE shock propagation angles increases which results in a phase shift in the shock forcing function. For the low reaction case (λ=28%) the LRS phase lags the high reaction case (λ=41%) by $0.1\Phi_{NGV}$ (Figure 117). This phase shift could be potentially important if it aligns with the other forcing functions to generate constructive interference. The nozzle TE LR and reflected RRS impinge onto the rotor and reflect back onto the nozzle suction side between the RRS impingement position and the nozzle TE.

At lower reactions the high strength of the nozzle TE shocks generate more numerous reflections across the inter-row gap before they dissipate or reflect through the rotor passage (Figure 116). The pressure rise across the reflected shocks periodically exacerbates the size of the separation in the nozzle SBLI region and the detached nozzle separation. The reflections also increase the adverse pressure gradient across the reflected RRS and the convected shock formed from the detached separation. The more numerous reflecting shocks generate higher frequency content in the unsteady forces.

8.3.1.2 Nozzle wakes

For a nozzle operating in the supersonic region the wake total pressure profile is sensitive to reaction due to:

- the change in shock strength
- the RRS impingement position
- the convecting nozzle separations
- blade row interaction effects

The change in the width and depth of the nozzle wake for each of the configurations is included in Figure 118. The wake total pressure profile is most sensitive to the increasing inter-row pressure, which results from the reaction cahnge. As the reaction increases, the higher back pressure causes the wake to widen and deepen. However other mechanisms which indirectly affect the nozzle wake from the change in reaction include, the shock strength, the length of nozzle chord downstream of the SBLI that the boundary layer has to develop along, the intermittent separation which convects from the SBLI region to the TE, and reflecting shocks.

As the reaction increases the SBLI generated by the weaker RRS impingement onto the nozzle SS does not displace the nozzle boundary layer streamlines as much. However, unlike the nozzle pressure side, the resulting boundary layer downstream of

the SBLI is sensitive to the higher inter-row pressure. This results in a broader, deeper wake, increasing the depth by as much as 15% at the sliding plane.

The wake profile is also in part a consequence of the RRS impingement position. As the reaction increases the RRS impinges onto the adjacent nozzle suction side further upstream (Figure 114), which increases the nozzle chord length from the SBLI to the nozzle TE that the boundary layer has to develop along generating a broader deeper wake, generating larger rotor forces.

8.3.1.2.1 Swirl within the wake

The periodically detaching Von Karman vortices from the nozzle TE modulate the swirl within the wake (Figure 119). The swirl can range by as much as 67-80° at the sliding plane. This variation in swirl periodically alters the incidence angle onto the rotor which modulates the rotor lift forces.

8.3.1.2.2 Wake turning

The LR and RRS turn the nozzle passage flow, but they do not directly turn the wake. The reflected RRS and the potential field change the wake trajectory (Figure 116). The reflected RRS turn the flow (including the wake) towards the axial direction. The rotor potential field turns the wake towards the tangential direction (Figure 119). For the considered cases the turning can be as much as much as 10% nozzle pitch (0.9°) at the sliding plane (Figure 118).

The wake turning through the reflected RRS is dependent upon the reaction (for a given nozzle geometry). If the nozzle wake convects through strong reflected shocks, generated at low reaction, it is deflected more towards an axial direction. However reducing reaction also generates a stronger rotor potential field which deflects the nozzle wake further towards the tangential direction (Figure 116). The turning effectively changes the length downstream of the nozzle in which the wake has to develop and phase shifts it as a forcing function relative to the shock.

8.3.1.3 Swirl angle

The time averaged absolute swirl angle at the sliding plane is 73.7, 73.9 and 74.2^{o} for reactions 28, 31 and 41% respectively. For reaction case λ=31% this equates to 63.3 degrees relative swirl angle[e10]. However the time averaged swirl across the nozzle pitch changes considerably. The flow is turned by as much as 9° through the TE shocks (Figure 120).[e11]

8.3.2 Rotor characteristics

8.3.2.1 Steady features

At lower reaction (λ=28-31%) more numerous shock reflections propagate between the rotor stages and across the rotor passage. The reflected RRS and the rotor passage L2 reflection impinge onto the crown generating a local maximum of static pressure (approximately 42% axial chord;Figure 121). For the high reaction case (λ=41%) the reflected LRS is relatively weak and the RRS terminates upon impingement to the adjacent nozzle, so there is no discernable (time averaged) increase in pressure at the rotor crown.

8.3.2.2 Unsteady rotor features

Unlike the low reaction cases, the high reaction case (λ=41%), does not include any significant shock reflections from the RRS (Figure 115), consequently the only shocks the rotor is subjected to is from the periodically impinging LRS and weak LRS reflections from within the rotor passage. This is most evident at the rotor crown when comparing the high reaction case rotor SS P_s (Figure 122). Other contributory mechanisms to unsteady force include the unsteady separations which convect along the rotor suction side, the unsteady NGV wakes and the unsteady oscillation of the rotor TE shocks which are implicit within this analysis.

8.3.2.2.1 Blade forces and pitching moments

As expected, the forces and pitching moments generally increase with reducing reaction (Figure 123), predominantly due to the shock forcing function (see section 8.6). The trends are presented as a function of reaction in Figure 124 and summarised in Table 23. Exceptions to the anticipated results include the tangential force at the BPF and 1st pitching moment harmonic which are both non-monotonic. Another interesting finding includes large forces at the higher harmonics due to the more numerous shock reflections. These include the tangential forces at the 1st harmonic and the axial forces at the 2nd harmonic, which are larger than the 1st harmonic axial forces.

8.3.2.2.2 Harmonic distribution

A more detailed evaluation of where the tangential forces are occurring around the rotor at the BPF is included in Figure 125. Generally the forces increase around the rotor as the reaction reduces. Areas where this does not occur are just downstream of the rotor crown ($0.56C_{rot}$) and towards the LE on the pressure side ($0.16\text{-}0.34C_{rot}$). The tangential forces on the pressure and suction side are most sensitive to reaction in the axial location of the rotor crown (approximately $0.42\text{-}0.5C_{rot}$), which is examined in more detail in section 8.3.2.2.3. On the pressure side this is also where the local maxima occurs for all cases, on the suction side it occurs between the LE and crown, depending upon reaction. This is primarily due to the higher shock strength at lower reaction.

Some consideration needs to be given to why the larger tangential forces around the rotor (Figure 125) do not manifest themselves in the net rotor forces (Figure 123). The reason is phase alignment of rotor forces. The higher tangential rotor forces on the rotor pressure and suction side for the lower reaction (λ=28%) destructively interfere generating a lower net tangential force. If each discrete force element were phase aligned then the expectation of the maximum tangential force at the BPF would be realised for this low reaction (λ=28%).

8.3.2.2.3 Forcing function

An analysis of the pressure time history at approximately 54% of axial chord on the pressure side gives some insight into the forcing mechanisms in the area where tangential forces are at local maxima and are most sensitive to reaction (Figure 126). For λ=41% the maxima pressure occurs at Φ_{NGV}=1.18, from the impinging LRS (position A), for λ=28% a local maxima at Φ_{NGV}=1.23 is also from the LRS impinging (position B), but more numerous rotor passage shock reflections for the low reaction case continue to impinge considerably increasing the unsteady pressure

up to the local maximum at Φ_{NGV}=1.64, where the wake and reflecting shock are coincident (position C).

8.3.3 Summary of findings

The flow field is affected in several ways by increasing reaction including:

- reducing the inter-row Mach number
- reducing the shock strength
- reducing the angle the shocks propagate from the NGV TE
- deflecting the wake through the reflected RRS towards an axial direction
- relatively phase shifting the shock and wake forcing functions
- altering the swirl angle through the shocks
- broadening and deepening the total pressure profile of the wake
- reducing the higher frequency content of the wake

The high frequency content of wakes and shocks in low reaction configurations is an important finding for the practical analysis of high work turbines. Typically the high frequency content of forcing functions is normally neglected in the design process. This analysis demonstrates that this process would result in erroneous results if applied to high work turbine configurations. The high frequency content has significant amplitude, and could significantly contribute to rotor forcing.

Other flow field differences between the reactions include the size of the separation generated by the supercritical SBLI on the nozzle and rotor and the size of the convecting nozzle separation, generated from the RRS impingement. For λ=28-31% the RRS is of sufficient strength to generate a significant sized convecting nozzle separation, for λ=41% the separation is considerably smaller. Although in practise it is unlikely that any supercritical SBLI would be tolerated in a HP turbine stage. Modern HP turbines operate at the extremity of the material temperature limits. The blades are designed to avoid any separations, such as supercritical SBLI, that would result in excessive temperatures and blade failure.

These flow field changes significantly affect the unsteady forces. Reducing the reaction from 41 to 28% increases the axial force at the BPF by more than 34%. For the low reaction cases (λ=28 and 31%) there are more numerous shock reflections between the blade rows and most significantly across the rotor passage. This is an important conclusion because the shock forcing function becomes a more significant for the lower reaction cases, primarily due to impinging nozzle shocks and rotor passage shock reflections.

The most important conclusion from this study involves the frequency content of the shock forcing function. Reducing reaction increases the shock strength and results in more numerous shock reflections. Phase alignment occurs between the reflecting shocks impingement on the rotor crown, resulting in significant increases in tangential forces, specifically at higher harmonics. Axial forces and moments also have significantly higher harmonic content.

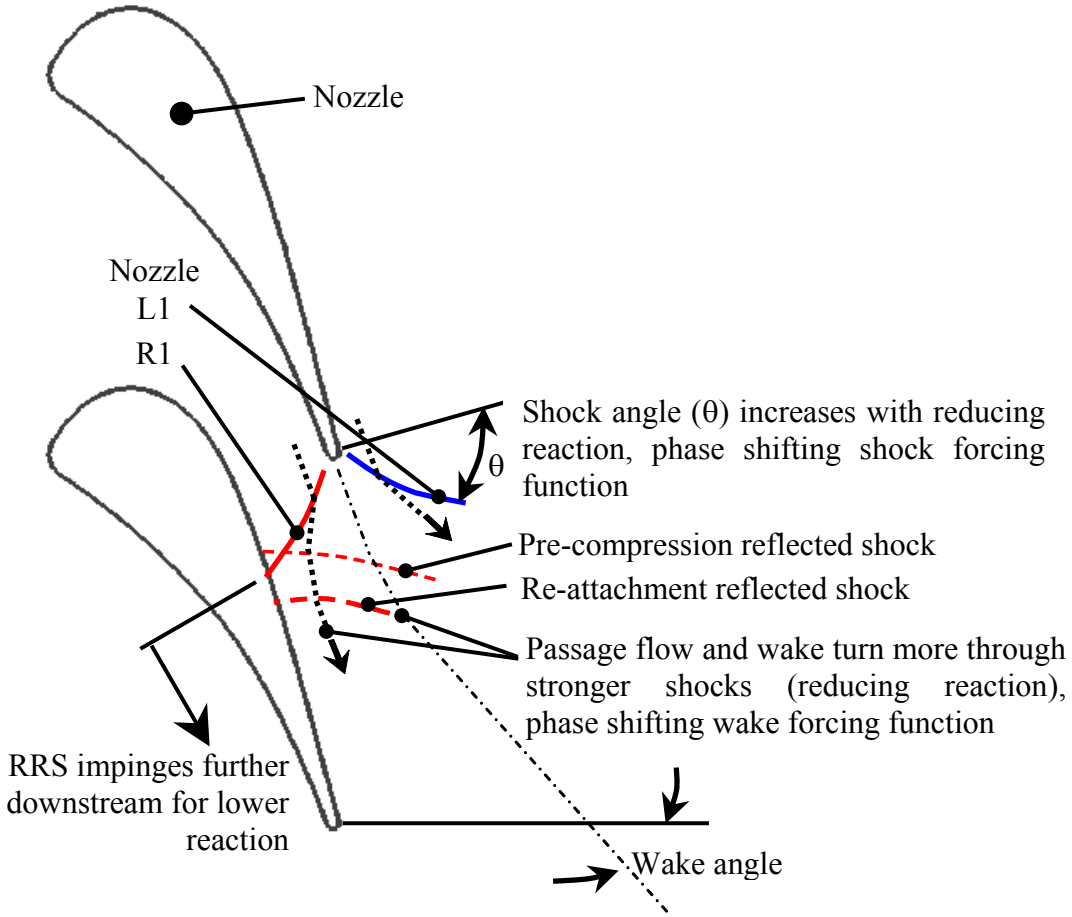

Figure 113 Swirl angle change through nozzle shock system

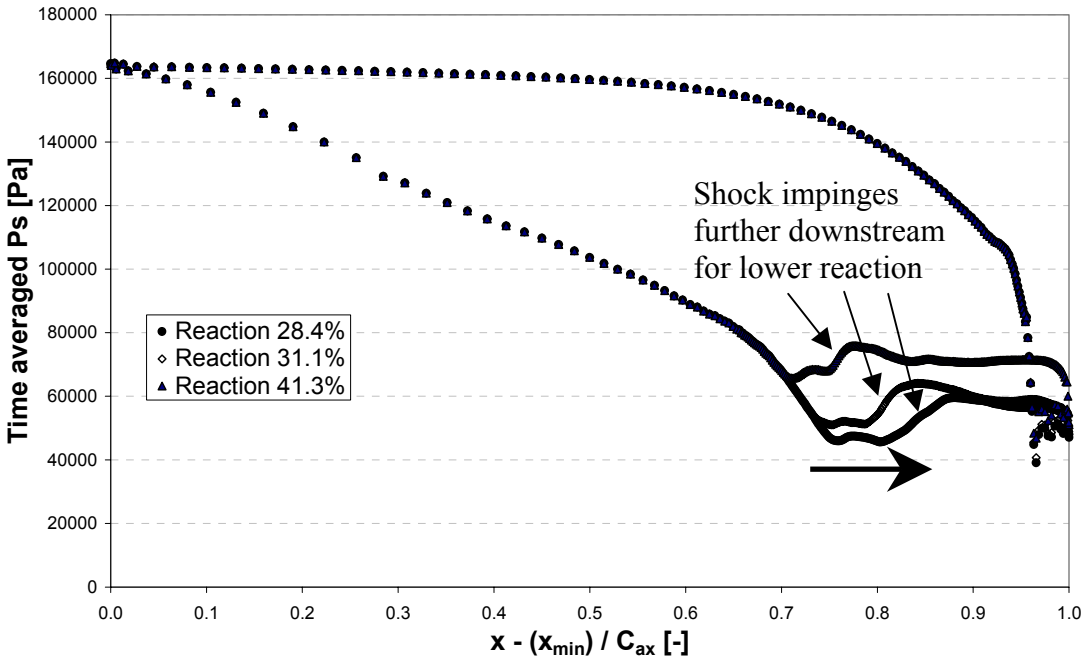

Figure 114 Time averaged, nozzle static pressure distribution

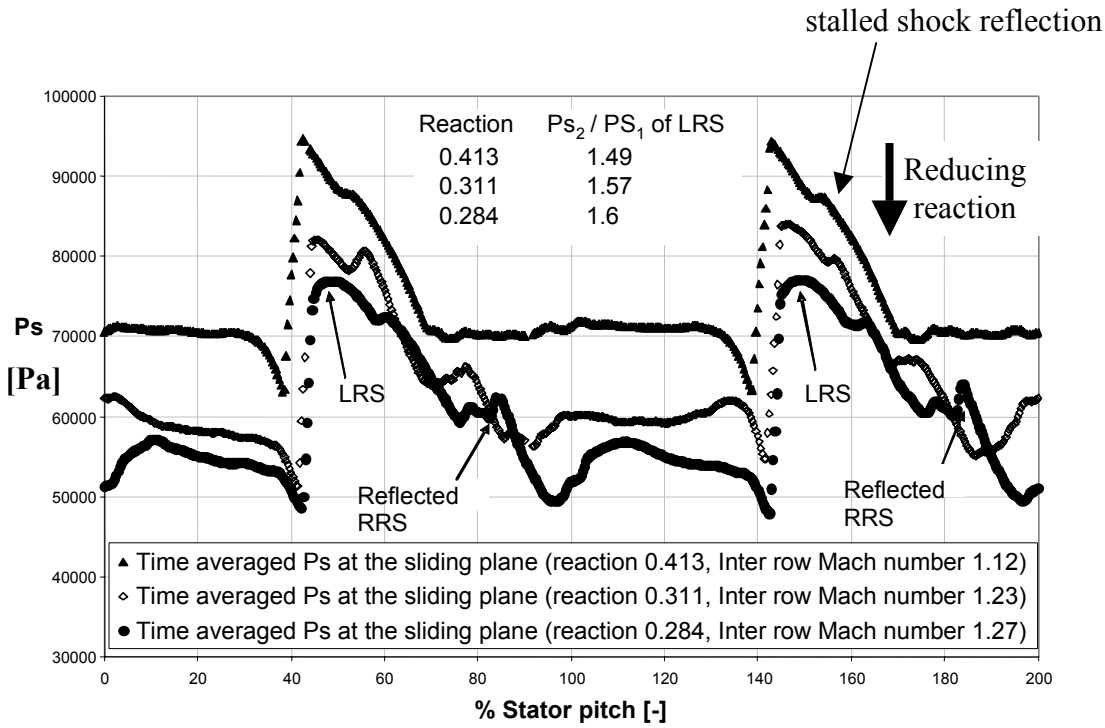

Figure 115 Time averaged static pressure at the nozzle domain exit (sliding plane) for reaction 41.3, 31.1 and 28.4%.

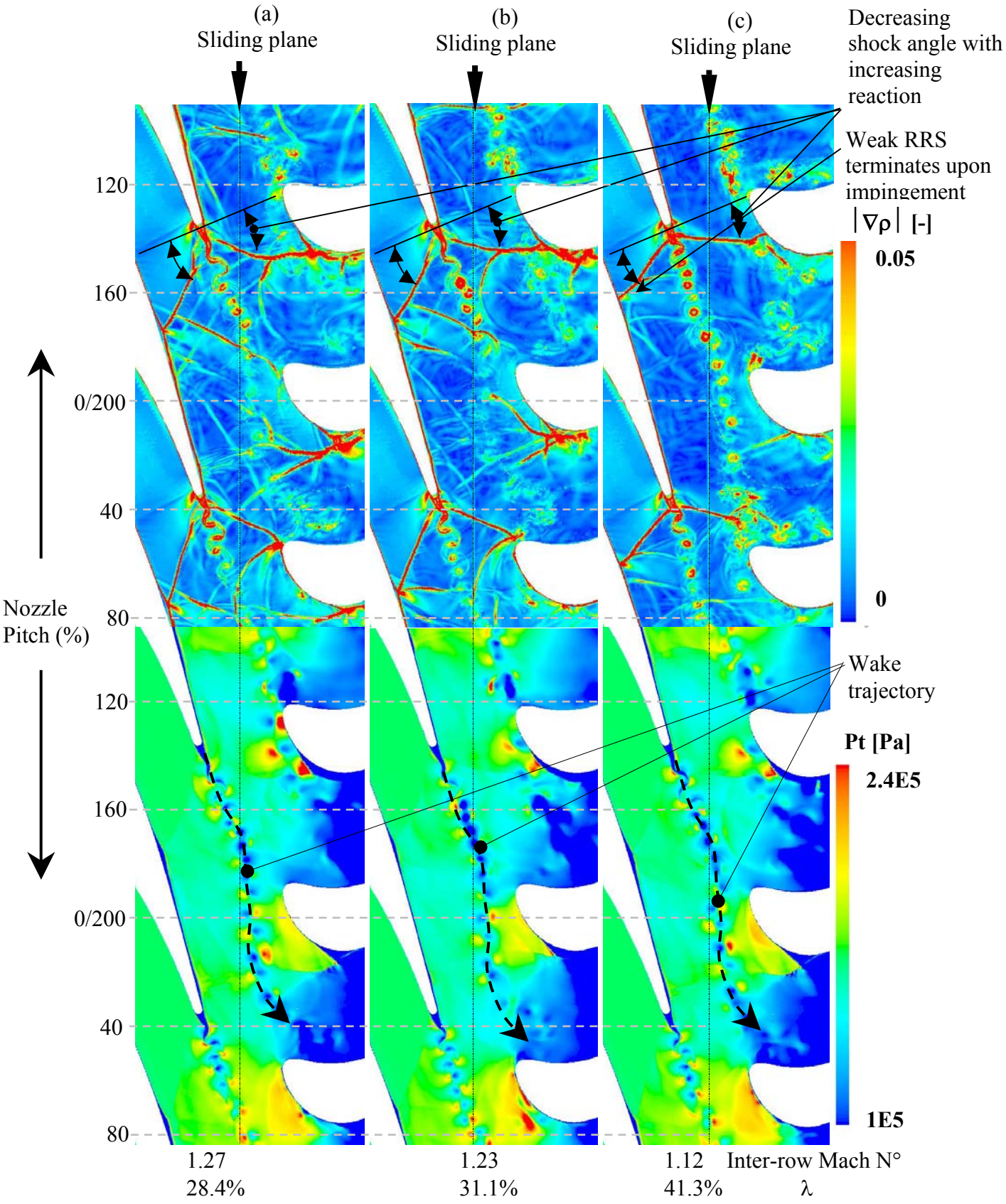

Figure 116 contours of $|\nabla\rho|$ (top) and absolute P_t (bottom) at Φ=0

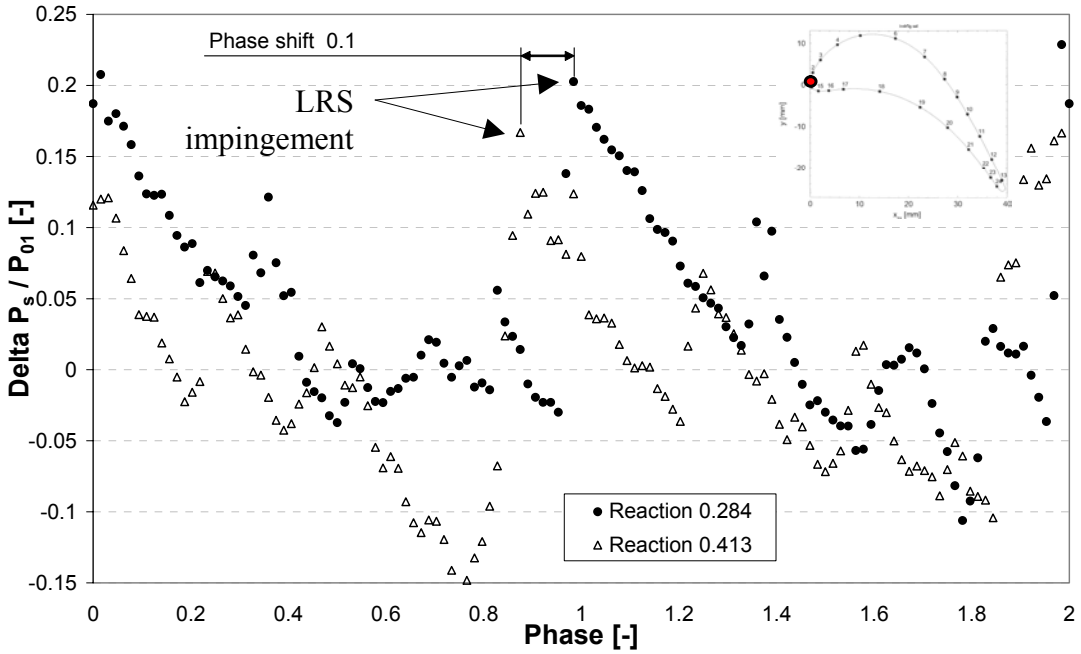

Figure 117 Comparison of pressure trace at rotor LE

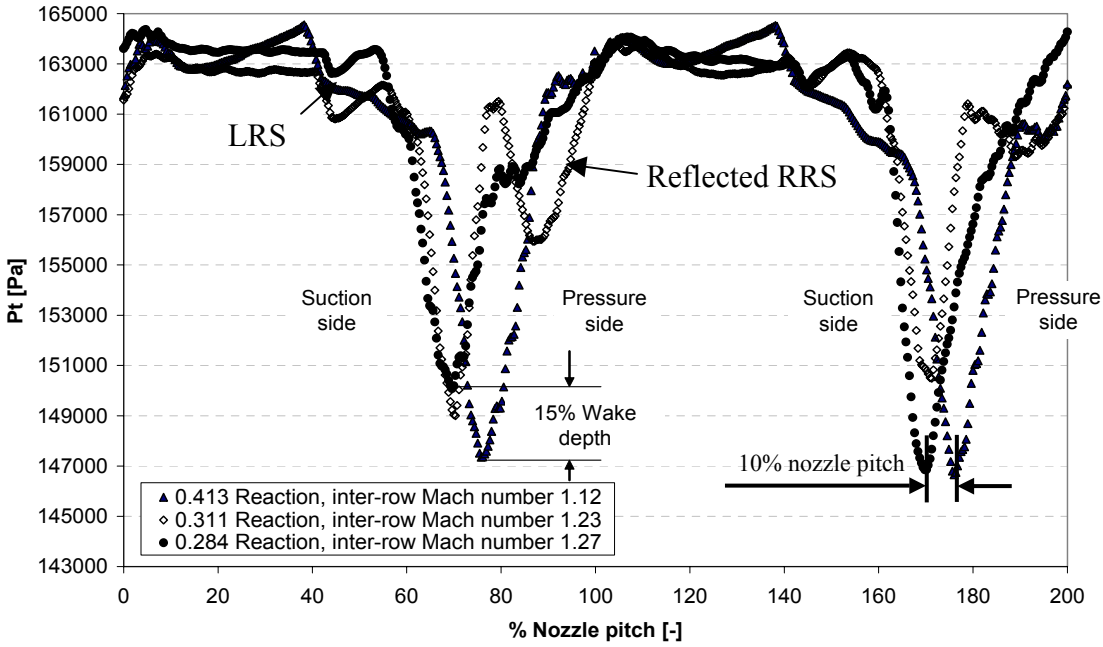

Figure 118 Time averaged total pressure at the nozzle domain exit (sliding plane) for reaction 41.3, 31.1 and 28.4%.

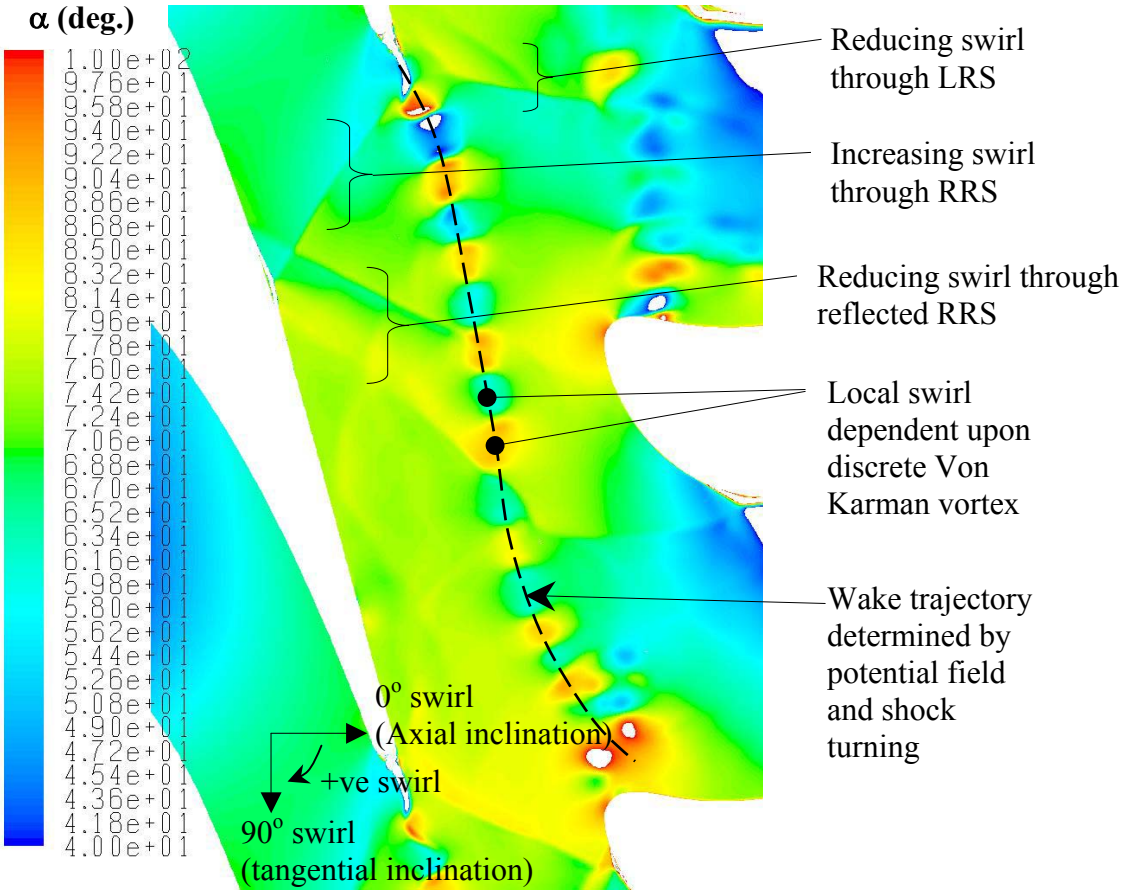

Figure 119 Contours of absolute swirl angle (α) [degrees] at Φ=0 for reaction case 31.1%.

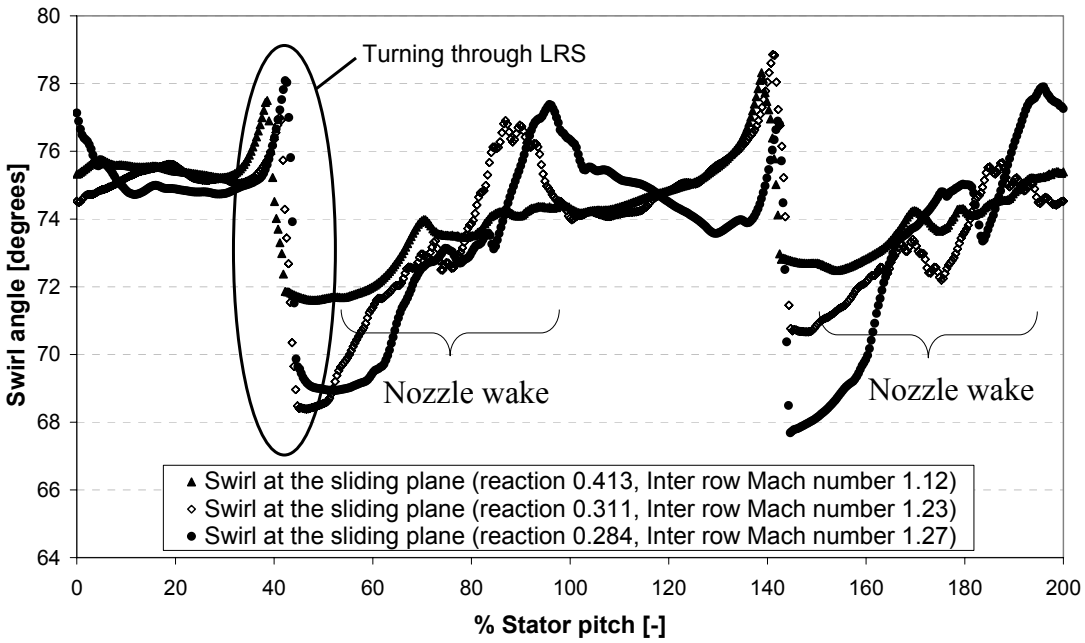

Figure 120 Time averaged absolute swirl at the nozzle domain exit (sliding plane) for reaction 41.3, 31.1 and 28.4%.

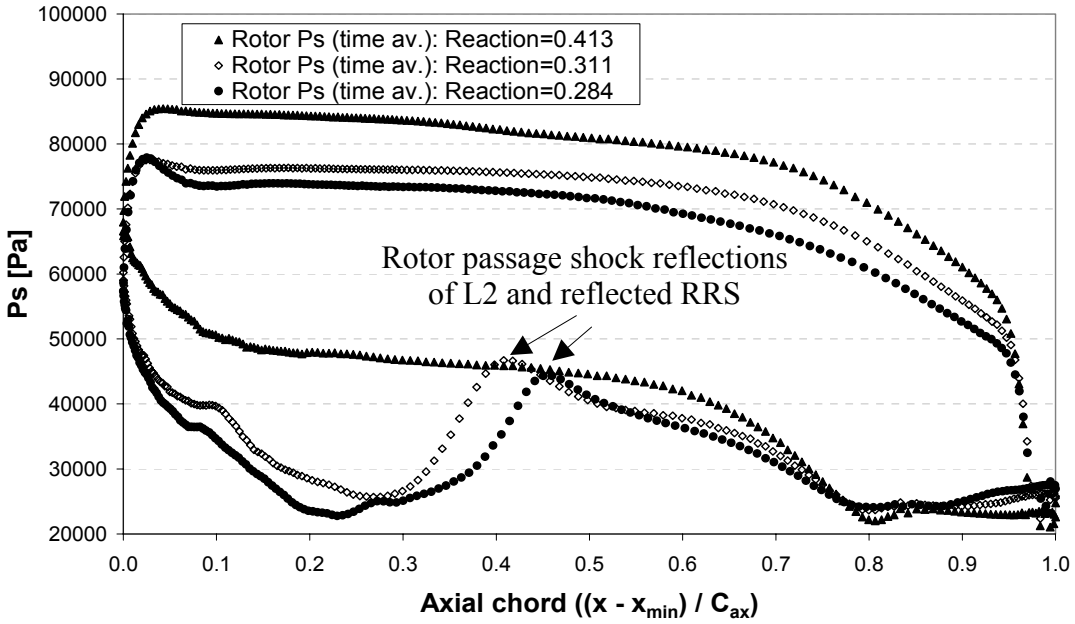

Figure 121 Comparison of time averaged rotor static pressure profile, including local maxim between 0.4 and 0.45 axial chord between λ=0.284 and 0.311 from rotor passage shock reflections

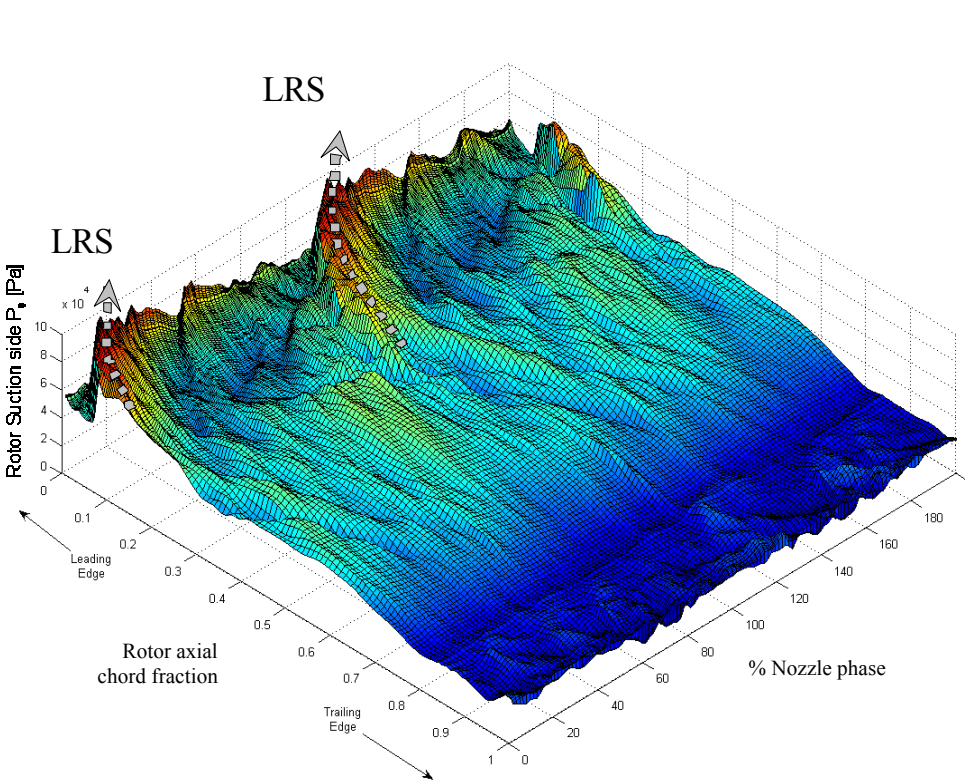

Reaction 0.413

Inter-row Mach number 1.12

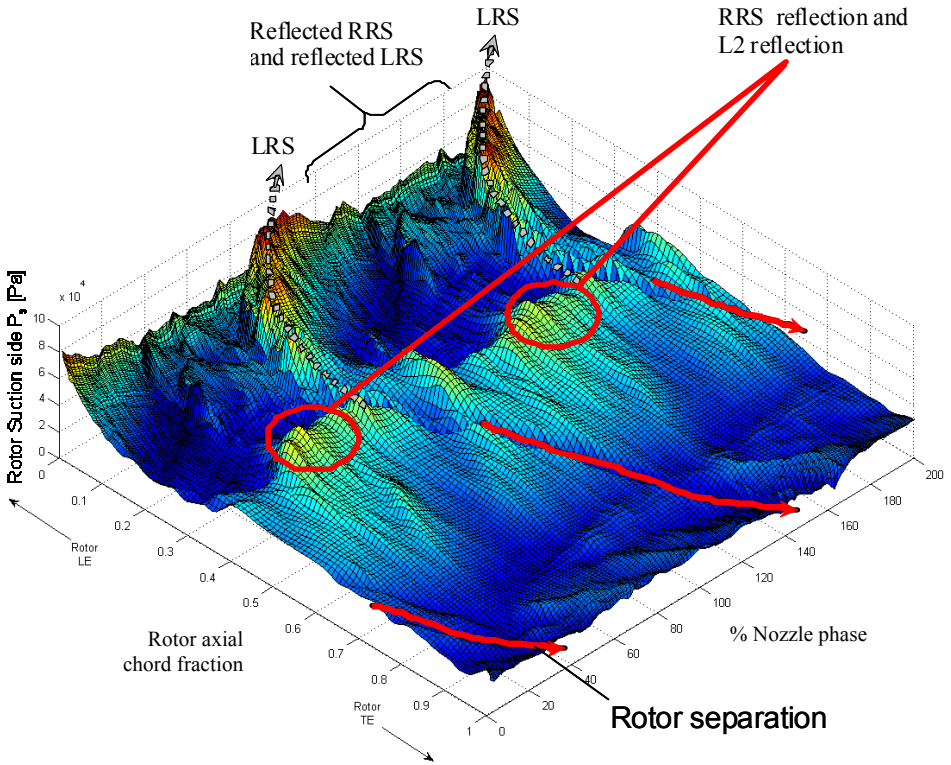

Reaction 0.311

Inter-row Mach number 1.23

Figure 122 Rotor suction surface static pressure development. High reaction case includes negligible shock reflections onto rotor crown

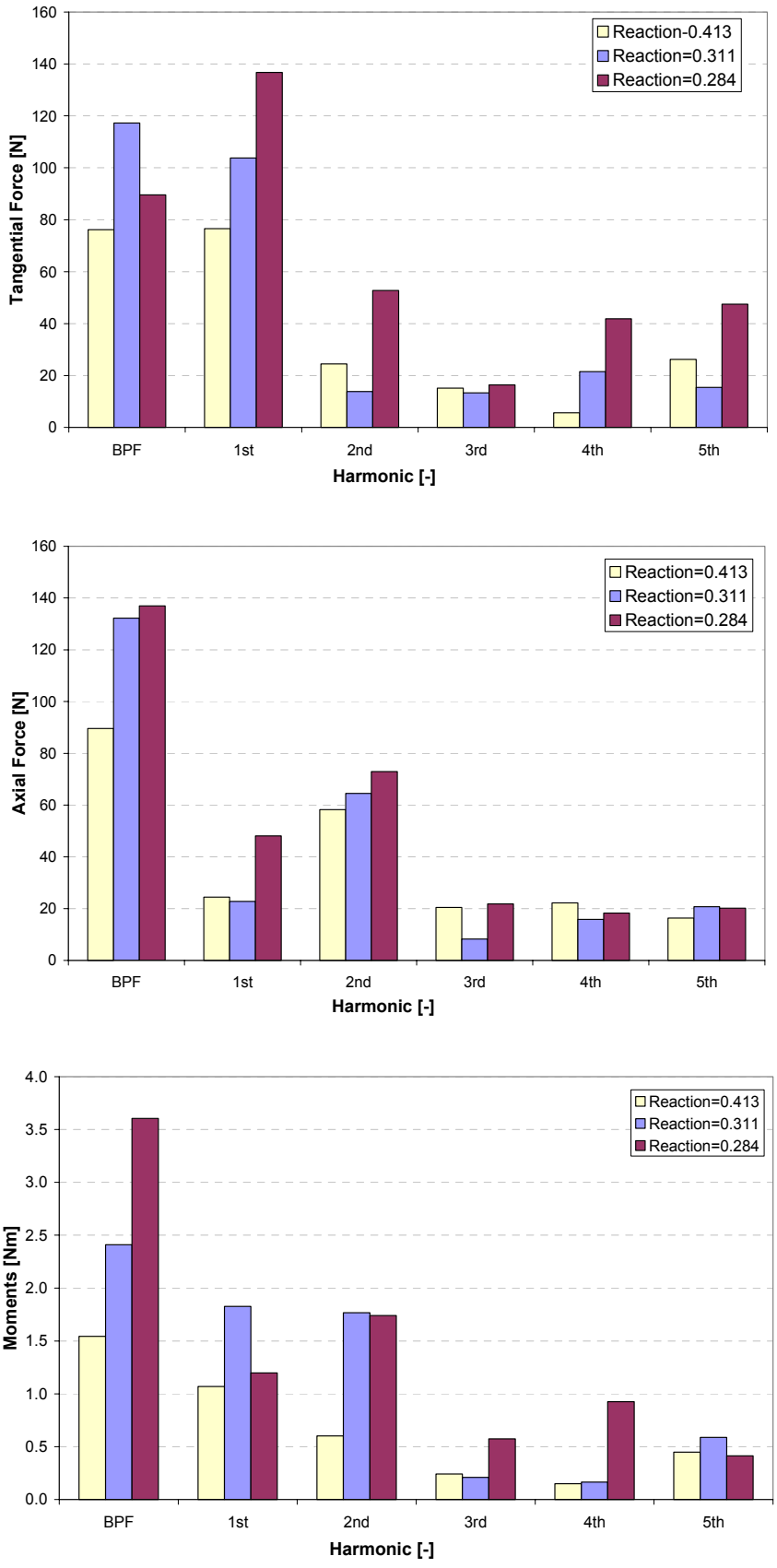

Figure 123 Harmonic distribution of unsteady tangential force (top) axial force (middle) and pitching moment (bottom) for various pressure ratios

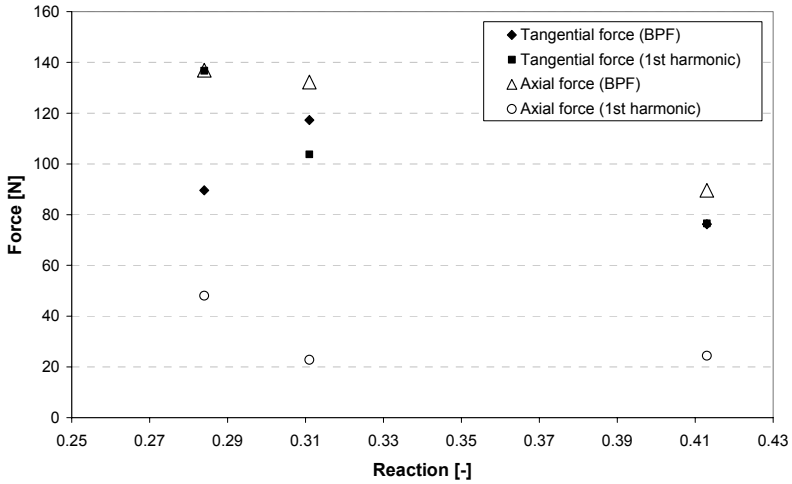

Figure 124 Net Axial and tangential force for multiple harmonics

Reaction [%]	28.4	31.1	41.3
Rotor skew [deg.]	2 (open)	0.5 (open)	2 (closed)
Tangential force (BPF) [N]	90	117	76
Tangential force (1st harmoinc) [N]	137	104	77
Axial force (BPF) [N]	137	132	90
Axial force (1st harmonic) [N]	48	23	24
Pitching moment (BPF) [Nm]	3.6	2.4	1.5
Pitching moment (1st harmonic) [Nm]	1.2	1.8	1.1

Table 23 Summary of the effect of reaction on the unsteady rotor forces and pitching moments.

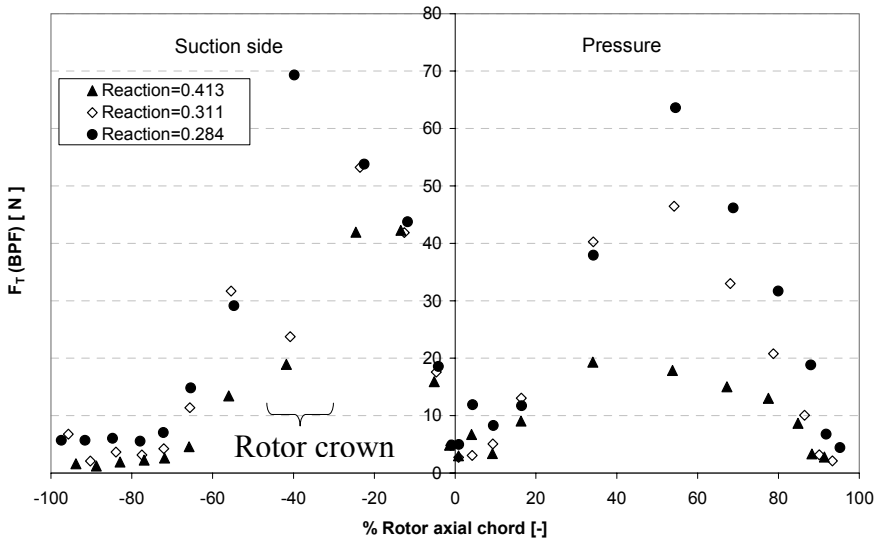

Figure 125 Effect of reaction on the rotor unsteady tangential force (BPF)

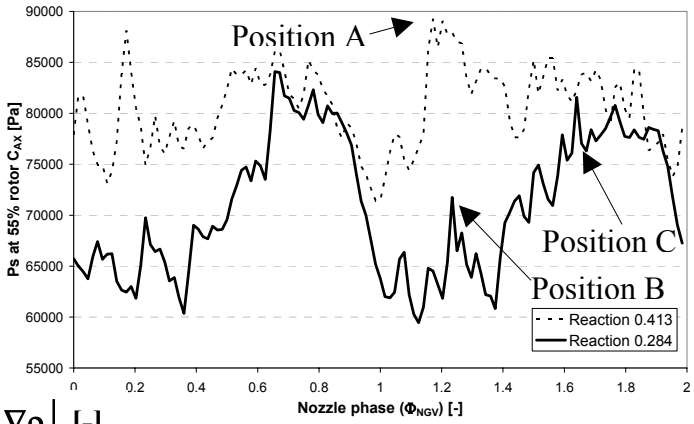

Position A: Pressure rise generated by impinging LRS

Position B: Pressure rise generated by impinging LRS

Position C: Pressure rise generated by rotor passage shock reflections (in phase with wake)

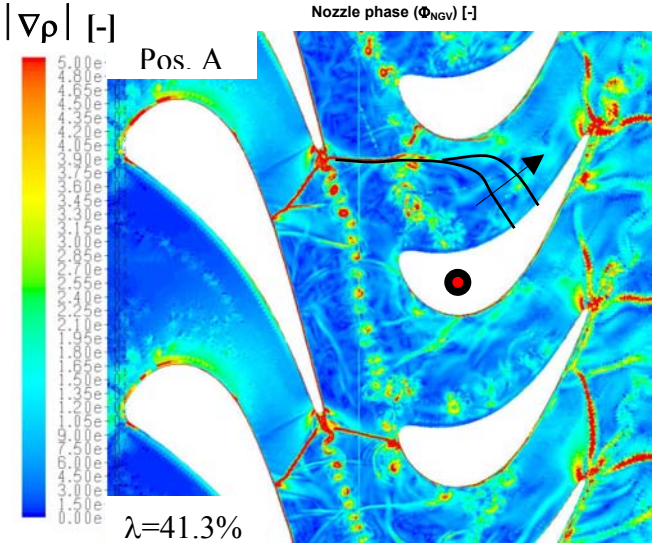

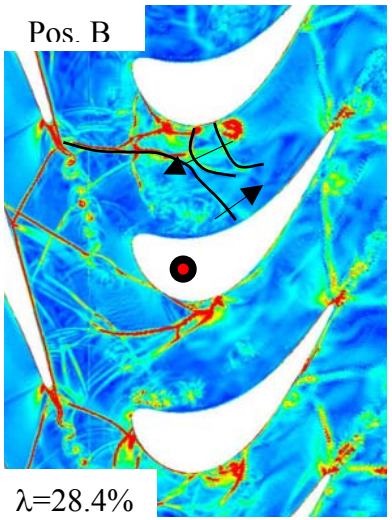

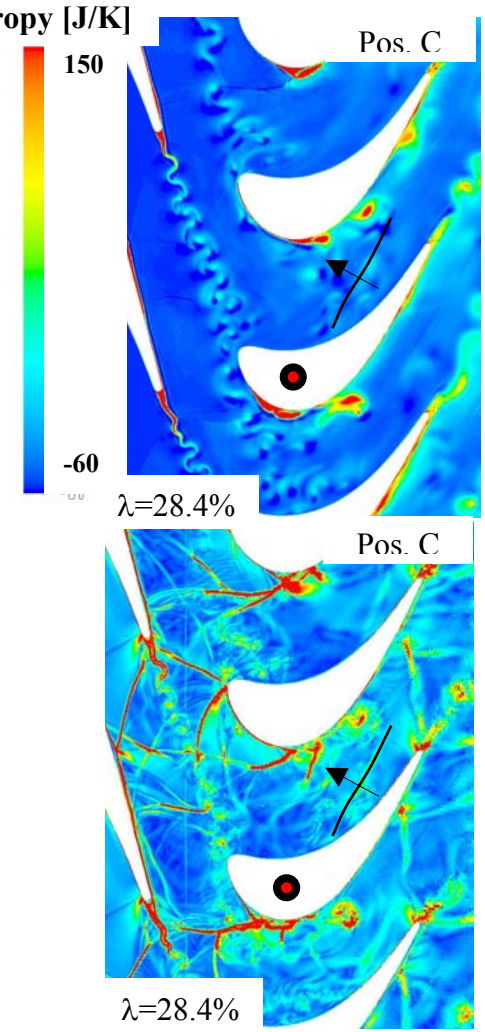

Figure 126 Pressure trace comparison at 55% axial chord on the pressure side and supporting contour plots of $|\nabla\rho|$ and entropy. Black lines indicate shocks

8.4 Effect of axial spacing

To reduce materials, cost and weight, current engine practise is to minimize the axial spacing between the nozzle TE and the rotor LE (the inter-row gap, x_g), normally expressed as a fraction of the nozzle axial chord (C_{NGV}) (x_g/C_{NGV}). This requirement conflicts with the requirement to minimize each primary rotor forcing function such as the potential field, nozzle wake and shocks. To different degrees, each forcing function increases in amplitude as the inter-row gap decreases. However the situation is further complicated by the relative phase alignment of each forcing function. As the disturbances become phase aligned, constructive interference generates higher unsteady rotor forces and pitching moments. As the inter-row gap decreases the wake and shock phase shift at different rates due to the wake convecting at an oblique angle from the nozzle TE at less than the free stream velocity, whilst the L1 shock propagates at a near axial inclination (Figure 127). Additionally the flow approaching the rotor is influenced by the axial spacing which can modify the unsteady aerodynamics including rotor passage shock reflections, which can ultimately change the unsteady force distributions around the rotor.

8.4.1 Wake features

For **conventional** turbines the two most prominent forcing functions are the nozzle viscous wake and potential flow field, both of which are sensitive to axial spacing. Blade wakes decay much more gradually than the potential flow field, they may still be measured several chords downstream of their origin, considerably beyond the typical inter-row gap (20-50% of the nozzle axial chord (Figure 128) {6 Parker, R. 1972}.

As the wake develops across the inter-row gap it broadens and reduces in depth, due to turbulent mixing that is generated by strong velocity gradients between the wake and free stream (Figure 129). Initially the velocity deficit within the nozzle TE wake is wider than the nozzle TE diameter; due to boundary layer development along the nozzle pressure and suction side. As the wake convects from the nozzle TE it broadens and the spatial harmonic content reduces. If the rotor is positioned too close to the nozzle, the limited mixing that occurs in the small inter-row gap results in a thin, deep total pressure profile which impinges onto the rotor with high harmonic content.

The primary forcing mechanism of the wake is the momentum deficit, however another more subtle forcing aspect includes the ‘negative jet’ affect {4 Giles, M. 1988}. The wake reduces the relative flow angle onto the rotor, resulting in negative incidence at the leading edge which also alters the rotor lift as it convects through the rotor passage.

8.4.2 Potential field features

As the inter-row gap reduces the nozzle potential field becomes a more significant forcing function. If the inter-row gap is small enough another aspect of the potential field includes nozzle and rotor potential field interactions. For **conventional** turbines {Fincher, 1966} and {Doak and Vaidya, 1969} suggest that the potential flow interaction becomes insignificant in comparison with the wake interaction above an inter-row spacing of approximately 30% of the blade chord. This analysis was later

improved to define this axial-spacing distance as a function of inter-row Mach number ($D=30/\sqrt{(1-M^2)}$), where D is the distance that the potential flow interaction becomes insignificant, as a percent of the blade pitch {Parker, 1969-70}. However this analysis is inappropriate for high work turbines where the potential field is relatively strong due to the high Mach numbers and shocks reflections across nozzle and rotor passages and across the inter-row gap.

8.4.3 Shock features

This study investigates a highly loaded turbine stage, which includes nozzle and rotor TE shocks. The high adverse pressure gradients across the shocks are a significant forcing function, which propagate distances considerably in excess of the wake. For a prescribed nozzle and rotor geometry at a given operating point in the supersonic regime the modulation of the nozzle TE shocks is a function of the axial spacing, primarily a consequence of the rotor potential field, inter-row shocks and a convergent divergent duct formed between the nozzle and rotor (see chapter 3).

8.4.4 Modelled Inter-row gaps

Numerous studies have demonstrated that shocks dissipate through boundary layers (e.g. { Delery, J. M. 1985}). What is less researched is the effect of shock dissipation and diffraction through a wake in which the initial subsonic low velocity central core develops into a supersonic wake. This research is relevant to supersonic turbines where shocks and shock reflections propagate through the nozzle wakes. Any diffraction or dissipation which occurs during the propagation will act as an aerodynamic damping process to the shock forcing function.

This study investigates three inter-row gaps that are typical of the ranges applied by designers (Figure 128 and Table 24). The rationale behind the configurations considered was for the strongest shock that impinges onto the rotor (LRS, L1) to lag the adjacent nozzles wake impingement onto the rotor LE (case Ax5C), to impinge onto the rotor LE at the same phase as the adjacent nozzles wake (Ax0, the datum case) and to lead the adjacent nozzles wake impingement onto the rotor LE (Ax5A) (Figure 127).

Case	Pressure ratio (P_{01}/P_{03})	Stage loading ($\Delta H/U^2_{50\%}$)	Specific work ($\Delta H/T_{01}$)	Non-dim. speed ($U_{50\%}/\sqrt{T_{01}}$)	Flow co-efficient ($V_A/U_{50\%}$)	Efficiency (η) (ideal expansion)	Reaction (λ)	x_g/C_{NGV}
Ax5C	3.85	2.1	305	12	0.49	0.92	0.33	0.27
Ax0	3.85	2.1	303	12	0.49	0.9	0.31	0.39
Ax5A	3.85	2.1	306	12	0.49	0.91	0.32	0.52

Table 24 Axial spacing study characteristics

There are considerable differences between how the TE and forward reflecting shocks propagate through the nozzle wake for the cases considered. As the wake develops the intensity of the velocity deficit in the central core reduces and the wake broadens. When shocks propagate through the wake before it has significantly developed the central core will be subsonic, specifically within each discrete Von Karman vortex. The shocks cannot exist in subsonic flow and can only diffract through the wake between each vortex where the flow is supersonic (section 8.2). When the rotor is further downstream the TE and reflected shocks propagate through larger proportions of the supersonic portion of the wake. This results in reducing the diffraction and dissipation of the shock (Figure 130). The primary affect of inter-row gap spacing for

the configurations considered is phase alignment of the wake and shock forcing functions, which is described in detailed below.

8.4.4.1 Shock diffraction and dissipation

8.4.4.1.1 Shock diffraction

There are considerable differences between how the shocks and reflected shocks propagate through the nozzle wake. The forward propagating reflected shocks diffract substantially through the Von Karman vortex street of the nozzle wake into discrete elements before impinging onto the nozzle SS (Figure 131). The nozzle TE LRS propagates through the wake with no discernable diffraction occurring (Figure 130). The extent that the shocks diffract through the nozzle wakes is a partial function of the impingement angle and the relative position of the discrete Von Karman vortices. The relatively weak reflected shocks diffract through nearly the entire nozzle wake, up to the adjacent rotors LE. The only portion of the wake the forward propagating reflected shocks do not propagate through is just downstream of the nozzle TE, between the wake and L1 shock were the forward propagating reflected shock stalls due to its tangential alignment to the upstream sonic flow. The diffraction through the wake takes place across a range of angles and wake Mach number profiles as the low velocity central core of the wake increases in velocity as it convects. The forward propagating shock propagates through the majority of the wake almost tangentially inclined to the wake which consequentially highly diffracts (Figure 131).

The LRS propagates through the nozzle wake at a relatively high impingement angle approximately one nozzle chord downstream of the wake origin where the low velocity central core of the wake is supersonic. The result is the LRS does not significantly diffract through the nozzle wake (Figure 130). The conclusion is that shock diffraction through supersonic nozzle wakes is a relatively insignificant flow phenomenon when considering rotor forcing.

8.4.4.1.2 Shock dissipation

The subsonic regions of the wake will dissipate the shocks (Figure 132). However the LRS propagates through the downstream supersonic portion of the wake, resulting in no significant dissipation (Figure 133). However large portions of the inter-row reflecting shocks do propagate through the nozzle wake in the subsonic region, dissipating in the process, although this is thought to have a relatively minor effect on rotor forcing. The result is that shock dissipation through nozzle wakes is a secondary effect when considering rotor forcing.

8.4.5 Rotor characteristics

8.4.5.1 Steady features

The axial spacing of the rotor has little impact on the rotor time-averaged pressures (Figure 134). The biggest difference occurs on the rotor suction side in the rotor crown region ($0.35C_{rot}$ - $0.45C_{rot}$) which is highly sensitive to rotor passage shock reflections. This is a simple indication that the relative phasing of the forcing functions are important and is explored in more detail below.

8.4.5.2 Unsteady rotor features

8.4.5.2.1 Blade forces and pitching moments

The anticipation is for higher forces and pitching moments to be generated at all harmonics as the inter-row gap reduces, however the results are varied (Figure 135). The trends are also presented as a function of inter-row gap in Figure 136 and summarised in Table 25.

As anticipated, generally the tangential force reduces as the inter-row gap increases for the lower harmonics. The relatively high tangential force at the 1st harmonic, for all of the considered configurations, is an indication that the previously detailed rotor passage shock reflections (see section 8.2) are insensitive to axial spacing. This is an indication that the shock does not significantly dissipate through the nozzle wake for the considered axial spacing configurations.

The relatively low axial forces at harmonics above the BPF is an indication that the axial force is relatively insensitive to shock reflections across the inter-row gap. In conclusion increasing the axial gap is a verified method of reducing the axial and tangential forces, specifically at the lower harmonics, although careful consideration needs to be given to the relative phasing of each forcing function to avoid phase alignment. A more detailed evaluation of where the forces are occurring along the rotor chord is included with accompanying plots of the shock and wake flow features, which are used to explain how the complex results are a consequence of forcing function phase alignment.

8.4.5.2.2 Harmonic distribution

To better understand the forcing a more detailed examination of the harmonic distribution of forces and pitching moments around the rotor blade is necessary. An examination of the tangential forces at the BPF shows the most sensitive regions to axial spacing are $0.13\text{-}0.55C_{rot}$ on the suction side and $0.34\text{-}0.79C_{rot}$ on the pressure side (Figure 137). Generally the forces reduce with increasing inter-row gap, with the exception at $0.13C_{rot}$ and $0.55C_{rot}$ on the suction side and $0.34C_{rot}$ on the pressure side. At $0.55C_{rot}$ on the suction side the smallest inter-row gap delivers the lowest unsteady force. This region is just downstream of the rotor crown, where reflecting rotor passage shocks impinge and the wake migrates towards. These discrete regions are where forcing interference is significant, detailed below.

8.4.5.2.3 Forcing function phase alignment

To better understand how the wake and shock forcing functions interact an understanding of their relative positions is required between the smallest and largest inter-row gap. Snapshots of the flow field between NGV phases (Φ_{NGV}) 1 and 2 are included in Figure 138 and Figure 139 for $x_g/C_{NGV}=0.27$ and 0.52 respectively. For $x_g/C_{NGV}=0.27$ the wakes and shocks become phase aligned on the rotor pressure side between $0.5C_{rot} - 0.7C_{rot}$ between $\Phi_{NGV} = 1$ and 1.375. This phase alignment of the forcing functions coincides with the maximum differences between the tangential forces at the BPF for each inter-row gap (Figure 137). An examination of the flow field for $x_g/C_{NGV}=0.52$ shows the nozzle LRS is phase aligned with the diffused nozzle wake just downstream of the rotor LE on the suction side. At this coincident locus ($0.13C_{rot}$) the maximum inter-row gap ($x_g/C_{NGV}=0.52$) has the highest tangential

force at the BPF (Figure 137), due to the shock and wake phase alignment. The high BPF tangential force for x_g/C_{NGV}=0.52 at $0.55C_{rot}$ on the suction side is due to shocks reflecting in the rotor passage impinging onto the late rotor suction side at the same phase (Φ_{NGV}=1.625 to 1.75) as the convecting nozzle wakes (Figure 139). This phase alignment increases the unsteady tangential forces at the BPF by 25%

8.4.5.2.4 Rotor blade unsteady pressure

An example of the forcing function phase alignment detailed above includes a region at approximately $0.55C_{rot}$ on the pressure side where large unsteady tangential forces occur and large differences between the inter-row gaps considered exist (Figure 140). An examination of the full time pressure history in this region includes a considerable rise for the small inter-row gap (x_g/C_{NGV}=0.27) between Φ_{NGV} = 1.17 and 1.28, a consequence of the wake and shock becoming phase aligned. The smaller amplitude pressure rise for the large inter-row gap between Φ_{NGV} = 1.23 and 1.33 is purely a consequence of the shock impinging.

8.4.6 Summary of findings and design recommendations

The unsteady rotor forces generally reduce with increasing axial distance, however the relative phasing of each discrete forcing function can become phase aligned which leads to constructively interference. This can produce significant changes in the local unsteady forces on the rotor. For example, in some of these cases the local rotor forcing is doubled even though the axial gap is increased., The phase change of the shock is considerably less ($0.175\Phi_{NGV}$) than the wake ($0.75\Phi_{NGV}$) for the $\Delta 0.25x_g/C_{NGV}$ investigated. Clearly the relative differences mean the forcing functions will become phase aligned at a particular axial spacing.

Designers need to avoid forcing function phase alignment where ever possible by maximising the phase differences between each respective forcing function, especially towards the lower harmonics. In the event that phase alignment is unavoidable the designer should carry out an evaluation to ensure the resultant forces and pitching moments are not excessive.

A simple approach that the designer might apply to achieve this philosophy would be to generate a scaled drawing of the nozzle and rotor similar to Figure 127, by assuming the wake convects at the nozzle TE angle (assuming negligible wake turning through the reflected R1 shock and potential rotor field effects) and by applying oblique shock theory to determine the L1 shock propagation angle.

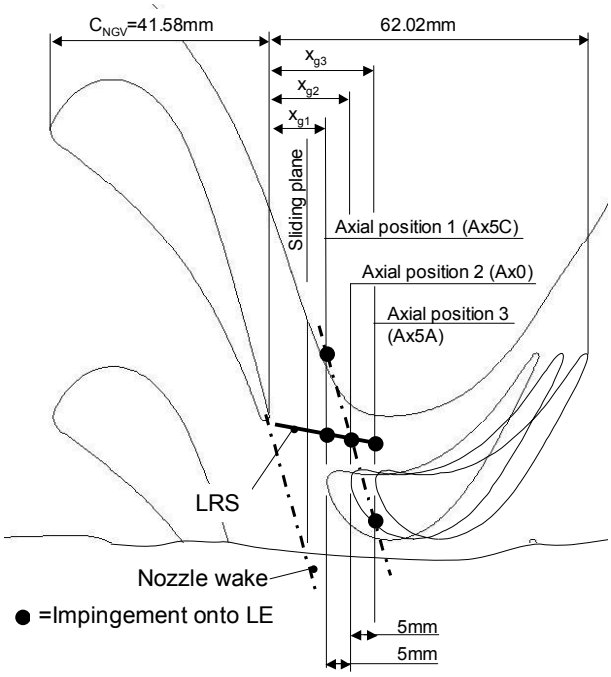

Axial position 1: Rotor LE passes through nozzle wake then LRS

Axial position 2: Axial location of LRS and wake interaction aligned with rotor LE.

Axial position 3: Rotor LE passes through LRS then nozzle wake

Figure 127 To scale diagram of L1 shock and nozzle wake impingement position on to the rotor LE for each of the three modelled inter-row gaps.

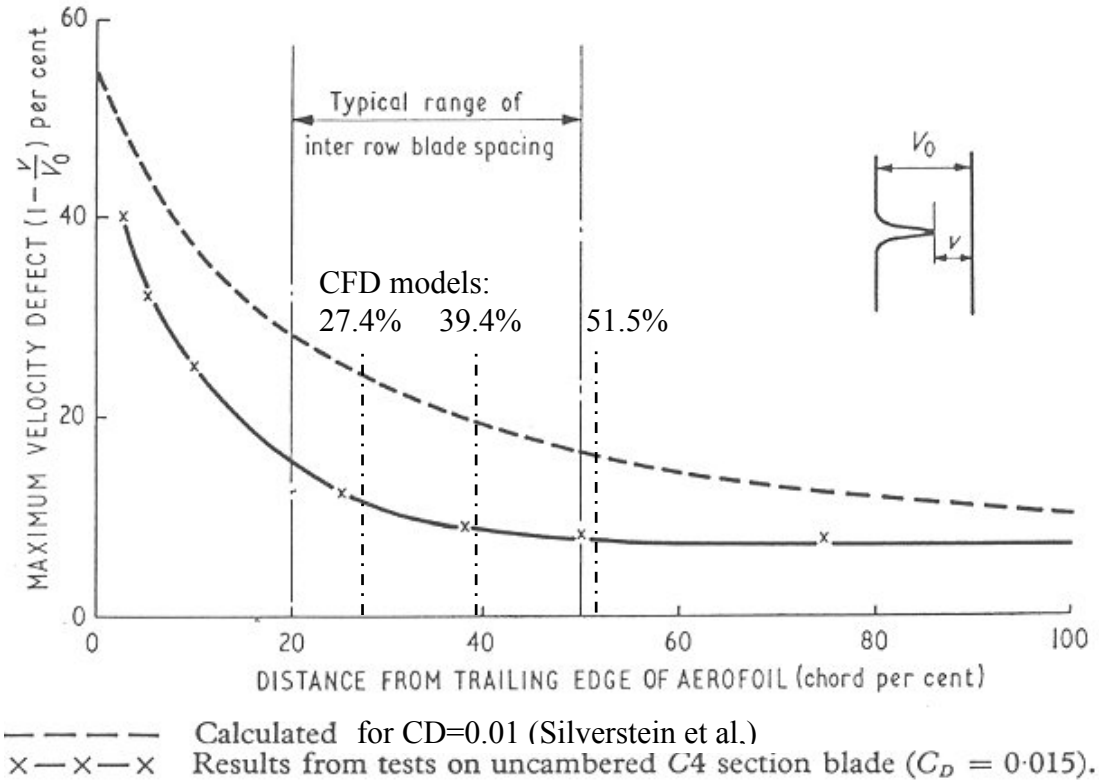

Figure 128 Variation of maximum velocity deficit in wake with distance from trailing edge of blade {Parker, R. 1972}

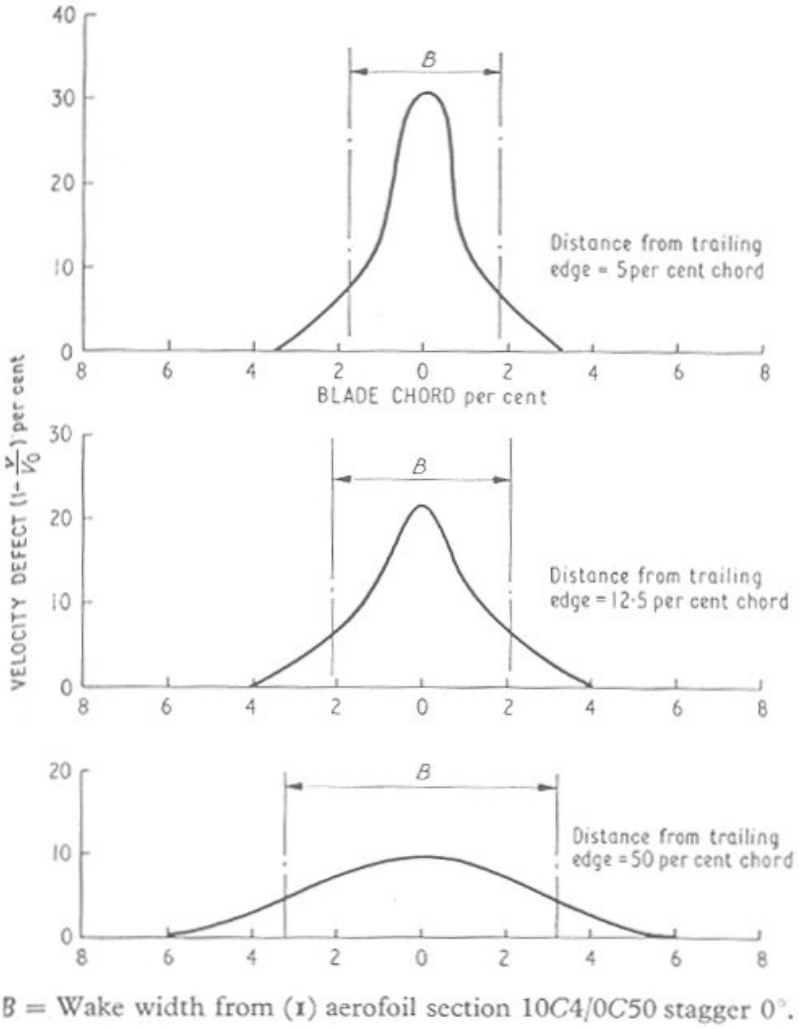

Figure 129 Variation of wake profile with distance downstream of aerofoil trailing edge {Parker, R. 1972}

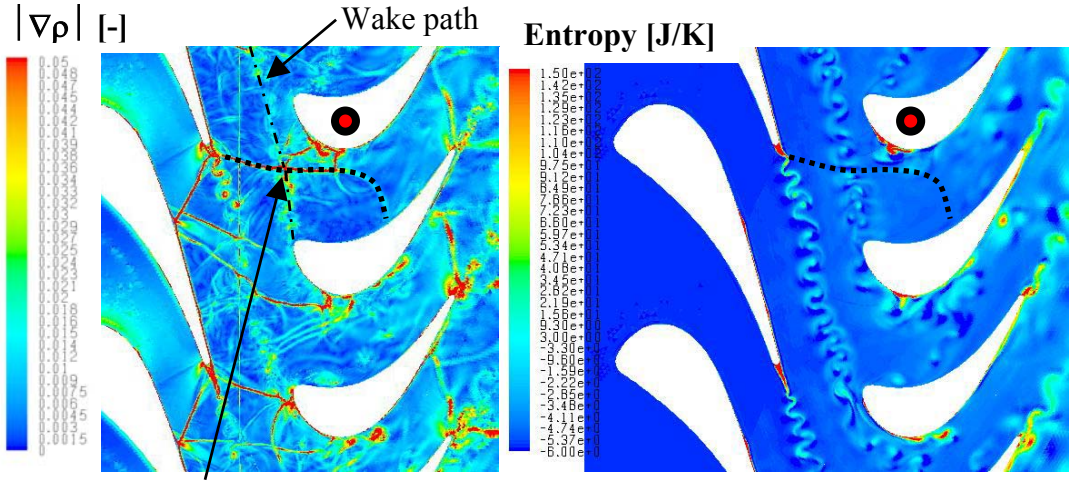

LRS shock does not diffract significantly through relatively developed (supersonic) nozzle wake at larger axial gaps

Figure 130 LRS propagates through nozzle wake with little diffraction: $|\nabla\rho|$ at Φ=0.6396 for x_g/C_{NGV}=0.52

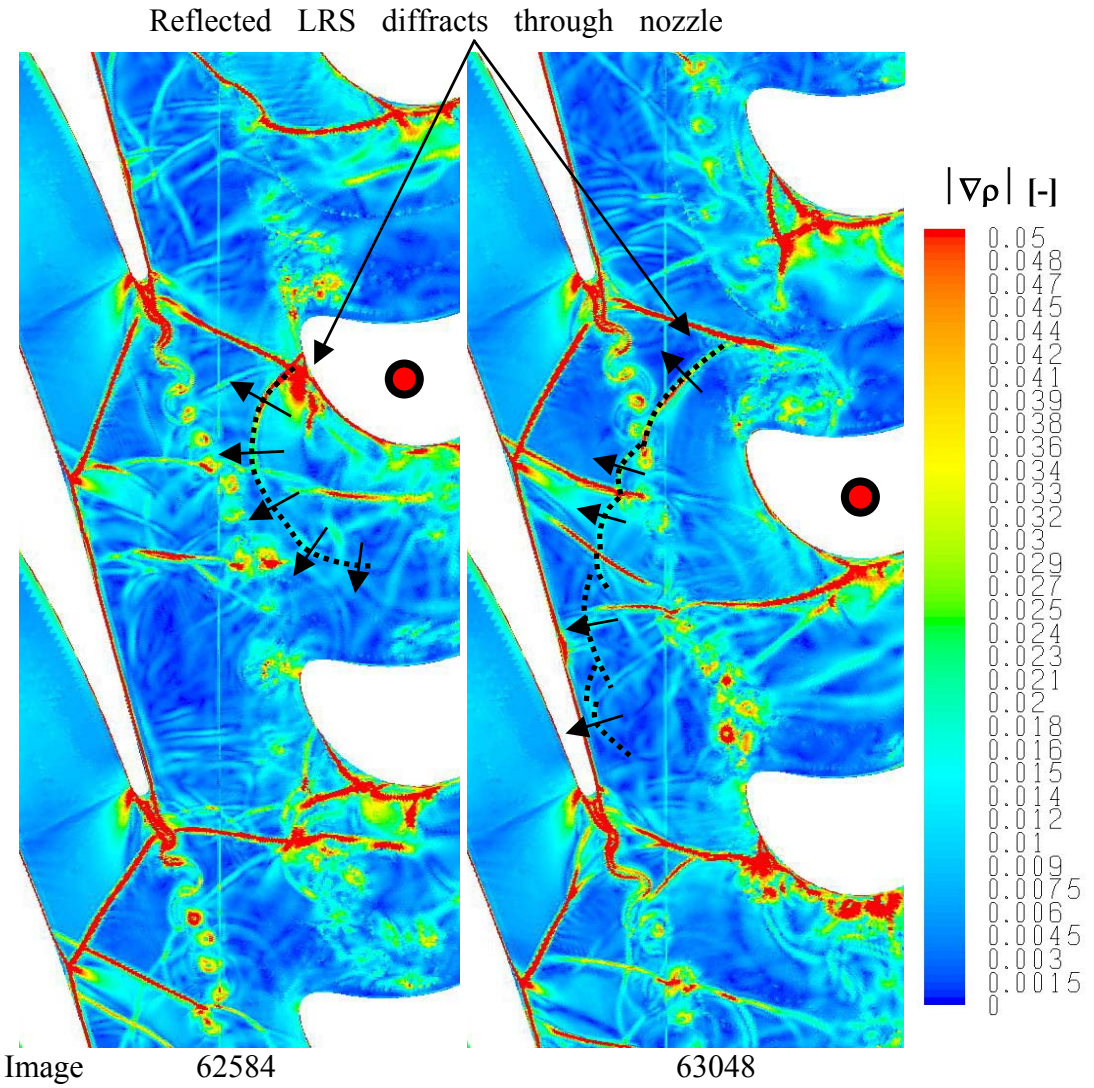

Figure 131 Upstream propagating diffracting shocks: $|\nabla\rho|$ at Φ=0.855 and 1.082 for x_g/C_{NGV}=0.39

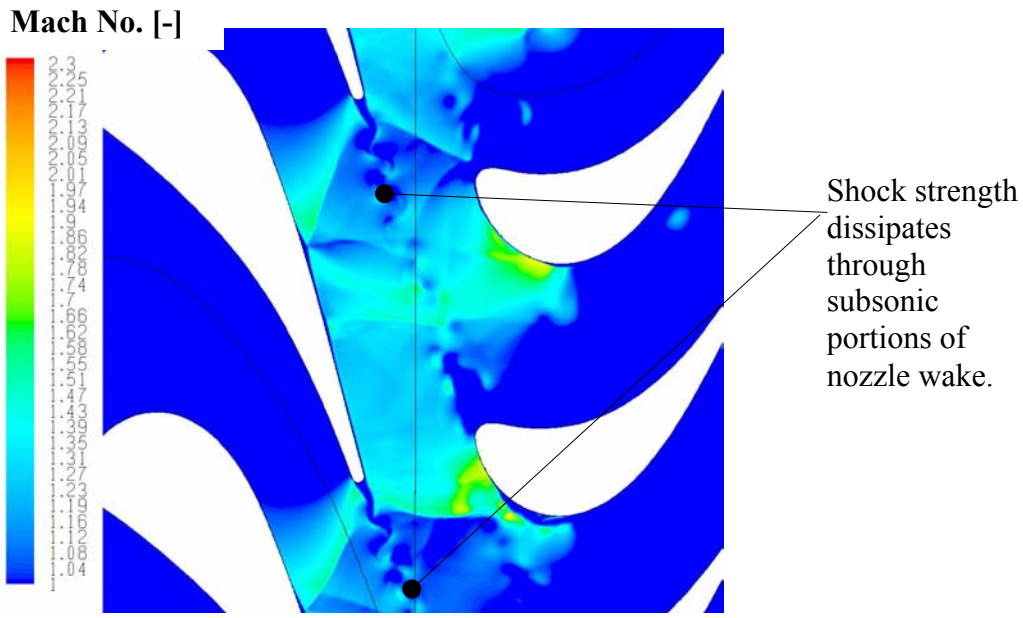

Figure 132 Absolute Mach number contour plots at Φ=0 for x_g/C_{NGV}=0.39 (unclipped contours)

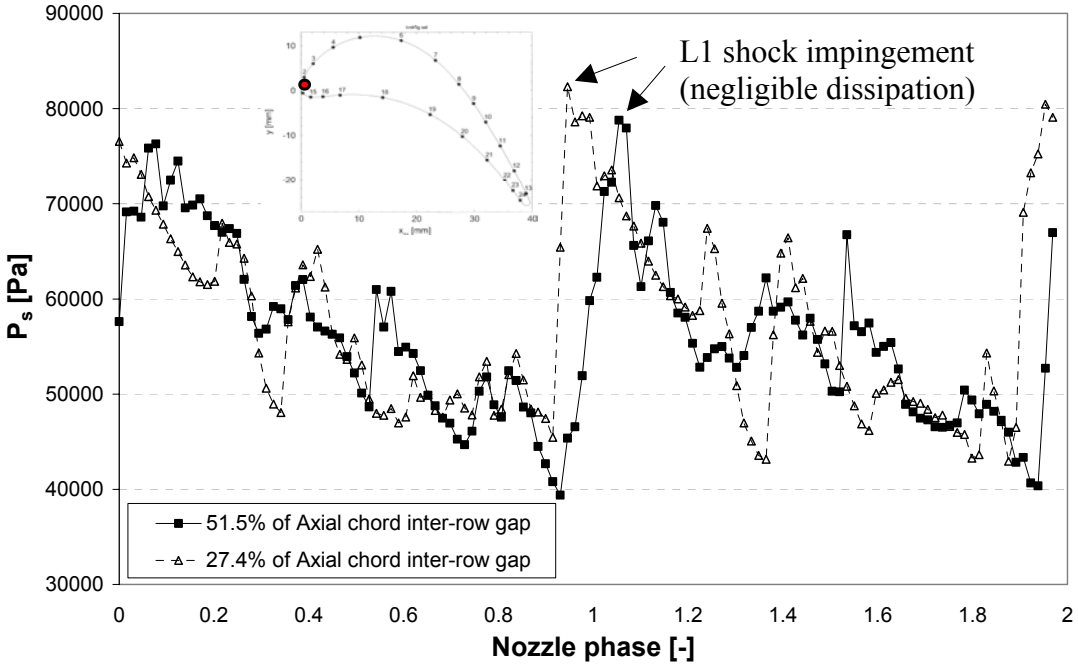

Figure 133 Pressure trace at rotor LE (insert included)

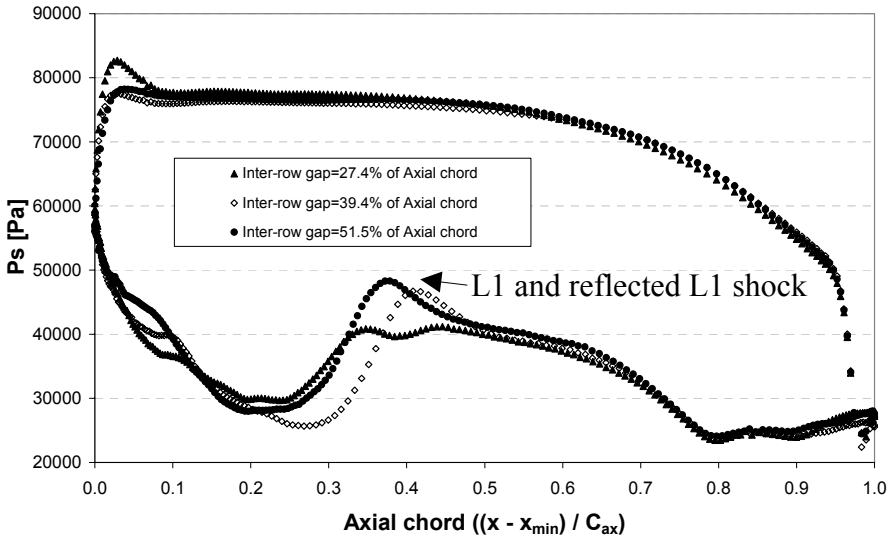

Figure 134 Time averaged rotor static pressure distribution.

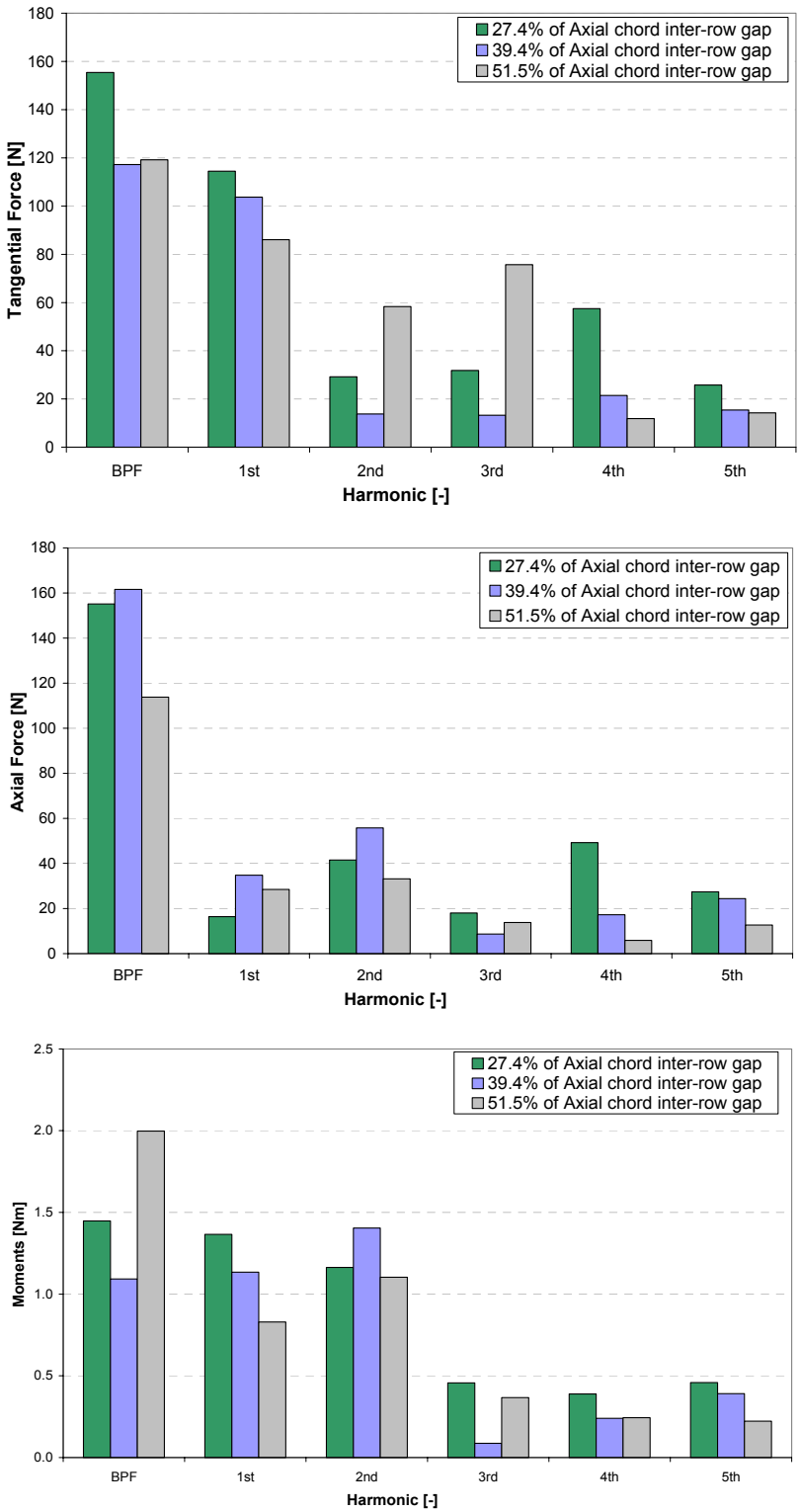

Figure 135 Harmonic distribution of unsteady tangential force (top) axial force (middle) and pitching moment (bottom)

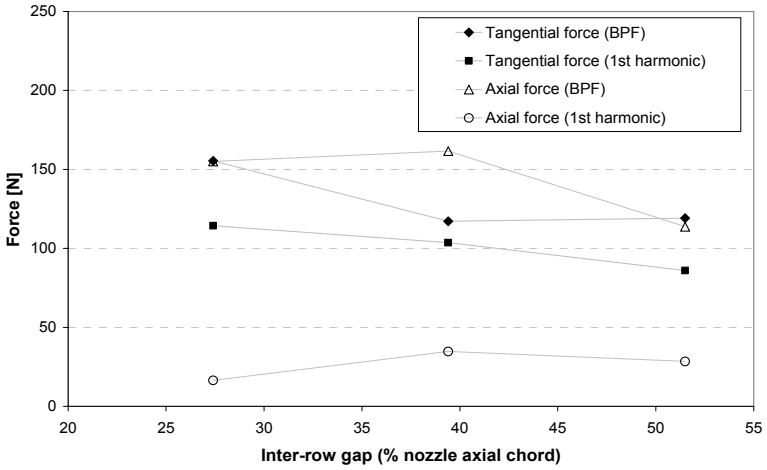

Figure 136 Unsteady axial and tangential force for BPF and 1st harmonic.

Inter row gap [% axial nozzle chord]	27.4	39.4	51.5
Reaction [%]	31.1	31.1	31.1
Tangential force (BPF) [N]	155	117	119
Tangential force (1st harmoinc) [N]	114	104	86
Axial force (BPF) [N]	155	162	114
Axial force (1st harmonic) [N]	16	35	29
Pitching moment (BPF) [Nm]	1.4	1.1	2.0
Pitching moment (1st harmonic) [Nm]	1.4	1.1	0.8

Table 25 Summary of the effect of inter-row gap on the unsteady rotor forces and pitching moments.

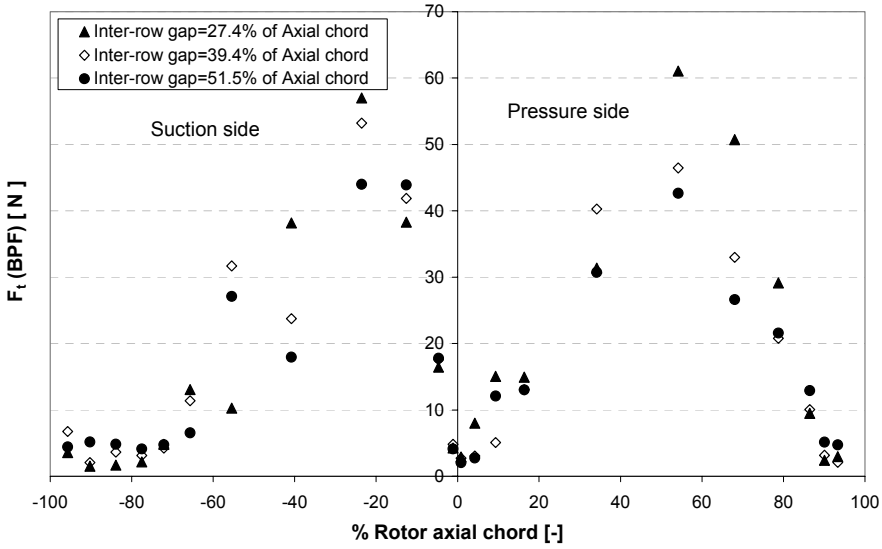

Figure 137 Effect of axial gap on the rotor unsteady tangential force (BPF)

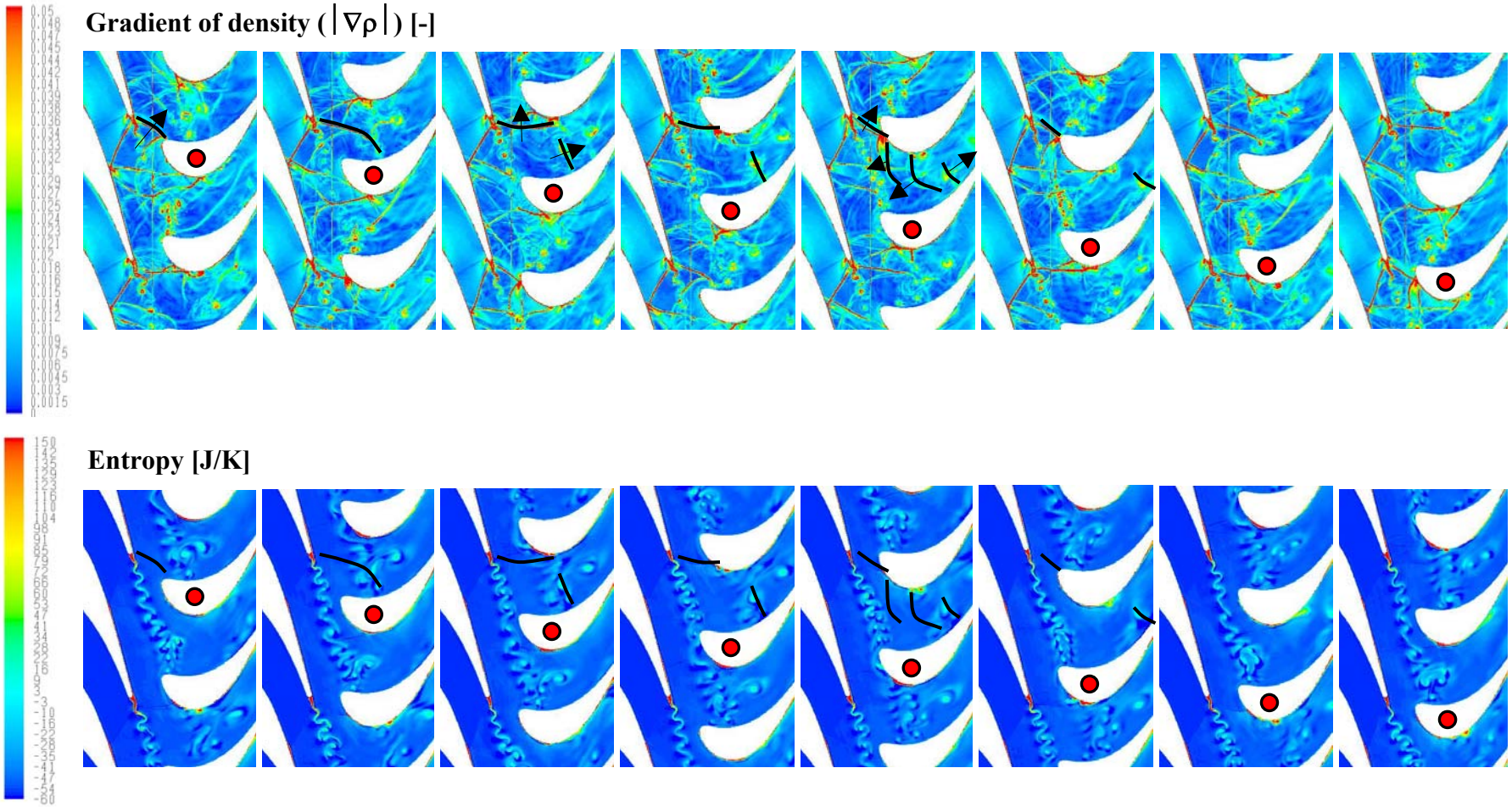

Nozzle phase (Φ_{NGV}) 1 1.125 1.25 1.375 1.5 1.625 1.75 1.875

Figure 138 Snapshots of $|\nabla\rho|$ (top) and entropy contours (bottom) for x_g/C_{NGV}=0.27. Shocks included as black lines, arrows indicate travelling shock direction.

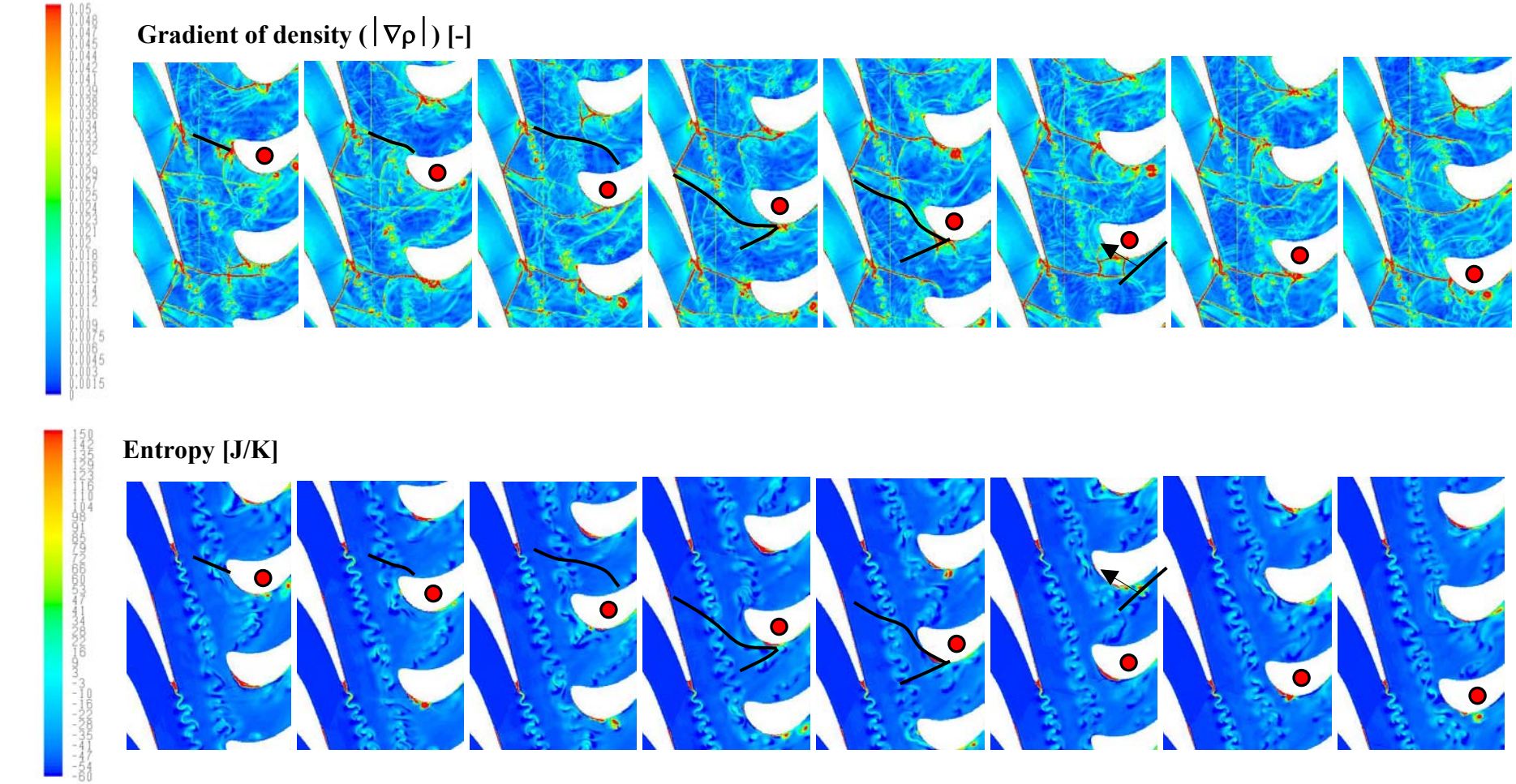

Figure 139 Snapshots of $|\nabla\rho|$ (top) and entropy contours (bottom) for x_g/C_{NGV}=0.52. Shocks included as black lines, arrows indicate travelling shock direction.

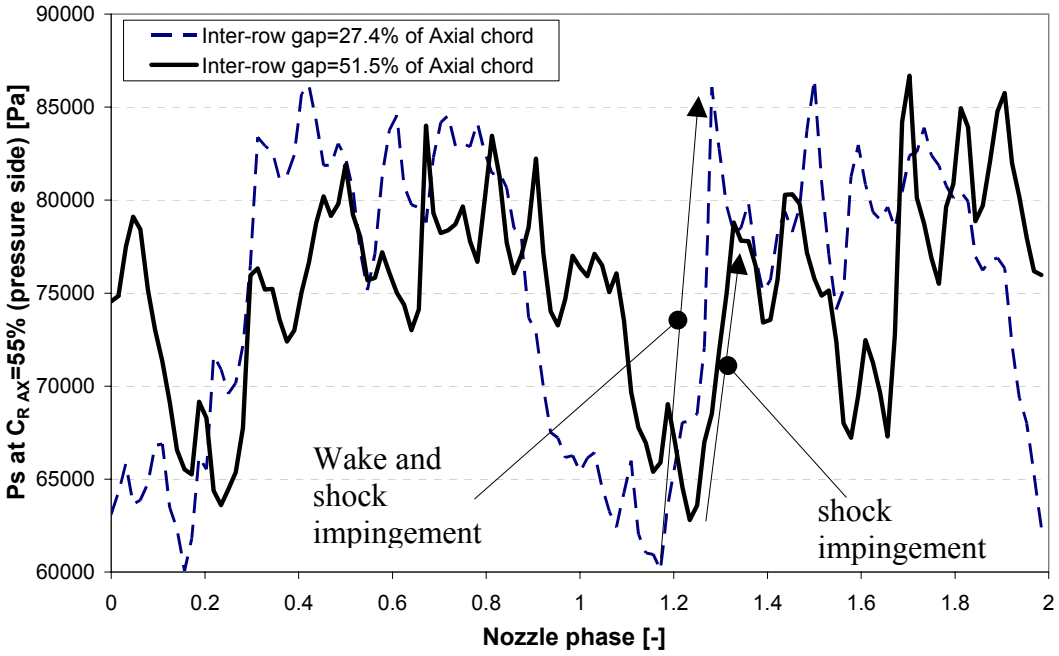

Figure 140 Unsteady pressure variation as a function of NGV phase (Φ_{NGV}). Comparison of x_g/C_{NGV}=0.27 and 0.52

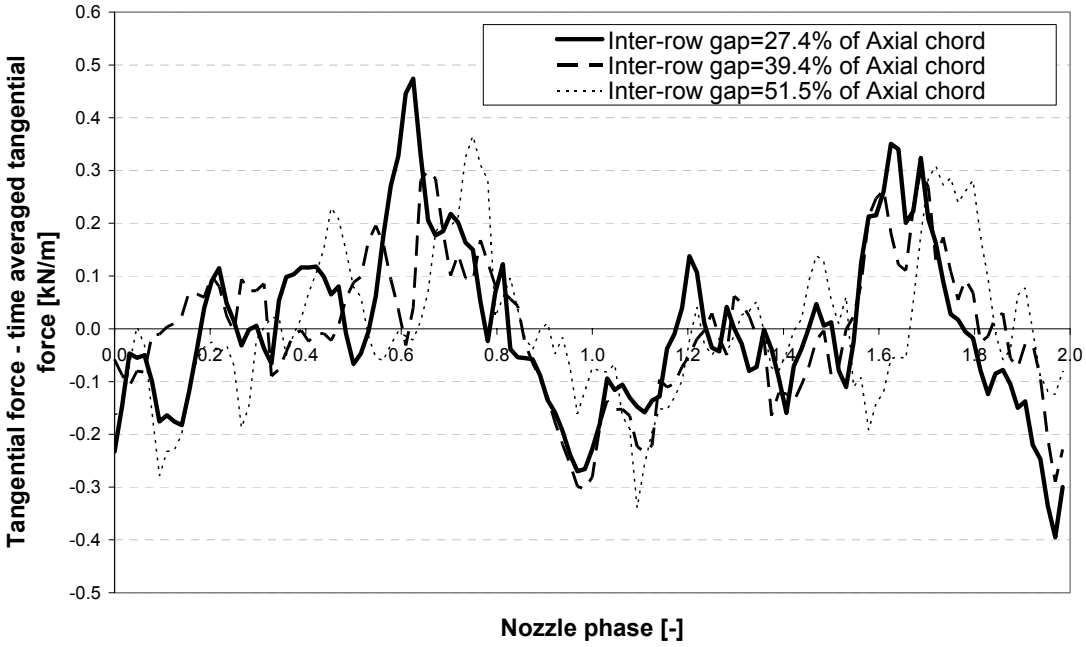

Figure 141 Unsteady component of net tangential force

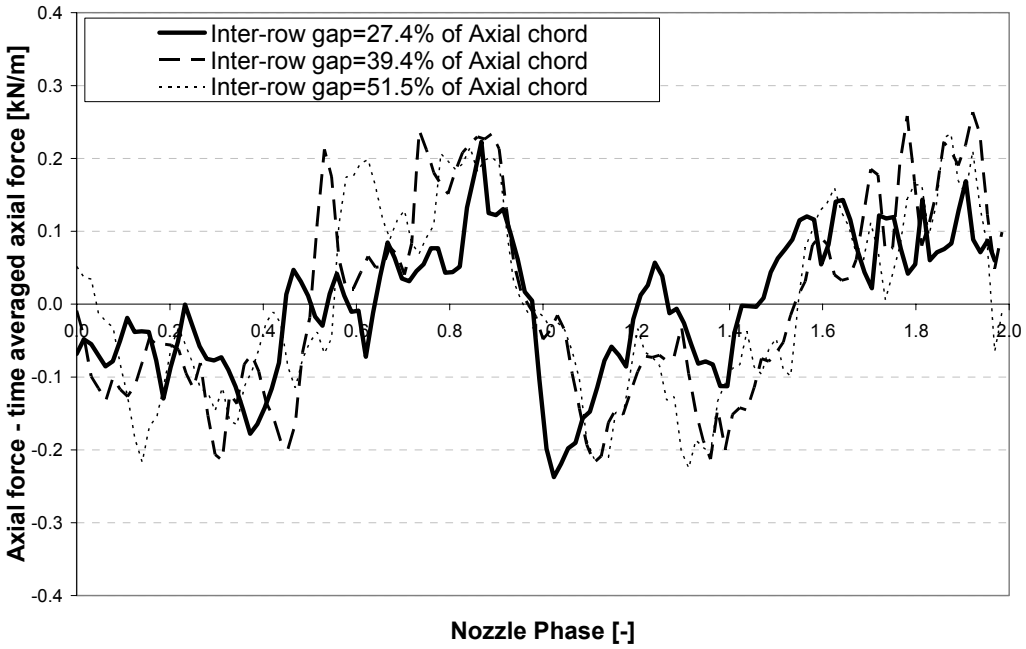

Figure 142 Unsteady component of net axial force

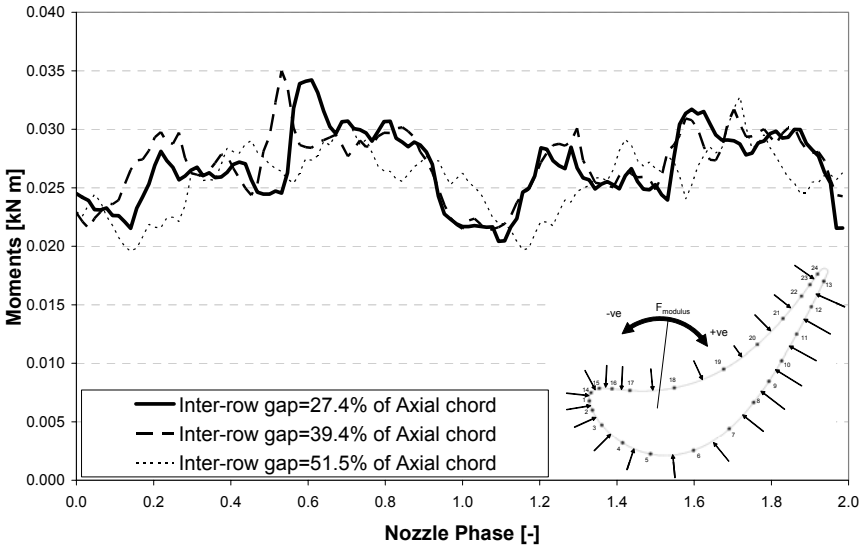

Figure 143 Unsteady component of moments

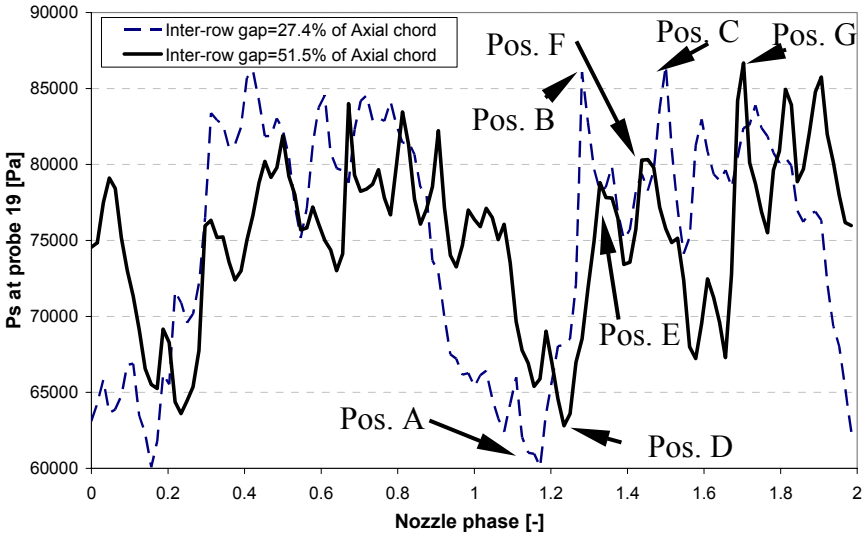

Figure 144 Probe 19 pressure trace (see Figure 145 for $|\nabla\rho|$ and $|\nabla S|$ contour plots)

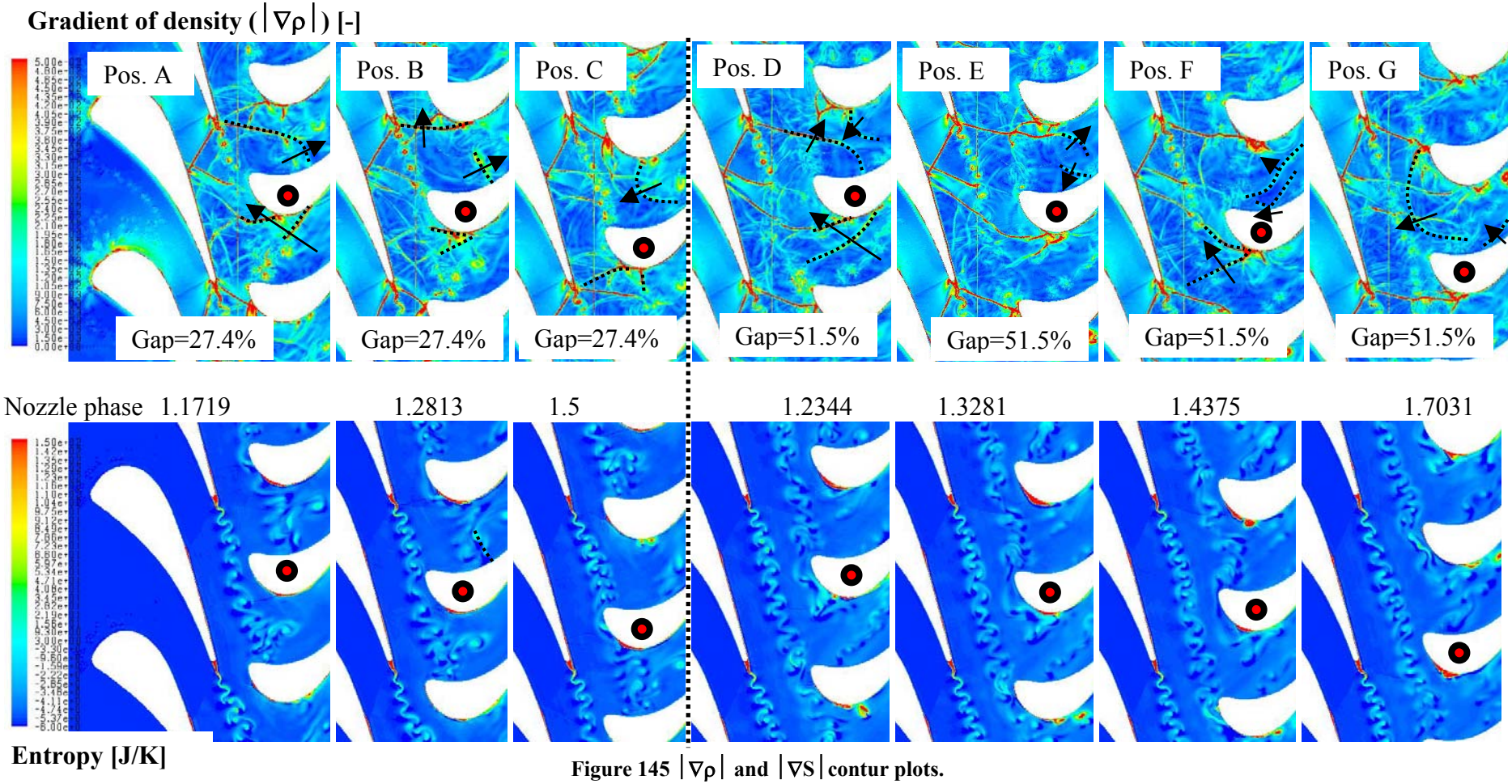

Figure 145 |∇ρ| and |∇S| contur plots.

8.5 Effect of pressure ratio

For a prescribed non-variable turbine geometry pressure ratio is an important design parameter. Increasing the turbine pressure ratio increases the inter-row Mach number, rotor lift and work, it can also affect the engine and turbine non-dimensional speeds by increasing the rotor angular velocity. For supersonic turbines the primary forcing functions are the nozzle TE shocks, the nozzle wake and the potential field. For the current configurations the most significant forcing functions are primarily the nozzle TE shocks (see section 8.6). The properties of the nozzle and rotor TE shocks, including the shock strength and propagation angle are determined by the turbine pressure ratio. As the pressure ratio increases the shocks increase in strength and propagate from the nozzle TE at a more oblique angle, which alters the phasing onto the rotor. The expectation is for the TE shocks to become a more significant forcing function as the pressure ratio increases until the stage chokes.

The study investigates three pressure ratios: 2.19, 3.19 and 3.85, where the pressure ratio is defined as P_{01}/P_{03}. Plane 01 is upstream of the nozzle LE and plane 03 is downstream of the rotor TE. The operating parameters of each CFD configuration and experimental equivalent are included in Table 26. Discrepancies between the predictions and experimental operating conditions can be attributed to the 2D nature of the CFD models. Each CFD configuration is a 2D section of the VKI rig at 50% span (S=0.5). The pressure ratio has been controlled by reducing the static pressure downstream of the rotor TE, at the domain exit. To put this in perspective a typical large civil aero-engine HP turbine stages operate at a pressure ratio of 2.48-2.55 [e12](cruise condition). For these engines the inter-row Mach number is usually designed to be sub-sonic (M_2=0.95).

Case	Pressure ratio (P_{01}/P_{03})	Stage loading ($\Delta H/U^2_{50\%}$)	Specific work ($\Delta H/T_{01}$)	Reaction (λ)	Non-dim. speed ($U_{50\%}/\sqrt{T_{01}}$)	Efficiency (η) (ideal expansion)	Flow co-efficient ($V_A/U_{50\%}$)	Inter-row Mach (M_2)
(2D) CFD								
PR219	2.19	1.3	188	0.12	11.97	0.904	0.43	1.04
PR319	3.19	1.9	276	0.22	11.97	0.926	0.49	1.23
PR385	3.85	2.1	303	0.31	12	0.902	0.49	1.24
(3D) Experimental								
WP22L	2.19	1.4	201	0.15	11.99	0.981	0.43	1.07
WP22N	3.19	1.8	263	0.21	11.97	0.915	0.49	1.24
WP22H	3.85	2.1	299	0.32	12	0.916	0.49	1.25

Table 26 Comparison of operating parameters for three configurations investigated (CFD) and experimental equivalents

For each of the considered pressure ratios (PR) the nozzle is choked. For PR3.19 and PR3.85 the rotor chokes which limits the output. If the rotor did not choke further reductions in backpressure would make the nozzle TE shock (L1) more oblique until they eventually formed a continuous annular shock, or more practically impeded from doing so by impingement onto the rotor. Further reductions in back pressure from PR3.19 are therefore limited to making the rotor TE shocks stronger and more oblique.

8.5.1 Nozzle characteristics

All configurations generate a SBLI on the nozzle suction side from the impinging nozzle TE RRS, just downstream of the throat ($0.64C_{noz}$, Figure 146). SBLIs with separations are known to be inherently unsteady (see chapter 3). The relatively low frequency unsteadiness (approximately 200Hz) is superimposed onto a modulated shock, caused by the rotor passing. This causes the impingement position along the nozzle suction side to oscillate. This oscillation occurs about a time averaged position which is dependent upon the pressure ratio. As the pressure ratio increases the R1 shock propagates and reflects at a more oblique angle, impinging onto the adjacent nozzle further downstream (Figure 146 and Figure 147) up to PR3.19. For the low pressure ratio case (PR2.19) the RRS propagates perpendicular to the flow from the nozzle TE, terminating on the adjacent nozzle suction side (SS), just downstream of the nozzle throat ($0.64\text{-}0.73C_{noz}$). For the two higher pressure ratio cases (PR3.19 and PR3.85) the RRS shock impinges further downstream ($0.79\text{-}0.84C_{noz}$) in approximately the same position due to the rotor choking. As detailed in the reaction study (section 8.6) a separated region periodically detaches from the SBLI region every rotor passing and convects with it the origin of an additional shock forcing function for each of the considered pressure ratios. The strength of the convecting shock and the size of the separation reduces with reducing pressure ratio (Figure 147).

8.5.2 Inter stage forcing function

As the pressure ratio increases the nozzle TE shocks become progressively stronger and propagate from the TE more obliquely until the rotor chokes at PR3.19. For configurations PR2.19, 3.19 and 3.85 the time averaged shock strength (Ps_2/Ps_1) increases to 1.42, 1.56 and 1.57 respectively (Figure 148).

The wake total pressure profile is also sensitive to pressure ratio. As the pressure ratio decreases the nozzle wakes become deeper and broader. For configurations PR2.19, 3.19 and 3.85 the time averaged wake depth (Pt_2/Pt_1) is 1.18, 1.11 and 1.08 respectively (Figure 149). Initially, just downstream of the nozzle TE, the wake at the high pressure ratio condition (PR3.85) has a high total pressue deficit and only extends across a small proportion of the nozzle pitch, but develops far more rapidly than the broad shallow wake at the low pressure condition (PR2.19) due to more intense shear between the wake and free stream (Figure 150). By the time the wake has convected from the nozzle TE to the sliding plane the depth of the wake for the high pressure ratio case (PR3.85) has reduced by more than a factor of 7, compared to the low pressure ratio case (PR2.19) which only reduces by a factor of approximately 0.6.

The wake trajectory is also sensitive to pressure ratio. The wake deflects more as the pressure ratio increases (Figure 151), relatively changing the wake and shock forcing function phase. As the pressure ratio increases the wake is deflected more through the reflected RRS towards an axial direction, paradoxically the higher potential field generated by the rotor turns the wake more towards a tangential inclination.

8.5.3 Rotor characteristics

8.5.3.1 Steady features

The rotor lift is highly sensitive to the stage pressure ratio until the rotor chokes (PR3.19), beyond which the rotor lift is predominantly limited to downstream of the rotor throat ($0.67C_{rot}$), and to reflecting rotor passage shocks impinging onto the rotor crown (Figure 152). For the low pressure ratio case (PR2.19) there is no significant reflected rotor passage shock reflections onto the rotor crown.

Also to be considered is the proportion of forces generated by the shock, relative to the wake for the pressure ratios considered. Neglecting potential flow field effects, for the high pressure ratio case (PR3.85) 0.61 of the tangential forces and 0.51 of the axial forces at the BPF are shock generated (see Section 8.6). However as the pressure ratio reduces the strength of the shock **reduces** by a factor of 0.9 (Ps_2/Ps_1, Figure 148), but the depth of the wake **increases** by a factor of 1.08 (Pt_2/Pt_1, Figure 149). Clearly as the pressure ratio reduces the shock forcing function becomes less significant compared to the wake.

8.5.3.2 Unsteady flow features

There is a rotor crown separation across all of the considered pressure ratios. An element of the separation periodically detaches from the crown region and convects down the rotor suction side, instigated by the LRS impingement (Figure 153). The more oblique nozzle TE shock at the high PR condition causes the detachment to occur at a later nozzle phase.

To understand the significance of the LRS impingement onto the rotor LE, a plot of the static pressure across $2\phi_{NGV}$ is presented in Figure 154 and summarised in Table 27. The maximum pressure rise considerably increases between PR2.19 and PR3.19 from the increased LRS strength. From PR3.19 the rotor is relatively insensitive to pressure ratio due to the flow choking across the rotor. [e13]

Pressure ratio (P_{01}/P_{03})	2.19	3.19	3.85
Maximum P_s rise (Ps_2/Ps_1)	1.5	1.85	1.86

Table 27 Maximum pressure rise at the rotor LE

8.5.3.2.1 Blade forces and pitching moments

Changing the pressure ratio from 3.85 to 2.19 demonstrates how significant the shock forcing function is. Even though the wake depth has increased by a factor of 1.08 the relatively small reduction in shock strength (factor of 0.9) reduces the axial force by a factor of approximately 4.3 and the tangential force by a factor of approximately 1.9 at the BPF.

As anticipated the amplitudes of the lower harmonic forces generally increase with increasing pressure ratio (Figure 155). At the BPF and 1st harmonic the unsteady tangential force become relatively insensitive to pressure ratio above 3.19 when the rotor chokes and the nozzle shock strength becomes insensitive to pressure ratio. However the unsteady axial force continues to rise from PR3.19-3.85 indicating that the rotor portion downstream of the rotor throat is significant. The pitching moments are difficult to understand due to the non-monotonic relationship with pressure ratio.

The trends are presented as a function of the pressure ratio in Figure 156 and summarised in Table 28.

8.5.3.2.2 Harmonic distribution

A more detailed evaluation of the distribution of the tangential forces at the BPF is included in Figure 157. Generally the unsteady forces increase from PR2.19 to 3.19. The relatively small changes between PR3.19 and 3.85 are due to the rotor choking. The largest differences occur at $0.54C_{rot}$ on the pressure side. This is primarily due to shock impingement which is described in more detail in section 8.5.3.2.3 below.

8.5.3.2.3 Rotor blade unsteady force

To better understand the large differences in unsteady tangential forces that occur between $0.34\text{-}0.54C_{rot}$ (pressure side) between PR2.19 and PR3.85 a time-history is included with supporting contours of $|\nabla\rho|$ to determine the relative position of the nozzle shocks (Figure 158 and Figure 159). Relative to the high pressure ratio cases (PR3.19 and 3.85) the unsteady tangential forces are insensitive to the shock forcing function. There is little difference between PR3.19 and 3.85 due to the rotor choking. There is a large increase in tangential force between 0.73 and $1.09\Phi_{NGV}$ for the PR3.19 and PR3.85 operating conditions due to the LRS impingement which does not occur for the PR2.19 operating condition. This is due to the higher shock strength and more oblique shock generated at the higher pressure ratio conditions. This results in the RRS impinging directly onto the rotor pressure side for the entirety of its axial chord, including just downstream of the LE where the design is inclined towards the flow due to shock bending through the boundary layer. At the low pressure ratio condition (PR=2.19) the nozzle TE shocks propagate nearly tangentially to the flow. The RRS terminates on the adjacent nozzle suction side, the LRS only impinges onto the late rotor pressure side due to its propagation angle.

8.5.4 Summary of findings

- The primary forcing function, the nozzle shock, becomes insensitive to increasing pressure ratio after the rotor chokes.
- For the lower harmonics the unsteady tangential rotor forces are sensitive to pressure ratio up to PR3.19. Beyond pressure ratio 3.19 the rotor chokes and the tangential forces become relatively insensitive. The axial forces are sensitive to all of the considered pressure ratios, which is an indication that forcing functions which generate axial forces on the portion of the rotor chord downstream of the rotor throat are an important contributory factor.
- The pitching moments are sensitive to pressure ratio across all of the modelled pressure ratios. Unlike the forces, the pitching moments are still sensitive above the choking pressure ratio due to the region downstream of the rotor throat which is still sensitive to pressure ratio. The pitching moments in this region are highly sensitive to unsteady forces due to the distance from the centre of rotation.
- The nozzle TE shock strength and wake depth change disproportionally in magnitude with pressure ratio.
- As the pressure ratio increases the nozzle wakes becomes thinner and deeper, however they develop more rapidly in the free stream due to mixing. The thinner wakes inherently include higher harmonic content.

- As the pressure ratio increases the nozzle TE shock angle increases, propagating more obliquely. This subjects all of the pressure side to shock impingement and smaller portions of the suction side. Conversely as the pressure ratio reduces the more tangentially inclined LRS shock impinges onto larger portions of the upstream suction side and smaller portions of the pressure side.
- Shock bending through the boundary layer subjects larger proportions of the rotor to impingement, increasing the rotor forcing.

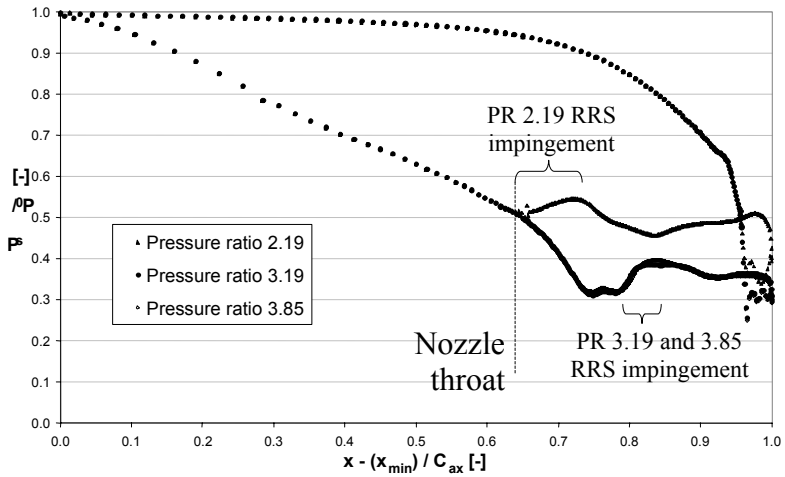

Figure 146 The effect of pressure ratio on the time averaged nozzle static pressure.

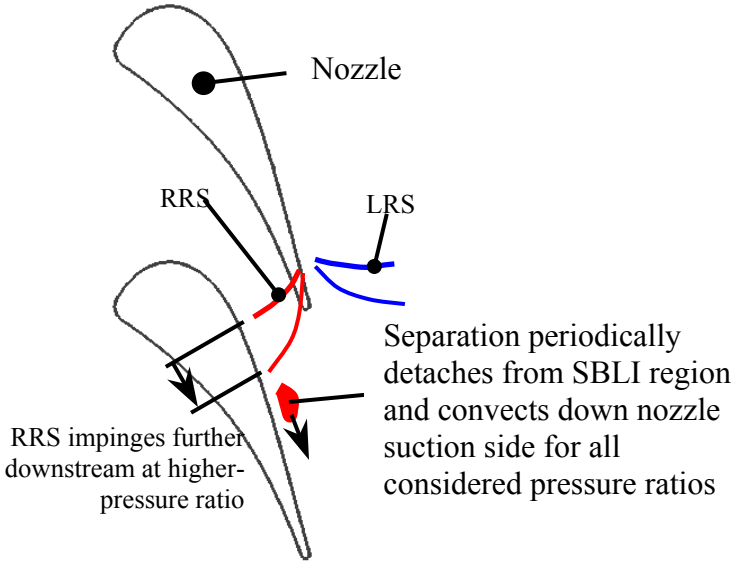

Figure 147 RRS impingement position and nozzle SBLI detached separation

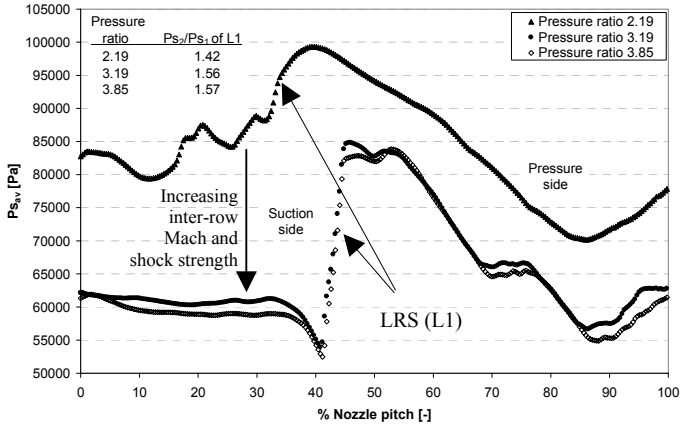

Figure 148 Time averaged static pressure at the nozzle domain exit (sliding plane).

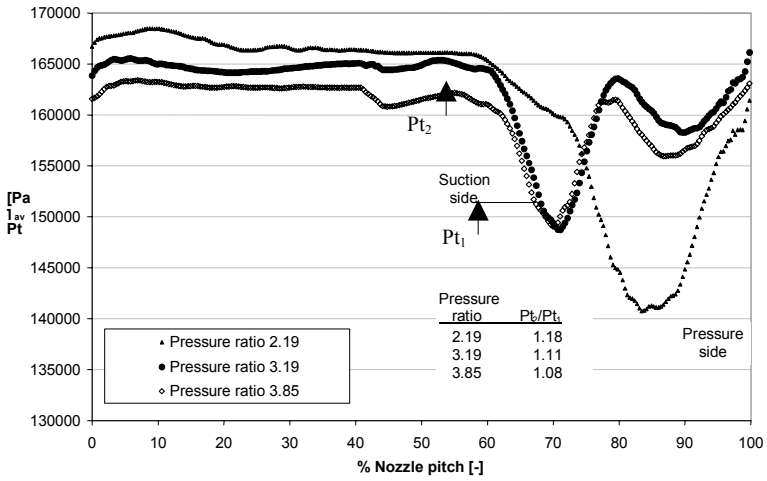

Figure 149 Time averaged total pressure at the nozzle domain exit (sliding plane).

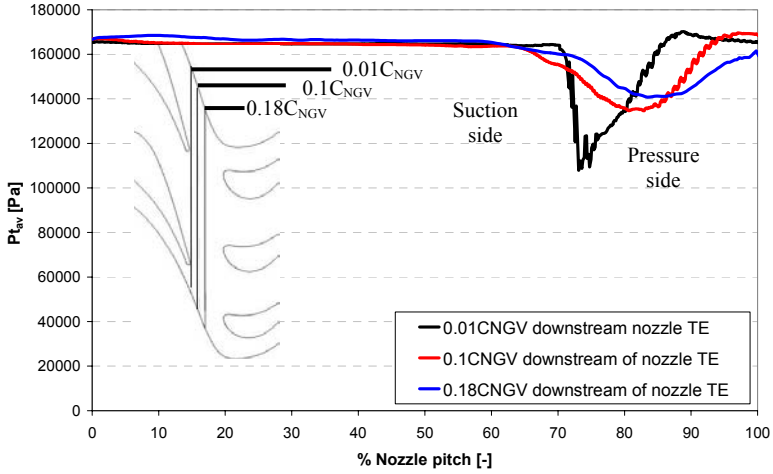

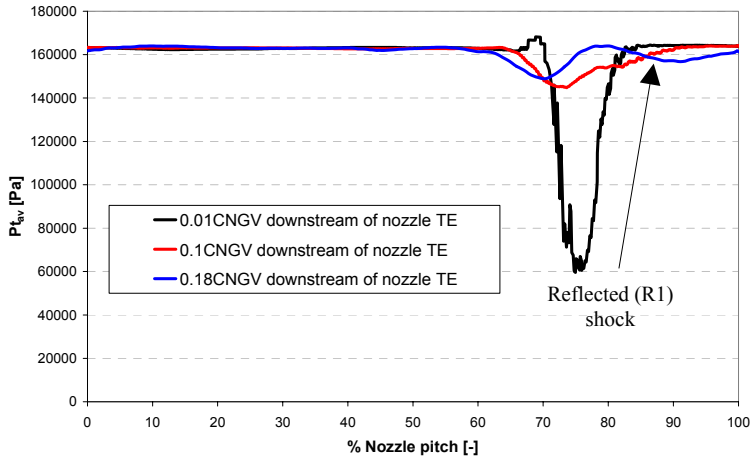

Figure 150 (Time averaged) wake development for PR 2.19 (top) and PR 3.85 (bottom)

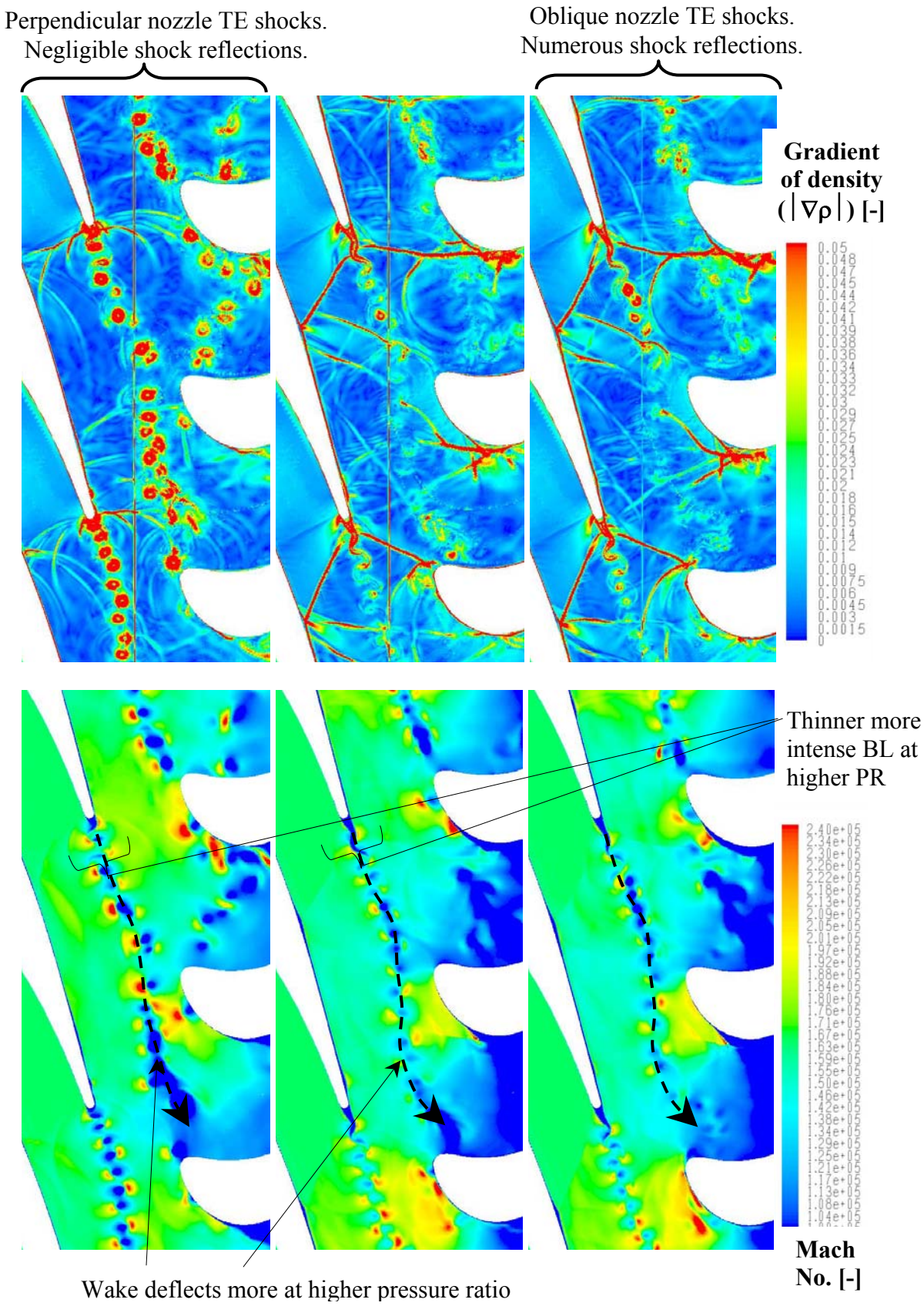

Figure 151 contours of $|\nabla\rho|$ (top) and total pressure (bottom) at Φ=0

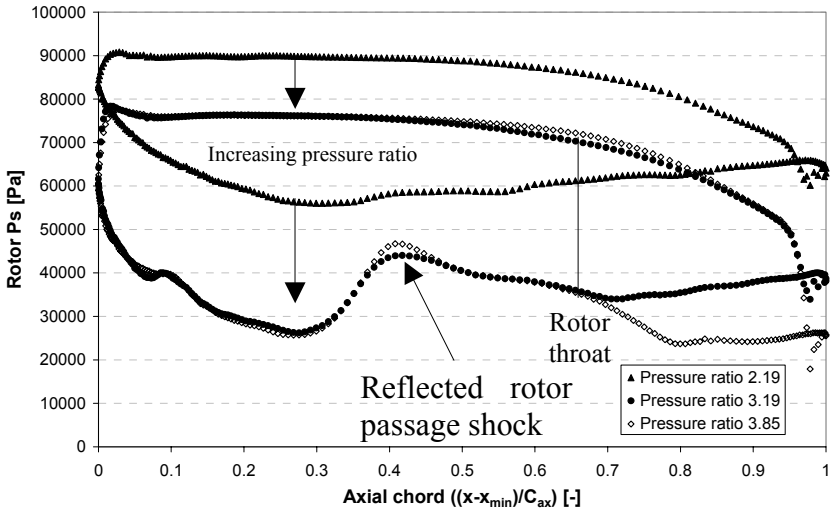

Figure 152 The effect of pressure ratio on the time averaged rotor static pressure.

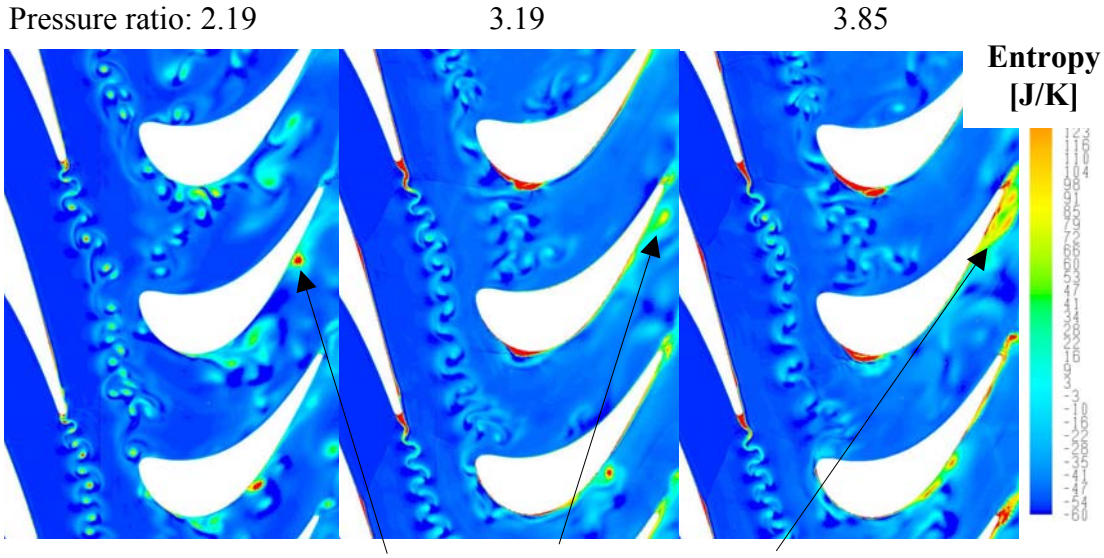

Separation detaches from rotor crown for all considered pressure ratios

Figure 153 contours of entropy at Φ=0

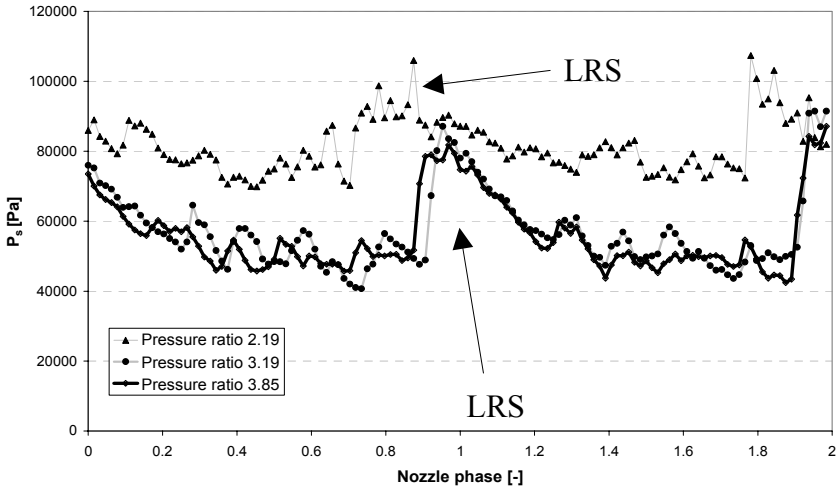

Figure 154 Static pressure trace at 0.001C_{rot} on the suction side

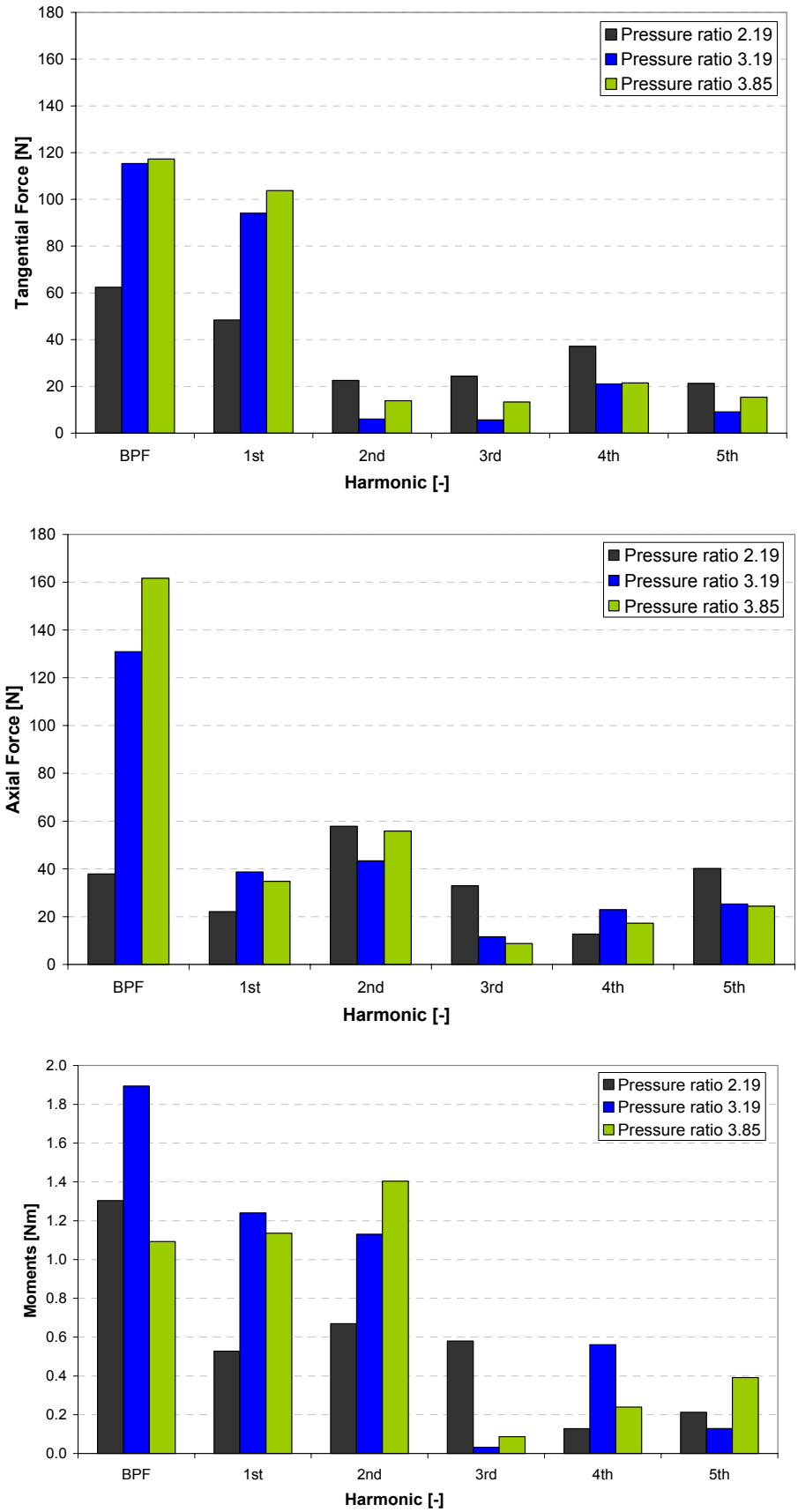

Figure 155 Harmonic distribution of unsteady tangential force (top) axial force (middle) and pitching moment (bottom) for various pressure ratios

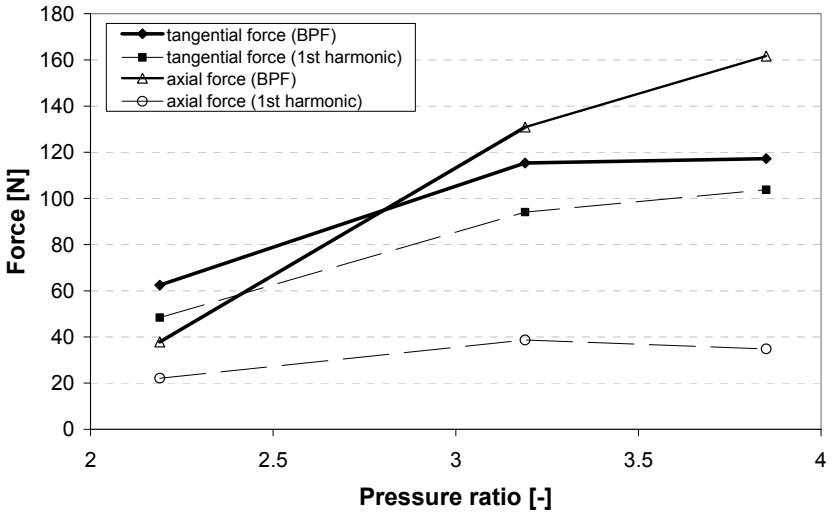

Figure 156 Axial and tangential force sensitivity to pressure ratio for multiple harmonics

Pressure ratio	2.19	3.19	3.85
Tangential force (BPF) [N]	62	115	117
Tangential force (1st harmoinc) [N]	48	94	104
Axial force (BPF) [N]	38	131	162
Axial force (1st harmoinc) [N]	22	39	35
Pitching moment (BPF) [Nm]	1.3	1.9	1.1
Pitching moment (1st harmoinc) [Nm]	0.5	1.2	1.1

Table 28 Summary of the effect of pressure ratio on the unsteady rotor forces and pitching moments.

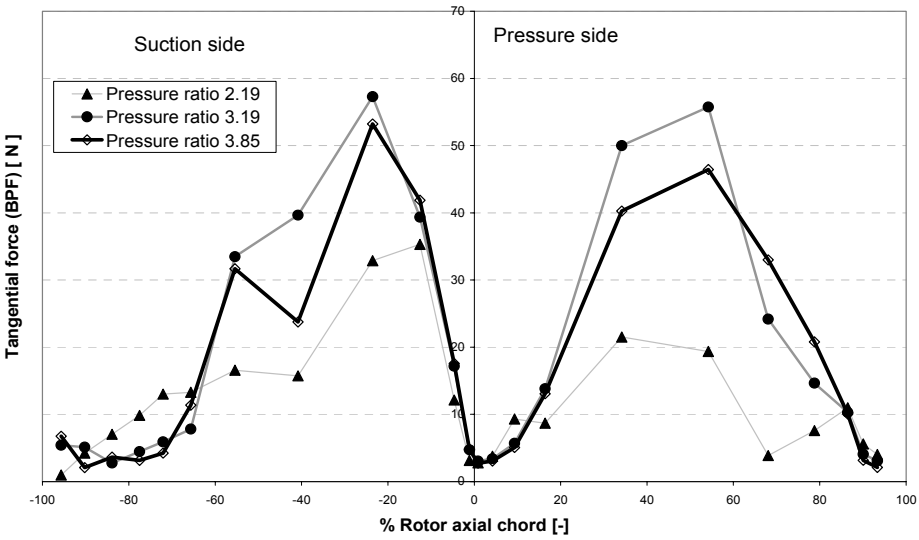

Figure 157 Effect of pressure ratio on the rotor unsteady tangential force (BPF)

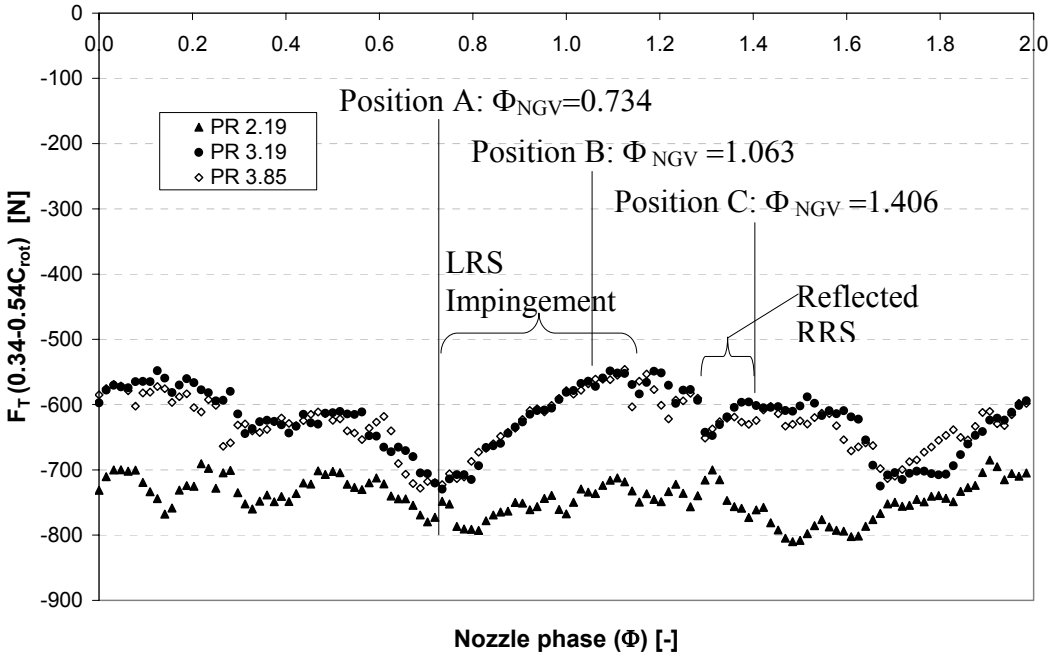

Figure 158 Comparison of unsteady tangential forces for different pressure ratios between 0.34-0.54C_{rot} (pressure side). See Figure 159 for contours of $|\nabla\rho|$

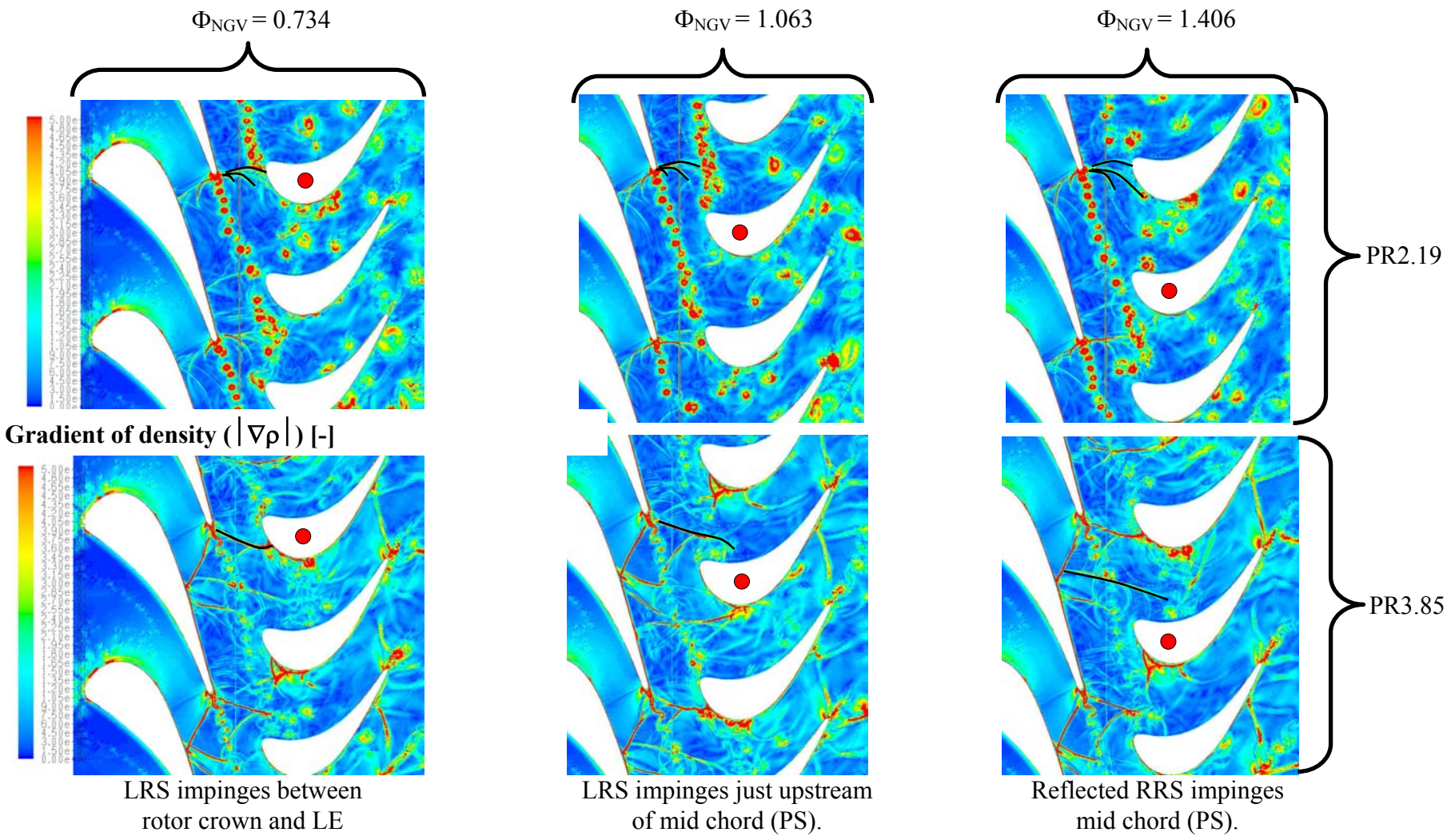

Figure 159 Comparison of contours of $|\nabla\rho|$ at Φ_{NGV} = 0.734, 1.063 and 1.406 (left to right) for PR2.19 (top) and PR3.85 (bottom), shocks highlighted

8.6 The importance of wake characteristics and shock forcing functions on rotor forces and pitching moments

This study investigates how the nozzle wake profile affects the unsteady rotor forces and pitching moments and the relative importance of the wake and shock forcing functions. Three aspects of forcing are addressed with five wake models:

- The wake forcing function relative to the shock forcing function
- The significance of the wake total pressure distribution
- The significance of the wake depth and harmonic composition

The nozzle wake profile is a function of several parameters, including the Reynolds number, the nozzle TE thickness, the nozzle back surface diffusion, shocks impinging onto the nozzle suction side, film cooling and TE ejection. This study simplifies this complex situation by altering a parametric, idealised, wake total pressure profile at the rotor domain inlet to investigate the effect on the unsteady rotor forces and pitching moments. By comparing the results with unsteady stage calculations, which include the shock forcing function, the relative importance of the wake and shock forcing function can be determined[MSOffice14].

For these predictions the computational domain comprises the rotor domain used in the unsteady stage calculations i.e. from the sliding plane to the exit plane (Figure 160). The rotor is modelled as a rotating blade and the imposed boundary conditions at the domain inlet are fixed in the absolute frame of reference. The boundary conditions are based on the 2D baseline unsteady stage model conditions at the sliding plane (31% reaction, datum axial gap, PR=3.85, Section 8.2). An investigation of the unsteady stage model showed the change in inlet swirl (α) through the wake is small (approximately 6°, absolute). For the wake studies, α is modelled as a constant across the inlet (74.4°). The static pressure is also considered uniform across the inlet ($P_s/P_{t\,max}$=0.39). There are no shocks present in this analysis. The total pressure profile (P_t) at the inlet varies for each configuration, defined by a Gaussian distribution of the form:

$$Pt\,(y) = -e^{-\left[\frac{(\theta-\theta_d)^2/2}{\sigma^2}\right]} \times \Delta P_t + z \qquad \textbf{Equation 6}$$

where θ is the angular position, θ_d is the angular position of Pt_{min} (see Figure 161), σ is the standard deviation, $\Delta P_t = P_{t\,max} - P_{t\,min}$ and z is a constant to align the Gaussian profile with the 2D datum unsteady stage model wake profile. A tabulation of the modelled profiles (cases A-E) is included in Table 29 where the integrated wake P_t deficit (ξ) is defined as:

$$\xi = \int_{\theta_1}^{\theta_2} (Pt_{max} - Pt)\, d\theta \qquad \textbf{Equation 7}$$

An overlay of each wake is included in Figure 162 for comparison. The wake model applied in case A is a simplification of the time averaged total pressure distribution of the 2D baseline unsteady stage model, matching the wake width at 0.5D, wake depth and total pressure deficit (ξ).

8.6.1 A comparison of the wake and shock forcing functions

By comparing the unsteady forces (F) and pitching moments (M) of the 2D unsteady baseline stage calculation and the wake baseline calculation (case A), the relative importance of the wake and shock forcing functions can be established. This is possible because the rotor is subjected to the nozzle wake and shock in the unsteady stage calculation, but only the equivalent wake in case A. This simple analysis neglects interaction effects between the shock and wake, such as wake broadening through the shock adverse pressure gradient but this is not expected to make significant difference. It also neglects unsteady interaction forcing terms such as rotor-stator-rotor reflections. Nevertheless, it is a useful to make an estimate of the relative importance of the wake and shocks.

The unsteady forces and pitching moments have been calculated as described in Appendix 1 and presented in Figure 163-Figure 165. The expectation that the nozzle TE shock would be the prominent forcing function has been established for the forces, but the inclusion of shocks reduces the pitching moments, primarily due to forcing function phase differences around the rotor.

The effect of the shock on tangential forces is expressed as:

$$RF_{tshock}=(F_{tstage}-F_{twake})/F_{tstage} \qquad \textbf{Equation 8}$$

where RF_{tshock} is the fractional unsteady tangential force resulting from the nozzle TE shock, F_{tstage} is the unsteady tangential force resulting from the shock and wake and F_{twake} is the unsteady tangential force resulting from the wake (case A). At the Blade Passing Frequency (BPF) the nozzle TE shocks account for $0.61F_t$ in the unsteady stage calculation. A comparison of the tangential forces across the rotor axial chord (C_{rot}) for each case is included in Figure 166 (left), where differences between the predictions are accountable to shock impingement. The largest differences occur in the regions around the rotor where the nozzle TE shocks directly impinge, on the pressure side and between the LE and rotor crown ($0\text{-}0.4C_{rot}$).

The axial forces are also highly sensitive to the nozzle TE shock. The effect of the shock in axial forces is expressed as:

$$RF_{ashock}=(F_{astage}-F_{awake})/F_{astage} \qquad \textbf{Equation 9}$$

where RF_{ashock} [e15]is the fractional unsteady axial force resulting from the nozzle TE shock, F_{astage} is the unsteady axial force resulting from the shock and wake forcing functions and F_{awake} is the unsteady axial force resulting from the wake (case A). The axial forces are less sensitive to the shock forcing function, they account for $0.51F_a$ (BPF). A more detailed comparison of the two predictions at the BPF is included in Figure 166 (middle). The higher forces that result from the combined shock and wake forcing functions primarily occur near the rotor LE on the suction side ($0\text{-}0.25C_{rot}$) and towards the downstream pressure side ($0.55\text{-}0.85C_{rot}$). These two regions have relatively large frontal areas that the shocks directly impinge onto. Both axial and tangential forces are most sensitive to the shock forcing function in regions which are perpendicular to the respective plane considered (i.e. axial or tangential plane) that the shock directly impinges on to.

The expectation that higher forces generated by the nozzle TE shock would result in higher pitching moment elements has been realized across the majority of the blade

chord (Figure 166, right). However the resulting one-dimensional net moment is sensitive to two factors:

- The distance from the centre of rotation that the forces act.
- Phase differences between pitching moment components which result in some degree of constructive or destructive interference.

For the combined shock and wake case the phase differences in the moment components result in considerable destructive interference resulting in a reduction in moments from 1.9Nm (for case A) to 1.1Nm at the BPF. In summary the shocks generate considerably higher forces, which actually reduce the pitching moments due to destructive interference.[MSOffice16]

8.6.2 Wake distribution study

This study investigates the significance of the nozzle wake profile. By comparing different wake profiles, the investigation demonstrates that as the nozzle wake reduces in width, and increases in depth, the unsteady forces and pitching moments predominantly increase (cases A-C, Figure 163-Figure 165). To investigate the impact of the nozzle wake, three models have been generated. Each of the models has the same integrated P_t wake deficit (ξ), see Figure 161, but a different width (W) and depth (D).

As previously detailed, the resulting nozzle wake profile is a consequence of several parameters, however at a given operating condition, excluding TE ejection, the wake distribution is considered to be primarily a consequence of the nozzle TE thickness. This investigation parametrically varies the wake characteristics, to investigate the effect of broadening the wake profile. The expectation is that higher forces and pitching moments will occur as the P_t deficit in the wake is concentrated into a smaller wake width, i.e. thin deep wakes result in higher forces than broad shallow wakes. The rationale behind this expectation is that thinner wakes impinge on to the rotor over a smaller nozzle phase (Φ_N). This hypothesis would extend to all harmonics, due to the high frequency content of thin wakes. The first modelled wake is based on the time averaged total pressure distribution of the 2D baseline unsteady stage prediction: it matches the wake depth, total pressure deficit and width at 0.5D (Figure 161). This model is referred to as the wake datum case (case A, Table 29). The second modelled wake is half the baseline wake depth and the third modelled wake is 1.5 times the baseline wake depth (case B and C respectively). A comparison of these wakes and the wakes used in the wake depth study (see section 8.6.3) is included in Figure 162 for comparison.

The results of this investigation are mixed. As anticipated, the unsteady axial forces reduce as the wake broadens at the BPF (Figure 164), however the unsteady tangential forces are relatively insensitive to the wake width for W=0.03 and 0.05, only reducing when the wake becomes relatively broad (W=0.1, Figure 163). There are two important conclusions. Firstly the unsteady axial and tangential forces are disproportionally affected by the wake width. For the wakes considered the axial forces increases by a factor of 3, compared to a factor of approximately 2 for the tangential forces. Secondly that unsteady tangential force are relatively insensitive to increasing wake width until the wake becomes relatively broad.

A detailed evaluation of where the unsteady forces and pitching moments occur is included in Figure 167. Clearly the pressure side forces and pitching moments reduce as the wake width reduces, however the results are more complicated around the suction side, specifically in the rotor crown proximity. In this region the high rotor loading generates separations for all of the considered cases, however the separation size increases as the wake broadens (Figure 168). The reduced swirl [MSOffice17]angle from the wake relieves the loading reducing the separation size, a [MSOffice18]more intense wake relieves more. This results in more numerous detaching separations along the late suction side for broad wakes[MSOffice19]. This complex transient effect of wake convection is considered to be the reason for the relatively insensitive result of the unsteady tangential forces between W=0.03-0.05 (Figure 163).

The pitching moments are highly sensitive to the wake profile (Figure 165). A reduction of the wake width by a factor of 3 increases the pitching moments by a factor of 3.5. The pitching moments are most sensitive to the wake profile towards the TE (Figure 167), due to the distance from the centre of rotation.

8.6.3 The effect of wake depth and frequency content

This study determines the sensitivity of unsteady rotor forces and pitching moments to wake depth by analysing two wake models of equal width and different depth (case D and E, Table 29). By maintaining the wake width and increasing the wake depth, both models inherently include different integrated total pressure deficits. This could be of benefit to a designer by applying wake filling technology, where TE ejection is engineered to reduce the total pressure deficit within the wake. Additionally by comparing cases B and E which have the same wake depth, but different widths and total pressure deficits the importance of the wake frequency content can be determined. This is possible due to the thin wake case (case E) inherently including relatively high amplitude harmonic content. To summarise, the study compares cases D and E to understand the importance of wake depth and cases B and E to understand the importance of wake frequency content[e20].

As anticipated, a comparison of cases D and E shows that as the wake deepens the unsteady forces and pitching moments increase (Figure 163 to Figure 165). A more detailed evaluation of where the unsteady forces occur across the rotor chord at the BPF is included in Figure 169. On the pressure side the forces and moments are most sensitive towards the TE (0.54-1C_{rot}). On the suction side the forces are most sensitive up to just downstream of the rotor crown (approximately 0.55C_{rot}), however the deeper wake (case D) relieves the rotor loading {Giles, M. 1988} more than the shallow wake case (case E), generating more unsteadiness across the entire suction side chord. The larger unsteady forces generated by the deeper wake, cause significantly higher moments, especially towards the TE.

To understand the relative importance of frequency content a comparison of the common wake depth cases B and E is included. It demonstrates that for the harmonics considered the overall total pressure deficit, not the frequency content is the most important aspect of the wake in generating large unsteady forces (Figure 163 to Figure 165). Predominantly the forces and pitching moments are higher for case B, only the tangential forces at the BPF, and the 2^{nd} harmonic forces and pitching moments are comparable. Like the previous wake studies the forces and pitching moments are most sensitive to the wake towards the TE on the pressure side (0.54-

$1C_{rot}$) (Figure 169), and up to just downstream of the rotor crown (approximately $0.55C_{rot}$) on the suction side.

8.6.4 Wake study conclusions

The wake studies have several important conclusions for designers:

- At the BPF the shock increases the unsteady rotor forces by more than a factor of 2.
- The addition of a shock forcing function (and blade row interactions) can potentially reduce the unsteady pitching moments by destructive interference.
- For a given integrated total pressure deficit the wake should be as broad as possible for forced response implications.
- The resultant rotor forcing from the nozzle wake is primarily a consequence of the integrated total pressure deficit of the wake, not the frequency content at the lower harmonics. This is a useful piece of information for designers who should minimize the nozzle trailing edge thickness and reduce the wake total pressure deficit by wake filling. However it should be noted that even if the practise of reducing the trailing edge thickness to a razor sharp edge was employed, a wake would still result from the boundary layer development along the nozzle. So in practise a combination of reducing the trailing edge to a manageable minimum and the application of wake filling would have to be included to achieve an optimum solution in minimizing the wake total pressure deficit.
- Modelling the rotor domain in a rotating reference frame about a fixed inlet boundary condition at the reported spatial and temporal resolution is sufficient to capture the unsteady flow features and accurately determine the unsteady rotor forces.

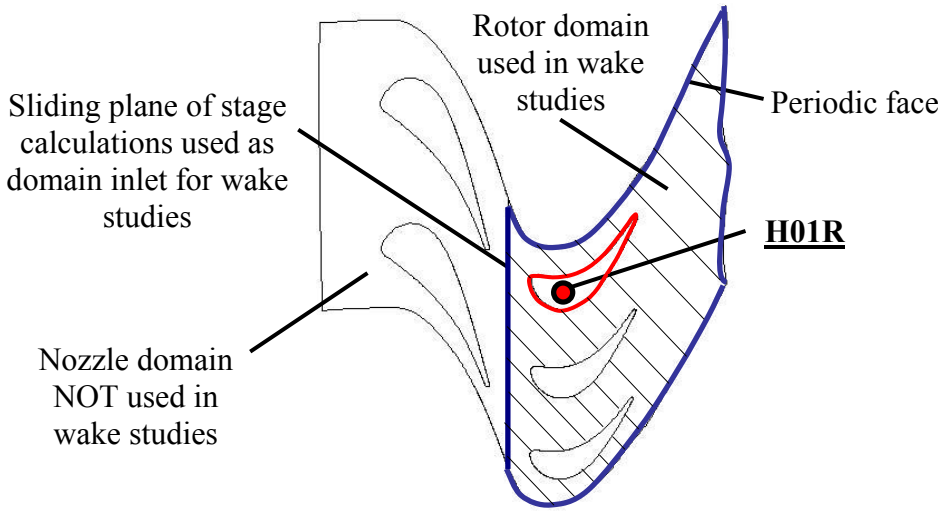

Figure 160 Rotor domain used for wake studies

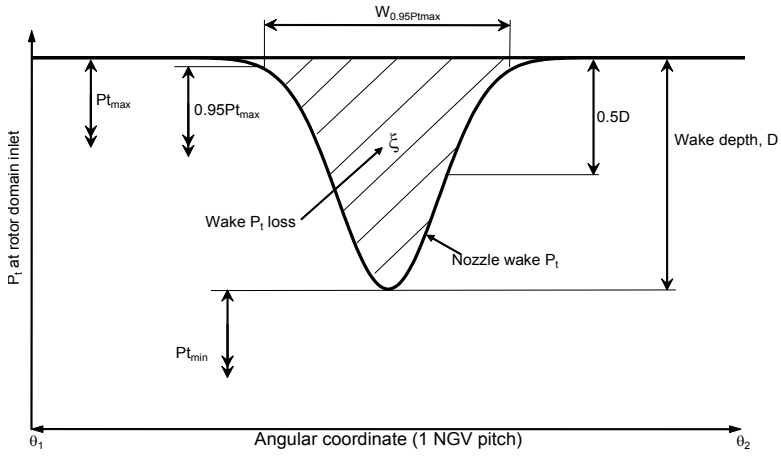

Figure 161 Sketch of nozzle wake P_t profile (see Table 29)

Case	ξ/Pt_{max} [-]	$W_{0.95Ptmax}$ [Rad]	D/Pt_{max} [-]	
A	0.0028	0.05	0.21	(Baseline case)
B	0.0028	0.1	0.1	
C	0.0028	0.03	0.31	
D	0.0018	0.01	0.31	
E	0.0006	0.01	0.1	

Table 29 Primary characteristics of modelled wakes at the rotor inlet domain (see Figure 161)

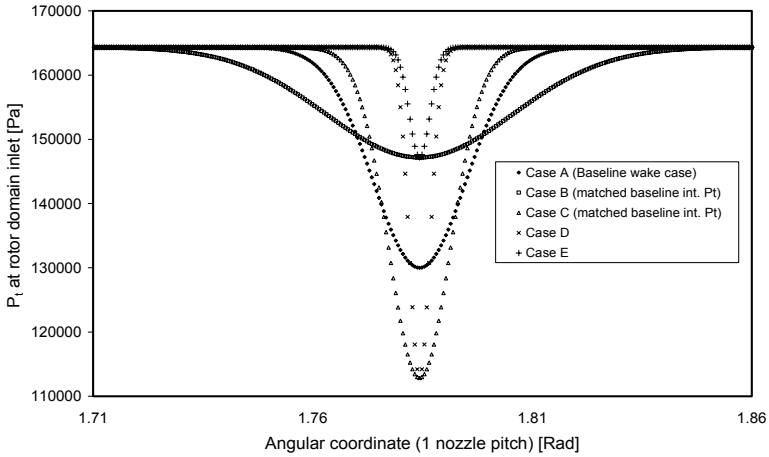

Figure 162 Comparison of P_t at the rotor domain inlet

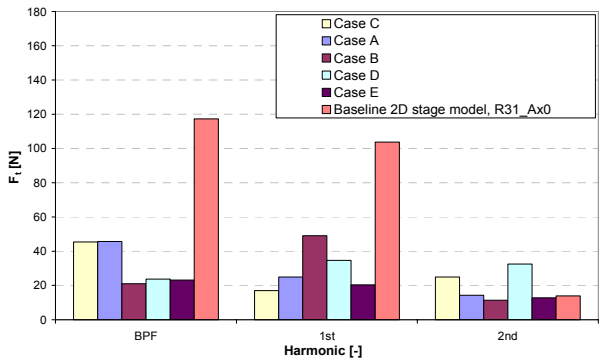

Figure 163 Tangential force (F_t) harmonic decomposition

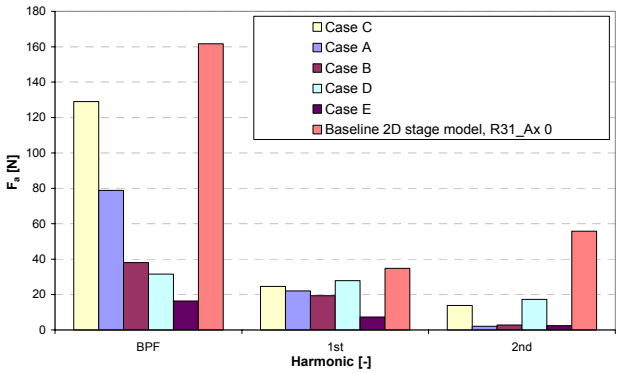

Figure 164 Axial force (F_a) harmonic decomposition

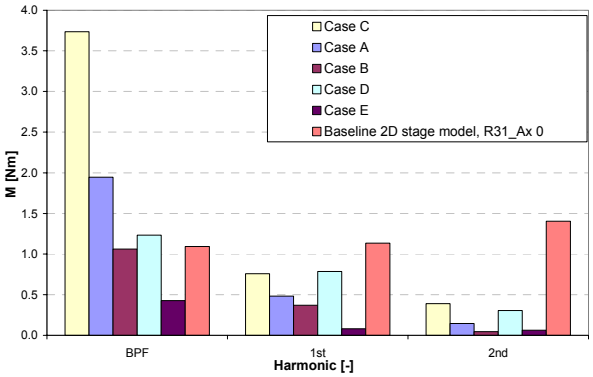

Figure 165 Pitching moments (M) harmonic decomposition

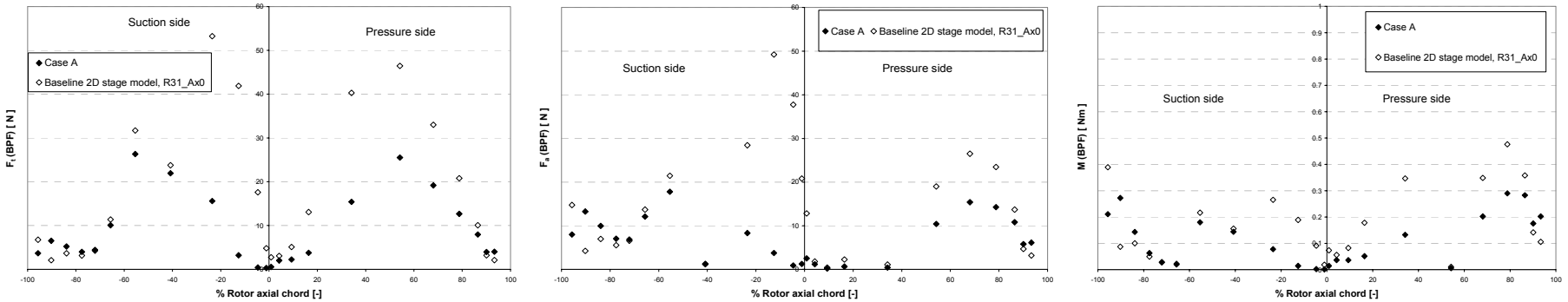

Figure 166 Comparison of temporally decomposed tangential forces (F_t, left), axial forces (F_a, middle) and pitching moments (M, right) (BPF). Differences between Case A and the baseline stage model are attributable to the shock forcing function.

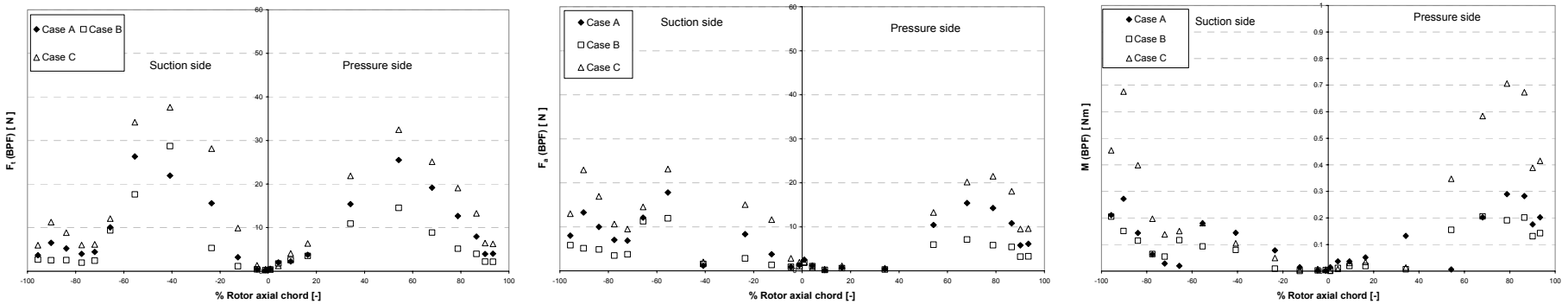

Figure 167 Comparison of temporally decomposed tangential forces (F_t, left) (F_a, middle) and pitching moments (M, right) (BPF) to understand the effect of the wake distribution

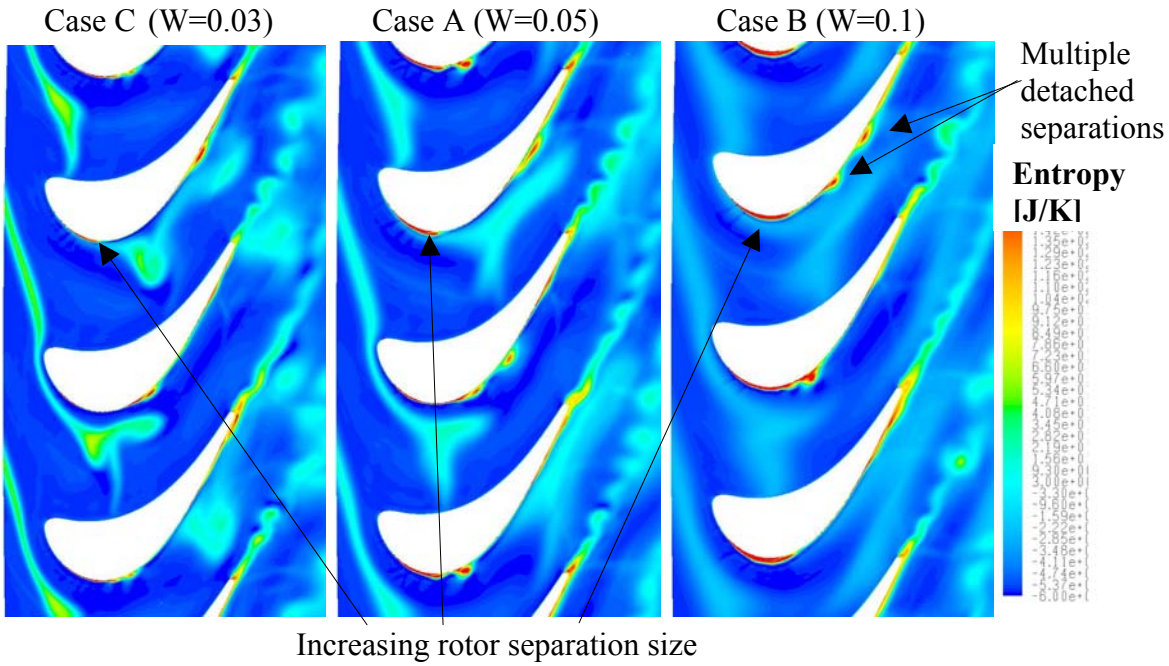

Figure 168 Effect of NGV wake width on the rotor flow field at Φ=0 for cases C, A and B respectively (contours of entropy). Separation size at rotor crown increases as wake broadens.

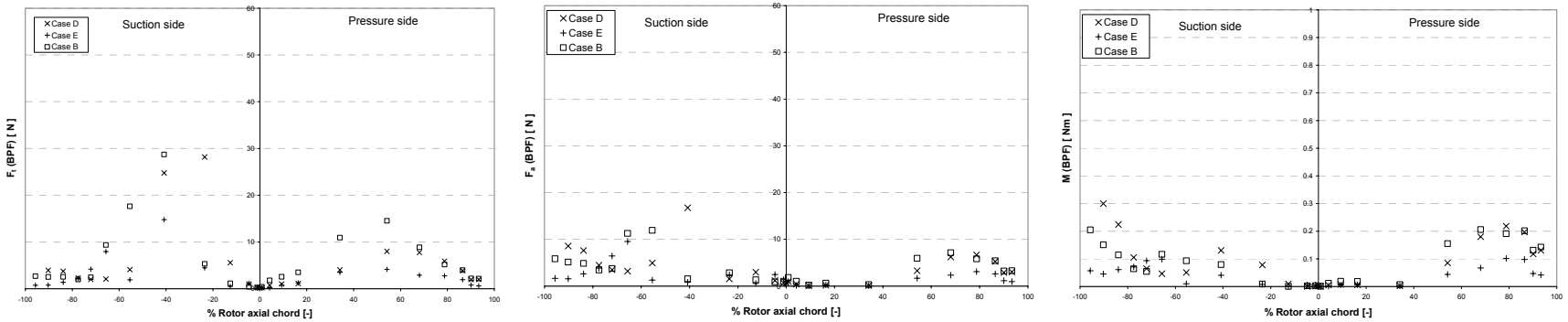

Figure 169 Comparison of temporally decomposed tangential forces (F_t, left) (F_a, middle) and pitching moments (M, right) (BPF) to understand the result of the wake depth

8.7 Effect of rotor boundary layer

In modern high pressure turbines the development of the rotor boundary layer is complicated by cooling air jets which are aligned to maximise the jet contact with the blade surface area. The primary function of the cooling jets is to cool the blade surface, however as a by-product they also re-energise the boundary layer. This has considerable implications for rotor forcing of supersonic turbines as the rotor boundary layer is known to dissipate impinging nozzle TE shocks. To better understand the significance of the rotor boundary layer the 2D baseline model was computed with a slip condition on the rotor. A comparison of the rotor slip configuration and the no slip configuration demonstrates how significant the rotor boundary layer is in dissipating the nozzle TE shocks (**Figure 170**). Even in the upstream portion of the rotor the shock pressure pulse is significantly dissipated through the relatively undeveloped rotor BL by 27%. This is an indication of the importance of accurate modelling of the boundary layer, ideally explicitly resolving the near wall region.

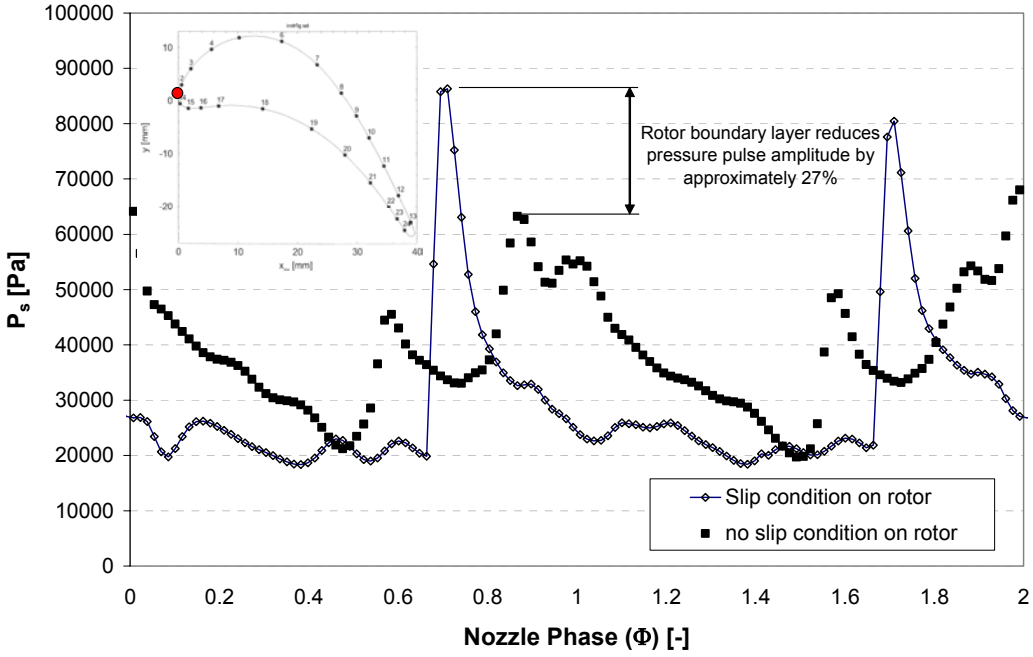

Figure 170 Comparison of a slip and no slip rotor boundary layer configuration (2D baseline model)

9 Conclusions

This study sets out the operating conditions where it is advantageous to consider a reduction in weight and cost of an engine by a parts count reduction. This might include reducing the number of HP turbine blades or even incorporating the work done by two turbines into a single high work turbine. Unlike conventional turbines, high work turbines include an additional forcing function from the strong nozzle trailing edge shocks which can have a significant detrimental affect on the unsteady aerodynamics. Computational modelling standards are explored to reduce the risk of High Cycle Fatigue (HCF) generated from all of the forcing functions being overlooked in the design phase of the engine program. An examination of the financial implications of unscheduled engine events, such as HCF, is also explored, which are at risk of becoming more numerous for high work turbines configurations. The study also explores the costs of addressing a forcing issue in the design and development stage as well as in-service. The study includes a detailed investigation of the unsteady aerodynamics of a high work turbine including the resulting unsteady forces and pitching moments and concludes with design recommendations and considerations for minimising rotor forcing.

9.1 Business conclusions

The business element of the study explores the cost of unscheduled events and concludes that the cost is significantly in excess of the small cost reductions achieved by diminishing gains in efficiency improvement. These costs will either be incurred by the operator for traditional contract methods or by the manufacturer for more modern contracts which oblige the manufacturer to guarantee availability. The risk of these unscheduled events is even higher for modern engines where engine cost and weight is reduced by parts count reductions and potentially through the adoption of high work turbines. These configurations are more susceptible to HCF due to the significant additional shock forcing function. Manufacturers need to be confident that these potentially dangerous HCF failures do not occur in operation. One method of reducing the likelihood of this happening in the design phase is to apply validated computational techniques and to develop a more sophisticated understanding of the complex unsteady aerodynamics.

Using structured interview techniques with senior engineers in the Rolls-Royce organisation the research has quantified the cost of addressing forced response events in the design ,development and in-service phase of an engine programme. The research highlights how forced response issues might progress through the design and development phase due to modelling standards and unrepresentative engine testing. The result is that re-designing for a forced response concern in the design phase is relatively cheap at less than 0.1% of a typical engine program cost. Rectifying in the development phase can cost up to 2% and in the unlikely event that the engine should get into service the cost can be up to 20%. Clearly there is a significant incentive to capture these events in the early phases of the engine program before tooling costs are committed or contractual obligations incur financial penalties.

9.2 Modelling standards

The modelling standard is a critical element of forced response analysis. Unsatisfactory modelling will generate erroneous results, including the predicted rotor forces. Factors include the mesh density, turbulence model selection and temporal

discretization. Coarse spatial discretization will not capture the high gradients of pressure and density across a shock. Another consequence of inappropriate meshing includes numerical diffusion across the sliding plane if the nozzle and rotor domain nodes do not align. This is an important aspect for high gradient shocks propagating through the sliding plane in high work configurations. Finally if the near wall mesh resolution is not fine enough, a wall function model will be applied as opposed to the more appropriate explicit resolution of the near wall region, which is necessary to capture the complex flow structures within the SBLI region. Inappropriate turbulence model selection can lead to erroneous results, such as the over production of turbulent energy. Furthermore, deciding the appropriate temporal discretization is an important aspect of the simulation during the design phase. If the temporal discretization is too coarse high frequency content will not be modelled. If the temporal discretization is too fine the simulation will take excessive periods of time to converge and not provide timely information during the design process.

A modelling standard is presented which is adequate in capturing the rotor forces at the lower harmonics. The standard applies approximately 1.2 million cells per blade passage for the high-pressure turbine stage. The near wall mesh resolution is fine enough to achieve Y^+ values of <0.6, which instigates the two-layer zonal model to be applied, explicitly resolving the near wall region, rather than the more crude wall function, which is inappropriate for impinging shocks. Modelling shock impingement onto the boundary layer is critical and the presence of the boundary layer is shown to dissipate the pressure pulse amplitude by approximately 27%. The number of nodes on both the nozzle and rotor side of the sliding plane should match and be a divisible integer of the number of rotor steps to ensure the nodes are always aligned and thereby eliminate numerical diffusion through the sliding plane. Ideally the number of time steps selected should satisfy 2^n to enable a simple Fast Fourier Transform analysis. The most appropriate turbulence model for this fine mesh density is the k-ω SST, however if more coarse mesh densities are applied, perhaps in the design process, the Spalart-Allmaras turbulence model is more appropriate. The temporal discretization is considered adequate enough to capture up to the 4^{th} harmonic without being excessive in computational time. This was achieved by 64 rotor movements past each nozzle with up to 1000 iterations per time step. However this resolution needs to be reconsidered for very high pressure ratio or low reaction turbines where more numerous shock reflections generate higher frequency content which requires relatively higher temporal discretization to capture. As a maximum the number of time steps should not exceed the number of cells across the sliding plane, which would implicitly generate numerical diffusion. The number of required iterations will reduce for these small timesteps due to relatively smaller changes in the flow field. For these extreme configurations a grid sensitivity study is recommended.

9.3 Forcing functions

For high work turbine configurations the L1 shock generated at the nozzle trailing edge is the most significant forcing function. The inclusion of the L1 and R1 shocks increase both the axial and tangential forces generated by just the wake by more than a factor of two. The shock strength is modulated by the transient-convergent throat formed between the nozzle and rotor. For the case considered in this work, the shock strength was increased by up to 20%. However, this observation is also expected to be sensitive to the axial spacing between the NGV and the rotor. For prismatic nozzle configurations the nozzle shock strength becomes progressively greater towards the

hub. The shock strength at the hub can be as much as 5% [MSOffice21]higher at the hub than the tip causing the hub shock propagation angle to be larger which results in the hub shock impingement to phase lag the tip shock impingement. Reducing reaction and increasing pressure ratio both increase the nozzle shock strength, until a critical pressure ratio is achieved, when the rotor chokes and the nozzle shock strength becomes insensitive to further increases. As the shock strength increases it generates more numerous inter-row and blade passage shock reflections. In the event that they impinge at a common location on the rotor at the same phase the significant adverse pressure gradient generates large separations and significantly increases the unsteady forces, specifically at higher harmonics.

An experimental program examined the unsteady pressure measurements of an impinging oblique shock. This data. has been used to characterise sub and supercritical SBLIs. For subcritical SBLIs the impinging shock only reflects as a single shock, the strength of which is reduced through reflection from the nozzle boundary layer. The reflected shock is steady. The only consideration for forced response applications is the amplification of the turbulent kinetic energy through the SBLI. This amplification is at potentially problematic frequencies (approximately 10kHz) as they are in the range of those considered for HCF conditions .However the magnitude of the pressure oscillations is less than 1000Pa which is far less than the pressure rise through the shock (approximately 40kPa) and can be considered negligible for forced response considerations. The supercritical SBLI also amplifies the turbulent kinetic energy at approximately the same frequency, but the magnitude of the oscillations is 5 times higher (approximately 5200 Pa) and should be considered as a contributory forcing function as this amplitude of oscillation is prevalent across most of the SBLI. Additionally the shock reflections oscillate at a frequency of approximately 150Hz, displacing the reflected pre-compression shock approximately 10% of rotor axial chord due to the separation mechanism. This reflected oscillation is not considered to be problematic for forced response considerations due to the low frequency.

Although the nozzle trailing edge shocks are the most significant forcing function, the nozzle wake is still significant and contributes up to a maximum of 50% of the unsteady axial forces. Reducing reaction or increasing pressure ratio results in thinner more intense nozzle wakes which inherently includes higher harmonic content. However the high shear generated at these operating conditions causes the wake to develop at a higher rate than low pressure ratio or high reaction operating conditions. The reduced swirl angle from the wake relieves the loading reducing the separation size. A more intense wake relieves loading more than a broad shallow wake. Mechanisms which affect the nozzle wake profile include the shock strength, the length of nozzle chord downstream of the SBLI that the boundary layer has to develop along, and any intermittent separations which convects from the SBLI region. The trajectory of the wake is changed through convection through the reflected RRS and the rotors potential field, relatively changing the phasing with respect to the other forcing functions. The wake directly affects the rotor forcing by the momentum deficit on to the rotor LE and indirectly by convection through the rotor passage which alters the rotor loading.

9.4 Rotor forces

One of the key findings is the importance of the relative phasing of unsteady forces at different positions along the rotor profile. As anticipated the rotor forces increase with reducing reaction, increasing pressure ratio and reducing axial spacing across most of the rotor profile. However, it is the relative phasing that plays a crucial role in the resulting net forces (irrespective of the forcing mechanism). An example of this is how the net axial and tangential force changes with reaction. The lowest axial and tangential forces occur at the highest reaction (λ=41.3%) and, as expected, these forces then increase as the reaction is reduced to λ=31.1%. However, they then decrease again as the reaction is lowered even further (λ=31.1%) in spite of the increase in the magnitude of the underlying forcing functions. This non-monotonic relationship with reaction is a result of the phasing between the different disturbances along the rotor. Designers can use this knowledge to potentially design near a desired operating point if the rotor forces are non-phase aligned. A parametric study for a given operating condition and nozzle and rotor profile is suggested for this investigation, making small adjustments in the axial spacing. Another key finding is the relative sensitivity of the rotor forces at each harmonic due to the change in reaction. An example includes the tangential force at the 4th harmonic which is more sensitive to reaction than the BPF.

Generally the rotor forces were found to reduce with increasing axial gap. However the critical aspect of using this technique is the relative phasing of each discrete forcing function - specifically the wake and the shocks. An example includes the close spacing model (x_g/C_{NGV}=0.27) where the wake and L1 shock become phase aligned on the pressure side at mid-chord resulting in an increase of approximately 25% in the tangential forces at the BPF.

The rotor forces increase with increasing pressure ratio at the lower harmonics primarily due to the increasing shock strength. There is no direct correlation above the 2nd harmonic due to the relative phase alignment of the wakes and numerous shock reflections. Like the axial spacing, consideration needs to be given to phase alignment of discrete forcing functions. The shock propagates more obliquely from the nozzle TE for high pressure ratio configurations, changing the relative phasing with the wake impingement onto the rotor.

The wake profile is an important aspect of the unsteady rotor forces, especially for the axial forces due to the impingement onto the LE. The critical factor is the distribution of the momentum deficit. As the deficit is concentrated into a smaller proportion of the nozzle pitch the axial and tangential forces increase. The axial force is especially sensitive and it increases by a factor of 4 when the wake width is reduced by a factor of 3 but with a common total P_t wake deficit. Although the distribution of the momentum deficit is critical, if the wake is especially thin then the inherently higher frequency content results in higher axial and tangential forces at the higher harmonics. This high frequency content is problematic for forced response considerations, due to the increased likelihood of phase alignment with the BPF.

Generally the axial and tangential forces are most sensitive to forcing functions in the regions of the rotor that are perpendicular to their respective direction. The axial forces are most sensitive around the LE and downstream pressure and suction side.

The tangential forces are most sensitive in the axial location of the rotor crown on the suction and pressure side.

In conclusion the unsteady rotor forces are sensitive to reaction, axial spacing, pressure ratio and the wake total pressure deficit. For the considered configurations the forces are most sensitive to pressure ratio, however the highest forces were achieved by reducing the inter-row gap.

9.5 Design recommendations

To reduce the most significant forcing function, the nozzle TE shocks, careful consideration needs to given to the nozzle profile design to minimize the shock strength. For conventional nozzle designs the nozzle turns the flow across the entire axial chord generating expansion fans which result in significant shocks near the trailing edge. To reduce the shock strength all of the turning should be done upstream of the nozzle throat. This results in no acceleration on the suction side beyond the nozzle throat and a weaker trailing edge shock system, generated by the finite trailing edge thickness. This generates a convergent-divergent nozzle from the nozzle throat to the exit or inter-row area, such that the design requires the exit to throat area ratio to be set to achieve the desired inter-row Mach number. This has the added benefit of increasing stage efficiency by reduced entropy.

To minimize the total pressure deficit within the wake, methods such as wake filling and minimizing the nozzle TE thickness should be practised. In the impractical scenario of completely eliminating the wake the axial forces would be reduced by a third and the tangential forces would be reduced by a half.

Designers should avoid phase alignment between each discrete forcing function. This can be done in a number of different ways including reaction, axial spacing and pressure ratio and wake shaping to ensure that the wake does not impinge onto the rotor across the entire span at a common phase. In the likely event that this is not achievable then the phase alignment should be concentrated in an area that does not generate excessive unsteady forces. If the unsteady tangential forces are not of particular concern then the phase alignment should be at the axial proximity of the rotor crown on either the pressure or suction side. If the unsteady axial forces are not of particular concern then the phase alignment should be concentrated at either the LE or the downstream pressure or suction side.

Designers should also avoid generating supercritical SBLIs which have serious implications for nozzle or rotor life due to the extreme temperature environment that they operate in and also generate additional forcing functions. For supercritical SBLIs the impinging shock generates two reflections a pre-compression and re-attachment shock. When inter-row shock reflections impinge onto the nozzle at the SBLI region they generate a separation which detaches and convects along the nozzle suction side. The convecting separation periodically impinges onto the downstream rotor, acting as an additional forcing function. During its convection it also locally displaces the boundary layer which generates a further shock forcing function, the origin of which convects with the separation. To avoid these additional forcing functions designer should employ the analytical criterion proposed by Reshotko. The tool will enable designers to determine if the adverse pressure gradient of the impinging shock, for a prescribed upstream boundary layer, is of sufficient magnitude to generate a

supercritical SBLI. In the event that this occurs designers should re-design using one of the detailed methods such as pressure ratio, reaction or re-design of the nozzle profile.

Another important aspect of how each discrete forcing function interacts is destructive interference. Previous work by Korakianitis has demonstrated that wake and pressure disturbances do not act independently, they interact. Designers can employ this knowledge to engineer turbine stages in which the forcing functions deliberately interact to generate destructive interference to minimise rotor forcing.

9.6 Further work

Future work might include the application of the Spalart-Allmaras model onto a finely discretized spatial model. An examination of different near wall modelling is advised along with a study of higher fidelity turbulence models such as Large Eddy Simulation (LES) and the Reynolds stress model. 3D models of multiple axial distances and different nozzle and rotor designs might be considered to minimize the unsteady forces. More realistic HP configurations should be modelled which include features such as film cooling, TE ejection, Profiled End Walls (PEW), cavities, leakage flows, tip designs (squealer or winglet) and Overall Temperature Distribution Factor (OTDF).

Appendix 1: Derivation of rotor forces and pitching moments.

To calculate the unsteady blade force the time resolved pressure distributions are integrated around the blade profile (Figure 171). The pitching moment was derived from applying the axial and tangential forces as a moment about a centre of rotation of x=9.8mm, y=-1mm from probe 1. The centre of rotation was derived from the HP turbine blade of a large civil engine.

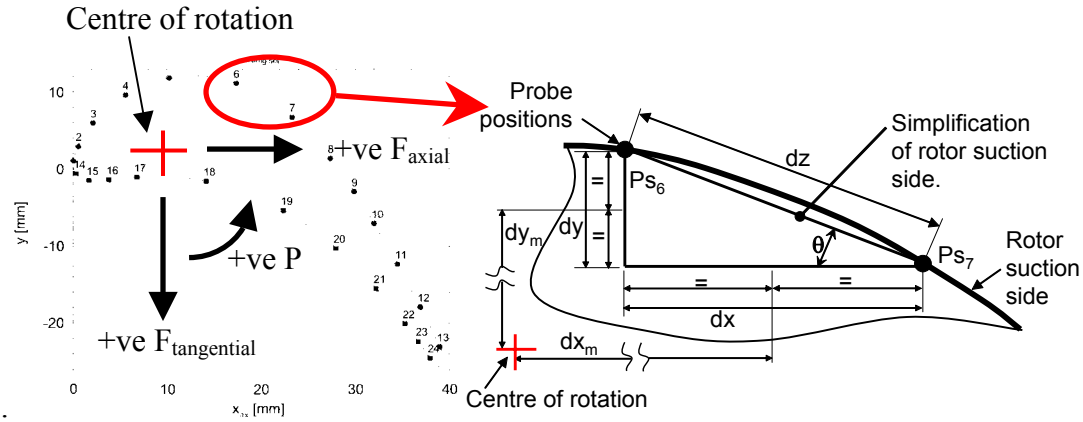

$$Force\ (F_{dz}) = \frac{(Ps_6 + Ps_7)}{2} \times \sqrt{dx^2 + dy^2}$$

$$Tangential\ component\ (F_{dx}) = Cos\ \theta \times \frac{(Ps_6 + Ps_7)}{2} \times \sqrt{dx^2 + dy^2}$$

$$Axial\ component\ (F_{dy}) = Sin\ \theta \times \frac{(Ps_6 + Ps_7)}{2} \times \sqrt{dx^2 + dy^2}$$

$$Pitching\ moment\ (P) = F_{dx} \times dx_m + F_{dy} \times dy_m$$

$$Tangential\ \ force = \sum_1^{24} F_{dz} \qquad Axial\ \ force = \sum_1^{24} F_{dy} \qquad Pitching\ moment = \sum_1^{24} P$$

Figure 171 Derivation of rotor forces and pitching moments (S=0.5)

The forces and pitching moments are temporally decomposed using Fast Fourier Transform (128 samples). Phase differences are accounted by summing the complex number of each force and pitching moment component ($FFT = \sum_1^{24}(x + yj)$). The resulting modulus is derived for each harmonic by $H_n = \frac{2\sqrt{x_n + y_n}}{n_s}$ to determine the amplitude of each force and pitching moment.

Appendix 2: SBLI experiments

All SBLI tests were conducted in the Cranfield 2.5” x 2.5” supersonic wind tunnel facility (Figure 172). The open-circuit tunnel achieves sonic velocities at the throat through a 144:1 contraction ratio. The intermittent rig is capable of operating between M_∞ from 0.5 to 2.5 in the test section with the specified configuration (i.e. compression ramp). The driving pressure ratio is achieved by running a vacuum pump to attain a vacuum pressure inside a $45m^3$ downstream chamber. Upon opening, the chamber sucks ambient air via an alumina drying bed. The drying bed prevents condensation forming, but reduces the stagnation pressure within the settling chamber by approximately 700Pa below atmospheric. The stagnation temperature in the settling chamber is assumed to be unaffected and equal to atmospheric conditions. The experiments used a sting mounted wedge which acted as shock generator in a convergent / divergent nozzle (Figure 173). The wedge generated incident shock reflects from an instrumented top liner (Figure 174).

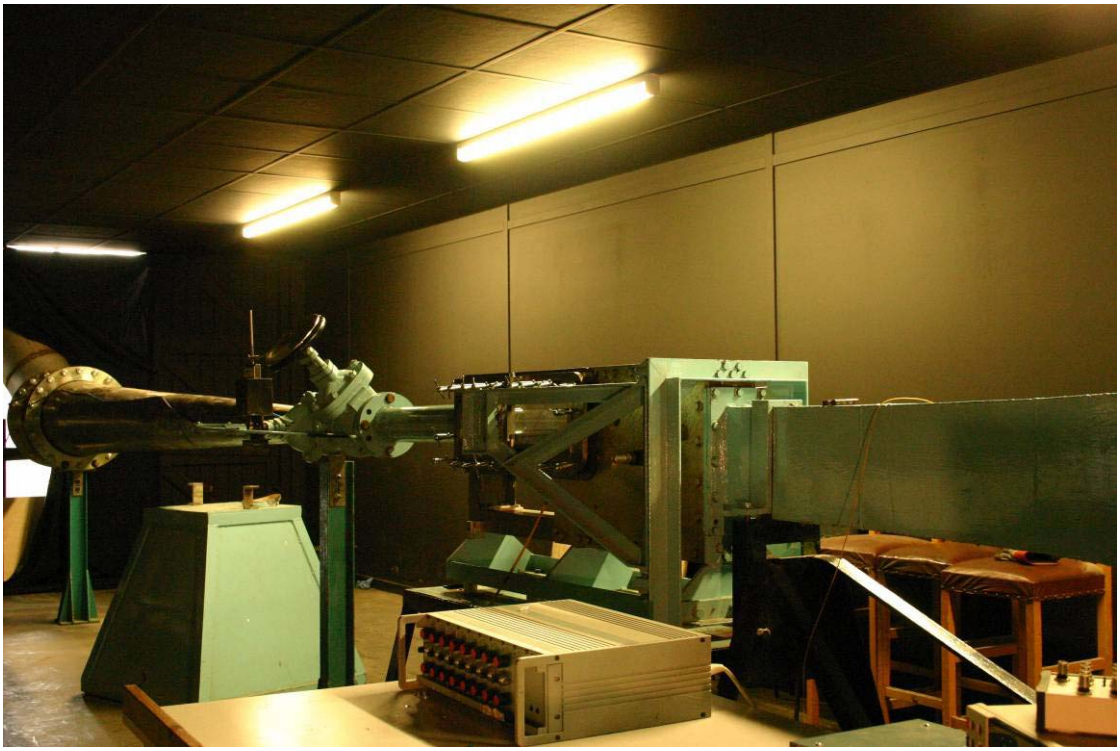

Figure 172 Cranfield 2.5" x 2.5” supersonic wind tunnel

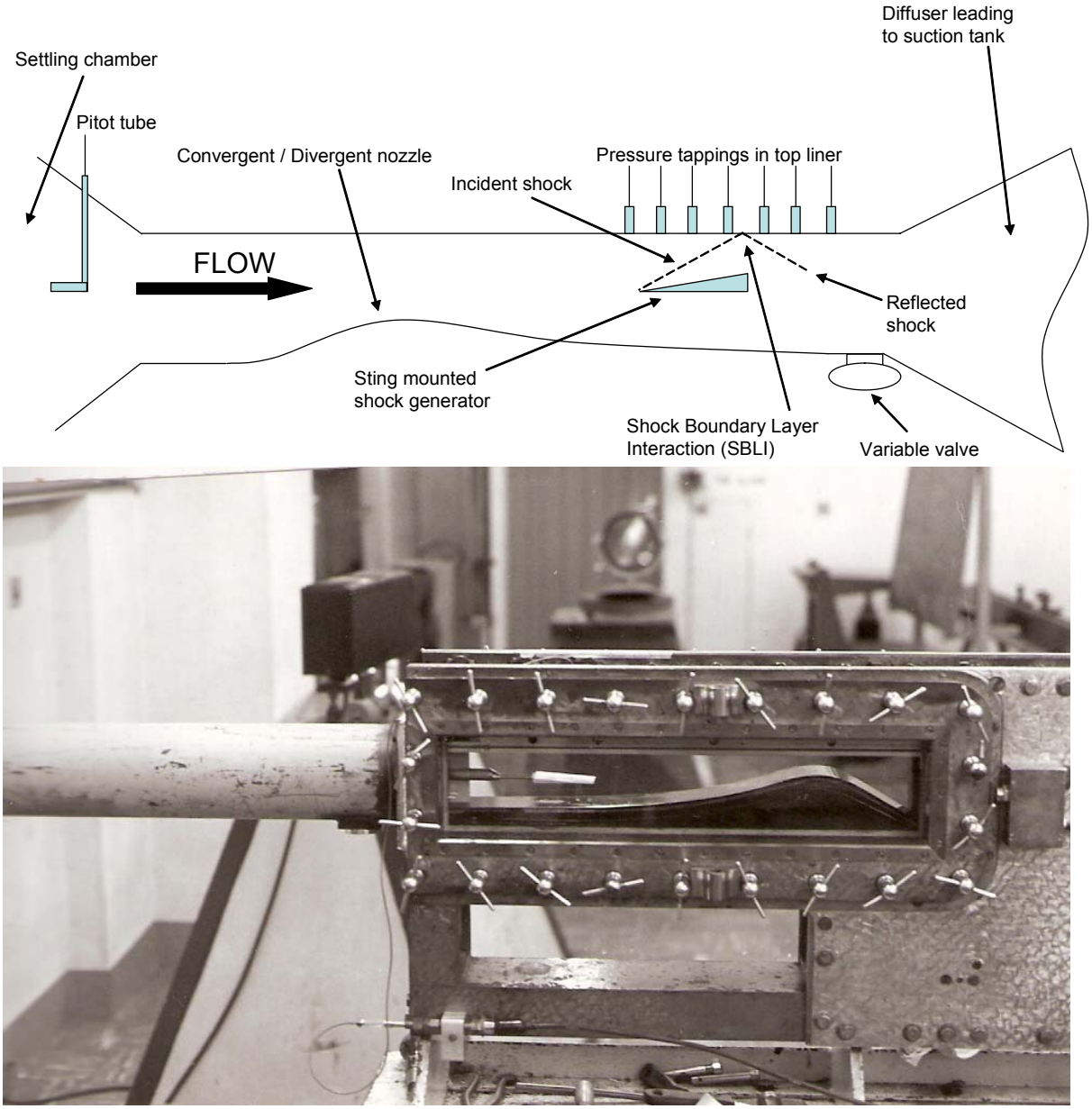

Figure 173 Diagrammatic arrangement of test section (top) and photo (bottom)

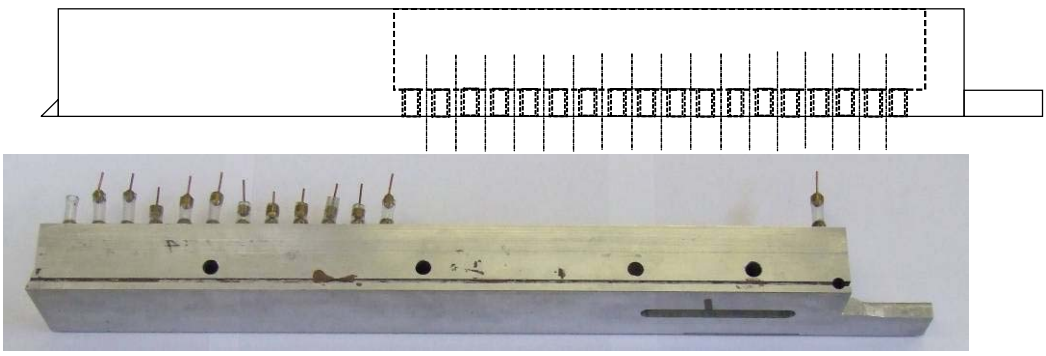

Figure 174 Instrumented top liner: Schematic (top: NTS), Photo bottom (insert removed)

Schlieren set-up

The Schlieren system, utilised to capture the SBLIs, used a continuous LED light source (9200mcd, 20º viewing angle), two parabolic mirrors (40.8" focal length and 4" diameter), a knife-edge (in horizontal position), a convex optical lens (+4) and a CCD camera (Canon EOS 300D). This set-up was at the height of the test section, which is approximately 1230 mm from the floor. The Schlieren system had a Z-type configuration, minimising any possible optical errors. A sharp image of the wedge and sting were obtained by examining the image on a viewing screen with all light extinguished. The exposure time of the photographs was of the order of milliseconds. A schematic of the schlieren set up is included in (Figure 175).

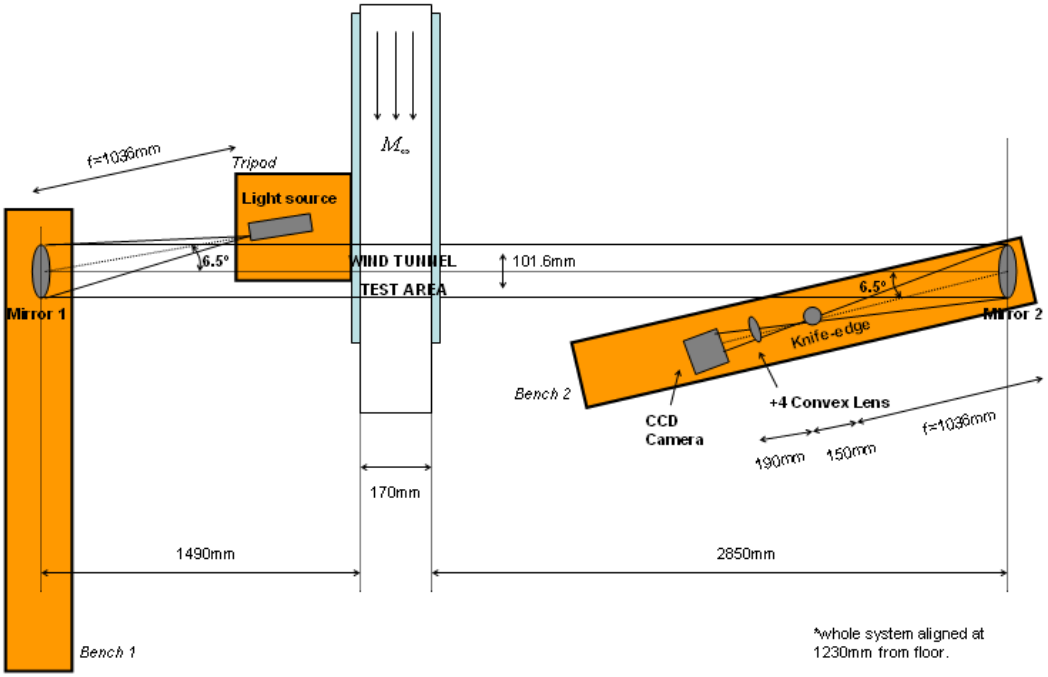

Figure 175 Schlieren system to capture SBLIs

Operating conditions

Shock generator angle (α)	3°	13°
Incident shock angle (θ)	27°	36°
Pressure ratio (p_2 / p_1)	1.2	2.2

Table 2 Shock generator configurations used and corresponding shock angles and theoretical pressure ratios across incident shock.

High speed wall pressure measurements

Wall pressure measurements were taken with fast-response pressure transducers (Kulite XCS-062) which were positioned at five locations along the interaction length. Their locations extend from the upstream flow to the relaxation region farther downstream in the interaction (Figure 10). The transducers have a diameter of 1.7mm and were flush mounted with the surface. They have a range of 0-100 kPa and a natural frequency of approximately 200kHz. The transducer output was amplified using a Fylde M14DS (gain=20) and low-pass filtered using a Fylde 301SF at 50kHz. For each transducer 262144 samples were acquired using a 16-bit National Instruments BNC-2110 DAQ with a sampling frequency of 100 kHz. Ensemble average spectral data was determined by performing FFT analyses on 63 blocks of 8192 samples with a 50% overlap. Each block was windowed using a Hanning function and a power correction factor of 8/3 was applied to counteract the windowing. The frequency resolution was 12.2 Hz.

The typical transducer combined linearity, hysteresis and repeatability error quoted by the manufacturer is ±0.25% full-scale output. The transducers were statically calibrated across their full range (0-100kPa) and the static calibration standard was estimated to have an uncertainty of ±0.13%. Repeatability tests were performed for each configuration. Based on the bias errors and on a statistical analysis of the measurements, an error of ±0.28% is estimated (i.e. ±285Pa relative to atmospheric pressure).

Appendix 3: VKI SBLI characteristics

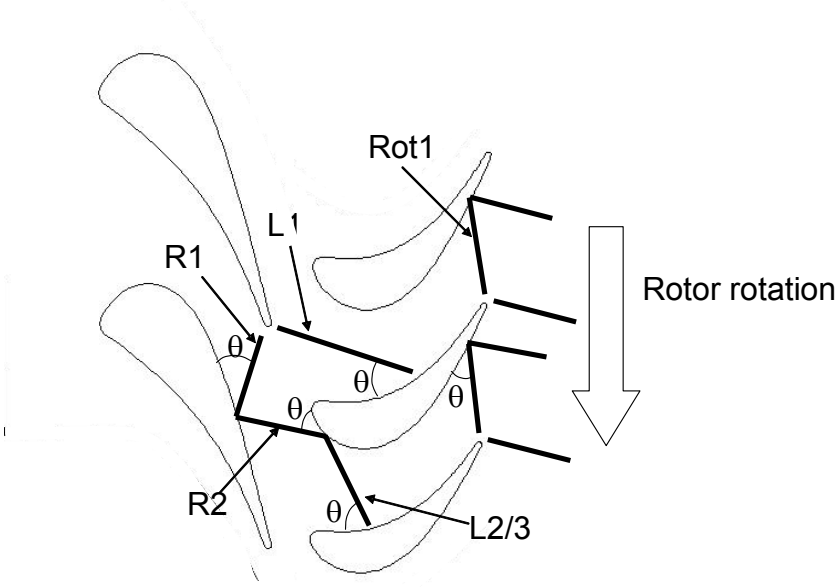

Shock ref.	M_0 [-]	M_2 [-]	θ [deg.]	δ_1 [mm]	Ps_2 / Ps_1 (Shock strength)	$Re_{\delta 1}$ [-]
R1	1.56	1.23	45 ± 3°	2	1.584	28,676
R2	1.34	1.25	0 - 90	upto 4	1.395	17,081
L1	1.56 1.05*	1.38 0.81*	0 – 90	upto 4	1.667	21,152 *
L2/3	Negligible shock strength					
Rot1	Instrumentation discounted					

WP2.2H operating condition (* denotes relative values)

Appendix 4: Computational wake characteristic investigation

Case	P_t profile at rotor domain inlet	
A (ξ/Pt_{max}=0.0028, W=0.05, D/Pt_{max}=0.21)	$Pt(y) = e^{\left[\frac{(\theta-1.784)^2/2}{0.0106^2}\right]} \times 34334.3 + 164336.9$	Wake distribution study
B (ξ/Pt_{max}=0.0028, W=0.1, D/Pt_{max} =0.1)	$Pt(y) = e^{\left[\frac{(\theta-1.784)^2/2}{0.0213^2}\right]} \times 17167.4 + 164336.9$	
C (ξ/Pt_{max}=0.0028, W=0.03, D/Pt_{max} =0.31)	$Pt(y) = e^{\left[\frac{(\theta-1.784)^2/2}{0.0071^2}\right]} \times 51500.3 + 164336.9$	
D (ξ/Pt_{max}=0.0028, W=0.01, D/Pt_{max} =0.31)	$Pt(y) = e^{\left[\frac{(\theta-1.784)^2/2}{0.00235^2}\right]} \times 51500.3 + 164336.9$	
E (ξ/Pt_{max}=0.0028, W=0.01, D/Pt_{max} =0.1)	$Pt(y) = e^{\left[\frac{(\theta-1.784)^2/2}{0.00235^2}\right]} \times 17167.4 + 164336.9$	

References.

ABHARI, R. and GILES, M., 1995. A Navier-Stokes analysis of airfoils in oscillating transonic cascades for the prediction of aerodynamic damping. ASME paper 95-GT-182.

ASHWORTH, D., LAGRAFF, J., SCHULTZ, D. and GRINDROD, K., 1985. Unsteady aerodynamic and heat transfer processes in a transonic turbine stage. ASME Journal of Engineering for gas turbines and Power, (ASME paper 85-GT-128), 107, 1022.

CHAPMAN, C., 2009, Private communication (Rolls-Royce).

CHIANG, H. and KIELB, R., 1993. An analysis system for blade forced response, Journal of Turbomachinery, Volume 115, Issue 4, pp762.

DAWKINS. A, , 2007. Private communication (Rolls-Royce).

DELERY, J.M., 1985. Shock wave/turbulent boundary layer interaction and its control. Progress in Aerospace Sciences, 22, 209-280.

DENOS, R., 2005. Effects of aerodynamic unsteadiness in axial turbomachines: Unsteady flow in turbines:Generalities. Von Karman Institute of fluid mechanics lecture series 2005-03

DENOS, R., ARTS, T., PANIAGUA, G., MICHELASSI, V. and MARTELLI, F., 2001. Investigation of the unsteady rotor aerodynamics in a transonic turbine stage, Journal of Turbomachinery, Volume 123, issue 1, pp81.

DIETZ, A. and AINSWORTH, R., 1992. Unsteady pressure measurements on the rotor of a model turbine stage in a transient flow facility. ASME paper 92-GT-156.

DOAK, P.E. and VAIDYA, P.G., 1969. A note on the relative importance of discrete frequency and broad band noise generating mechanisms in axial fans. Journal of sound and vibration, 9(2), 192-196.

DOORLY, D. and OLDFIELD, M., 1985. Simulation of the effect of shock wave passing on a turbine rotor blade. ASME Journal of Engineering for Gas Turbines and Power, 85-GT-112, 107, 998.

DRING, R., JOSLYN, H., HARDIN, L. and WAGNER, J., 1982. Turbine Rotor-Stator Interaction, Journal of Engineering for Power, Vol. 104, pp729-742.

DUPONT, P., HADDAD, C., ARDISSONE, J. and DEBIEVE, J., 2005. Space and time organization of a shock wave/turbulent boundary layer interaction. Aerospace Science and Technology, Volume 9, Issue 7, pp561-572

DUSSAUGE, J., DUPONT, P. and DEBIEVE, J., 2006. Unsteadiness in shock wave boundary layer interactions with separation, Aerospace Science and Technology, Volume 10, Issue 2, pp 85

DUSSAUGE, J. and PIPONNIAU, S., 2008. Shock/boundary-layer interactions: Possible sources of unsteadiness, Journal of Fluids and Structures, Volume 24, Issue 8, pp1166-1175

ELLIOT, B., 2008. Private communication

ESTRUCH, D., LAWSON, N., MACMANUS, D., GARRY, J. and STOLLERY, J., 2008. Measurement of shock wave unsteadiness using a high-speed Schlieren system and digital image processing. Rev. Sci. Instrum., 79 (12), 126108.

FINCHER, H.M., 1966. Fan-noise, the effect of a single upstream stator. Journal sound and vibration, 3(1), 100-110.

FLUENT Users guide, 2009, ANSYS.

FRANSSON, T., 2007. Flutter-Free Turbomachinery (FUTURE) collaborative project with Rolls-Royce.

GALLUS, H., GROLLIUS, H. and LAMBERTZ, J., 1981, The influence of blade number ratio and blade row spacing on axial-flow compressor stator blade dynamic load and stage sound pressure level. ASME Paper No. 81-GT-165.

GILES, M., 1988. Stator / rotor interaction in a transonic turbine. (AIAA-88-3093),.

GÖTTLICH, E., WOISETSCHLÄGER, J., PIERINGER, P., HAMPEL, B. and HEITMEIR, F., 2005. Investigation of vortex shedding and wake-wake interaction in a transonic turbine using laser-doppler-velocimetry and particle-image-velocimetry. ASME paper GT2005-68579.

HASELBACH, F., et al., 2005, Private communication.

HAWTHORNE, W., 1955. Some Formulae for the calculation of secondary flows in cascades. Aero Research Council, Report No. 17519.

HEMSCH, M. and NIELSEN, J., 1986. Tactical missile aerodynamics: general topics, ISBN 0930403134, American Institute of Aeronautics & Astronautics

HODSON, H., 1983. Boundary layer and loss measurements on the rotor of an axial-flow turbine. ASME paper 83-GT-4.

KAMMERER, A., 2003. Numerical Simulation of Unsteady Flow in a 1.5 Stage Shroudless High Pressure Turbine using SZ02, JA74 and JM51(HYDRA). Rolls-Royce report DHC 127528.

KEMP, N. and AND SEARS, W., 1953. Aerodynamic interference between moving blade rows, Journal of aerospace Science, pp585-597.

KEMP, N. and SEARS, W., 1955. The unsteady forces due to viscous wakes in turbomachines, Journal of Aeronautical Sciences 22, pp478-483.

KIELB, J. and ABHARI, R., 2003. Experimental study of aerodynamic and structural damping in a full-scale rotating turbine. Journal of Engineering for Gas Turbines and Power, 125, 102.

KLEIN, A., 1966. Investigation of the entry boundary layer on the secondary flows in the blading of axial turbines (English translation). BHRAT, BHRAT 1004.

KORAKIANITIS, T., 1992. On the prediction of unsteady forces on gas turbine blades: Part 1- Description of the approach, Journal of turbomachinery, Volume 114, issue 1, pp114.

KORAKIANITIS, T., 1991. On the propogation of viscous wakes and potential flow in axial-turbine cascades," ASME paper No. 91-GT-373.

LANGSTON, L., 1980. Crossflows in A turbine Cascade Passage, 1980, pp866.Journal of Engineering for gas turbines and power, Volume 102, Issue 4, pp866

LEFCORT, M., 1965. An investigation into unsteady blade forces in turbomachines, ASME, Journal of Engineering for gas turbines and power, pp345-354.

MACMANUS, D., 2008. Component aerodynamics lecture Cranfield University.

MANN, D., 2009. Fluent technical support: Stagnation pressure predictions using RANS solvers. Private communication

MEYER, R., 1958. The effects of wakes on the transient pressure and velocity distributions in turbomachines. ASME Vol 80.

MILLER, R., MOSS, R., AINSWORTH, R. and HARVEY, N., 2002. Wake, shock and potential field interactions in a 1.5 stage turbine: Part 1: Vane-rotor and rotor-vane interaction," ASME Paper 2002-GT30435.

MOORE, J. and ADHYE, R., 1985. Secondary flow and losses downstream of a turbine cascade, Journal of Engineering for gas turbines and power, pp961

PARKER, R., 19690-70, Relation between blade row spacing and potential flow interaction effects in turbomachiness, Proceedings of the Institute of Mechanical Engineering, Vol. 184, Pt. 3G, No. 11, 1969-70, pp. 1-8

PARKER, R. and WATSON, J.F., 1972. Interaction effects between blade rows in turbomachines, 1972, Proceedings of the Institute of Mechanical Engineers, Vol. 186, No. 21, pp331-340.

PEREZ, G., 2002, Investigation of the steady and unsteady performance of a transonic HP turbine, Von Karman Institute for fluid dynamics Thesis, ISBN 2-930389-04-4

RESHOTKO, E. and TUCKER, M., 1955. Effect of a discontinuity on turbulent boundary-layer-thickness parameters with application to shock-induced separation. NACA TN 3454.

SANLITURK, K., EWINS, D. and STANBRIDGE, A., 1999. Underplatform dampers for turbine blades: Theoretical modelling, analysis, and comparison with experimental data. ASME, 99-GT-335.

SAXER, A. and GILES, M., 1993. Predictions of 3-D steady and unsteady inviscid transonic stator/rotor interaction with inlet radial temperature non-uniformity. ASME, (ASME 93-GT-10),.

SHARMA, O. and BUTLER, T., 1987. Predictions of endwall losses and secondary flows in axial flow turbine cascades, Journal of turbomachinery, Vol. 109, issue 2, pp229

SIEVERDING, C., VAN HOVE, W. and BOLETIS, E., 1984. Experimental study of the three dimensional flow field in an annular turbine nozzle guide vane, Journal of Engineering Gas Turbines and Power, Vol. 106, No 2, pp437.

SRINIVASAN, A. and CUTTS, D., 1984. Measurement of relative vibratory motion at the shroud interfaces of a fan, ASME Journal of Vibration, Acoustics, Stress and Reliability Design, 106, pp189.

TAYLOR, M. 2003 Rolls-Royce personal communication.

VASCELLARI, M., DENOS, R. and BRAEMBUSSCHE, R., 2004. Design of a transonic high-pressure turbine stage 2D section with reduced rotor/stator interaction. ASME paper, GT-2004-53550

WALKER, G. and OLIVER, A., The effect of interaction between wakes from blade rows in an axial flow compressor on the noise generated by blade interaction. ASME, ASME Paper No. 72-GT-15.

WISLER, D., 1998. The technical and economical relevance of understanding blade row interaction effects in turbomachinery. Von Kármán Institute for Fluid Dynamics, Lecture Series 1998-02 on Blade Row Interference Effects in Axial Turbomachinery Stages.

YAMAMOTO, A., 1987. Production and development of secondary flows and losses in two types of straight turbine cascades: part-1 a stator case, Journal of Turbomachinery , Volume 109, Issue 2, pp186 (8 pages)

YANG, B. and MENQ, C., 1997. Characterization of contact kinematics and application to the design of wedge dampers in turbomachinery blading. ASME, 97-GT-97.